博士論文

Measurement of muonium hyperfine structure at J-PARC

（J-PARC でのミュオニウム超微細構造測定）

東京大学大学院総合文化研究科
広域科学専攻

田中　香津生

２０１５年１２月１０日

Contents

List of Figures

List of Tables

Chapter 1

Introduction

Measurement of the hyperfine structure (HFS) of the ground state of muonium is planned at Japan Proton Accelerator Complex (J-PARC). The experimental apparatus has been constructed at Muon Science Establishment (MUSE) at Material and Life Science Experimental Facility (MLF) in J-PARC, which provides the world ' s highest intensity pulsed muon beam.

Muonium is a hydrogen-line bound state of positive muon and electron, and its chemical symbol is Mu. The HFS of Mu is a good probe for testing Quantum electrodynamics(QED) theory. The muon mass m_μ and magnetic moment μ_μ which are fundamental constants of muon are determined from the Mu HFS experiment at Los Alamos Meson Physics Facility (LAMPF). This thesis describes the technical design of the experiment and provides a detailed analysis of systematic uncertainties.

Muonium HFS can be determined by both a direct measurement in zero field and an indirect measurement of Zeeman effect in strong magnetic field. For the precise experiment, the RF system should have a stable RF feedback system and a tunability of resonance frequency in the cavity. The gas system has a precise pressure gauge and sampling bottles to analyze the purity in a gas. A magnetic shield is need for zero field experiment to suppress external magnetic field at the level of 100 nT.

From the simulation, uncertainties of both measurements are less than that of previous experiments. We aim to start zero field experiments in 2016, high field experiment in 2017.

This thesis is organized as follows: experimental and theoretical backgrounds and physics of Mu HFS measurement are described in Chapter 2. Chapter 3 gives a description of procedure of the measurement. Developments and performance tests of apparatuses is introduced in Chapter 4. Estimation of systematic uncertainties and procedure of analysis are discussed in Chapter 5. Finally, conclusion of this thesis and the future prospect of the experiment are described.

Chapter 2

Overview of Mu HFS experiment

In this chapter, The overview of the Mu HFS experiment is described. The history of measurement of hyperfine structure of hydrogen-like atom is described in Section 2.1.

Breit-Rabi diagram which describes the energy diagram of hydrogen-like atoms in a strong magnetic field is introduced in Section 2.2. Section 2.3 describes the latest theoretical results of the Mu HFS value and the progress of the calculation.

Section 2.5 describes latest results of both Mu HFS measurement in a zero magnetic field and a high magnetic field.

2.1 Measurement of HFS transition of Hydrogen-like atoms

Spectroscopy of hydrogen-like atom has played a great role in scientific developments since the birth of quantum physics. Bohr model of atoms was constructed by from spectroscopic data of hydrogen. In a similar way, current quantum mechanics is based on spectroscopy of hydrogen as shown in Figure 2.1 (e.g. formulation of Bohr's model, explaining fine structure by relativistic quantum mechanics and explaining lamb shift by QED). Recent technology upgrades enable all the higher precision spectroscopy. For instance, the accuracy of spectroscopy of the 1s-2s transition in hydrogen is 0.0042 ppt [13] and that of ground state hyperfine structure (HFS) is 0.6 ppt [14, 15].

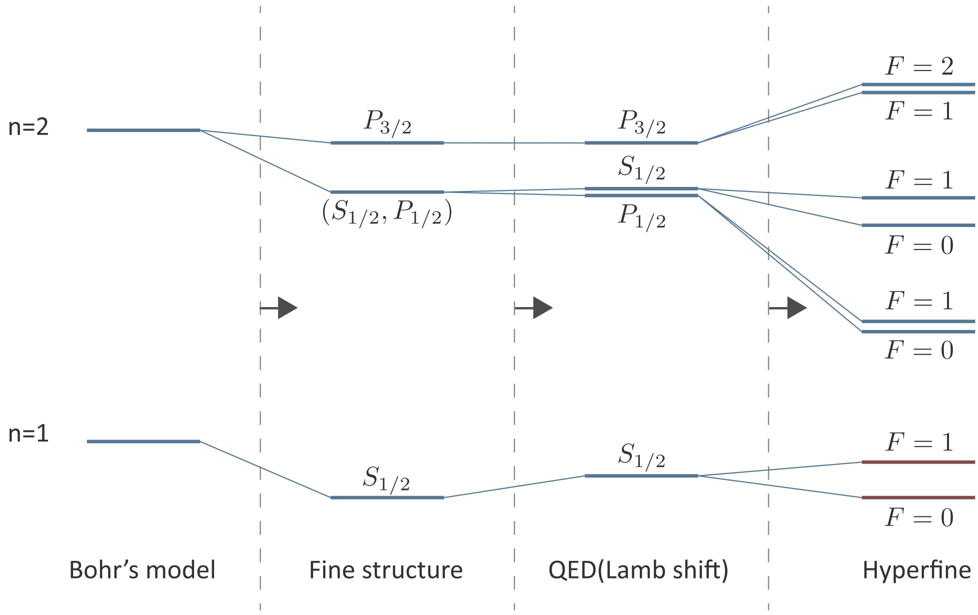

Figure 2.1: Developments of spectroscopy of hydrogen atom. Energy splitting between the red lines is ground state hyperfine splitting.

2.1.1 HFS transition of hydrogen

The latest result of ground state HFS transition of hydrogen is

$$\Delta\nu_{\mathrm{H}}^{\mathrm{ex}} = 1.4204057517667(9)\ \mathrm{GHz}\ (0.6\ \mathrm{ppt})\ [15]. \tag{2.1}$$

Theoretical calculation predicts as high as 560 ppb like

$$\Delta\nu_{\mathrm{H}}^{\mathrm{th}} = 1.4204031(8)\ \mathrm{GHz}\ (560\ \mathrm{ppb})\ [16]. \tag{2.2}$$

The accuracy of the experimental result is much better than that of the theoretical calculation. The main reason comes from the proton internal structure. Thus such a system which contains a composite particle is not suitable for precise test of QED theory.

2.1.2 HFS transition of positronium

Another example of hydrogen-like atom is positronium. Positronium is a bound state of electron e^- and positron e^+, and its chemical symbol is Ps. Since it is a purely leptonic atom and effectively free from the hadronic effects and the weak interactions, it is suitable for the test of bound-state QED compared with hydrogen. The combined value of the two most precise experiments is

$$\Delta\nu_{\mathrm{Ps}}^{\mathrm{ex}} = 203.38865(67)\ \mathrm{GHz}\ (3.3\ \mathrm{ppm})\ [17]. \tag{2.3}$$

The value of theoretical calculation is

$$\Delta\nu_{\mathrm{Ps}}^{\mathrm{th}} = 203.39169(41)\ \mathrm{GHz}\ (2.0\ \mathrm{ppm})\ [18]. \tag{2.4}$$

The value of theoretical calculation has 3σ deviation from the experimental result which has been under discussion for a long time. Recently, a new precision measurement of Ps-HFS free from possible common uncertainties from Ps thermalization effect was performed to check the Ps-HFS discrepancy at University of Tokyo. The new experimental value is

$$\Delta HFS_{\mathrm{Ps}}^{\mathrm{th}} = 203.3942 \pm 0.0016(\mathrm{stat.}) \pm 0.0013(\mathrm{sys.})\ \mathrm{GHz}\ (2.0\ \mathrm{ppm})\ [19], \tag{2.5}$$

in which the first uncertainties are statistical and the second are systematic. It favors the QED calculation within 1.2 standard deviation.

2.1.3 HFS transition of muonium

Ground state hyperfine transition of muonium is also studied many times in the past. Muonium is a bound state of positive muon μ^+ and electron e^-, it is also a leptonic system as positronium. The latest result by LAMPF is

$$\Delta\nu_{\mathrm{M}}^{\mathrm{ex}} = 4.463302765(53)\ \mathrm{GHz}\ (12\ \mathrm{ppb})\ [4]. \tag{2.6}$$

The latest theoretical calculation is

$$\Delta\nu_{\mathrm{M}}^{\mathrm{th}} = 4.463302891(272)\ \mathrm{GHz}\ (61\ \mathrm{ppb})\ [1], \tag{2.7}$$

which are consistent with each other. Since muonium is a pure leptonic atom, the value of Mu HFS transition is able to be calculated with great precision from QED as Equation 2.7, unlike the case of hydrogen (see Equation 2.2). Moreover, the accuracy of theoretical calculation of Mu HFS will be improved by higher-order QED calculation (see Section 2.3).

2.2 Breit-Rabi diagram

There are two methods to measure Mu HFS, in a zero magnetic field and in a high magnetic field. We aim to measure the value by using both methods to control systematic uncertainties. In this section the theoretical background of measurement in high field is described.

In a magnetic field, the Zeeman effect splits the energy levels of the muonium ground state. Spin Hamiltonian of muonium is expressed as[20]

$$\hat{H} = \omega_\mu \boldsymbol{I}_z + \omega_e \boldsymbol{S}_z + \omega_0 \boldsymbol{I}\boldsymbol{S}, \tag{2.8}$$

where ω_μ is muon Zeeman interaction, ω_e is electron Zeeman interaction and ω_0 is hyperfine interaction, expressed as

$$\omega_\mu = g'_\mu \mu_B^\mu B = +\frac{g'_\mu}{2}\frac{|e|}{m_\mu}B, \tag{2.9}$$

$$\omega_e = g_J \mu_B^e B = -\frac{g_J}{2}\frac{|e|}{m_\mathrm{e}}B, \tag{2.10}$$

where g'_μ and g_J are from the free muon and electron g values g_μ and g_e with the relativistic binding correction as[21]

$$g'_\mu = g_e(1-\frac{1}{3}\alpha^2+\frac{\alpha^2}{2}\frac{m_e}{m_\mu}), \tag{2.11}$$

$$g_J = g_\mu(1-\frac{1}{3}\alpha^2+\frac{\alpha^2}{2}\frac{m_e}{m_\mu}+\frac{\alpha^3}{4\pi}), \tag{2.12}$$

where α is fine structure constant. To determine the energy eigenvalues, we must diagonalize the matrix of the Hamiltonian function $\hat{H}$ as

$$\hat{H}\begin{pmatrix}|\alpha\alpha\rangle\\|\alpha\beta\rangle\\|\beta\alpha\rangle\\|\beta\beta\rangle\end{pmatrix} = \begin{pmatrix}\frac{1}{2}\omega_e+\frac{1}{2}\omega_\mu+\frac{1}{4}\omega_0 & 0 & 0 & 0\\ 0 & \frac{1}{2}\omega_e-\frac{1}{2}\omega_\mu-\frac{1}{4}\omega_0 & \frac{1}{2}\omega_0 & 0\\ 0 & \frac{1}{2}\omega_0 & -\frac{1}{2}\omega_e+\frac{1}{2}\omega_\mu-\frac{1}{4}\omega_0 & 0\\ 0 & 0 & 0 & -\frac{1}{2}\omega_e-\frac{1}{2}\omega_\mu+\frac{1}{4}\omega_0\end{pmatrix}\begin{pmatrix}|\alpha\alpha\rangle\\|\alpha\beta\rangle\\|\beta\alpha\rangle\\|\beta\beta\rangle\end{pmatrix}, \tag{2.13}$$

where α and β are eigenfunctions of muon and electron corresponding to spin orientation in the positive z direction and negative z direction. The spin eigenfunctions are

$$|1\rangle = |\alpha\alpha\rangle, \tag{2.14}$$

$$|2\rangle = c\,|\alpha\beta\rangle + s\,|\beta\alpha\rangle, \tag{2.15}$$

$$|3\rangle = |\beta\beta\rangle, \tag{2.16}$$

$$|4\rangle = c\,|\beta\alpha\rangle - s\,|\alpha\beta\rangle. \tag{2.17}$$

s and c are

$$s = \frac{1}{\sqrt{2}}(1-\frac{x}{\sqrt{1+x^2}})^{1/2}, \tag{2.18}$$

$$c = \frac{1}{\sqrt{2}}(1+\frac{x}{\sqrt{1+x^2}})^{1/2}, \tag{2.19}$$

where x is the term proportional to the magnetic field (B) as

$$x = \frac{(g_J \mu_B^e + g'_\mu \mu_B^\mu)}{\omega_0} B. \tag{2.20}$$

The energy eigenvalues(E_{HFS}^B) are given in the above matrix as

$$\begin{aligned}
E_{\mathrm{HFS}}^B(|1>) &= +\frac{\omega_0}{4} + \frac{1}{2}(\omega_e + \omega_\mu), && (2.21)\\
E_{\mathrm{HFS}}^B(|2>) &= -\frac{\omega_0}{4} + \frac{\omega_0}{2}\sqrt{1+x^2}, && (2.22)\\
E_{\mathrm{HFS}}^B(|3>) &= +\frac{\omega_0}{4} - \frac{1}{2}(\omega_e + \omega_\mu), && (2.23)\\
E_{\mathrm{HFS}}^B(|4>) &= -\frac{\omega_0}{4} - \frac{\omega_0}{2}\sqrt{1+x^2}. && (2.24)
\end{aligned}$$

These four eigenvalues can be organized as,

$$E_{\mathrm{HFS}}^B(F = \frac{1}{2} \pm \frac{1}{2}, m_F) = -\frac{\omega_0}{4} + g'_\mu \mu_B^\mu m_F B \pm \Delta \frac{\omega_0}{2} \sqrt{1 + \frac{4 m_F x}{2I+1} + x^2}. \tag{2.25}$$

where m_F is represented as magnetic quantum number.

Figure 2.2 is the Breit-Rabi diagram which shows that the ground state splits into four substates in a static magnetic field. ν_{12} and ν_{34} are calculated from Equation 2.25 as

$$\begin{aligned}
h\nu_{12} &= -g'_\mu \mu_B^\mu B + \frac{\omega_0}{2}[(1+x) - \sqrt{1+x^2}], && (2.26)\\
h\nu_{34} &= +g'_\mu \mu_B^\mu B + \frac{\omega_0}{2}[(1-x) - \sqrt{1+x^2}]. && (2.27)
\end{aligned}$$

According to Equation 2.26 and 2.27, transition frequency of Mu HFS in zero magnetic field ω_0 is obtained by

$$\omega_0 = \nu_{12} + \nu_{34}. \tag{2.28}$$

Thus the Mu HFS transition energy is obtained by summing ν_{12} and ν_{34} in a common magnetic field.

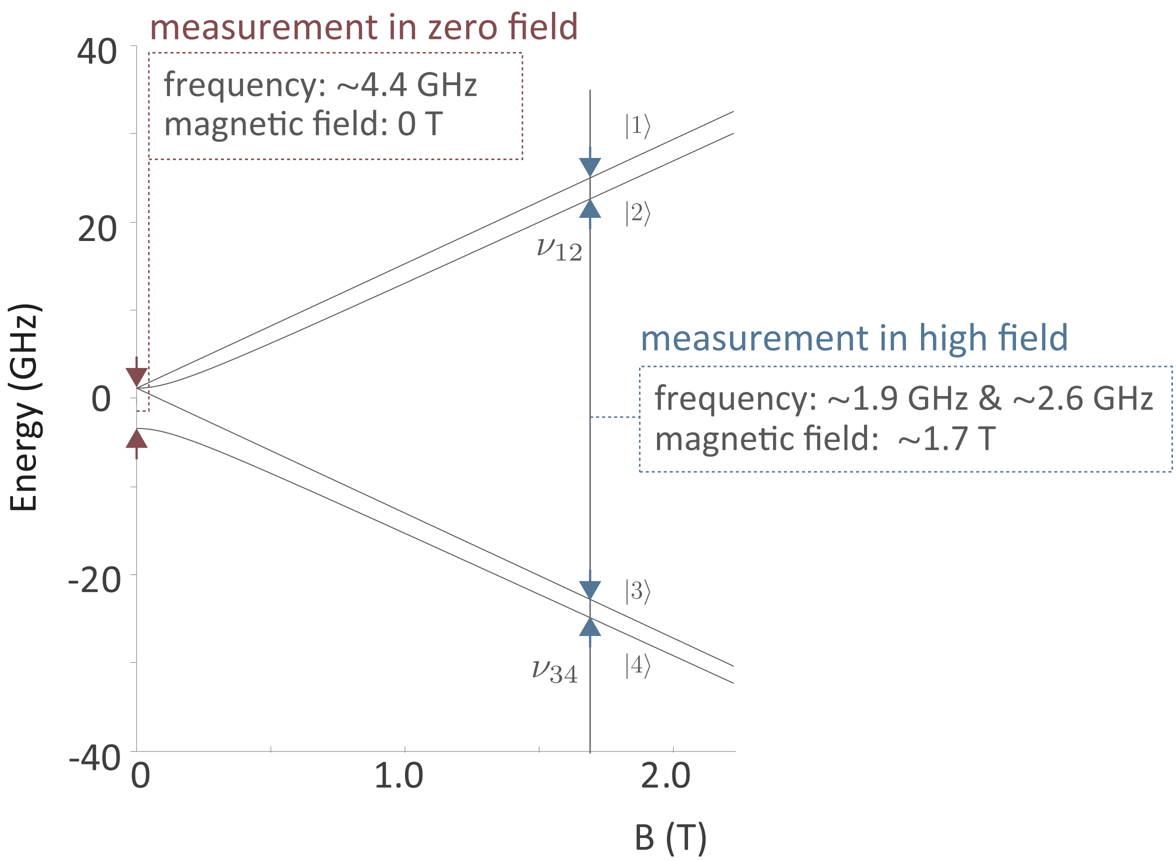

Figure 2.2: Energy levels of the Mu HFS as a function of external magnetic field. There are two methods to measure Mu HFS, in a zero field and in a high magnetic field.

2.3 Theory of Mu HFS

Theoretical calculation of Mu HFS is reviewed in CODATA2010 [1] as follows.

Following QED theory, Mu HFS is able to expressed as

$$\begin{aligned}\Delta\nu_{\mathrm{M}}^{\mathrm{th}} &= \Delta\nu_{\mathrm{F}}(1+\alpha_\mu)(1+\frac{3}{2}(Z\alpha)^2+\frac{17}{8}(Z\alpha)^4+...)\\ &+ \Delta\nu_{\mathrm{rad}}+\Delta\nu_{\mathrm{rec}}+\Delta\nu_{\mathrm{r-r}}+\Delta\nu_{\mathrm{weak}}+\Delta\nu_{\mathrm{had}}. \end{aligned} \tag{2.29}$$

where Z is the charge number of the nucleus which for muonium is 1, α is the fine structure constant, a_μ is the muon magnetic moment anomaly, E_F is Fermi energy given by

$$E_F = \frac{16}{3}(Z\alpha)^2 R_\infty \frac{\mu_\mu}{\mu_p}(1+\frac{m_{\mathrm{e}}}{m_\mu})^{-3}, \tag{2.30}$$

the terms labeled, rad, rec, r–r, weak, had account for the radiative recoil, radiative-recoil, electroweak, and hadronic contributions to the hyperfine splitting, respectively.

The radiative corrections are

$$\Delta\nu_{\mathrm{rad}} = \Delta\nu_{\mathrm{F}}(1+a_\mu)(D^{(2)}(Z\alpha)(\frac{\alpha}{\pi})+D^{(4)}(Z\alpha)(\frac{\alpha}{\pi})^2+D^{(6)}(Z\alpha)(\frac{\alpha}{\pi})^3), \tag{2.31}$$

where the functions $D^{(n)}(Z\alpha)$ are contributions from n virtual photons. The leading term is

$$\begin{aligned}D^{(2)}(Z\alpha) &= \frac{1}{2}+(\ln 2-\frac{5}{2})\pi Z\alpha\\ &+ (-\frac{2}{3}\ln^2(Z\alpha)^{-2}+(\frac{281}{360}-\frac{8}{3}\ln(2))\ln(Z\alpha)^{-2}+16.9037...)(Z\alpha)^2\\ &+ ((\frac{5}{2}\ln 2-\frac{547}{96})\ln(Z\alpha)^{-2})\pi(Z\alpha)^3\\ &+ G(Z\alpha)(Z\alpha)^3. \end{aligned} \tag{2.32}$$

The function $G(Z\alpha)$ accounts for all higher-order contributions in powers of $Z\alpha$; it can be divided into self-energy and vacuum polarization contributions, $G(Z\alpha) = G_{\mathrm{SE}}(Z\alpha)+G_{\mathrm{VP}}(Z\alpha)$.

The one-loop self-energy for the Mu HFS have calculated with the result

$$G_{\mathrm{SE}}(\alpha) = -13.8308(43)[1]. \tag{2.33}$$

The vacuum polarization part is

$$G_{\mathrm{SE}}(\alpha) = 7.227(9)[1]. \tag{2.34}$$

The leading term of weak interaction is induced by the neutral currents given by a Z-boson exchange. The contribution is expressed as [22, 1]

$$\Delta\nu_{weak} \approx -65 \text{ Hz}. \tag{2.35}$$

where G_F is the Fermi constant of the weak interaction. Second largest contributions of weak interaction are 1 % of the leading contribution (see Equation 2.35) and thus negligible [23].

The leading term of hadronic contribution is presented in the form [24, 1]

$$\Delta\nu_{had-vp} = 236(4) \text{ Hz}. \tag{2.36}$$

where Z is the nuclear charge.

The total uncertainty of four principle sources ν_{rad}, ν_{rec}, $\nu_{\mathrm{r-r}}$, and , ν_{had} is 98 Hz. Then the theoretical value is obtained as

$$\Delta\nu_{\mathrm{M}}^{\mathrm{th}} = 4.463302891(272) \text{ GHz (61 ppb) [1]}, \tag{2.37}$$

by using values of the constants obtained from the 2010 adjustment without the two LAMPF measured values of ν_{12} and ν_{34}. The main source of uncertainty in this value is the mass ratio $\frac{m_\mu}{m_{\mathrm{e}}}$.

2.4 Muon magnetic moment and mass from MuHFS experiment

The muon–proton magnetic moment ratio $\frac{\mu_\mu}{\mu_{\mathrm{p}}}$ is obtained by measurement of Mu HFS in high field as

$$\frac{\mu_\mu}{\mu_{\mathrm{p}}} = \frac{\Delta\nu_{\mathrm{M}}^{\mathrm{ex}2} - \nu^2\left(f_{\mathrm{p}} + 2s_{\mathrm{e}} f_{\mathrm{p}} \nu_{f_{\mathrm{p}}}\right)}{4s_{\mathrm{e}} f_{\mathrm{p}}^2 - 2f_{\mathrm{p}}\nu(f_{\mathrm{p}})} \left(\frac{g_\mu(\mathrm{Mu})}{g_\mu}\right)^{-1}, \tag{2.38}$$

where $\Delta\nu_{\mathrm{M}}^{\mathrm{ex}}$ and $\nu_{f_{\mathrm{p}}}$ are the sum and difference of two measured transition frequencies, f_{p} is the free proton NMR reference frequency corresponding to the magnetic field used in the experiment, $\frac{g_{\mathrm{e}}(\mathrm{Mu})}{g_{\mathrm{e}}}$ is the bound-state correction for the muon in muonium and

$$s_e = \frac{\mu_{\mathrm{e}}}{\mu_{\mathrm{p}}}\frac{g_\mu(\mathrm{Mu})}{g_\mu}, \tag{2.39}$$

where $\frac{g_\mu(\mathrm{Mu})}{g_\mu}$ is the bound-state correction for the electron in muonium.

The most precise value for $\frac{\mu_\mu}{\mu_{\mathrm{p}}}$ obtained by the Mu HFS experiment at LAMPF [4] and the recommended value of $\frac{\mu_\mu}{\mu_{\mathrm{p}}}$ from CODATA2010 [1] are

$$\frac{\mu_\mu}{\mu_{\mathrm{p}}}_{\mathrm{HFS}} = 3.18334524(37), \tag{2.40}$$

$$\frac{\mu_\mu}{\mu_{\mathrm{p}}}_{\mathrm{CODATA}} = 3.183345107(84). \tag{2.41}$$

$\frac{m_\mu}{m_{\mathrm{e}}}$ is also obtained by $\frac{\mu_\mu}{\mu_{\mathrm{p}}}$ and the equation

$$\frac{m_\mu}{m_{\mathrm{e}}} = \frac{g_\mu}{2}\frac{\mu_{\mathrm{p}}}{\mu_\mu}\frac{\mu_B^e}{\mu_{\mathrm{p}}}. \tag{2.42}$$

The value from the experiment and the recommended value of $\frac{m_\mu}{m_{\mathrm{e}}}$ from CODATA2010 [1] are

$$\frac{m_\mu}{m_{\mathrm{e}}}_{\mathrm{HFS}} = 206.768276(24), \tag{2.43}$$

$$\frac{m_\mu}{m_{\mathrm{e}}}_{\mathrm{CODATA}} = 206.7682843(52). \tag{2.44}$$

The uncertainty of the value from Mu HFS is about five times higher than the uncertainty of the recommended value of CODATA2010[1]. The reason is that the value from CODATA is obtained by the comparison of experimental value of Mu HFS($\Delta\nu_{\mathrm{M}}^{\mathrm{ex}}$) and theoretical value($\Delta\nu_{\mathrm{M}}^{\mathrm{th}}$) whose parameter α is coming from the average of other data (see Figure 2.3) which is siginificantly small uncertainty.

2.4.1 Testing QED theory

Contrary to Subsection2.4, fine structure constant α can be obtained from comparison of experimental value of Mu HFS($\Delta\nu_{\mathrm{M}}^{\mathrm{ex}}$) and theoretical value($\Delta\nu_{\mathrm{M}}^{\mathrm{th}}$) without parameter

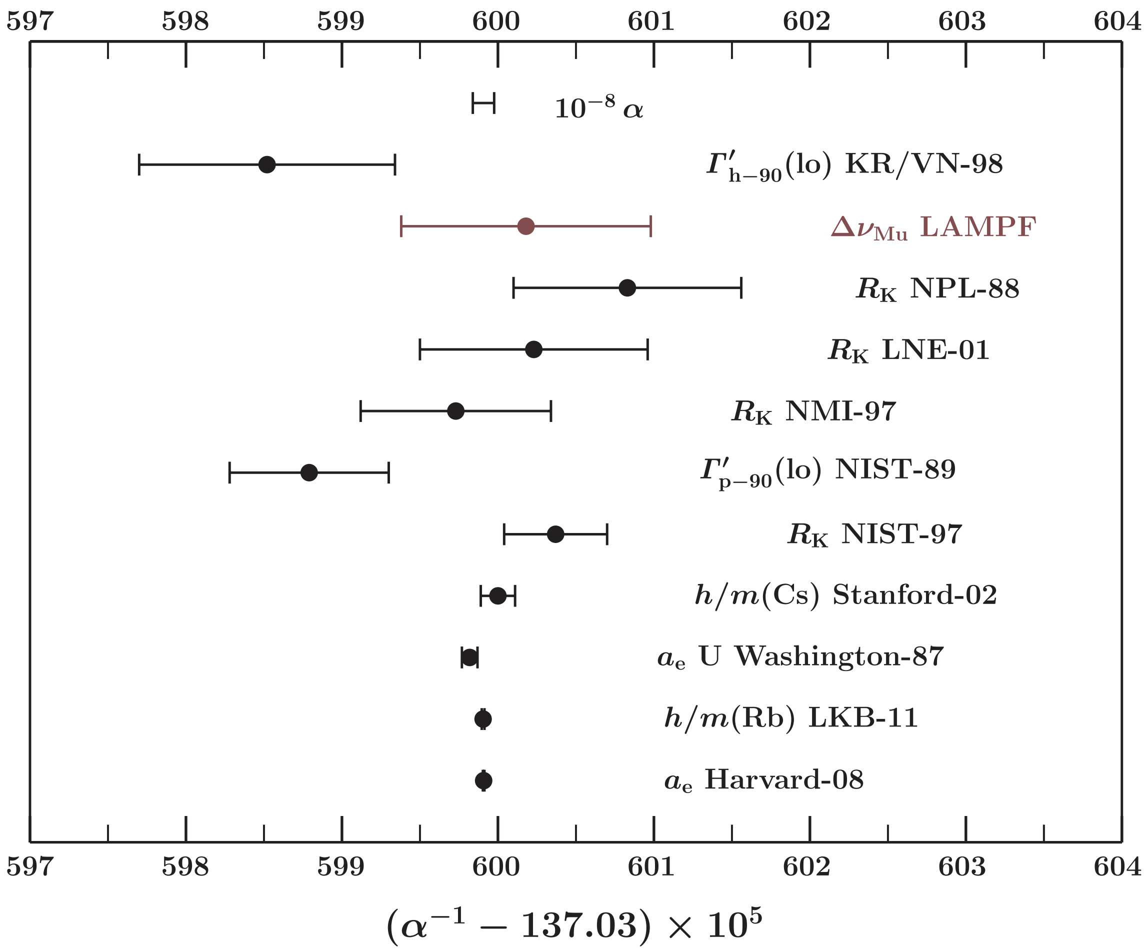

Figure 2.3: Values of fine structure constant publication of the CODATA 2010 [1].

α from other experimental data. Accordingly, it can also be said that comparison between *alpha* from a MuHFS experiment and average from other experiments can be good test of two-body bound state QED for muon sector.

2.4.2 Contribution to g–2 experiment

The precise determinations of $\frac{\mu_\mu}{\mu_p}$ and $\frac{m_\mu}{m_p}$ by the Mu HFS experiment can contribute to the understanding of the muon anomalous magnetic moment (muon g–2) puzzle. BNL E821 experiment measured muon g–2, and reported 3.3 σ deviation from the calculation based on the Standard Model (see 2.4).

A new experiment with a new concept of very low-emittance muon beam is planned at J-PARC can improve the experimental uncertainty by a factor of 5.

Figure 2.5 shows a conceptual drawing of the experimental setup of g–2 experiment. Polarized muons travel on a circular orbit in a constant magnet field. The muon spin direction is corresponded to muon momentum direction when muons enter the storage ring. By the motion of the muon magnetic moment in the homogeneous magnetic field the spin axis varies in a particular way as described by the Larmor precession. Larmor angular frequency ω_s is slightly bigger than cyclotron angular frequency ω_c by the difference $\omega_\alpha = \omega_s - \omega_c$ after each cycle.

$$\omega_c = \frac{eB}{2m_\mu}, \tag{2.45}$$

$$\omega_s = \frac{eB}{2m_\mu} + \alpha_\mu \frac{eB}{m_\mu}, \tag{2.46}$$

$$\omega_\alpha = \alpha_\mu \frac{eB}{m_\mu}, \tag{2.47}$$

where $\alpha_\mu = (g-2)/2$ is a anomalous magnetic dipole moment of muon. The magnetic field B is measured by NMR using a standard probe of H_2O at sub-ppm level. This standard probe can be related to the magnetic moment of a free proton by

$$B = \frac{\omega_p}{2\mu_\mathrm{p}}. \tag{2.48}$$

where ω_p is the Larmor precession angular velocity of a proton in a water. By using a common NMR probe with Mu HFS experiment, this value can be substituted to $\frac{\mu_\mu}{\mu_p}$

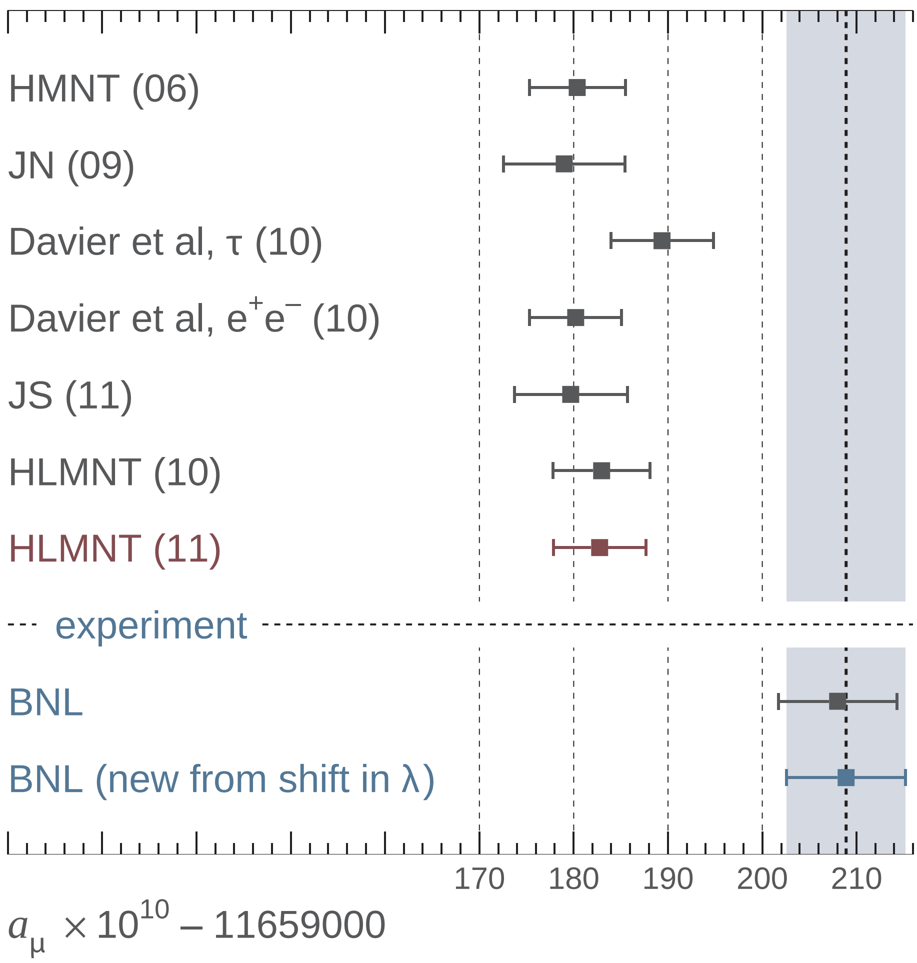

Figure 2.4: A result of g–2 measurement at BNL. The significance of the deviation is 3.3 standard deviations from the existing theory [2].

which is determined more accurate than the precision of NMR probe. Therefore, actual value of the measurement is

$$
\begin{aligned}
R &= \frac{\omega_\alpha}{\omega_\mathrm{p}} && (2.49)\\
&= \alpha_\mu \frac{e}{m_\mu}\frac{1}{2\mu_\mathrm{p}} && (2.50)\\
&= \alpha_\mu \frac{e}{2m_\mu}\frac{1}{\mu_\mu}\frac{\mu_\mu}{\mu_\mathrm{p}} && (2.51)\\
&= \alpha_\mu \frac{1}{g_\mu}\frac{\mu_\mu}{\mu_p} && (2.52)\\
&= \frac{\alpha_\mu}{1+\alpha_\mu}\frac{\mu_\mu}{\mu_p}. && (2.53)
\end{aligned}
$$

Thus g–2 value is obtained by both R obtained by g–2 experiment and $\frac{\mu_\mu}{\mu_p}$ determined by Mu HFS. For 5 times improvement such as the level of 100 ppb, 170 ppb uncertainty of $\frac{\mu_\mu}{\mu_p}$ from latest MuHFS experiment is no more ignorable. Therefore, more precise measurement of Mu HFS is required as input parameter for next g–2 experiment.

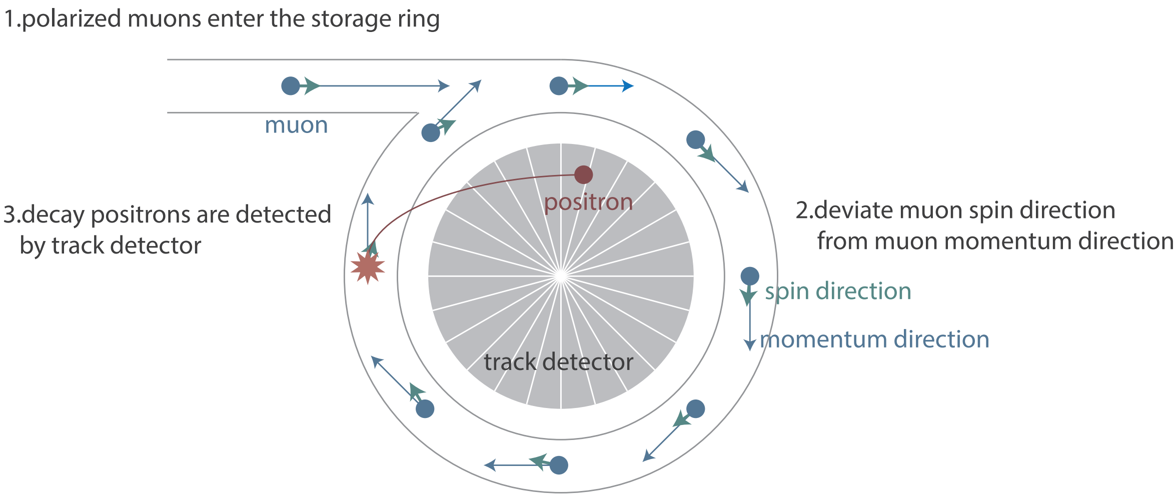

Figure 2.5: A conceptual drawing of the experimental setup of the g–2 experiment.

2.4.3 Testing CPT and Lorentz invariance

Here have been several attempts to formalize Standard Model Extension (SME) which contains the Standard Model and all possible operators that break CPT and Lorentz symmetries. Additional Hamiltonian terms which violate CPT and Lorentz invariance would shift frequencies of muonium transitions. Such shifts would result sidereal oscillation in ν_{12} and ν_{34} frequencies. The leading-order Lorentz-violating energy shift in muonium can be obtained from Hamiltonians using perturbation theory and relativistic two-fermion techniques [25]. The corresponding shifts $\delta\nu_{12}$ and $\delta\nu_{34}$ in the frequencies ν_{12} and ν_{34} can be determined as

$$\delta\nu_{12} \approx -\delta\nu_{34} \approx -\tilde{b}_3^{\mu}/\pi, \tag{2.54}$$

where $\tilde{b}_3^{\mu}$ is laboratory frame parameter of muon sector, mass dimension is 3.

A suitable choice of basis $\hat{X}, \hat{Y}, \hat{Z}$ for a nonrotating frame is standard celestial equatorial axes, with the $\hat{Z}$ direction oriented along the Earth's rotational north pole. an experimental constraint on $\delta\nu_{12}$ implies

$$\frac{1}{\pi}|\sin\chi|\sqrt{(\tilde{b}_X^{\mu})^2 + (\tilde{b}_Y^{\mu})^2} \leq \delta\nu_{12} \tag{2.55}$$

in which χ is the angle between $\hat{Z}$ and the quantization axis defined by the laboratory magnetic field where the muonium experiment is performed. The transformation from the lab frame quantity $\tilde{b}_3^{\mu}$ to the non-rotating celestial frame quantities $\tilde{b}_J^{\mu}$ (where $J = X, Y, Z$) is given by

$$\tilde{b}_3^{\mu} = \tilde{b}_Z^{\mu}\cos\chi + (\tilde{b}_X^{\mu}\cos\Omega t + \tilde{b}_Y^{\mu}\sin\Omega t)\sin\chi. \tag{2.56}$$

Figure 2.6 shows that no time dependence was found at a level of 20 Hz at the LAMPF experiments, which corresponds to a 68% confidence level limit on the non-rotating frame components

$$\sqrt{(\tilde{b}_X^{\mu})^2 + (\tilde{b}_Y^{\mu})^2} \leq 2 \times 10^{-23}\ \text{GeV}[3]. \tag{2.57}$$

On the other hand, Lorentz violation signatures were searched from a sidereal variation of $\omega_{\alpha}^{\mu^{\pm}}$ in g–2 experiment at BNL (see Subsection 2.4.2). Limits on the non-rotating frame components are

$$\sqrt{(\tilde{b}_X^{\mu^+})^2 + (\tilde{b}_Y^{\mu^+})^2} \leq 1.4 \times 10^{-24} \text{ GeV}, \tag{2.58}$$
$$\sqrt{(\tilde{b}_X^{\mu^-})^2 + (\tilde{b}_Y^{\mu^-})^2} \leq 2.6 \times 10^{-24} \text{ GeV[26]}, \tag{2.59}$$

which is one of the strongest constrain of Lorentz violation for muon sector[27]. Thus improvement of the uncertainty of Mu HFS by a factor of 10 enables the test of Lorentz violation comparably to g–2 experiment at BNL.

2.4.4 Proton radius puzzle

The measurement of a Lamb shift of muoniuc hydrogen results 7σ deviation from world average of electron scattering data on proton rms charge radius defined as

$$r_{\mathrm{C}} = \sqrt{\int r^2 \rho_E(\boldsymbol{r}) \mathrm{d}^3 r}, \tag{2.60}$$

where $\rho_E(\boldsymbol{r})$ is the charge distribution and further precise measurement is in the planning stage [28]. On the other hand, the Zemach radius of the proton is defined in terms of an integral of the charge and magnetic form factors of the proton as

$$r_{\mathrm{Z}} = \int \mathrm{d}^3 r r \int \mathrm{d}^3 r' \rho_E(\boldsymbol{r} - \boldsymbol{r'}) \rho_M \boldsymbol{r}'. \tag{2.61}$$

Difference between ground-state hyperfine splitting in hydrogen and muonium after correcting for magnetic moment and reduced mass effects, is due solely to proton structure. HFS.[29] Furthermore, Mu HFS is a good probe for new light particle search, such as dark photon, axionlike particles [30, 31, 32].

2.5 Review of Mu HFS experiment

The previous results of Mu HFS measurements are summarized in Table 2.1 and Figure 2.7. As seen in the table, the precision has greatly improved during 1970s but the pace of improvement became slower in 1980s, and there has been no measurement since 1999. The rapid improvement in 70s is mainly thanks to the construction of so-called Meson

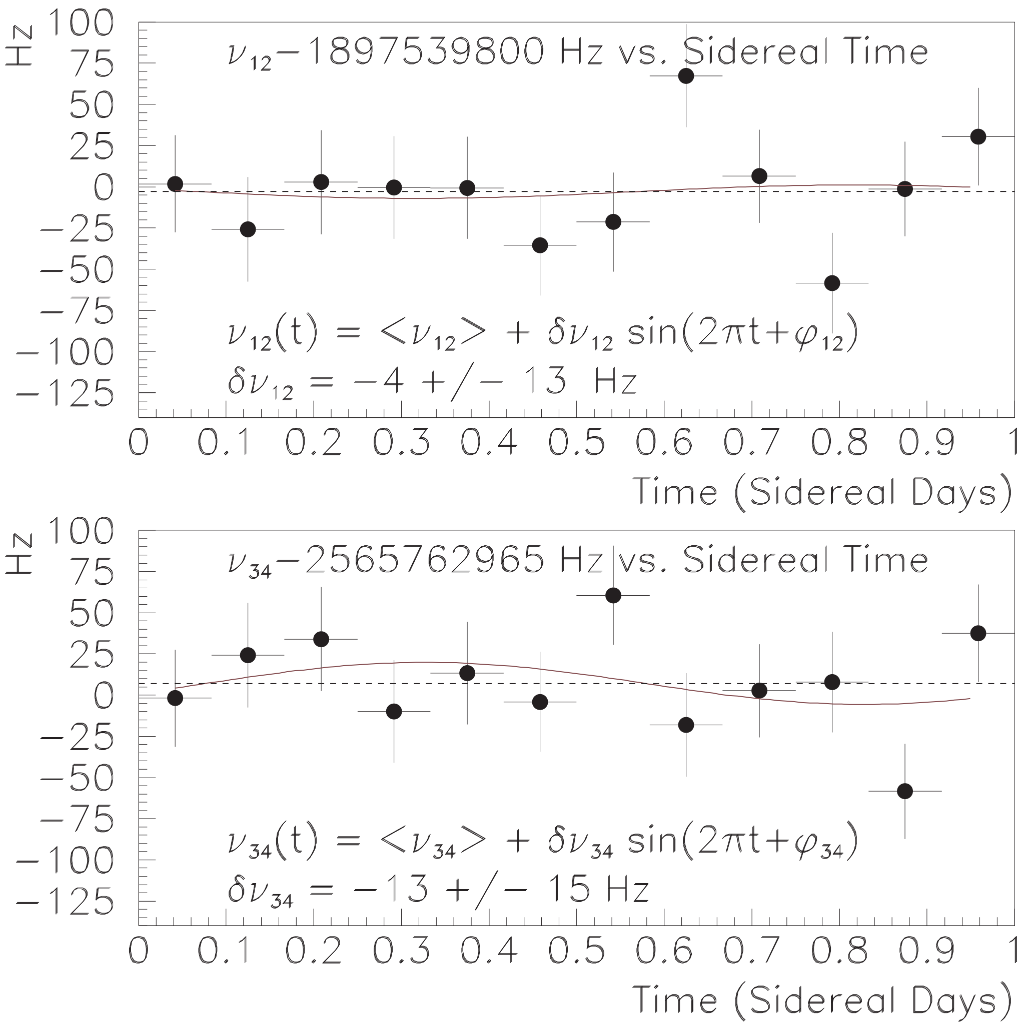

Figure 2.6: Two years of data on ν_{12} and ν_{34} at the LAMPF experiment are shown binned versus sidereal time and fit for a possible sinusoidal variation. The amplitudes are consistent with zero [3].

Facilities over the world. Newly-built accelerators provided intense muon beams, which made precision measurements possible. The inauguration of J-PARC MUSE is very important - it gives the most intense pulsed muon beam in the world. This gives a unique opportunity to put Mu HFS measurement into new level of precision.

Time	Group	$\Delta\nu$	ppm	B field (T)	Ref
1961	Yale-Nevis	5500^{+2900}_{-1500} MHz		0.01-0.58	[33, 34]
1962	Yale-Nevis	4 461.3(2.0) MHz	450	1.1353	[35, 36]
1964	Yale-Nevis	4 463.24(12) MHz	27	0.5	[37, 38]
1966	Yale-Nevis	4 463.18(12) MHz	27	2.7×10^{-4}	[39]
1969	Yale-Nevis	4 463.26(4) MHz	9.0	3×10^{-4}	[40]
1969	Chicago	4 463.317(21) MHz	4.7	1.1353	[36, 41]
1970	Chicago	4 463.302 2(89) MHz	2.0	1.1353	[42]
1971	Yales-Nevis	4 463.308(11) MHz	2.5	3×10^{-4} and 1×10^{-6}	[43]
1973	Chicago-SREL	4 463 304.4(2.3) kHz	0.5	0	[44]
1975	LAMPF	4 463 302.2(1.4) kHz	0.3	very weak	[45]
1977	LAMPF	4 463 302.35(52) kHz	0.12	1.36	[46, 47]
1982	LAMPF	4 463 302.88(16) kHz	0.036	1.36	[48]
1999	LAMPF	4 463 302.765(53) kHz	0.012	1.7	[4]

Table 2.1: Comparison of Mu HFS measurements.

2.5.1 Latest zero field experiment

The latest zero field experiment of Mu HFS is carried out at LAMPF[45],

$$\Delta\nu_{\mathrm{M}}^{\mathrm{zf}} = 4463302.2(1.4)\ \mathrm{kHz}\ (0.3\ \mathrm{ppm}). \tag{2.62}$$

The strength of the magnetic field is less than 100 nT. However, the leakage magnetic field from outside of the magnetic shield is the main contributor to the systematic uncertainty.

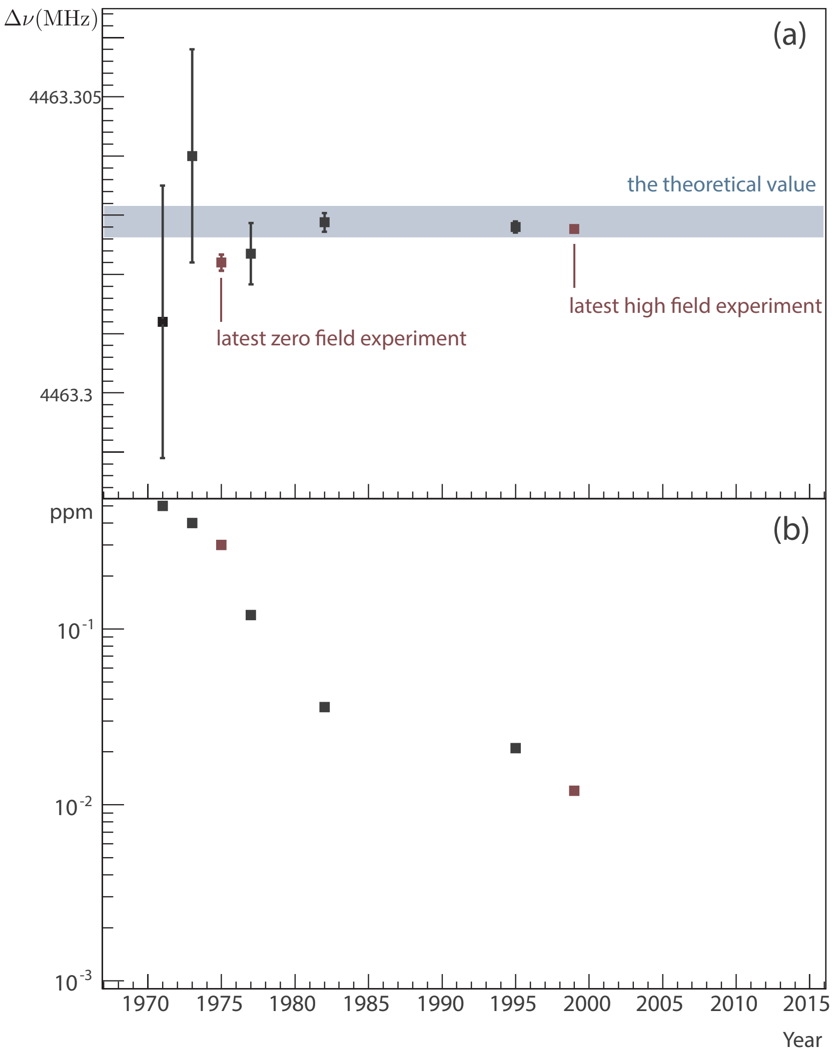

Figure 2.7: (a) Values of Mu HFS at several past experiments since 1970. A blue area is a range of the theoretical value from Equation 2.7. (b) An accuracy of those values. The accuracy of the Mu HFS measurement have been exponentially increase.

2.5.2 Latest high field experiment

The latest high field experiment of Mu HFS is carried out at LAMPF[4] as

$$\Delta\nu_{\mathrm{M}}^{\mathrm{hf}} = 4463302.765(53)\ \mathrm{kHz}\ (12\ \mathrm{ppb}). \tag{2.63}$$

Figure 2.8 shows a schematic diagram of the experimental setup of the latest high-field measurement at LAMPF. Muons enter the apparatus through beam counters and moderators, and stop in a pressure vessel where muons form muonium atoms. Microwave is irradiated, and the transition is detected by change of ratio of number of positrons detected by counters placed at downstream side of the pressure vessel. A superconducting magnet is surrounding the apparatus to apply a high magnetic field. The precision is mainly limited by statistics. But there is a reason that there have been no new measurements to improve statistics. The muon beams available at Meson Facilities are all DC beams, which mean muons are delivered one by one intermittently. When we want to observe transition of muonium atom under RF field, the time structure of DC beam poses a substantial challenge - if we want to control irradiation time for muonium atom, we need to intentionally stop muons to arrive at the target while RF field is on, thus making effective beam intensity reduced seriously. For example, the last Mu HFS measurement at LAMPF chopped muon beam to 3.9 μsec pulses separated by 9.9 msec when measuring frequency using "oldmuonium method" (see Section 5.3). This means although the LAMPF accelerator can provides about 1×10^7 muons per second, the experiment uses less than 28% of available muons for measurement. The inauguration of J-PARC MUSE changed the whole picture. J-PARC MUSE provides a pulsed muon beam, which means all muons are bunched to pulses, and we know their arriving time to the target. This means our experiment at J-PARC can fully use available muons, thus gives a significant advantage over previous experiments.

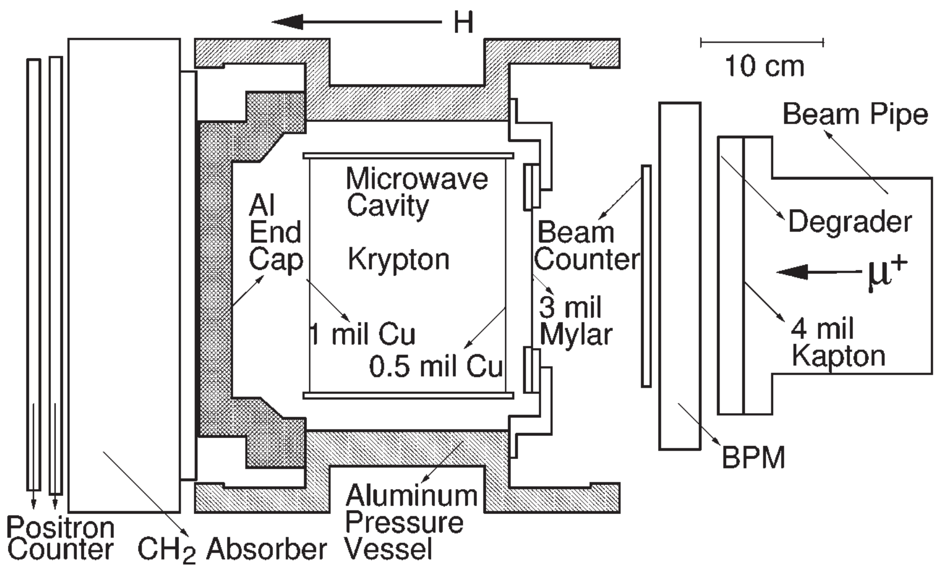

Figure 2.8: Schematic diagram of the experimental apparatus used for high field experiment at LAMPF [4].

Chapter 3

Measurement procedure

In this chapter, measurement procedure of the experiment is introduced as following (Figure 3.1).

1. Muons polarized to upstream are provided from J-PARC/MLF muon beam line (Production of muons is discussed in Section 3.1, beam line at J-PARC MLF is introduced in Section 3.2).

2. RF cavity located in a center of the magnet containing pure Krypton gas. Muons stop by collisions in the gas and polarized muonium is formed by electron capture process with Krypton (discussed in 3.3).

3. High momentum decay positrons are emitted preferentially in the direction of the muon spin (see Section 3.5). By driving the transitions with an applied microwave magnetic field, the muon spin could be flipped (see Section 3.4) and the angular distribution of high momentum positrons changed from predominantly upstream to downstream with a respect to the beam direction.

This section described details of apparatus: magnet, detector, profile monitor. Designing of the cavity and the gas chamber are described in Chapter 4.

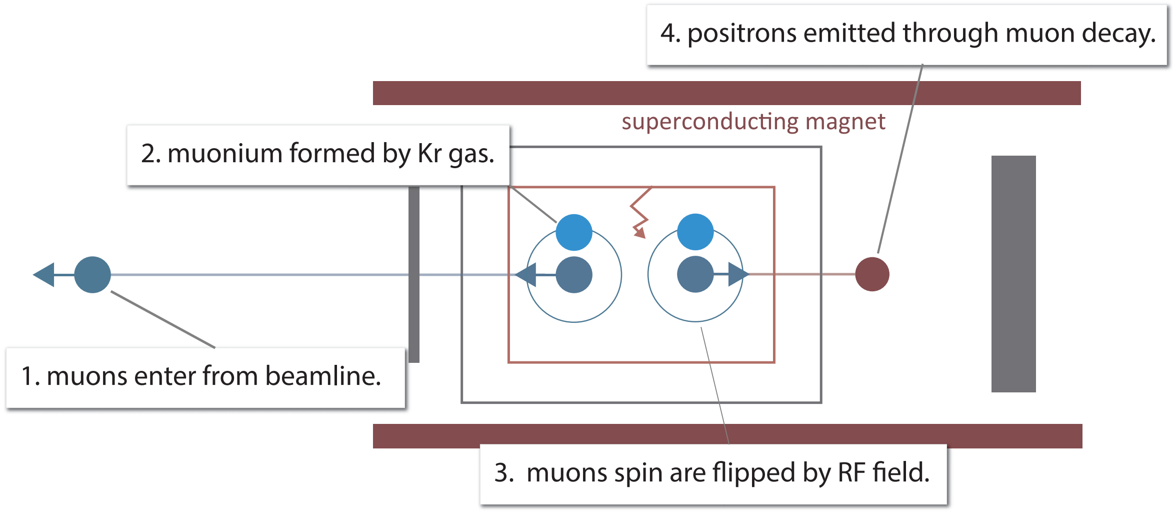

Figure 3.1: A schematic overview of the experimental setup of the Mu HFS experiment.

3.1 Production of muons

Positive muons are produced from parity-violating positive pion π^+ decays

$$\pi \rightarrow \mu^+ + \nu_\mu. \tag{3.1}$$

The lifetime of charged pion is

$$0.26033(5)\ \text{ns [49]}. \tag{3.2}$$

Because of the helicity of neutrino, muons are 100 % polarized in the direction opposite to their momentum.

3.2 Muon beamline

Muon beam is provided from MLF in J-PARC (Figure 3.5). A rotating graphite target is used to generate an intense pulsed muon beams from the 3 GeV proton beam from Rapid Cycling Synchrotron (RCS) with 25 Hz repetition (Figure 3.2). The Proton beam from RCS has double-pulsed structure (600 ns separation).

Muon beams are distributed to 4 beamlines, D Line, U Line, S Line, H Line. These 4 beamlines have own characteristics for each purposes [50]. High field experiment is planned at H Line, and zero field experiment will be held at D Line.

D Line D Line can provide both negative and positive decay muons up to a momentum of 120 MeV/c, as well as 30 MeV/c surface muons at 200 MW beam power. This high momentum-tunability meets the wide demands of user programs. Figure 3.3 shows a typical beam profile at D Line. $\sigma_x = 14$ mm and $\sigma_y = 28$ mm. Beam intensity was measured to be 3.1×10^6 surface muons per second under 220 kW proton beam[5].

U Line U line is the large acceptance beamline. It provides the most intense surface muon beam of the four secondary lines. This intense beam is used to generate an ultra-slow muon beam(0.05 eV - 30 KeV) by the laser resonant ionization method.

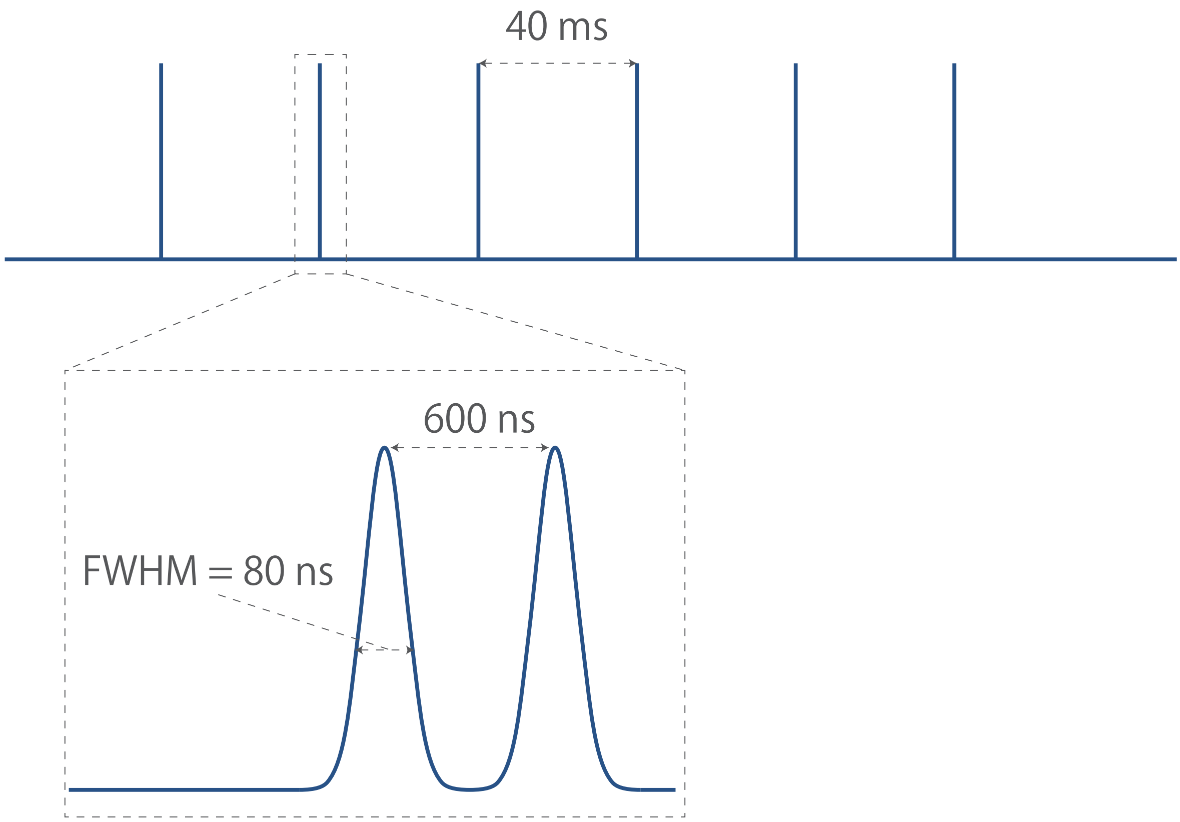

Figure 3.2: The muon beam produced at J-PARC has a double-pulsed structure with 600 ns interval in 25 Hz repetition.

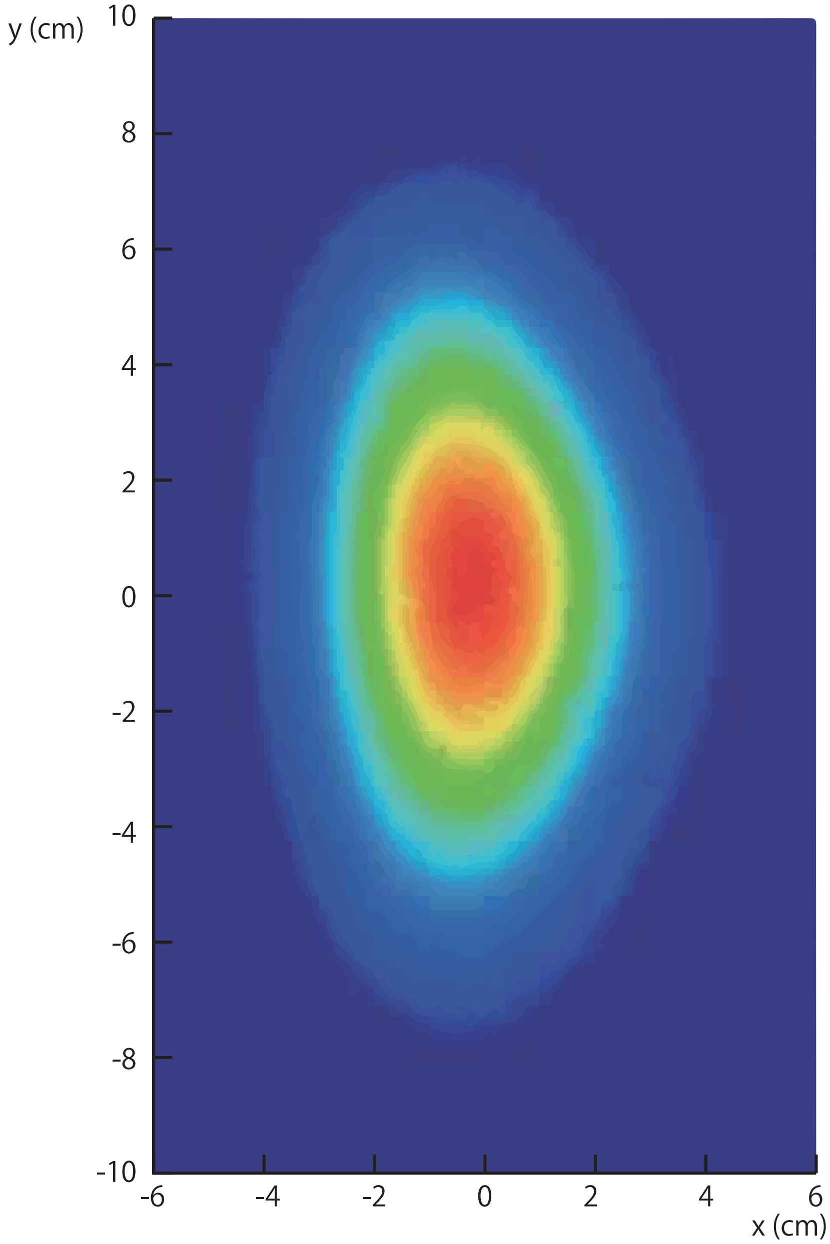

Figure 3.3: A typical beam profile obtained by the imaging plate. [5]

S Line S line is designed to transport surface muons to several experimental areas by using kicker devices to dedicated μSR spectroscopy.

H Line H Line provide surface muons for fundamental physics experiments which demand high statistics for a long period. A captured solenoid on the beamline enables high transmission efficiency more than 80 % of the captured muon. The intensity of the beamline is estimated as 1×10^8 s at 1 MW beam power. The installation of the frontend device, i.e. the muon-capture solenoid, HS1, the first bending magnet, HB1, and the vacuum components took precedence and were installed in 2012 as shown in Figure 3.4. The beamline will be ready in 2016.

3.3 Production of muoniums

Muonium atoms for precision experiments have been produced using three different methods (see Figure 3.6) [51, 52].

3.3.1 Beam foil

Metastable muonium in the 2s state have been produced with a beam foil technique at LAMPF and the TRIUMF [53, 54]. This method cannot apply to our experiment but the measurement of lamb shift transition ($2^2\mathrm{S}_{1/2} - 2^2\mathrm{P}_{1/2}$).

3.3.2 Silica powder

Muonium generated by stopping muons near the surface of a SiO_2 powder target. Muons stopped in the silica powder capture electrons and form muonium, some percent of which diffuse to the target surface and then emitted in vacuum [55]. Advantage of this method is that formed in vacuum unlike in the case of gas target. However, this is not appropriate for our experiment because both the production rate and the polarization are insufficient. Moreover, signals of muon decay in vacuum are not able to distinguish from that in a powder target.

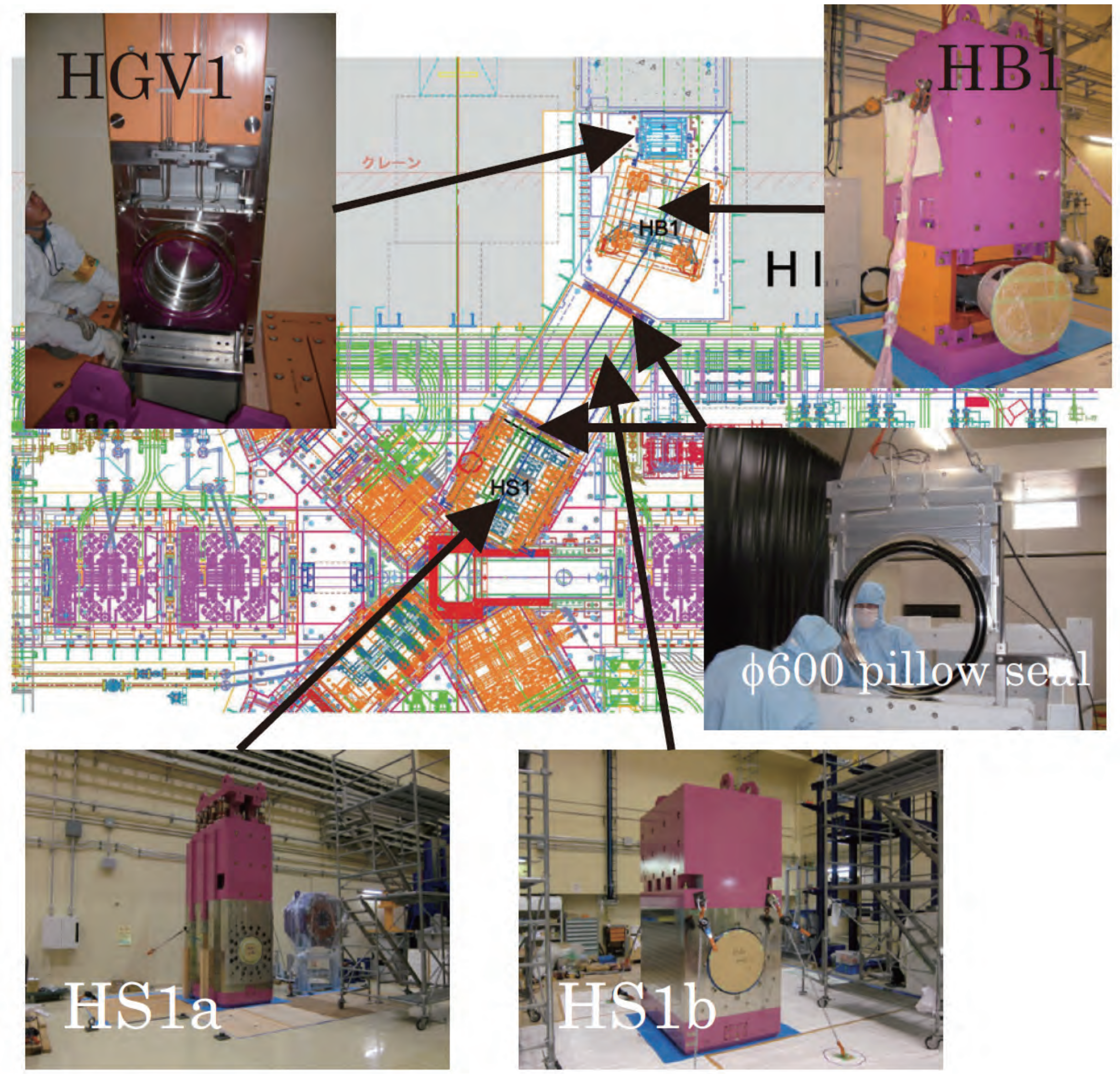

Figure 3.4: Devices for H Line installed in 2012[6].

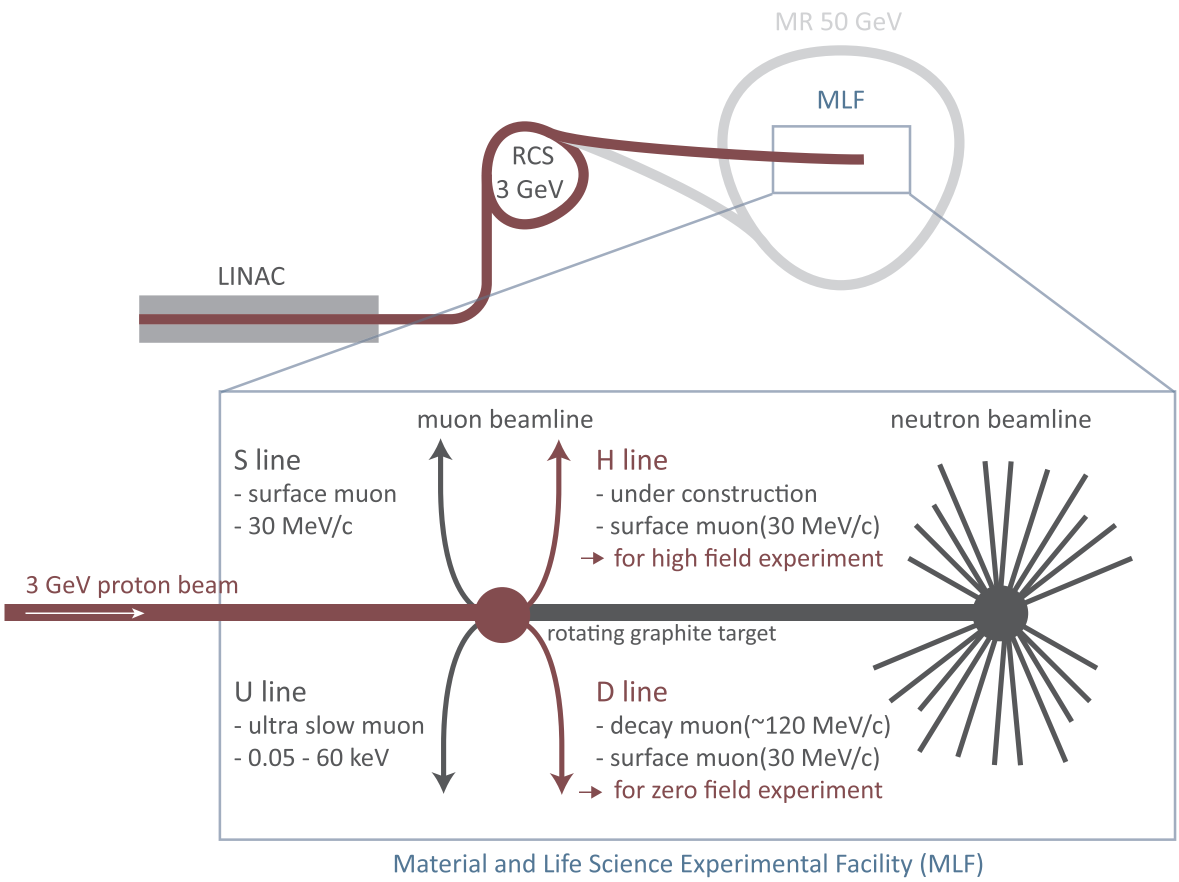

Figure 3.5: A schematic drawing of MLF in J-PARC. There are 4 beamlines to provide muons for various purposes.

3.3.3 Gas target

Muonium is generated by an electron capture after stopping muon in a suitable noble gas. This technique was employed already in the experiment observed of the muoniums for the first time atom in 1960 in argon gas. The production rate in this experiment was 65(5) %. In the case of LAMPF HFS experiment, the production rate was 80(10) % with Kr gas [51]. Muon moderation processes involve dominantly electronic interaction and practically no muon depolarization take place in a strong axial magnetic field ($B \gg 0.16$ T) [20]. Thus gas target is a most suitable method for muonium HFS experiments from the aspect of production rate and the rate of polarization.

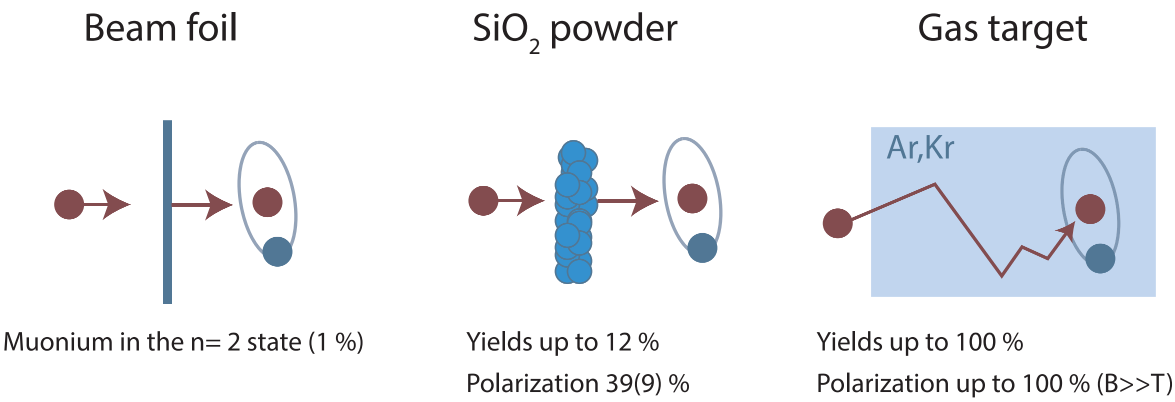

Figure 3.6: A comparison of the methods of muonium production. Gas target is the most suitable method for the muonium HFS experiment from the aspect of a production rate and a rate of polarization.

Comparison of gas targets

In order to avoid chemical reactions and depolarizing collisions, noble gases are candidates for a gas target. Muoniums are formed when positive muons are stopped in a gas target by the following electron capture reaction,

$$\mu^+ + \mathrm{Kr} \rightarrow \mu^+ e^- + \mathrm{Kr}^+. \tag{3.3}$$

In the case of krypton, the ionization energy of krypton is 14.00 eV and that of muonium is 13.54 eV. A muon can capture an electron from a krypton atom to form muonium in the ground state if the kinetic energy of the muon-krypton system in its center of mass is greater than the threshold value of 0.46 eV. And the muonium fractions is about 100 %. Thus krypton is a ideal gas target to form a low energy muoniums (see Table 3.1).

atom or molecule	threshold energy (eV)	pressure (atm)	f_{Mu}
He	+11.04	1.2–3.1	0(1)
Ne	+8.02	1.2	7(5)
Ar	+2.22	1.0–2.8	74(4)
Kr	+0.46	0.4–0.95	100(5)
Xe	-1.41	0.4–0.65	100(4)
N_2	+2.0	1.0–2.4	84(4)
CH_4	-0.6	1.2–3.0	87(4)

Table 3.1: Threshold energies for muonium formation [9] and the pressure-independent muonium fractions f_{Mu} [10].

3.4 Resonance line shape

There are two measurement method depend on the time window (from t_1 to t_2) of decay positron observation. One is the case of $t_1 = 0$ and $t_2 = \infty$ which is called "conventional method". In this case, a resonance line shape is Lorentzian. The other is the case that t_1 and t_2 is defined arbitrary which is called "old muonium method". In this section, correlation between statistical uncertainties and both methods are discussed. The signal is defined as

$$S = \frac{N_{\mathrm{ON}} - N_{\mathrm{OFF}}}{N_{\mathrm{OFF}}} \tag{3.4}$$

where N_{ON} (N_{OFF}) is the number of positrons detected with microwaves on (off).

The general case that the muonium of $|m\rangle$ state transits to $|n\rangle$ state induced by microwave is as follows. State amplitudes (a_m and a_n) of both $|m\rangle$ and $|n\rangle$ are described as [56]

$$\dot{a}_n(t) = -\frac{1}{2}\gamma a_n(t) - i a_m b f_{mn}(t) \tag{3.5}$$

$$\dot{a}_m(t) = -\frac{1}{2}\gamma a_m(t) - i a_n b f_{nm}(t), \tag{3.6}$$

where

$$\gamma = \frac{1}{\tau}, \tag{3.7}$$

$$b = \frac{1}{2\hbar}\langle m|H_0'|n\rangle, \tag{3.8}$$

$$H_0' = (g_J \mu_B^e \boldsymbol{J} - g_\mu' \mu_B^\mu \boldsymbol{I})(\boldsymbol{H_1}), \tag{3.9}$$

$$f_{mn} = \exp(-i(\omega_{mn} - \omega)t) + \exp(-i(\omega_{mn} + \omega)t), \tag{3.10}$$

$$\omega_{mn} = \frac{E^B_{\mathrm{HFS}}(|m>) - E^B_{\mathrm{HFS}}(|n>)}{\hbar}. \tag{3.11}$$

τ is the muon lifetime (see subsection 3.5), $\boldsymbol{H_1}$ is a general microwave field as $\boldsymbol{H_1} = H_x\boldsymbol{x} + H_y\boldsymbol{y}$ and ω_{mn} is an angular velocity of a microwave field.

The first term of Equation 3.5 and 3.6 expresses muon decay, and the second term expresses transitions transition between the states. Equation 3.5 is calculated as

$$\begin{aligned} |a_n(t)|^2 &= |a_m(0)|^2(\cos\frac{\Gamma t}{2} + \frac{\omega'^2}{\Gamma^2}\sin^2\frac{\Gamma t}{2})e^{-\gamma t} \\ &+ |a_n(0)|^2\frac{4|b|^2}{\Gamma^2}\sin^2\frac{\Gamma t}{2}e^{-\gamma t} \\ &+ 2\mathrm{Re}(a_m(0)a_n(0)(\cos\frac{\Gamma t}{2} - i\frac{\omega'}{\Gamma}\sin\frac{\Gamma t}{2} \times i\frac{2b*}{\Gamma}\sin\frac{\Gamma t}{2}))e^{-\gamma t}. \end{aligned} \tag{3.12}$$

If muons are sufficiency polarized, it can be considered that $a_n(0) \approx 0$. Then

$$a_n(t) = |a_m(0)|^2\frac{4|b|^2}{\Gamma^2}\sin^2\frac{\Gamma t}{2}e^{-\gamma t} \tag{3.13}$$

where $\sin^2\frac{\Gamma t}{2}$ expresses an oscillation to $|n>$ state and $e^{-\gamma t}$ expresses muon decay. Decay probability of $|n>$ from t_1 to t_2 (old muonium method) is proportional to the signal S. It can be expressed as

$$S \propto \int_{t_1}^{t_2} |a_n(t)|^2 \mathrm{d}t = \frac{2|b|^2}{\Gamma^2}(e^{-\gamma t_1}(1-(\cos\Gamma t_1 - \frac{\Gamma}{\gamma}\sin\Gamma t_1)\frac{\gamma^2}{\Gamma^2+\gamma^2})) \\ -\frac{2|b|^2}{\Gamma^2}(e^{-\gamma t_2}(1-(\cos\Gamma t_2 - \frac{\Gamma}{\gamma}\sin\Gamma t_2)\frac{\gamma^2}{\Gamma^2+\gamma^2})). \tag{3.14}$$

By substituting $t_1 = 0$, $t_2 = \infty$, the signal of conventional method is calculated as

$$S \propto \frac{2|b|^2}{\Gamma^2+\gamma^2}, \tag{3.15}$$

where

$$\Gamma^2 = \omega'^2 + 4|b|^2. \tag{3.16}$$

Thus the resonance line shape of the conventional method is Lorentzian.

3.5 Muon decay

Muons decay via weak interaction like

$$\mu^+ \to e^+ + \nu_e + \bar{\nu_\mu}. \qquad \text{(branching ratio} \approx 1\text{) [49]} \tag{3.17}$$

Also there are following other processes

$$\mu^+ \to e^+ + \nu_e + \bar{\nu_\mu} + \gamma, \qquad \text{(branching ratio} \approx 10^{-2}\text{) [49]} \tag{3.18}$$

$$\mu^+ \to e^+ + \nu_e + \bar{\nu_\mu} + e^+ + e^-. \qquad \text{(branching ratio} \approx 10^{-5}\text{) [49]} \tag{3.19}$$

Equation 3.17 is a dominant process and other processes are rare enough to be neglected.

Muon life time

Muon life time is measured as

$$\tau = 2.19703(4)\ \mu\mathrm{s}\ (18\ \mathrm{ppm})\ [49]. \tag{3.20}$$

Angular distribution of decay postrion

The angular distribution of decay postiron is described by the following equation and depends on a muon magnetic moment (see Figure 3.7),

$$N(y, \theta) = \frac{\gamma}{2\pi} y^2[(3 - 2y) + (2y - 1)\cos\theta][35], \tag{3.21}$$

in which y is the positron momentum in units of $\frac{1}{2}m_\mu c$; θ is the angle between the muon spin direction and the positron momentum.

A decay positron has its maximum momentum when the two neutrinos are emitted in the opposite direction to the direction of the positron emission and the value is,

$$P_{\text{max}} = \frac{m_\mu^2 - m_e^2}{2m_\mu} c \approx \frac{1}{2} m_\mu c = 52.83 \text{ MeV/c}[56]. \tag{3.22}$$

3.6 Advantage of the measurement

The dominant part of the uncertainty of high field experiment in LAMPF experiment is statistical uncertainty[4]. On the other hand, the intensity of H Line is 1×10^8/s at 1 MW beam power which is ten times more than that of muon beam line at LAMPF experiment. In addition to this, the beam has 25 Hz pulse structure in favor of this spectroscopy. As a result, the statistical uncertainty can be improved 10 times by a measurement for 100 days measurement at H Line.

Also main parts of uncertainties of previous zero field experiment are statistical uncertainties and from magnetic field [45]. One day measurement at D Line can accumulate the statistics equivalent to latest zero field experiment. And the uncertainty from the magnetic field can be improved by correction with the precise measurement data of magnetic field map.

Both estimations are specifically described in Chapter 5. We aim to measure Mu HFS by using both methods complementary.

Since the angular distribution depends on the energy of decay positrons, detection threshold of kinetic energy is set for optimize the signal ratio of the upstream detector and the downstream detector.

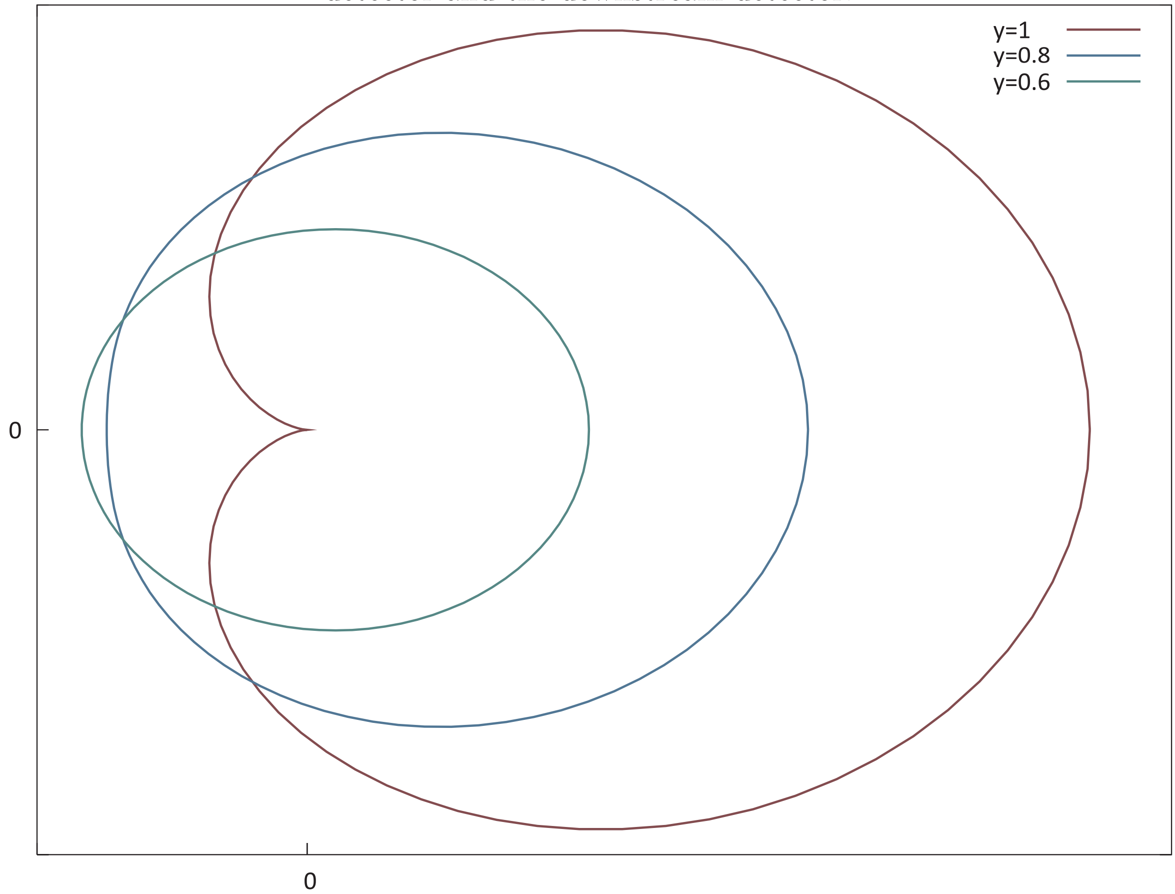

Figure 3.7: An angular distribution of decay positron at several y values expressed in polar coordinates. The direction of muon magnetic moment is rightward.

Chapter 4

Appratuses

In this chapter, developments of following apparatuses are described.

for zero field experiment (Figure 4.1)

- RF cavity for zero field experiment (Section 4.3)
- RF system (Section 4.5)
- gas chamber (Section 4.6)
- gas system (Section 4.7)
- magnetic shield (Section 4.8)
- beam monitoring system described in Section 4.10
- positron detector (Section 4.11)

for high field experiment (Figure 4.2)

- RF cavity for high field experiment (Section 4.1)
- RF system (common)
- gas chamber (common)

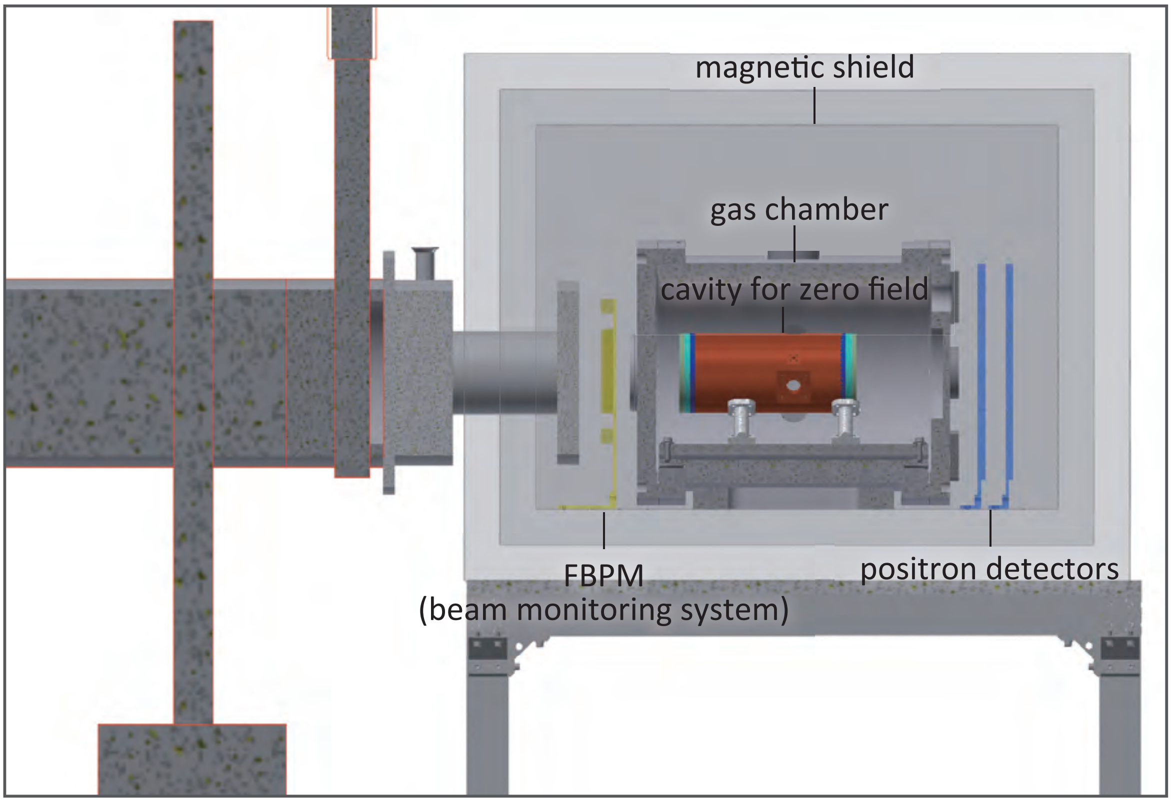

Figure 4.1: A schematic view of the setup for zero field experiment. Muons enter the apparatus through FBPM (beam monitoring system), and stop in a gas chamber where muons form muonium atoms. Microwave is irradiated, and the transition is detected by change of ratio of number of positrons detected by counters placed at downstream side of the chamber. The whole apparatus is surrounded by a magnetic shield.

- gas system (common)
- superconducting magnet (Section 4.12)
- beam monitoring system (common)
- positron detector (common)

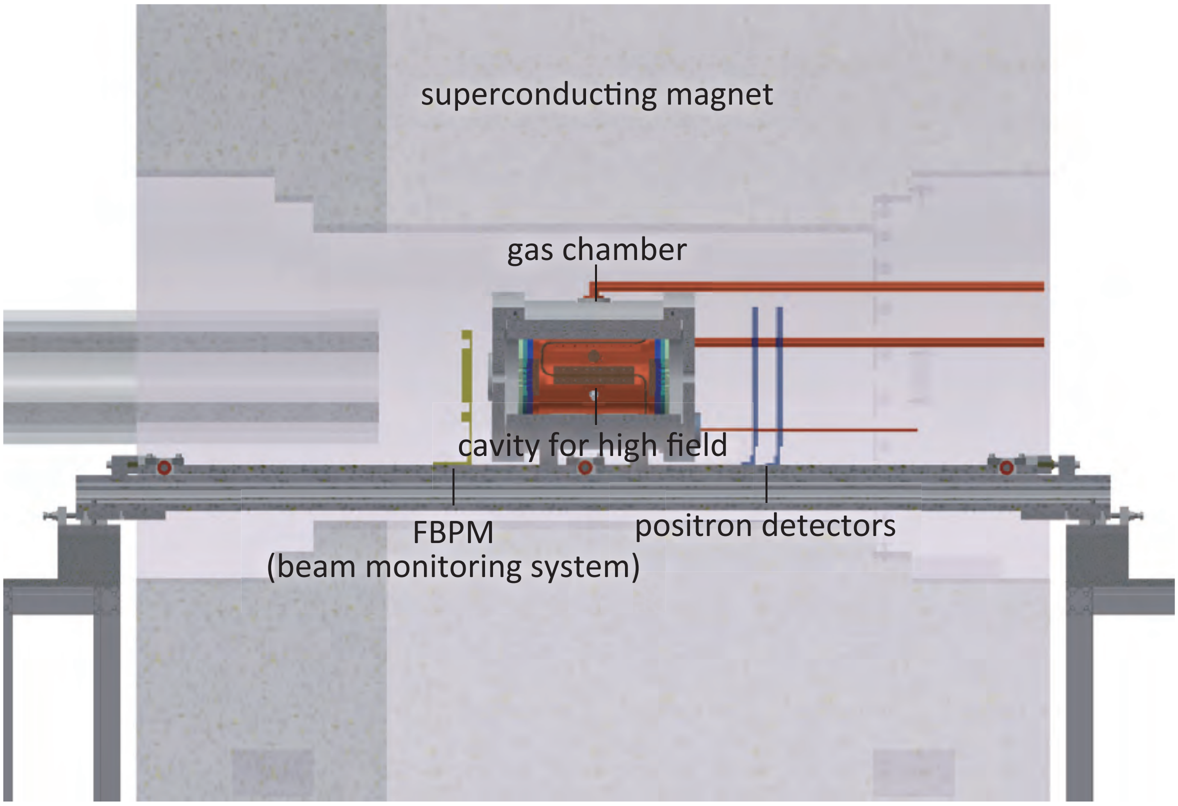

Figure 4.2: A schematic view of the setup for high field experiment. The setup is very similar to the zero field experiment, but a superconducting magnet is surrounding the apparatus to apply a high magnetic field.

4.1 RF cavity for high field

In this section, development of the RF cavity for high field is introduced. We choose the TM110 mode to drive ν_{12} transition and the TM210 mode to ν_{34} transition (Subsection

4.1.1). The diameter of the cavity is determined to match each resonance frequencies as transition frequencies (Subsection 4.1.2). Resonance frequencies are adjusted by displacement of tuning bars from inner surface of the cavity (Subsection 4.1.5). Front window of the cavity should be thin enough to through muons (Subsection 4.1.4).

4.1.1 Resonance modes

The resonance frequencies should be tuned into the ν_{12} and ν_{34} transition frequencies. There are following requirements,

(a) Static magnetic field and oscillating field are perpendicular to each other,

(b) The transition efficiencies should be maximized at the center of cavity, that is region muonium formed,

(c) The oscillating field is constant along the axis.

By the requirement (a), Transverse Magnetic (TM) resonant modes are more appropriate than Transverse Electric (TE) modes since a static magnetic field vector is parallel to the axial direction of the cavity. By the requirement (b) and (c), TMmn0 which does not have node in the axial direction are candidates. (The TM mnp mode is characterized by three subscripts m, n and p that corresponding to the number of half waves of the electric or magnetic field that fit along the diameter, circumference, and length of the resonator.). Therefore, TM110 and TM210 modes which are lower-order modes of TMmn0 are appropriate from these requirements.

Figure 4.4 shows the electromagnetic field of TM110 and TM210 modes (see Appendix A). The resonance frequencies for TM modes are

$$f_{mnp} = \frac{c}{n}\sqrt{(\frac{x_{mn}}{\pi D})^2 + (\frac{q}{2L})^2}. \tag{4.1}$$

Here c is the speed of light, D and L are the diameter and length of the cavity, n is the index of refraction for the medium inside the cavity, and x_{mp} is the pth root of the Bessel function $J_m(x)$.

Figure 4.3 shows a relation between a ratio of the ν_{12} and the ν_{34} transition frequencies and a ratio of the resonance frequencies of the TM110 mode and the TM210 mode. For measurement of both transitions, static magnetic field is defined so as to equalize these ratios one another. Although one of the solution is 1.55 T, optimum magnetic field is estimated as 1.7 T including cavity perturbations by tuning bars (See Subsubsection 4.1.5).

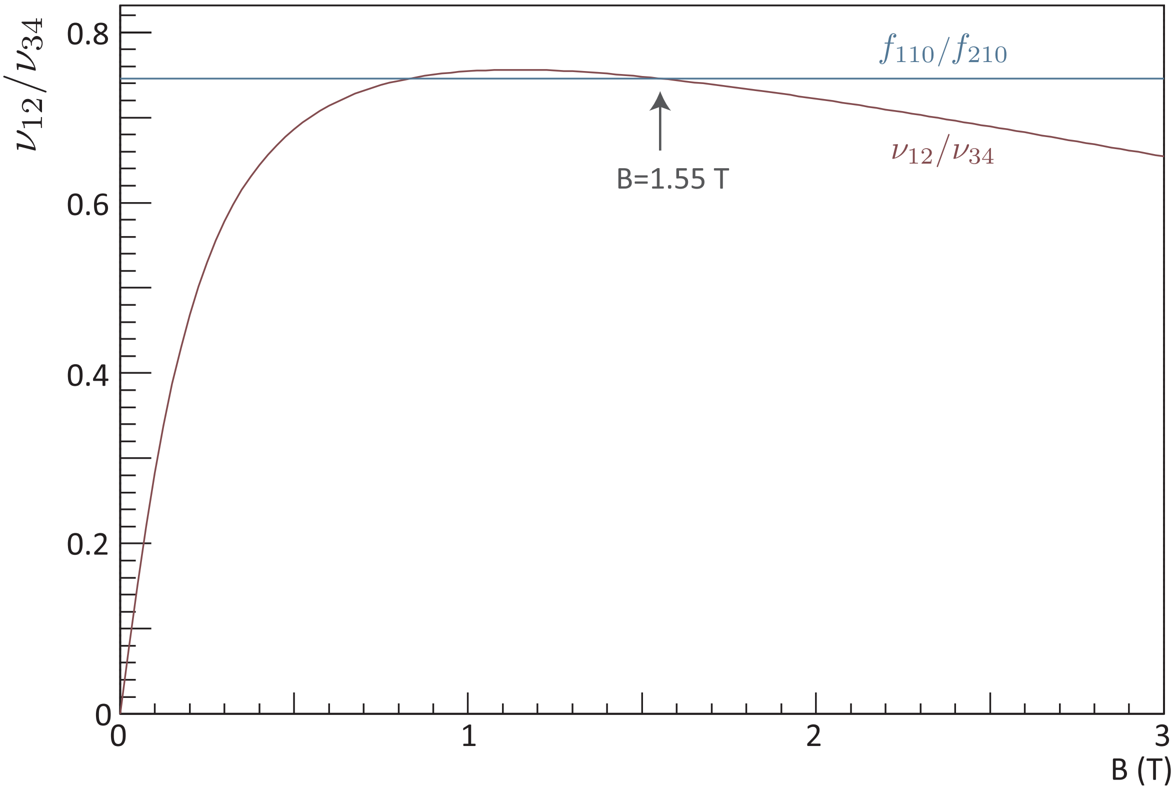

Figure 4.3: A relation between a ratio of the ν_{12} and the nu_{34} transition frequencies and a ratio of resonance frequencies of the TM110 mode and the TM210 mode. Since the ratio of the TM110 mode and the TM210 mode is constant at a cylindrical cavity, there only two solutions to be tuned in to both transitions.

Figure 4.5 shows positions of RF ports. To accumulate RF power in the cavity, RF ports without one transporting RF power should not be coupled to the cavity. The positions of input ports for TM110 (TM210) mode are chosen not to be coupled to TM210 (TM110) mode. The position of the output port is chosen couple to both

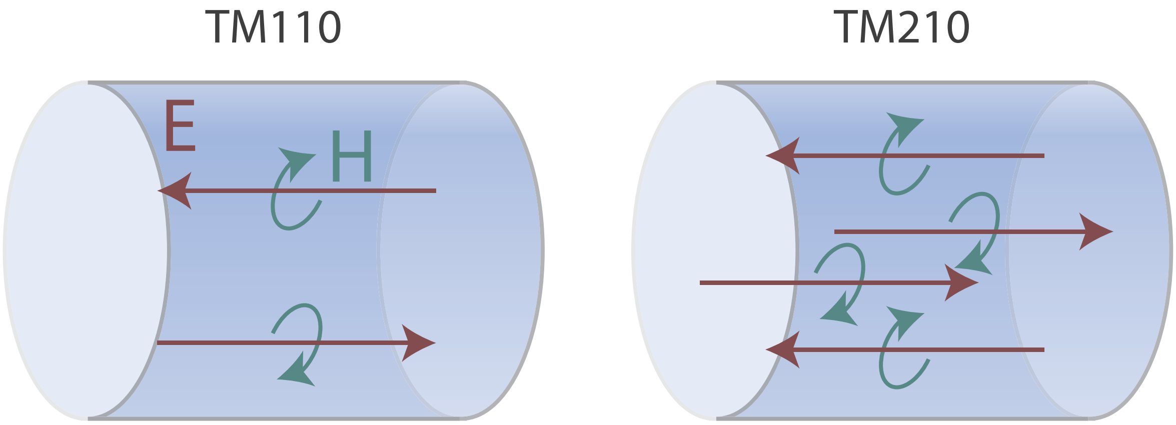

Figure 4.4: RF fields of the TM110 mode and the TM210 mode. The red arrow shows the electric field vector and the green one shows the magnetic field vector.

modes weakly.

4.1.2 Diameter of the cavity

Transition frequencies of ν_{12} and ν_{34} are obtained by Equation 2.26 and 2.27 as

$$\nu_{12} = 1.906 \text{ GHz}, \tag{4.2}$$

$$\nu_{34} = 2.556 \text{ GHz}. \tag{4.3}$$

The resonance frequencies of the cavity should be a little higher than the transition frequencies since tuning bars in the cavity increase resonance frequencies (see Section 4.1.5). The resonance frequencies of the TM110 mode and the TM210 mode are 1.955 GHz and 2.620 GHz for a diameter of the cavity of 187 mm (see Equation 4.1). RF fields of the TM110 mode and the TM210 mode are described in Appendix A.

4.1.3 Axial length of the cavity

Measurement in low gas pressure

Transition frequencies ν_{12} and ν_{34} in vacuum are determined by fitting measured frequencies at several different gas pressures (see Subsection 4.7.2). To assure accuracy of

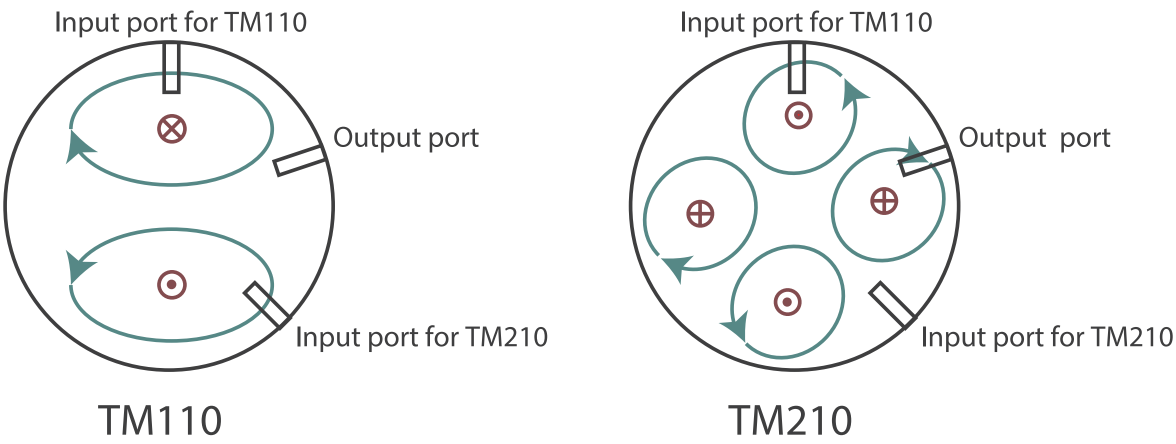

Figure 4.5: A cross-sectional view of the cavity with the TM110 mode and the TM210 mode. The red arrows indicate electric fields and green arrows indicate magnetic fields. Positions of input ports for the TM110 (TM210) mode are chosen not to be coupled the TM210 (TM110) mode. The position of the output port is chosen couple to both modes weakly.

this fitting, measurements in wide range of Krypton gas pressures are necessary. Long cavity is preferred for measurement at low pressure Krypton gas, since the muonium distribution spread broadly in the longitudinal direction. Figure 4.6 shows the longitudinal distribution of muonium in 0.3 atm by Monte Carlo simulation using SRIM [57]. SRIM is a group of programs which calculate the stopping and range of ions into matter using a quantum mechanical treatment of ion-atom collisions. In this simulation, the moderator is loaded in front of the cavity to stop muons in the region of the cavity whose axial length is 15.973 cm which was used at LAMPF experiment. In this case, 68 % of muons stop in the cavity.

On the other hand, Figure 4.7 shows the corresponding distribution for the cavity for J-PARC/MLF experiment whose axial length is 304 mm. Because of the length of this cavity, the moderator can be thin and the muon stopping distribution is brought within the cavity (94 % of muons stop in the cavity). Thus measuring in a lower pressure is possible by using a long cavity and our cavity is available in over 0.3 atm by this simulation.

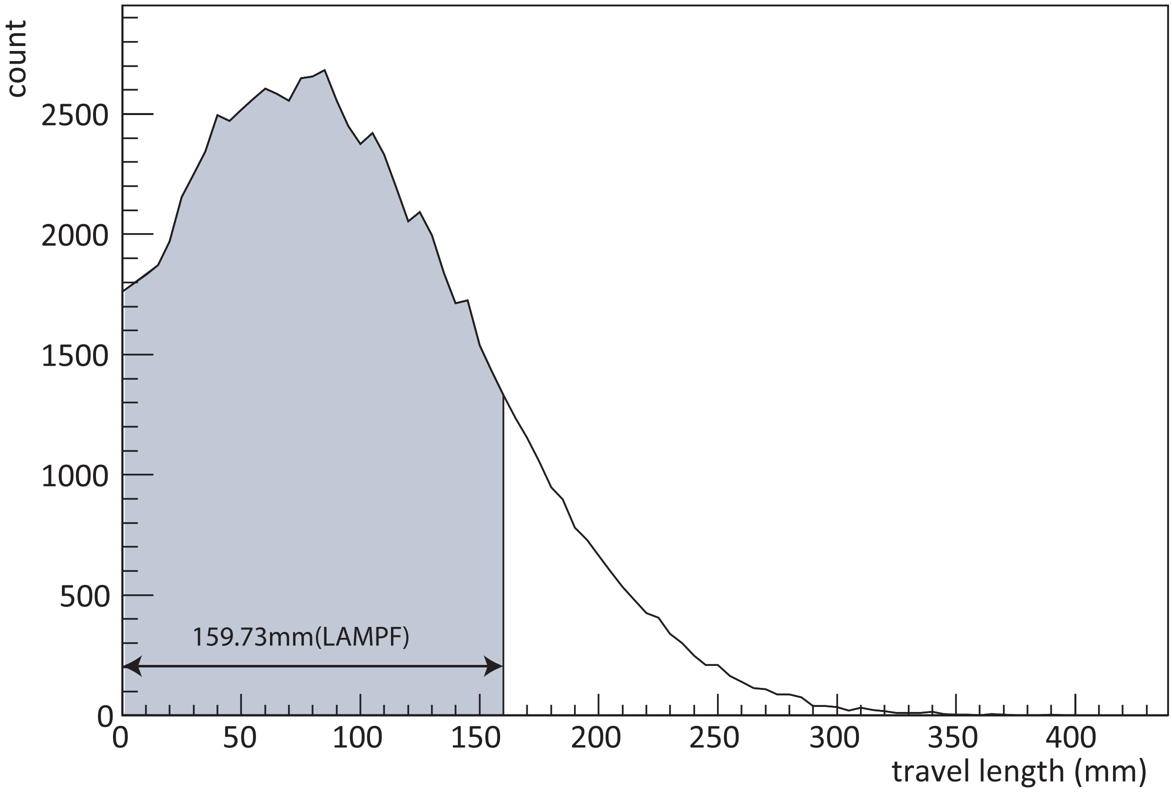

Figure 4.6: A muon stopping distribution in 0.3 atm Krypton gas. Trajectories of 100000 muons were simulated by a Monte Carlo simulation program SRIM. The cavity axial length is 159.73 mm designed for the latest experiment at LAMPF. To stop muons in a narrow region, a thick moderator is required at upstream side of the cavity. 68 % of muons are brought within the cavity.

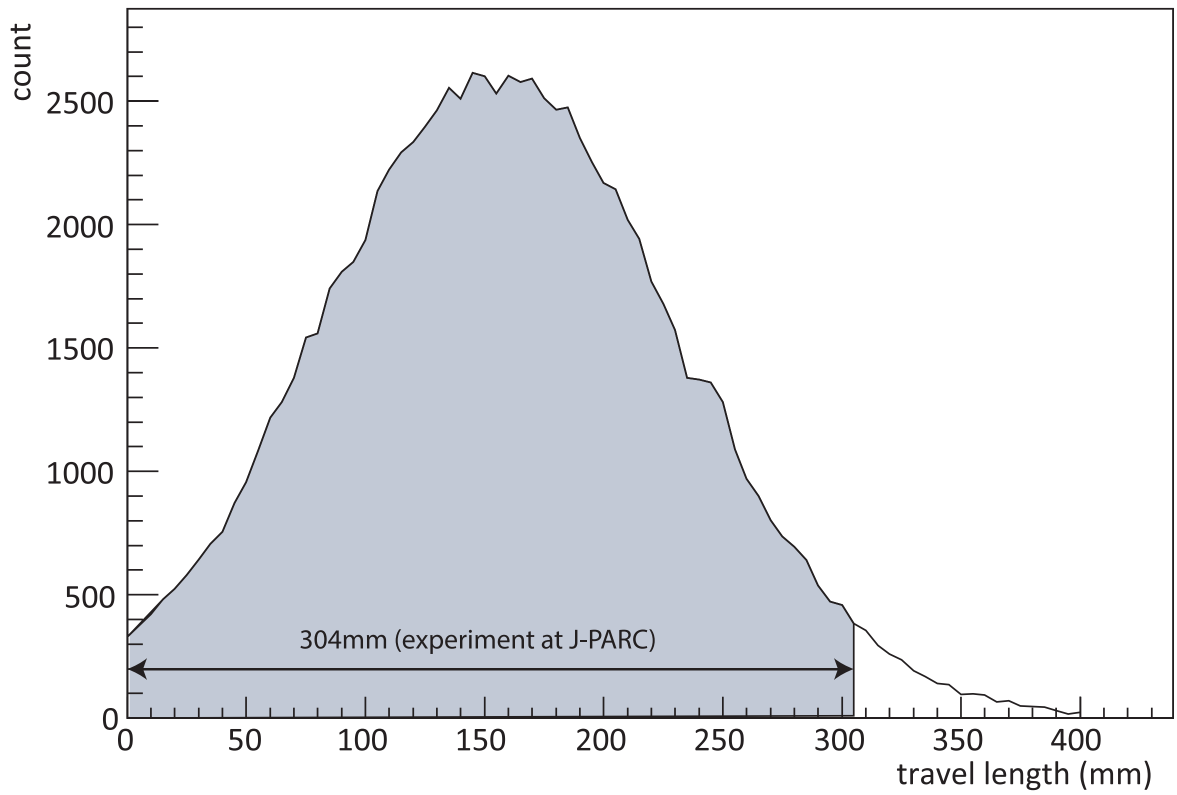

Figure 4.7: A muon stopping distribution in 0.3 atm Krypton gas. The cavity axial length is 304 mm designed for the experiment at J-PARC. 94 % of muons are brought within the cavity.

Avoiding other resonance modes

There are many other resonance modes depending on the cavity length (see Figure 4.8). On the other hand, resonance frequencies of the TM110 mode and the TM210 mode do not depend on the cavity length. The cavity length is determined to avoid other modes. Figure 4.9, 4.10 and 4.11 show resonance modes nearby the TM110 mode. If the cavity axial length is 300 mm, a TM012 mode is located between splitted the TM110 modes (the TM110-1 mode and TM110-2 mode) which is undesirable. In case axial length is 304 mm, resonance frequency of the TM012 mode is low enough to be separated from the TM110 mode.

4.1.4 Foils of the cavity

Since muons enter through the front foil of the cavity and the gas chamber, the front foil must be thin not to stop muons. Also the back foil must be thin not to stop decay positrons emitted through the back foil. According to Figure 4.12, there are three flanges at the front and back of cavity. Foil is fixed by F2 and F3, and stretched by F1. This foil is made of a 99.97 % copper and the thickness is 25 μm.

4.1.5 Tuning bar

Resonance curves are obtained from microwave frequency sweep. Frequency sweep is achieved by tuning bars located inside the cavity. Inserting a tuning bar into the cavity results in an increasing resonant frequencies.

Cavity perturbations

When a dielectric material is inserted into the cavity, resonance frequency is shifted. A corresponding change in resonance frequency is able to approximated as

$$\frac{\omega - \omega_0}{\omega_0} \approx \frac{\int\int\int_{\Delta V}(\Delta\mu|H_0|^2 + \Delta\epsilon|E_0|^2)\mathrm{d}v}{\int\int\int_{\Delta V}(\mu|H_0^2 + \epsilon|E_0|^2)\mathrm{d}v} \text{ [58]}, \tag{4.4}$$

where ω_0 is the resonance frequency of the original cavity and ω is one of the perturbed cavity. The perturbed field are approximated by the original fields E_0 and H_0. However,

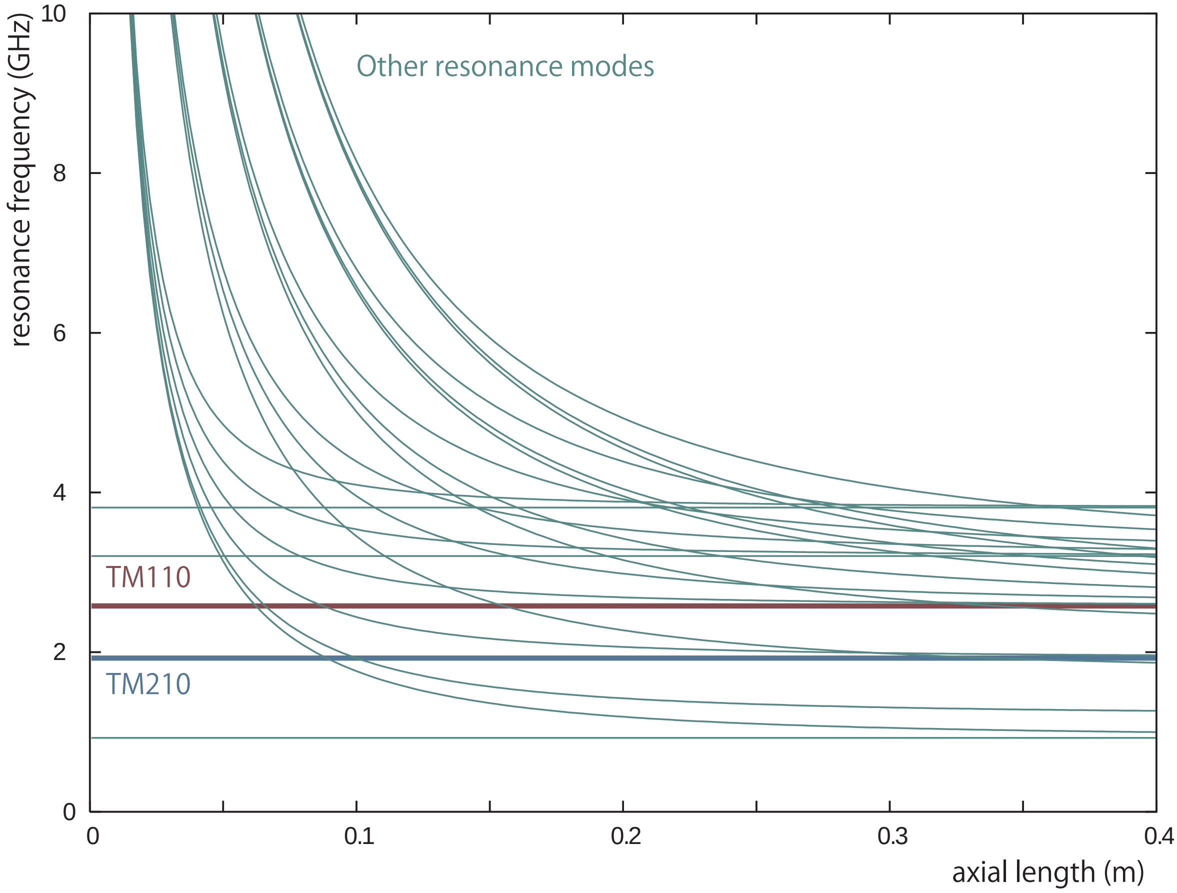

Figure 4.8: Other resonance modes around the mode TM110 and the TM210 mode by analytical calculation. The horizontal axis is the axial length of a cavity. Resonance frequencies of the mode TM110 and the TM210 mode does not depend on the cavity axial length. On the other hand, resonance frequencies of many other modes which have nodes in axial direction decrease by axial length of the cavity. In case of the cavity whose axial length is 304 mm, many modes are close to the TM110 mode and the TM210 mode.

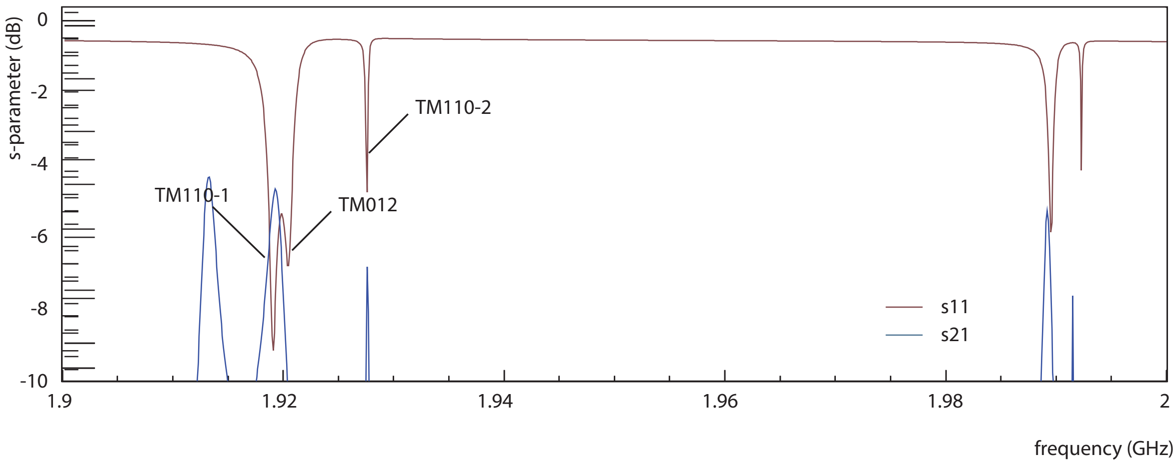

Figure 4.9: Resonance modes around the TM110 modes in case axial length is 300 mm. The TM012 mode is located between splitted the TM110-1 mode and the TM110-2 mode.

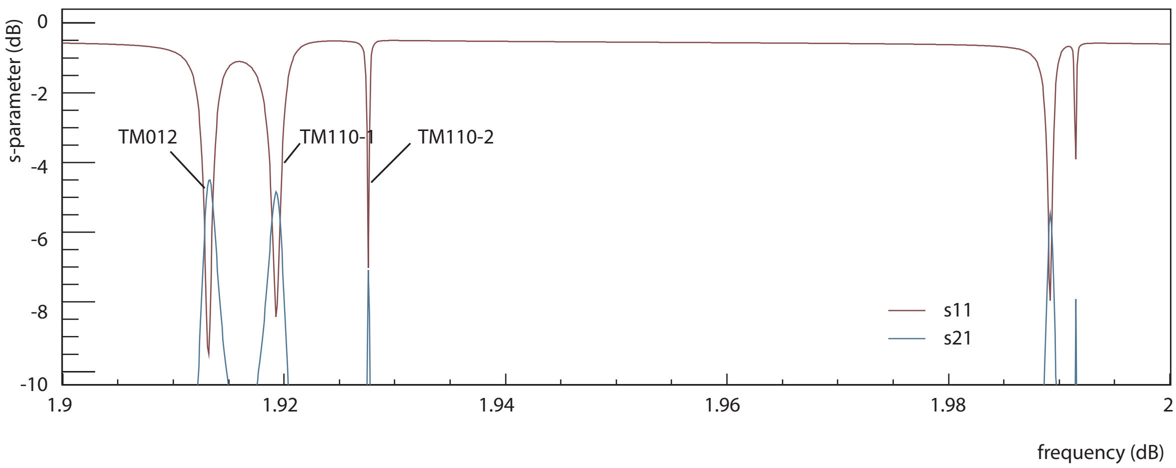

Figure 4.10: Resonance modes around the TM110 modes in case axial length is 302 mm. Resonance frequency of the TM012 mode is lower than that of a 300 mm cavity. Resonance frequencies of the TM110-1 mode and the TM110-2 mode are not changed because they are independent of cavity length.

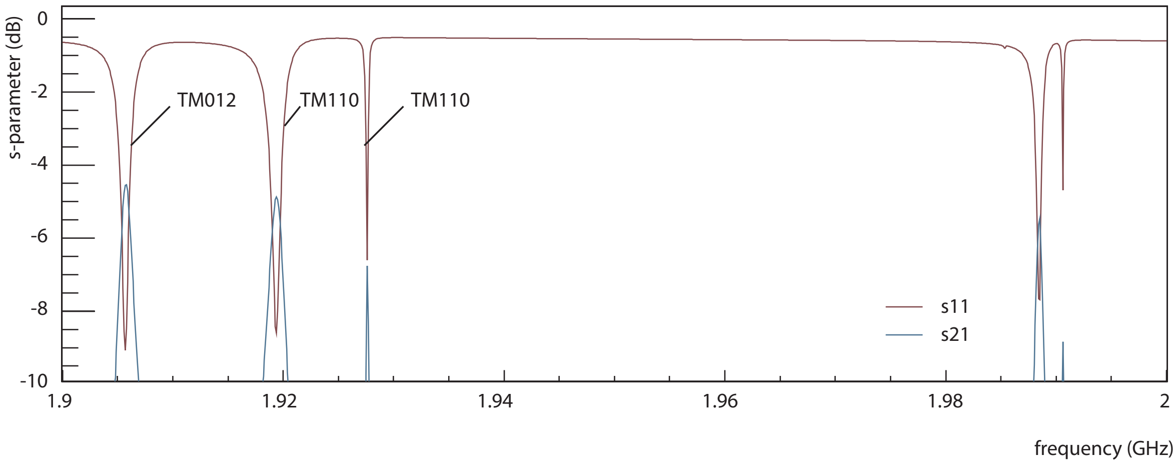

Figure 4.11: Resonance modes around the TM110 modes in case axial length is 304 mm. Now the TM012 mode is far from the TM110-1 mode and the TM110-2 mode enough to be distinguished.

analytical evaluation using this equation is not realistic so that a simulation software using a finite element method is used.

Material for tuning bar

As for the material of the tuning bar, there are critical differences between conductive one and dielectric one. A conductive tuning bar affects electric field as shrink a diameter of the cavity. On the other hand, dielectric tuning bar affect as widen it by absorbing RF power (see Figure 4.13). As a result of these characters, conductive tuning bar decrease resonance frequencies and dielectric one increase them.

Although a conductive material is sensitive to resonance frequency, it affects the uniformity of RF electric field (see Figure 4.14). Moreover, whereas sweep range of conductive tuning bar is defined by a position of its surface, that of dielectric tuning bar is defined by its volume so that it is possible to adjust sweep range flexibly. Therefore, dielectric material is a candidate list of material for tuning bar.

For choosing better material for tuning bar in dielectric materials, following parameter should be considered.

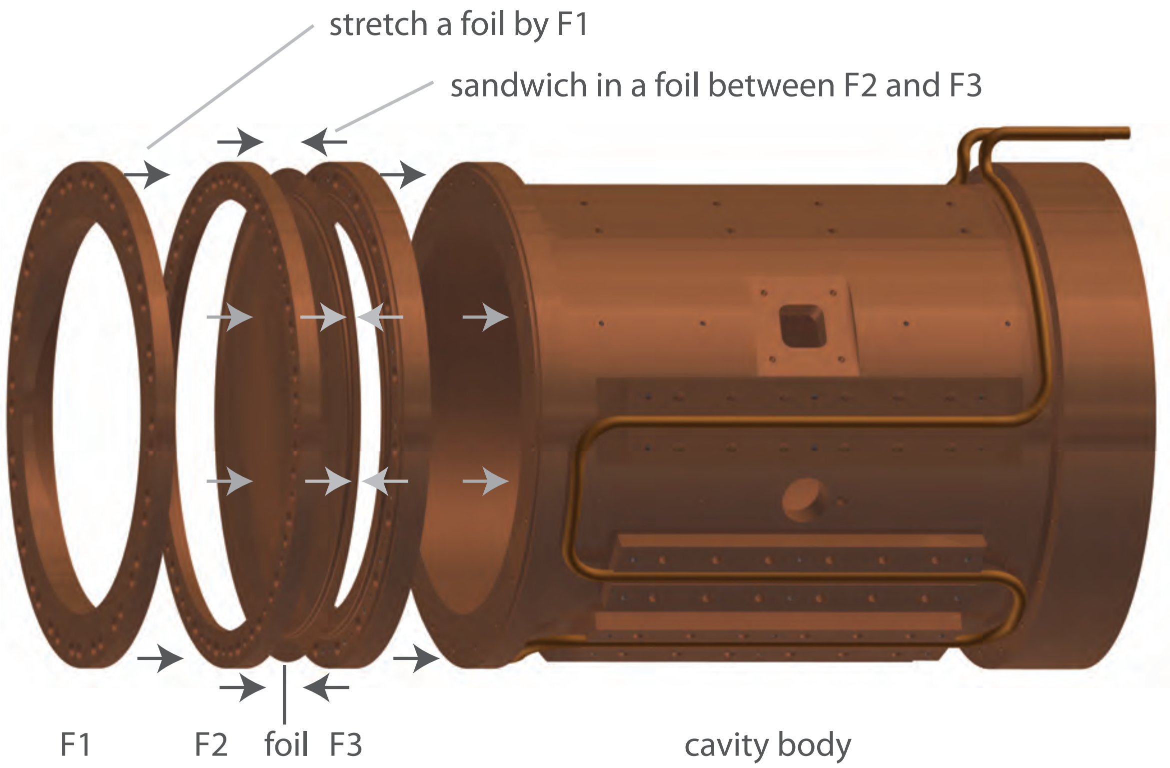

Figure 4.12: How to stretch foils of the cavity. At first, foils are temporally jointed between a F2 and a F3 flanges. Then stretch them again and mount to the cavity by a F1 flange.

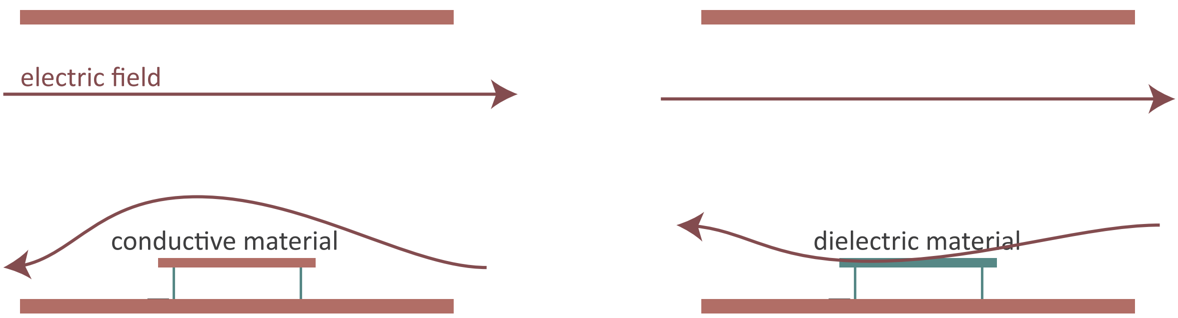

Figure 4.13: A different between electric fields using a tuning bar made of a conductive material and a dielectric material. The conductive tuning bar affects electric field as shrink a diameter of the cavity. On the other hand, the dielectric tuning bar affect as widen it by absorbing RF power.

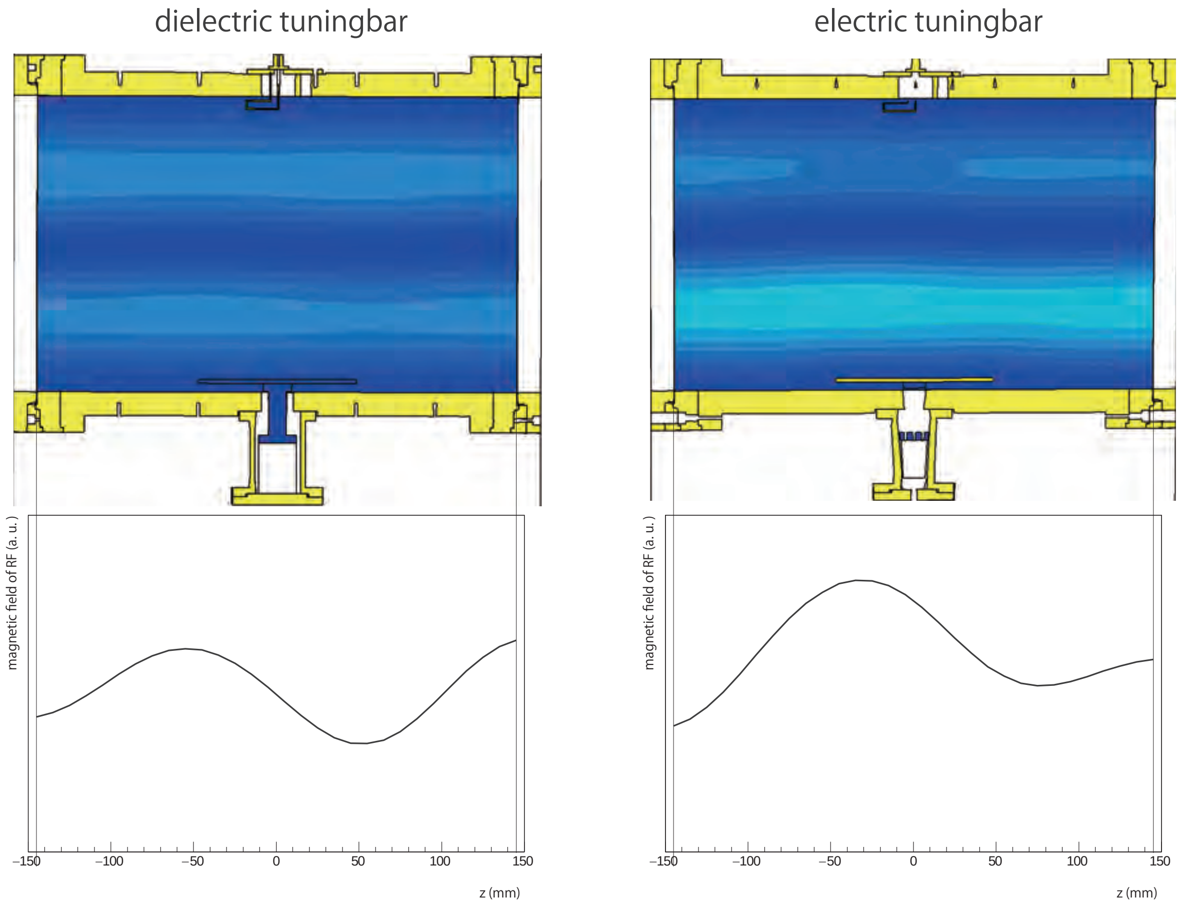

Figure 4.14: A comparison of uniformity of RF field between by using the dielectric tuningbar and the electric tuning bar. Uniformity on the axis by using the dielectric tuning bar is prefer for the cavity of zero field as shown in below figures.

electric permittivity

Complex dielectric constant is described as

$$\epsilon = \epsilon' - j\epsilon'', \tag{4.5}$$

$$\tan\delta = \frac{\epsilon''}{\epsilon'}. \tag{4.6}$$

Real part of permittivity (ϵ') is expressed phase difference from oscillation electric field and amplitude of polarization. Wavelength of RF is shortened in the dielectric material. Effective volume of the cavity is expanded by inserting tuning bar made by dielectric material. As a result, the resonance frequency of the cavity is increased.

dielectric tangent

Imaginary part (ϵ") is expressed dielectric loss. A part of RF power is converted into heat in the dielectric material. It causes reduction of Q factor of the cavity (see Appendix B). In general, dielectric tangent ($\tan\sigma$) is used for estimation of it.

small density

Total weight of a tuning bar and a support must be under 200 g which is the maximum vertical load of the positioner (see Section 4.1.6).

Therefore, a good material for tuning bar should have

1. large electric permittivity

2. small dielectric tangent

3. small density

Tuning bars are loaded on dielectric supports. (see Figure 4.15). Contrary to tuning bars, supports should not affect resonance frequencies. Therefore, good material for support of tuning bar should have

1. small electric permittivity

2. small dielectric tangent

3. small density

According to this, we choose a alumina for the tuning bar and Teflon to the tuning bar support of the tuning bar with reference to Table 4.1.

material	electric permittivity	dielectric tangent	density
macor	6.03	0.007 (8.6 GHz)	2.52
alumina	9.5	0.0002 (1 GHz)	3.9
quartz	3.5	0.0002 (100 MHz)	
silicon	12	0.005 (1 GHz)	2.2
Teflon	2.1	0.00028 (3 GHz)	2.2

Table 4.1: Characteristics of materials for the tuning bar.

4.1.6 Movement mechanism for tuning bar

Precise movement is achieved by piezo positioner ANPz101eXT12/RES/UHV (attocube Systems) us (see Figure 4.17). Piezo element converts electrical energy into mechanical energy. Positioner is drived by sawtooth pulses from a controller. For precise positioning, feedback from displacement sensor is required since displacement of positioner doesn't bear a proportionate relationship to applied voltage. This positioner using a resistor located in a positioner as displacement sensor. Absolute positioning is enabled by reading a resistance value. Table 4.2 shows a spec of ANPz101eXT12/RES/UHV.

Piezo positioner has following advantages for our experiments.

Simple wiring Since the positioner is drived and read resistance value by only electrical wirings, only simple feed through port at gas chamber is needed. It is ideal for purity of Krypton gas in a chamber. Since this positioner is UHV compatible model, it enable over 150 °C baking and outgassing rate is below a level of 1×10^{-11} Pa $\cdot$ m^3/s.

Compactness Space between inner surface of superconducting magnet and gas chamber is limited to load such as a linear manipulator.

Nonmagnetism It is made of Titanium so that hardly affect to uniformity of the magnetic field.

travel (step mode)	12 mm
typical minimum step size	50 nm
maximum vertical load	200 g

Table 4.2: Spec of ANPz101eXT12/RES

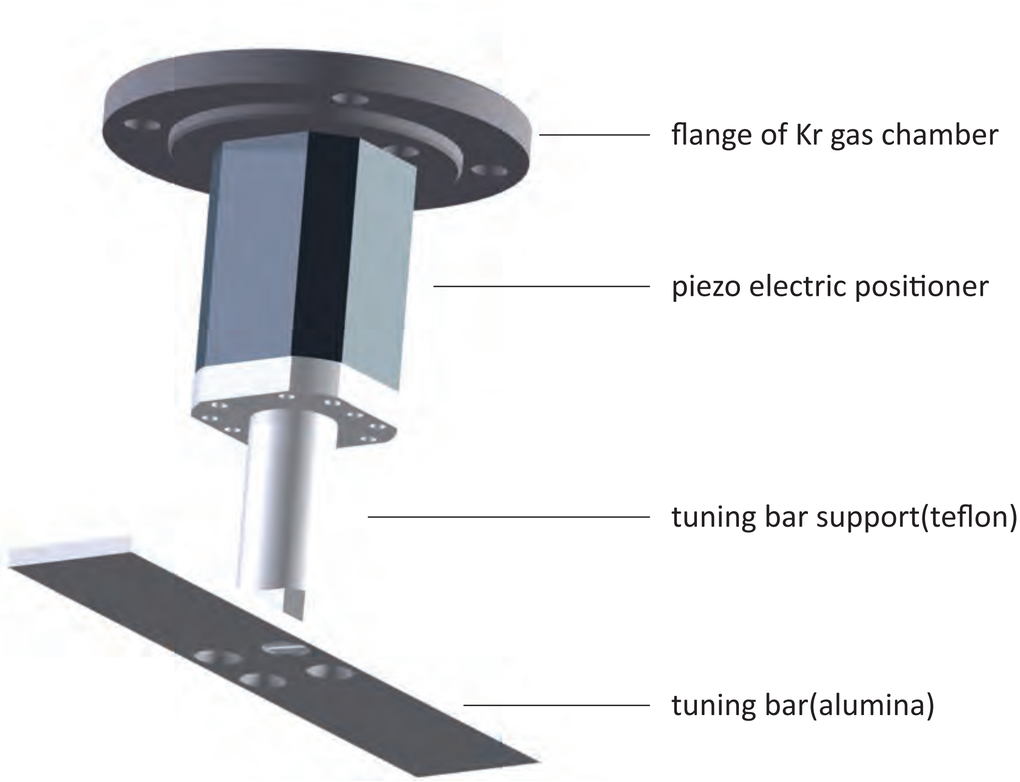

Figure 4.15: A schematic drawing of the tuning bar for high field experiment.

Piezo controller

Piezo positioners are controlled by piezo controller ANC350/3/RES (attocube systems) (see Figure 4.18). As shown in Figure 4.16, it has 3 channels for manipulating each positioner.

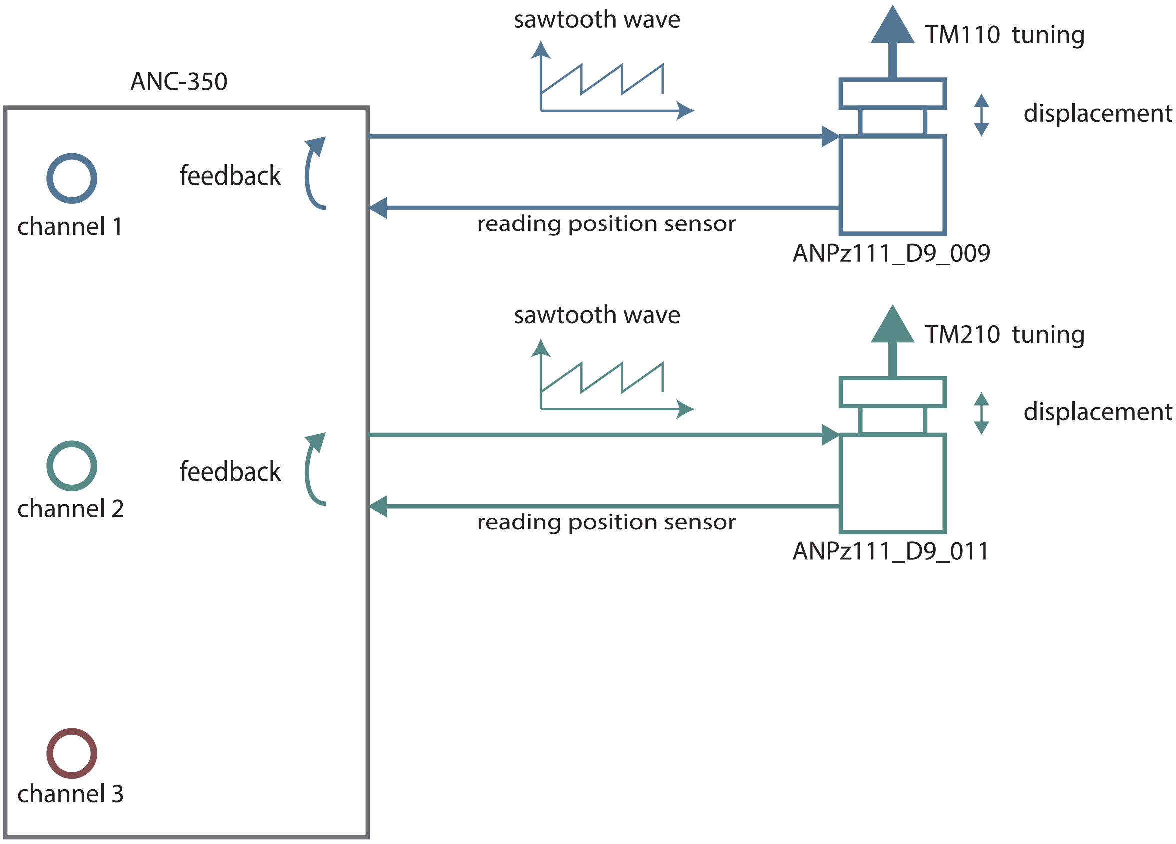

Figure 4.16: A diagram of a positioner system. ANC-350 has three channels to operate the positioners. It transmits sawtooth waves to each positioner and displace their stages in proportion to amplitude of waves. Precise displacement is achieved by feedback from a positioner sensor.

Sweeping

The TM110 (TM210) mode and split into two sub modes by tuning bars. The first one named TM110-1 (TM210-1) is affected by the tuning bar strongly, and another mode named TM110-2 (TM210-2) is not affected comparably. The resonance frequency of former modes is used for obtaining resonance curves. Figure 4.19 and 4.20 shows the location of tuning bar in a cross section drawing of the cavity. There are two tuning

Figure 4.17: A photograph of piezo positioner.

Figure 4.18: A photograph of piezo controller.

bars for each of the mode. The tuning bars are located to affect RF electric field efficiently. Figure 4.21 shows the relation of frequency sweep and a displacement of tuning bar by the simulation. Using this tuning bar, the range of frequency sweep is estimated at about 20 MHz and minimum step size is about 100 Hz.

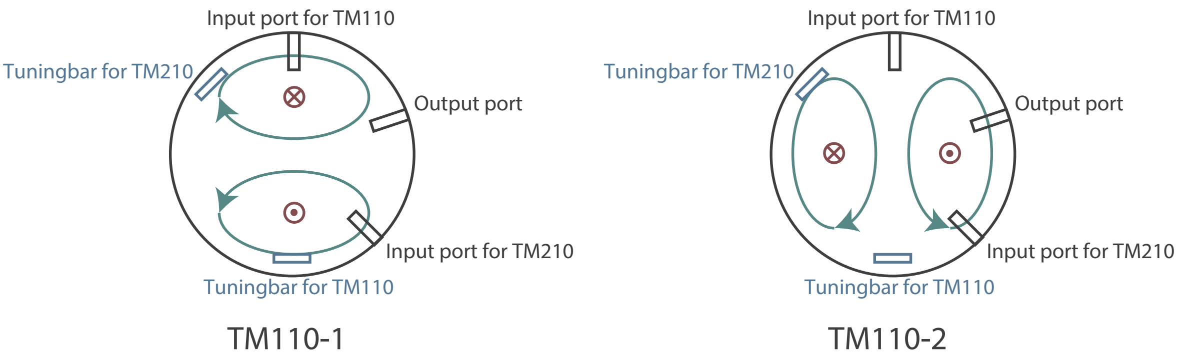

Figure 4.19: Degenerated modes of the TM110. The left side (TM110-1) of resonance mode is affected by tuning bar for TM110 stronger than the right side (TM110-2). Then this mode is appropriate to using for the resonance frequency sweep.

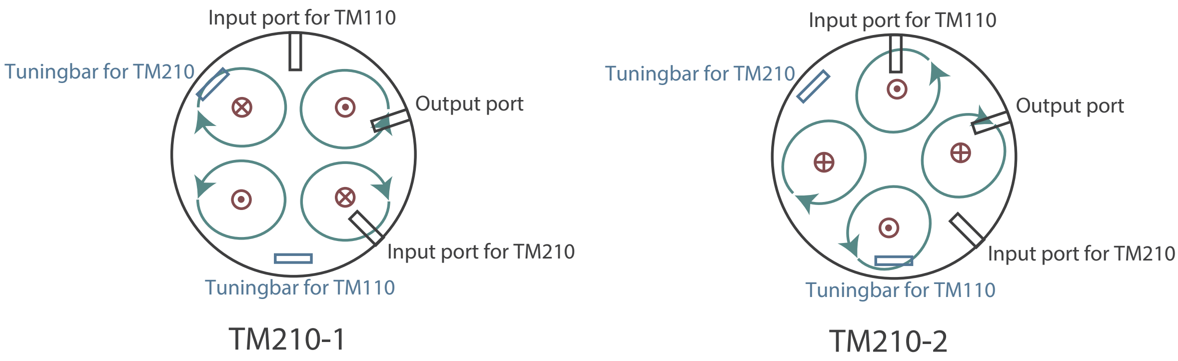

Figure 4.20: Degenerated modes of TM210. The left side (TM210-1) of resonance mode is affected by tuning bar for TM110 stronger than the right side (TM210-2). Then this mode is appropriate to using resonance frequency sweep.

4.1.7 Summary of designing the cavity

Figure 4.22 is an outline view of the cavity and Table 4.3 is a summary of the dimension of the cavity. It is situated in the gas chamber and transit muonium by oscillating magnetic field. There are three ports for two RF input loop and one output loop. The resonance frequencies are tuned by two tuning bars. The temperature in the RF cavity is maintained by cooling tube wound around it.

material	oxygen-free copper
inner diameter	187 mm
axial length	304 mm
thickness in a radial direction	15 mm
thickness of foil	25 μm
ports	2 $\times$ for tuning bar
	2 $\times$ for RF input
	1 $\times$ for RF output

Table 4.3: Summary of the dimension of the cavity.

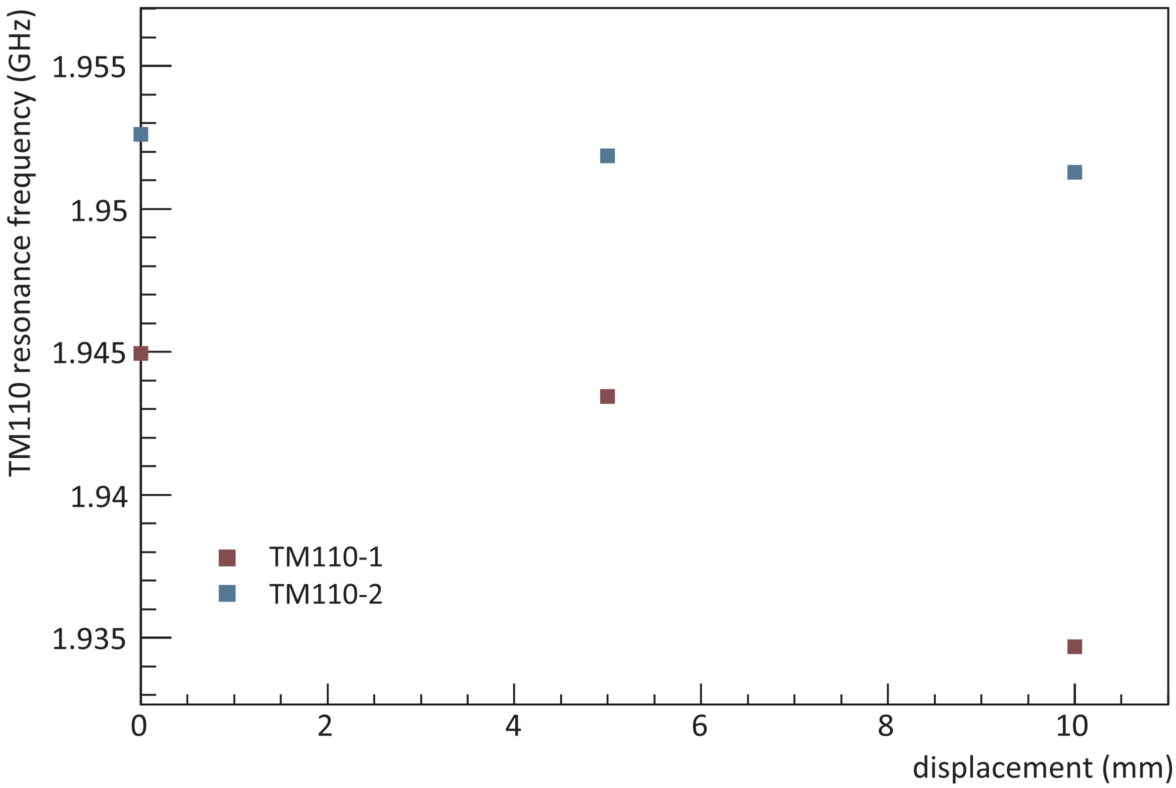

Figure 4.21: A relation between resonance frequency of the TM110 mode and the displacement of the tuning bar. This is a result of the simulation using a alumina tuning bars (20 mm $\times$ 200 mm $\times$ 2.5 mm). Origin points of tuning bars are defined as 5 mm far from the cavity face. The TM110 mode is splitted into two degenerated modes. The red point is the TM110-1 mode and the blue point is the TM110-2 mode. The TM110-1 mode is more sensitive to the displacement.

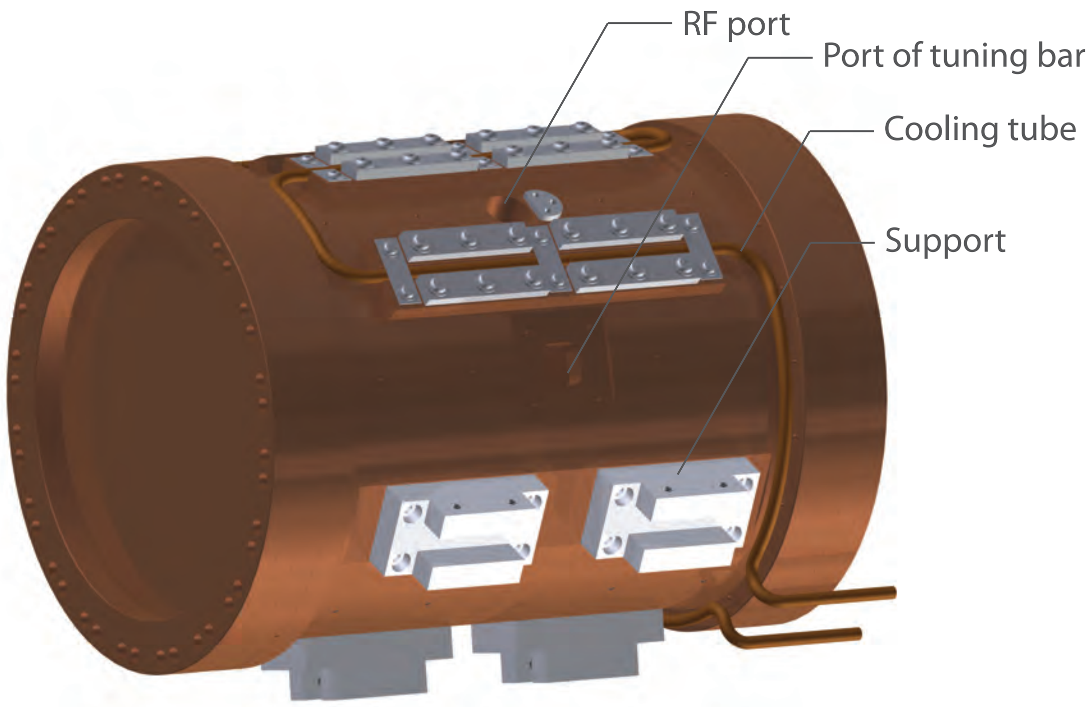

Figure 4.22: An isometric view of the cavity. There are three RF ports and two ports for tuning bars. There are a cooling water pipe for a stability of temperature and a support for loading in the gas chamber.

4.2 Performance test for the cavity for high field

This section describes the measurements of

1. Frequency character of the cavity (Subsection 4.2.1),
2. Q factors of the cavity (Subsection 4.2.2),
3. Performance evaluation of tuning bars (Subsection 4.2.3, 4.2.4).

4.2.1 Frequency character of the cavity

The characteristic of the cavity without tuning bars is measured. Resonance frequencies of the TM110 mode and the TM210 mode are determined by S_{11} and obtained Q factor of each mode by S_{21} (see Appendix B). Figure 4.23 shows a resonance line shape of the TM110 mode. A red arrow indicates the resonance frequencies of the TM110 mode in the measurement. Figure 4.24 is a close-up of Figure 4.23. These peaks are determined as the TM110 mode by the reason that there should be two degenerated TM110 modes. The TM110-1 mode is coupled input port for TM110 strongly and the TM110-2 mode is coupled weakly as mentioned in 4.1.6. In addition to this, the TM110-1 mode should be affected strongly by tuning bar for TM110 than the TM110-2 mode.

Thus the resonance frequencies of the TM110 modes are 1.9532 GHz (TM110-1) and 1.9541 GHz (TM110-2) in the measurement. It is slightly different from the value obtained by Equation 4.1, 1.9553 GHz. This is coming from RF ports and tuning bars which are not included in the analytical calculation.

Figure 4.25 shows a resonance line shape of the TM210 mode. The determination of the TM210 mode is by same way of the TM110 mode. The resonance frequencies of the TM210 modes are 2.6423 GHz (TM210-1) and 2.6455 GHz (TM210-2) in the measurement. It is also slightly different from the value obtained by Equation 4.1, 2.6207 GHz.

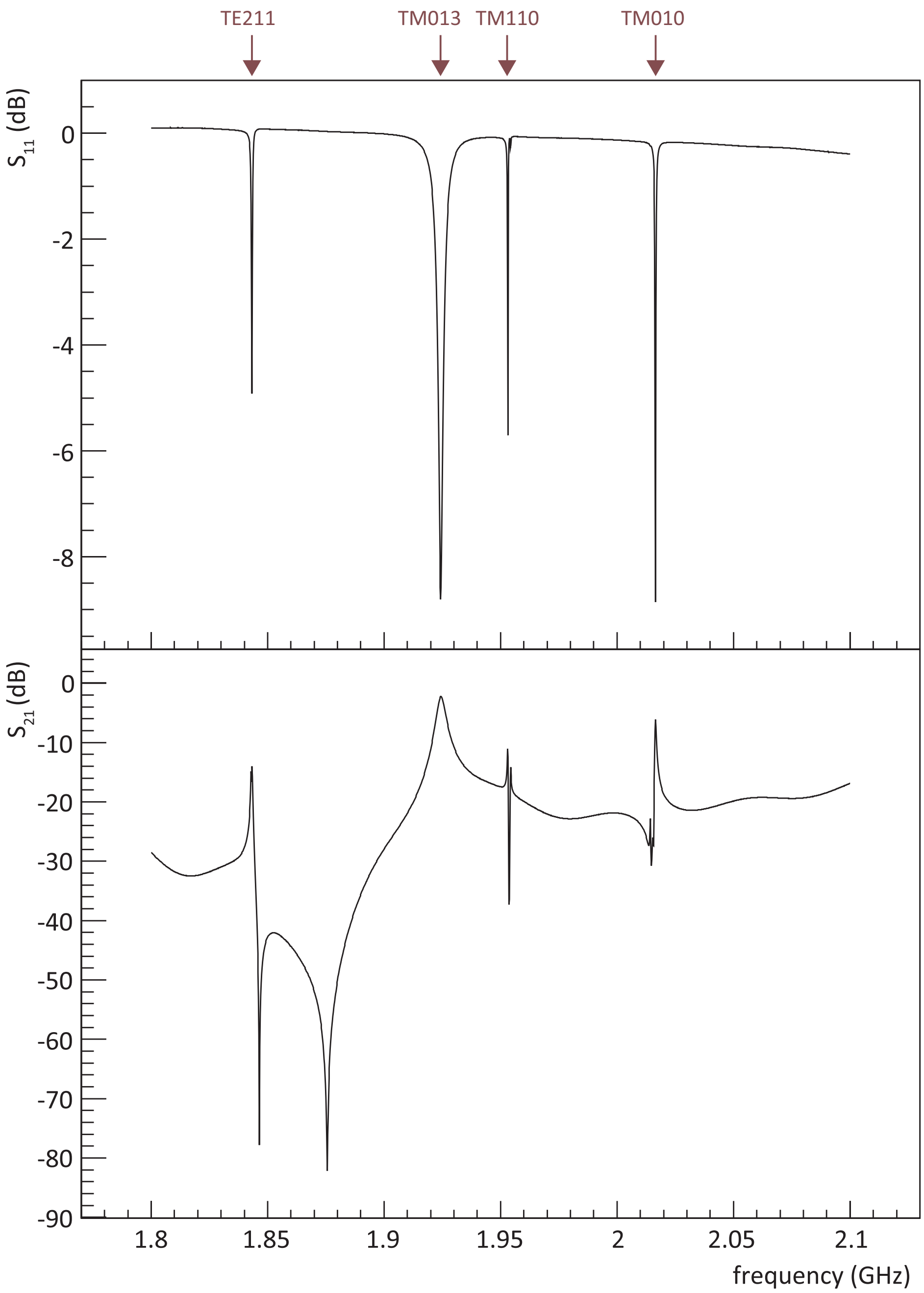

Figure 4.23: (a) S_{11} near the TM110 modes by the measurement. The red arrows show resonance frequencies of each mode. (b) S_{21} by the measurement.

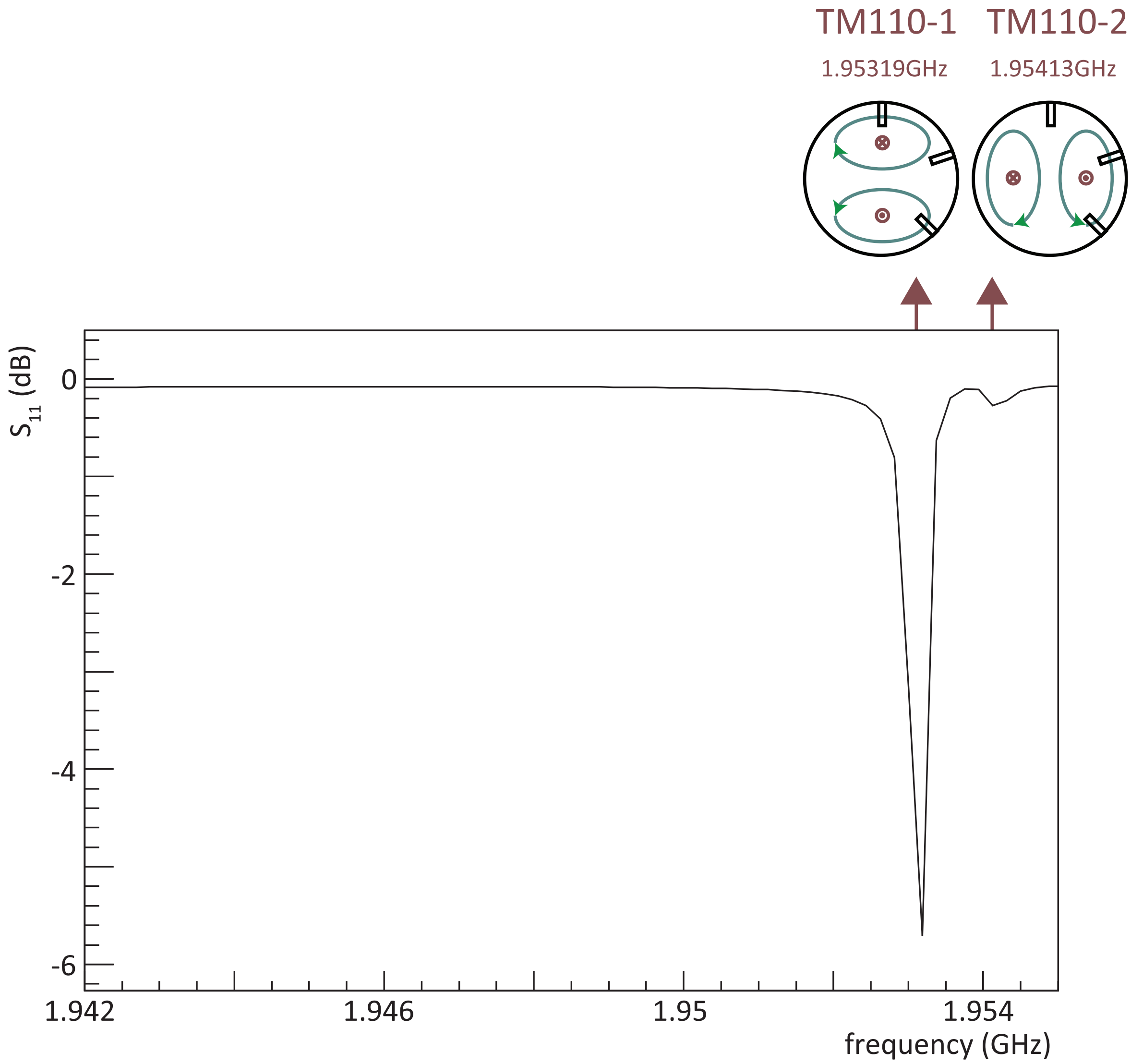

Figure 4.24: A Close-up of Figure 4.23 (a). The red arrows show resonance frequencies of the TM110 modes.

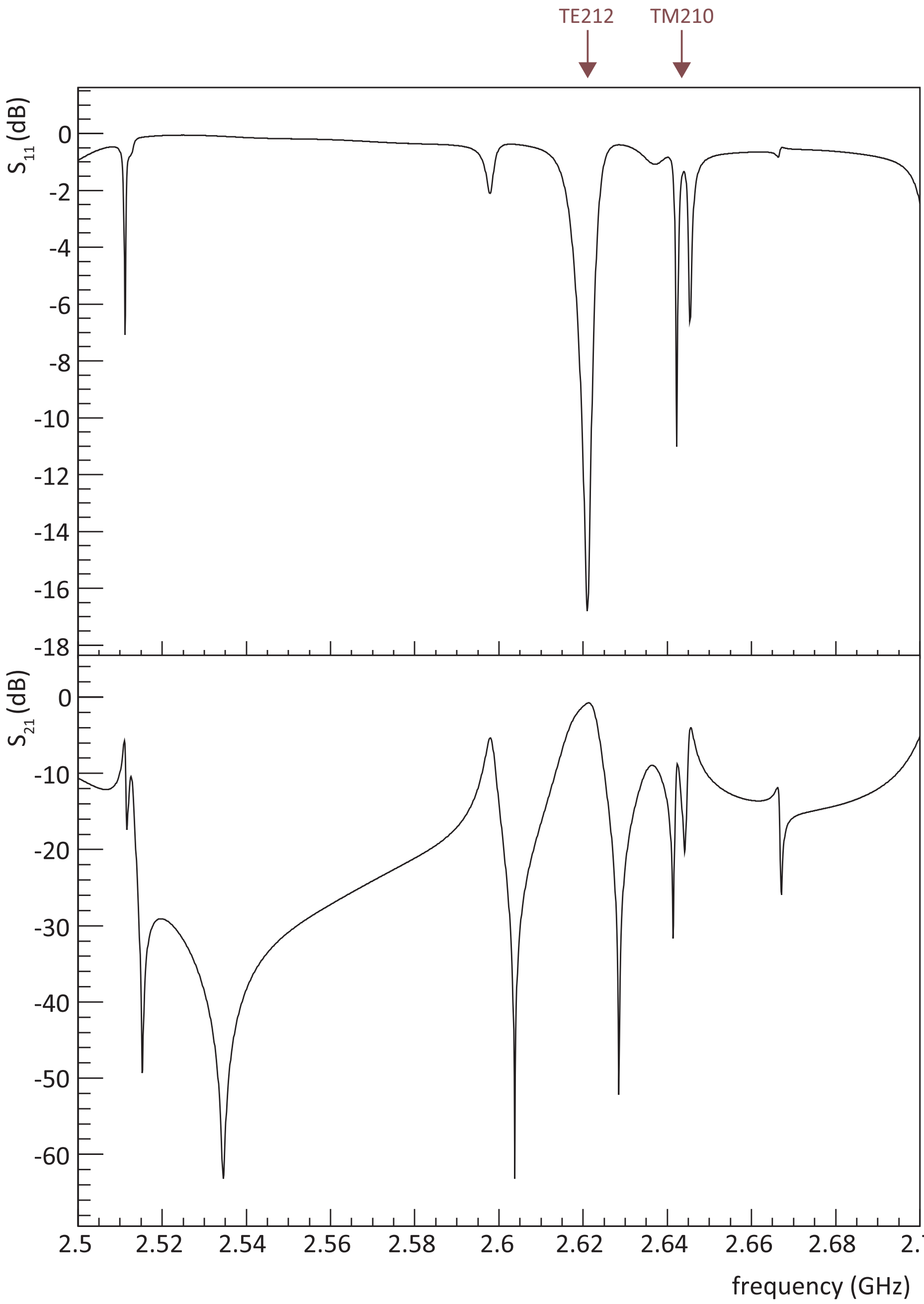

Figure 4.25: (a) S_{11} near the TM210 modes by the measurement. The red arrows show resonance frequencies of each mode. (b) S_{21} by the measurement.

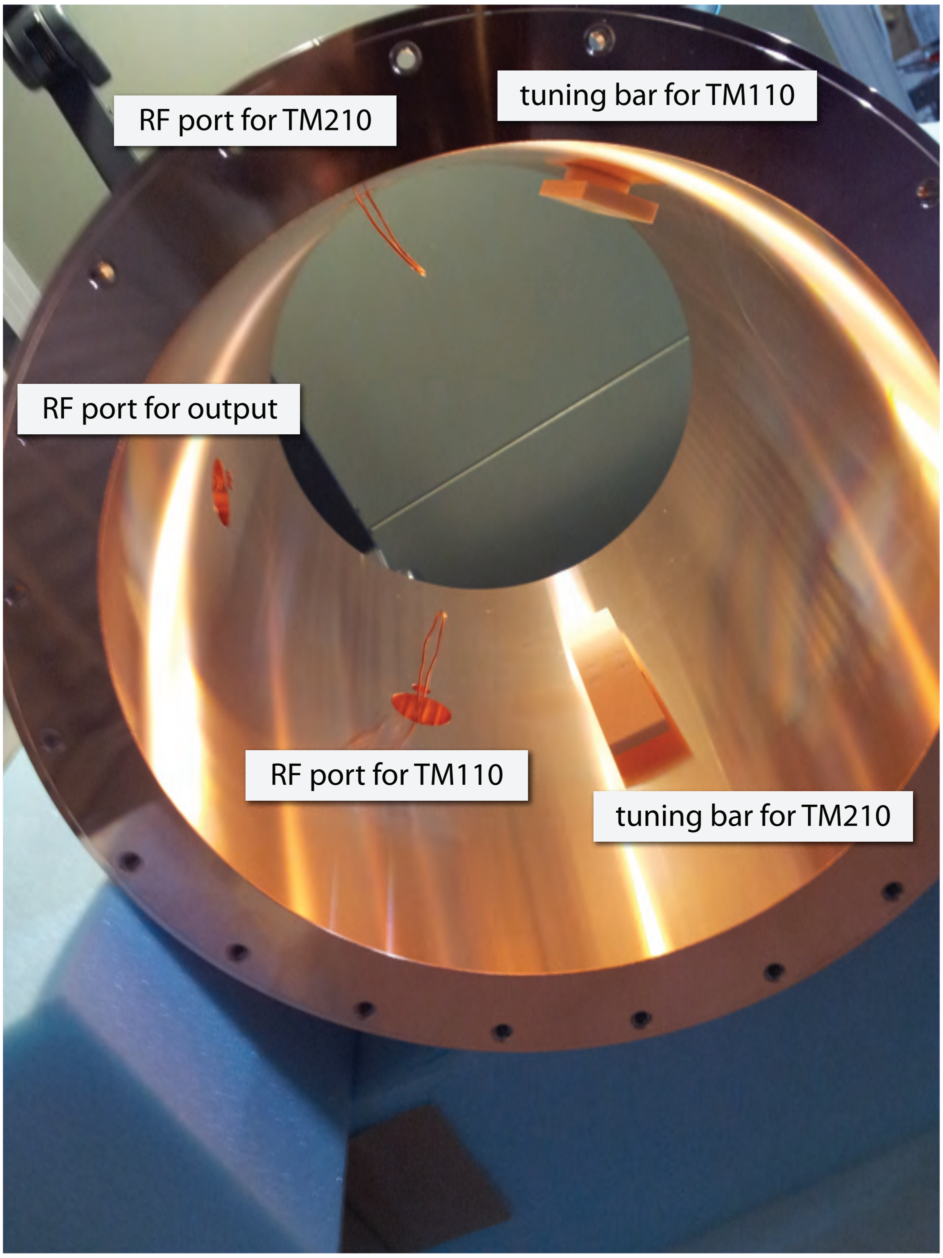

Figure 4.26: A photograph of inner view of the cavity. The RF antennas and the tuning bars are installed.

4.2.2 Q factors of the cavity

Q factors from simulations

Table 4.4 and 4.5 show a result of calculation of Q factor of the TM110 mode and the TM210 mode by CST STUDIO. In this simulation, the main part of the power losses is caused by surface current of the cavity.

	Loss/W (peak)	Q
Q_{ext}	1.19×10^5	2.04×10^5
Q_{c}	7.19×10^5	3.75×10^4
Q_{d}	5.17×10^5	4.72×10^5
Q_{L}	8.21×10^4	2.97×10^4

Table 4.4: Q factor of the TM110 mode. Loss of Q is caused by surface current at the cavity face and loss tangent of tuning bar. Definition of Q_{ext}, Q_{c}, Q_{d}, and Q_{L} are described in Appendix B.

	Loss/W (peak)	Q
Q_{ext}	9.71×10^4	3.32×10^5
Q_{c}	7.19×10^5	4.48×10^4
Q_{d}	3.00×10^5	1.07×10^5
Q_{L}	1.12×10^6	2.89×10^4

Table 4.5: Q factor of the TM210 mode. Loss of Q is caused by surface current at the cavity face and loss tangent of tuning bar.

Q factors from measurements

Q factor of the cavity was measured in case of the alumina (99.6 %) tuning bar (20 mm$\times$ 100 mm$\times$5 mm) is used (see Figure 4.34). Figure 4.27 shows a result of the measured Q factor of the TM110 mode. By fitting with a Lorentzian function, Q factor is calculated as 1.13×10^4. Similarly, the measured Q factor of the TM210 mode is calculated as 8.05×10^3 (Figure 4.28).

These values are far less than the Q factors estimated by the simulation. (see Table 4.2.3).

One of reasons of the Q factor depression is a coupling with input antennas. As mentioned Appendix B, Q_L of the cavity is equivalent to Q_{ext} when the cavity and the input port is coupled. The peak of the S_{11} of the TM110-1 mode is only -15 dB. In this case, 3 % of the RF power is reflected. On the other hand, the peak of the S_{11} of the TM210-1 mode is only -2 dB so that about 63 % of RF power is reflected to the input port. Thus it is not able to said that Q_L is equivalent to Q_{ext}, and optimization of the antennas is needed to estimate accurate Q factor.

modes	Q (in the measurement)	Q (in the simulation)
TM110	1.13×10^4	2.97×10^4
TM210	8.05×10^3	2.89×10^4

Table 4.6: A comparison of Q factor between in the measurement and in the simulation.

4.2.3 Relation between displacement of tuning bars and resonance frequencies

Figure 4.29 shows resonance frequency sweeps of the TM110. Although the TM110-2 mode are not affected from the tuning bar for TM110, TM110-1 is tunable from 1.948 GHz to 1.934 GHz by the tuning bar for TM110.

On the other hand, Figure 4.31 shows resonance frequency sweeps of the TM210 mode. Although the TM210-2 mode are not affected from the tuning bar for TM210, TM210-1 is tunable from 2.608 GHz to 2.537 GHz by the tuning bar for TM210.

Figure 4.30 and 4.32 show comparisons of TM110-1 and TM210-1 resonance frequency sweep by tuning bars for TM110 and TM210 in the measurement, simulation by CST STUDIO, and analytical calculation.

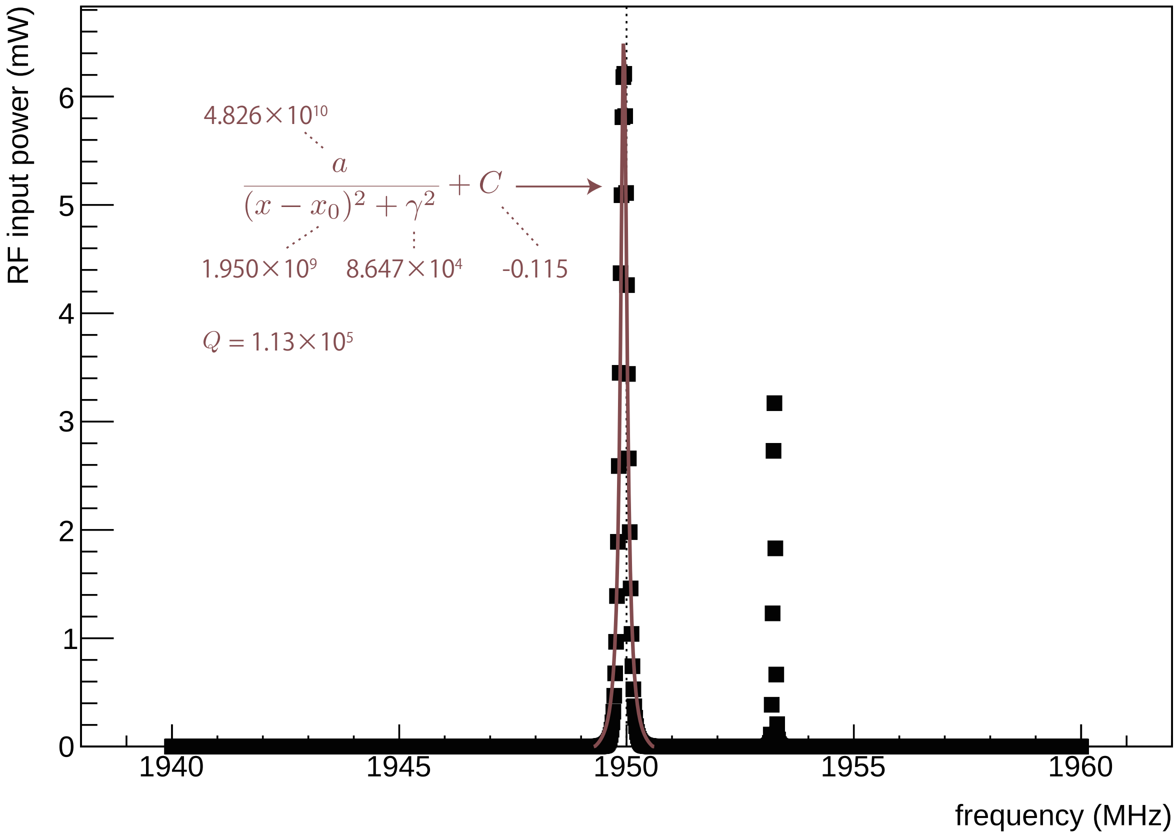

Figure 4.27: The measured Q factor of the TM110 mode. Q factor is calculated from FWHM of the resonance shape. FWHM is obtained from fitting with Lorentzian function.

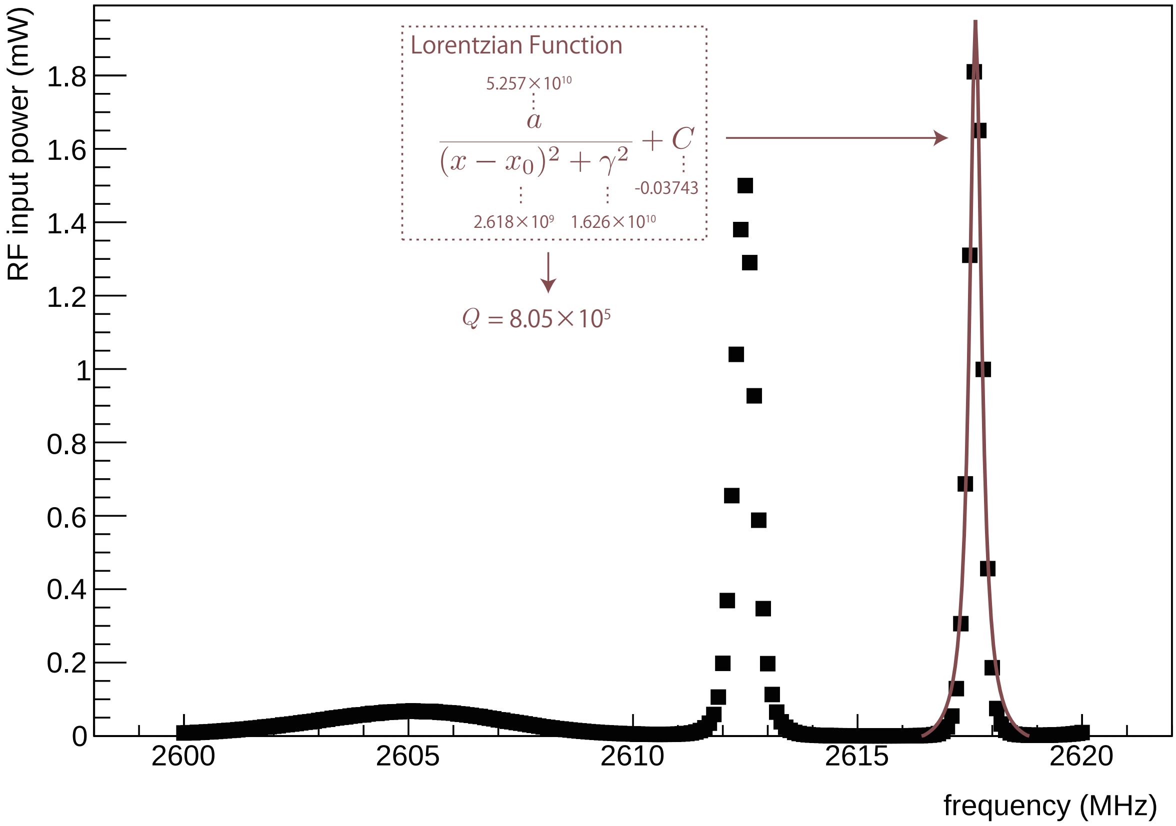

Figure 4.28: The measured Q factor of the TM110 mode.

Analytical calculation is done under assumption that the frequency shift by a cavity perturbations is expressed as Equation 4.4. Compared results of analytical calculation, simulation results are in good agreement with results in measurements.

Figure 4.33 shows the result of TM110 resonance frequency sweep by the tuning bar for TM210 which is not used for sweeping the TM110 mode originally. Unlike in the case of using the tuning bar for TM110, the TM110-2 resonance frequency slightly varies with the displacement. The reason is that the position relationship between the tuning bar and the electric field of TM110-2 is different from the case of using the tuning bar for TM110 (see Figure 4.19). Since the TM110-1 resonance frequency also sweep by the tuning bar for TM210, the sweep range can be larger than using only the tuning bar for TM110.

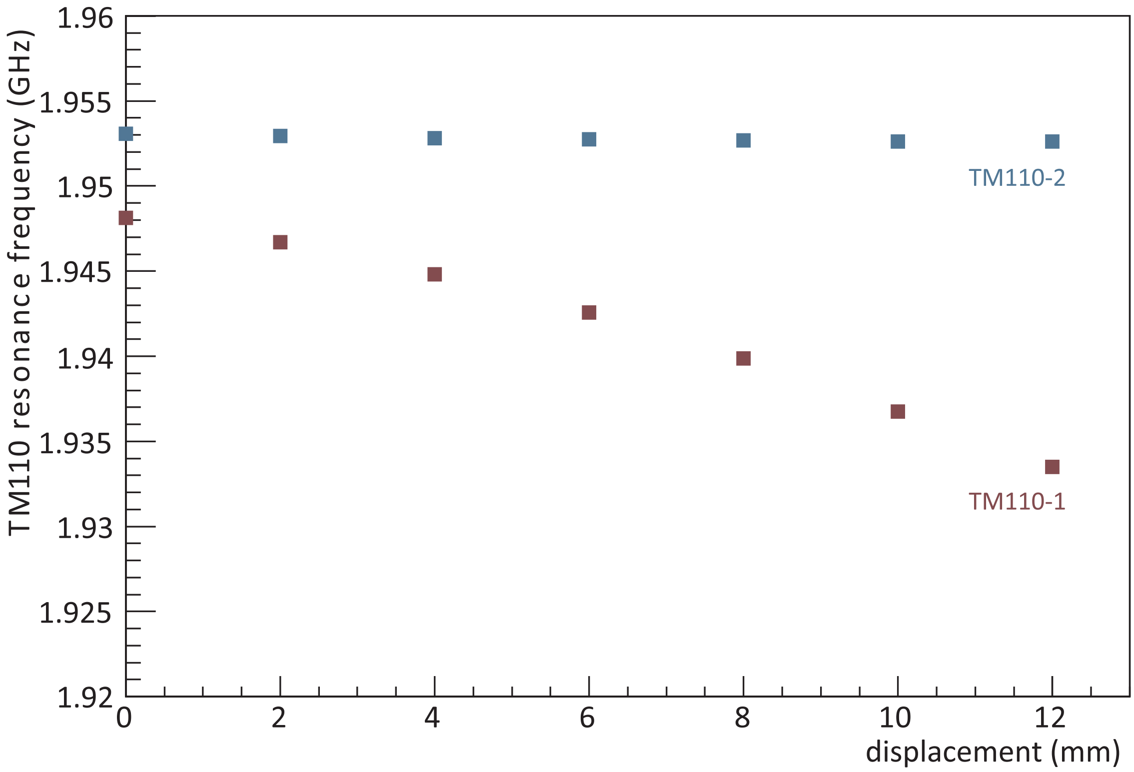

Figure 4.29: A TM110 resonance frequency sweep by the tuning bar for TM110. Red markers show resonance frequencies of TM110-1, blue markers show of TM110-2. TM110-2 is not affected by the tuning bar for TM110.

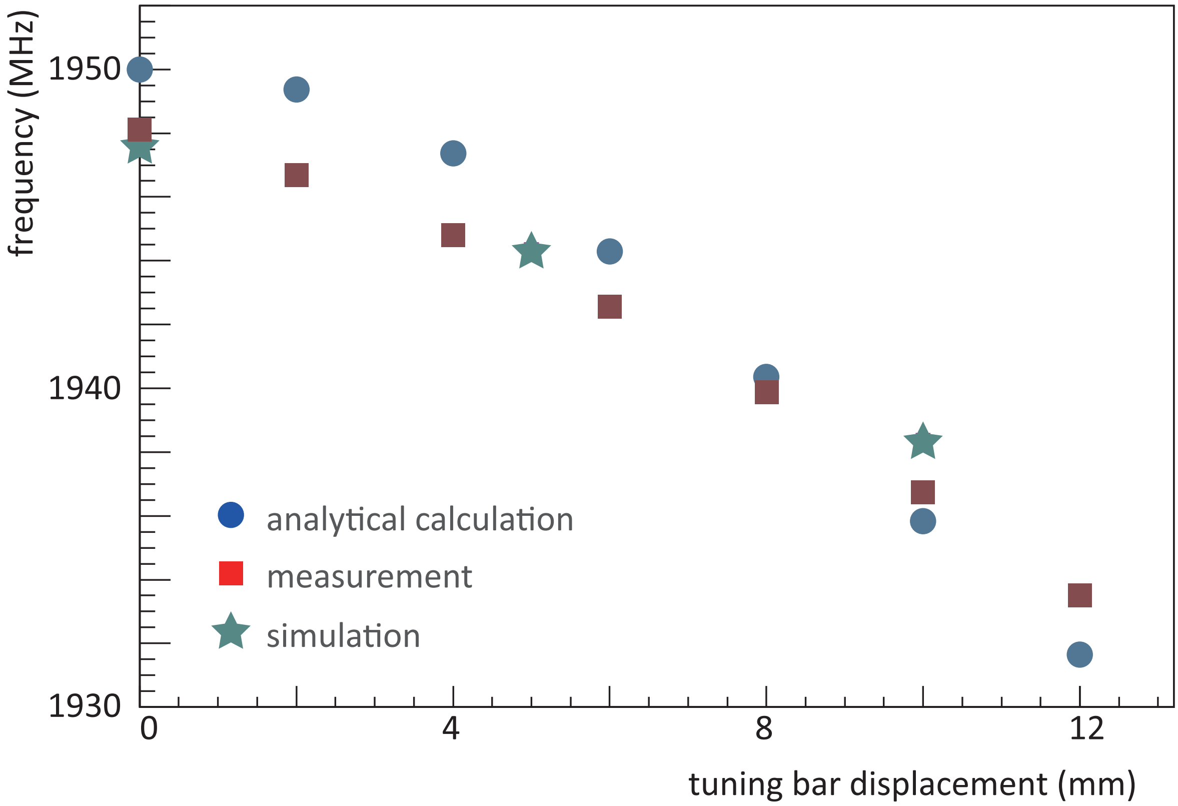

Figure 4.30: Comparison of TM110-1 resonance frequency sweep by the tuning bar for TM110 in the measurement, simulation, and analytical calculation.

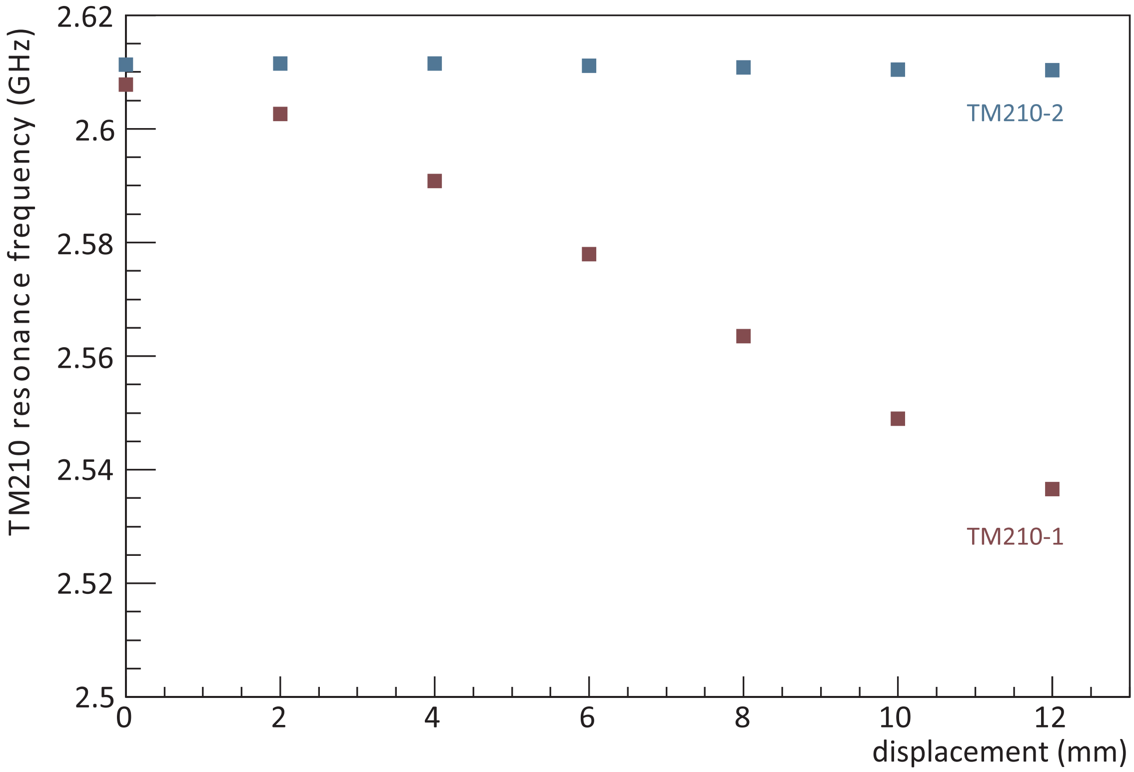

Figure 4.31: A TM210 resonance frequency sweep by the tuning bar for TM210. Red markers show resonance frequencies of TM210-1, blue markers show of TM210-2. TM210-2 is not affected by the tuning bar for TM210.

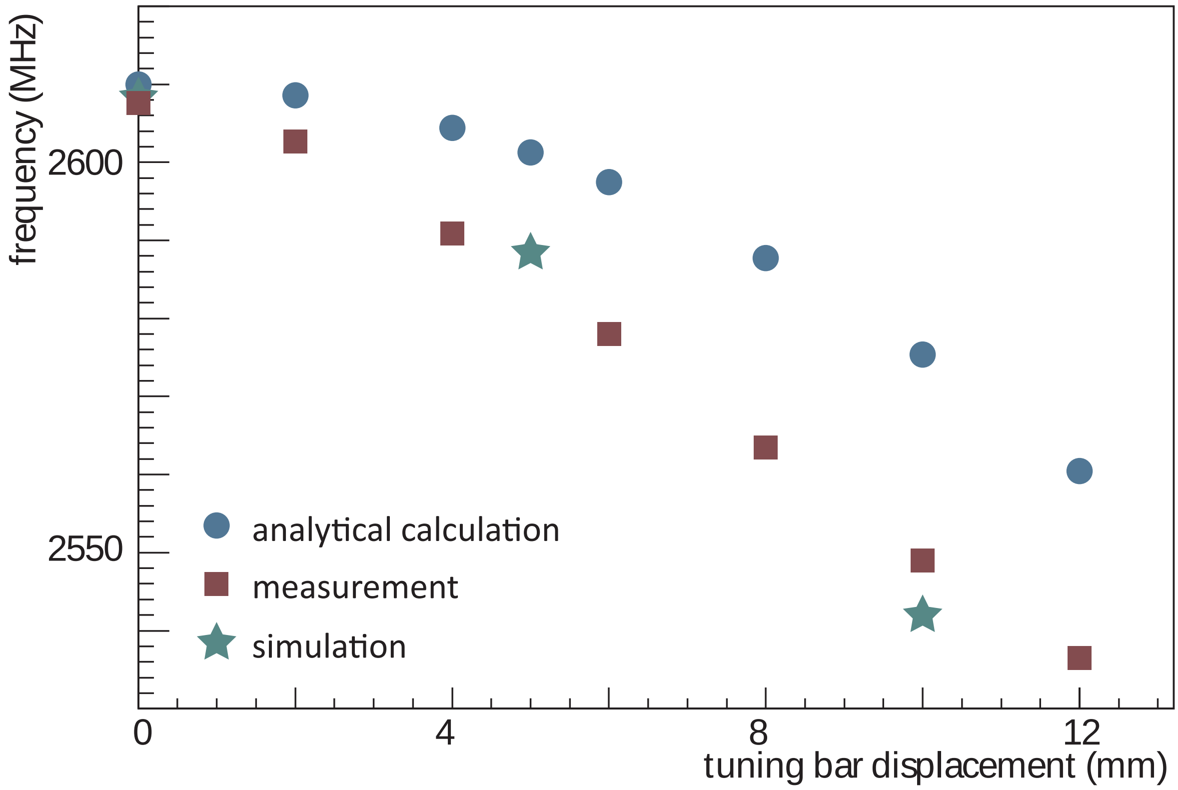

Figure 4.32: Comparison of TM210-1 resonance frequency sweep by the tuning bar for TM210 in the measurement, simulation, and analytical calculation.

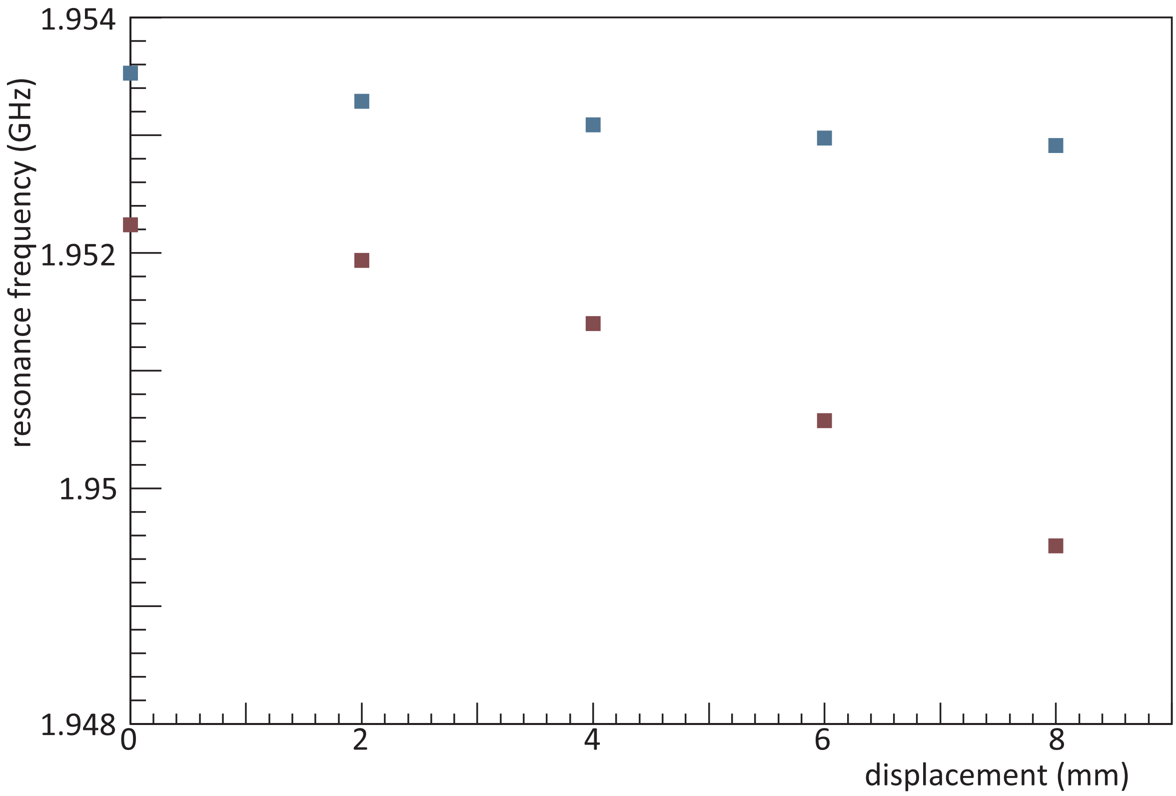

Figure 4.33: A TM110 resonance frequency sweep by the tuning bar for TM210. Red one is that of TM210-1 and blue one is that of TM210-2.

4.2.4 Difference between several types of tuning bars

Figure 4.34 shows three tuning bars to compare performance. Tuning bar1 is used for the performance test in Subsection 4.2.3. Tuning bar2 is the double long of tuning bar1 and tuning bar3 is the half thickness of the tuning bar1.

Figure 4.35 shows resonance frequency sweeps of the TM110-1 mode by three tuning bars. As mentioned Appendix B, a sweep range is defined by volume of the tuning bar. In addition to this, since displacement of tuning bar is defined as a length between inner surface of the cavity and that of tuning bar, a thick tuning bar is inserted deeply at the same displacement. Therefore, the sweep range of tuning bar3 is shorter than other bars and the line shape of tuning bar2 is parallel to that of tuning bar1. Figure 4.36 shows a same relation of the TM210-1 mode. Since the RF field of the TM210 mode rotates on axis of the cavity (see Figure 4.37), the parallel relationship of the line shape of tuning bar1 and tuning bar2 is not kept.

4.2.5 Discussion about the performance test of the cavity

Summary of the performance test

Both frequency characteristics of TM110 and TM210 are measured and consistent with simulation results. Candidates of reasons of difference between measurements and simulations are shapes (see Section 4.5.3) of antennas and parameters of tuning bars such as dielectric tangent or electric permittivity. Such material parameters are varied with a manufacturing process of alumina. Compared with the case dielectric tangent is ($\tan\delta = 0.0004$) which is default value at CST STUDIO and $\tan\delta = 0.004$, the resonance frequency of TM110-1 is shifted of 4 MHz.

Optimization of the inner diameter of the cavity

The sweep range of the TM110 mode by tuning bar1 is 1.948 GHz to 1.934 GHz and that of the TM210 mode by tuning bar2 is 2.608 GHz to 2.537 GHz (see Figure 4.29 and 4.31). Compared to transition frequencies of ν_{12} and ν_{34} (see Equation 4.2 and

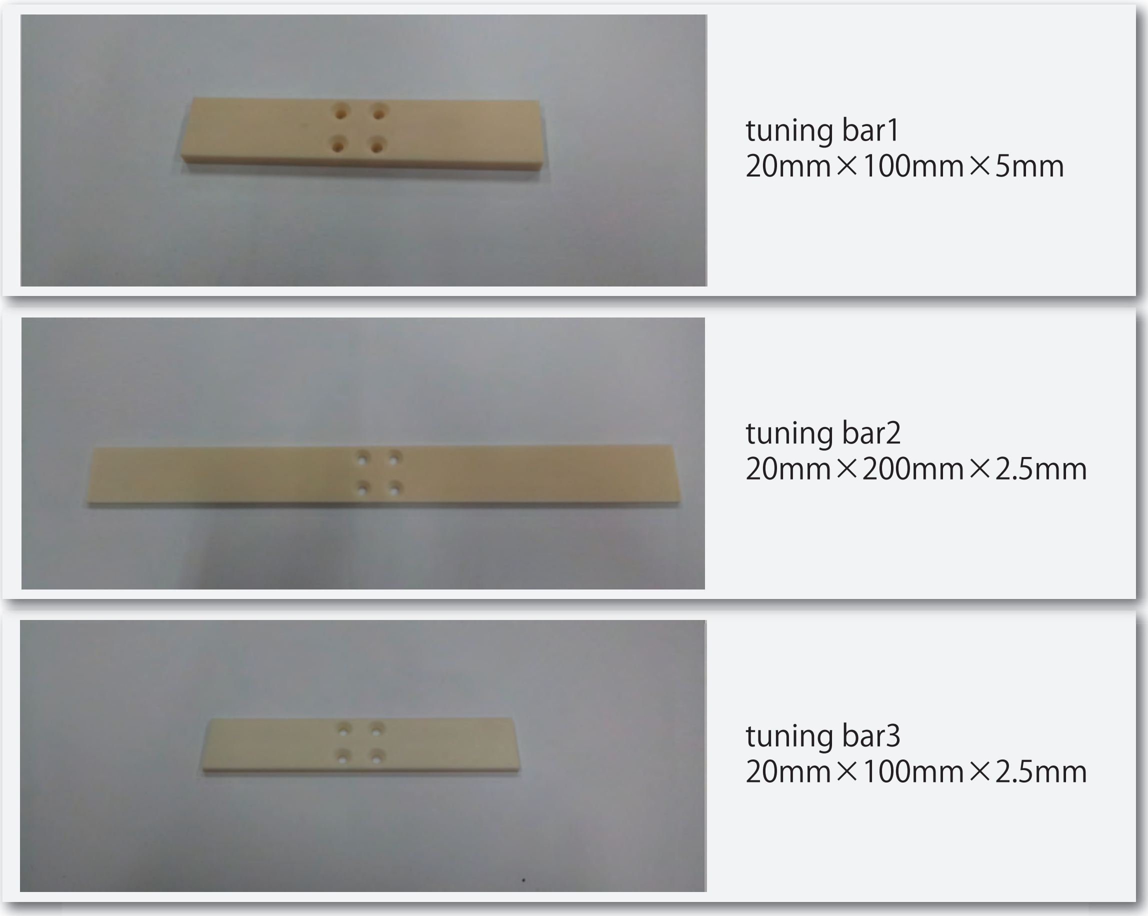

Figure 4.34: Three tuning bars are used for this measurement. The sweep range of tuning bar3 is shorter than other bars and the line shape of tuning bar2 is parallel to that of tuning bar1.

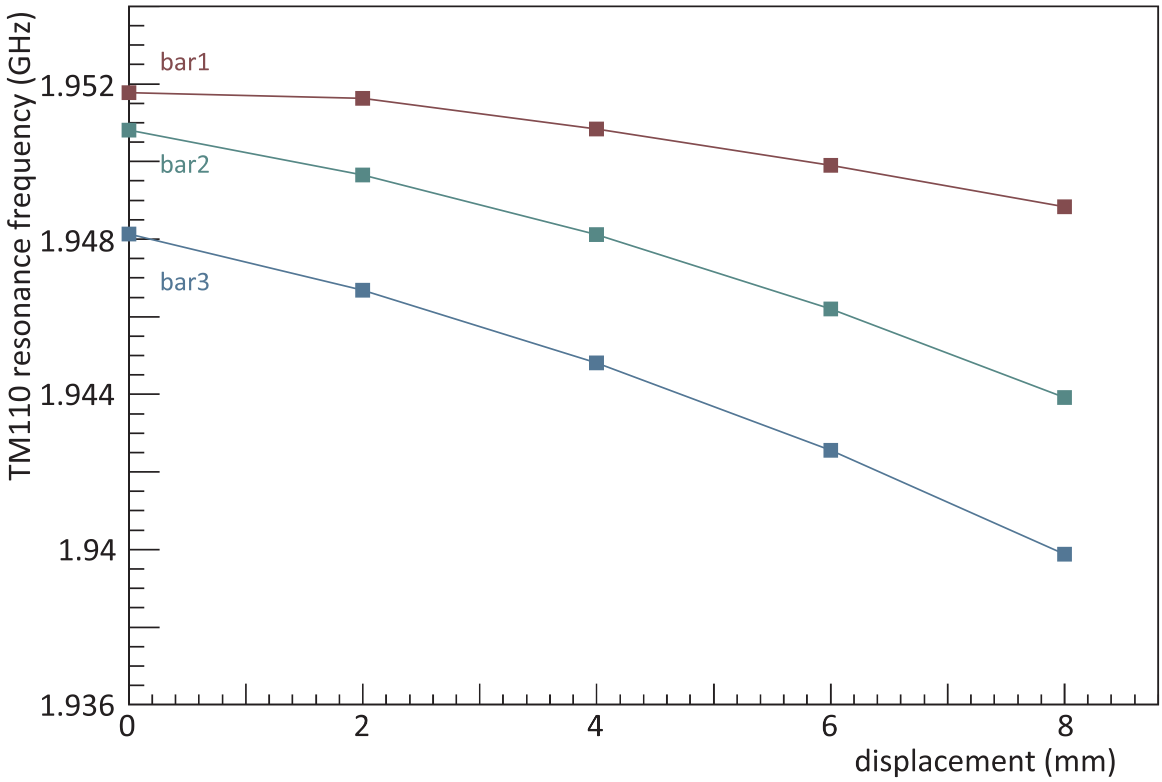

Figure 4.35: A difference of sweep range of the TM110 mode between several tuning-bars.

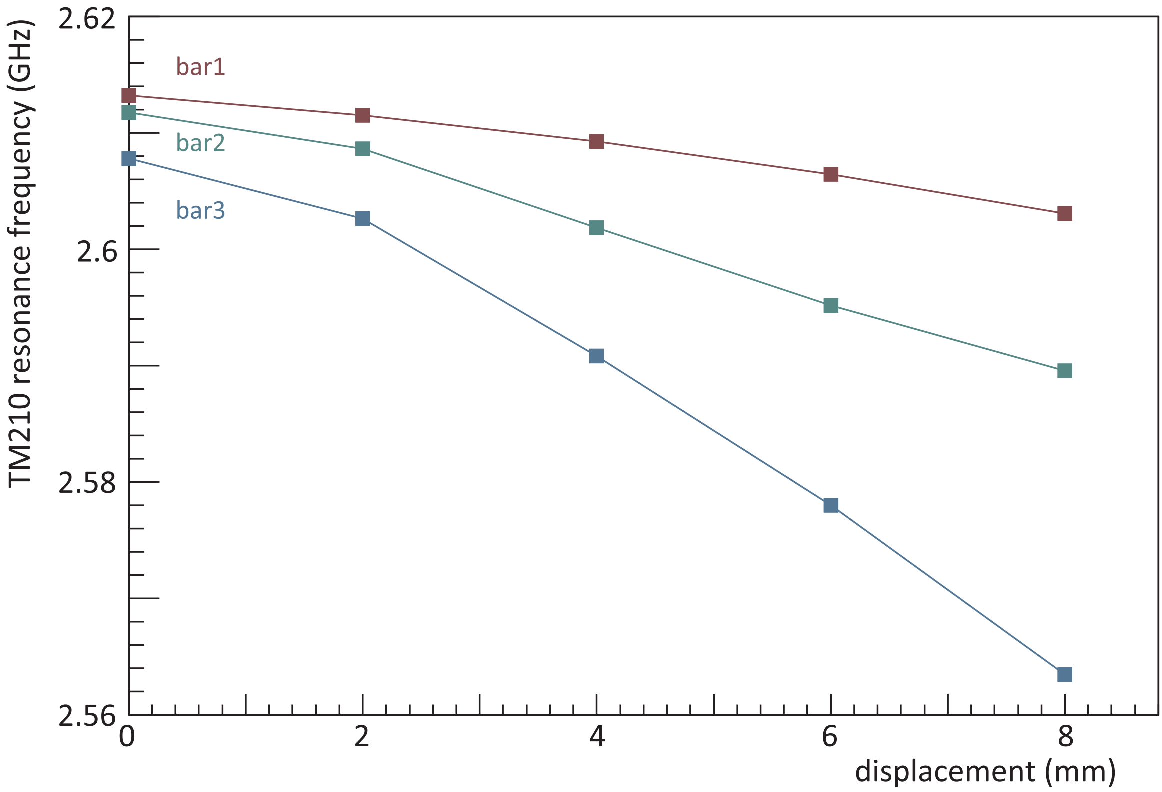

Figure 4.36: A difference of sweep range of TM210 mode between several tuningbars. the parallel relationship of the line shape of tuning bar1 and tuning bar2 is not kept.

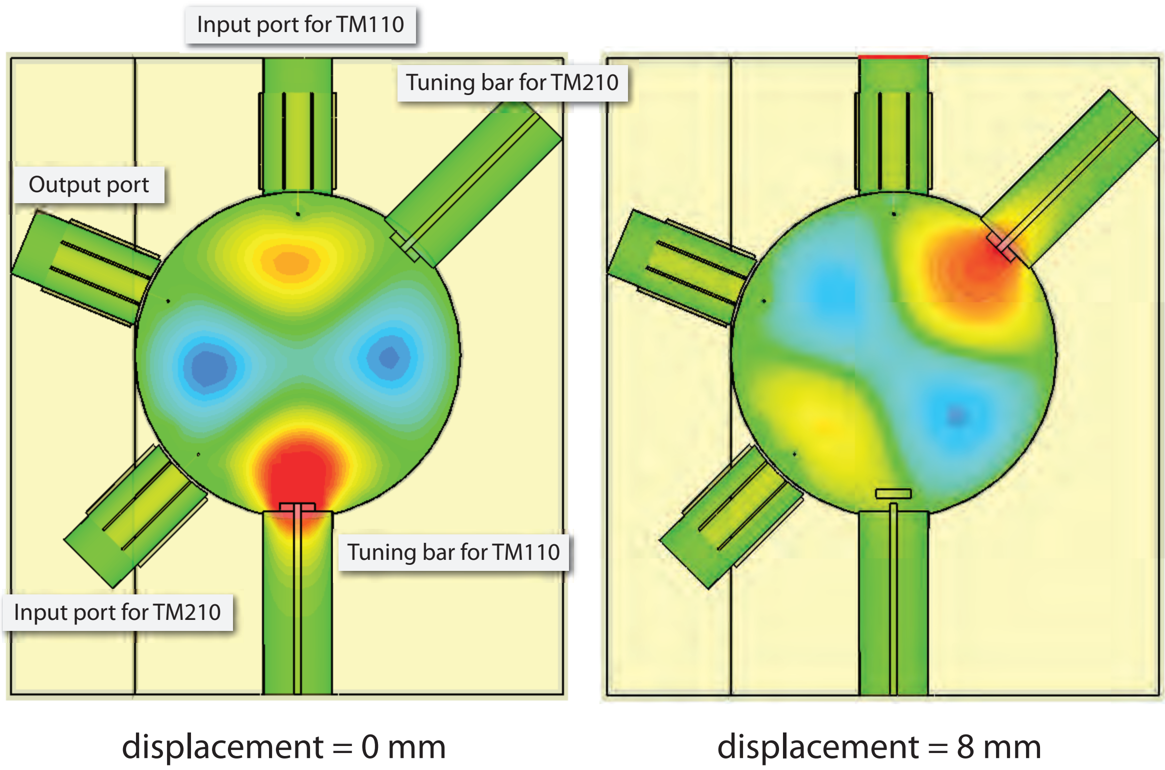

Figure 4.37: A cross-sectional view of the electric fields of the TM210 mode. The RF field is rotates on axis of the cavity by inserting the tuning bar.

4.3), transition frequency of ν_{34} is in the sweep range while ν_{12} is out of the range. To reach both transition frequencies, some improvements are needed. Moreover, about 10 mm displacement is needed to reach transition frequencies in the case of ν_{34} and there is still a room to optimize. This section describes improvement of the sweep range and uniformity of RF fields.

A possible improvement of sweep range is moving the resonance frequencies of the cavity close to the transition frequencies. It is possible by changing the diameter of the cavity. The thickness of the cavity is 15 mm and it is possible to widen inner diameter by several millimeter. Figure 4.38 and 4.39 show relations between diameter of the cavity and the resonance frequencies of the TM110 mode and the TM210 mode by the simulation. The red line shows a resonance frequency without tuning bars and the blue line shows a one with tuning bars (20 mm $\times$ 100 mm $\times$ 5 mm) placed at origin. Since inserting the tuning bar decrease a resonance frequency, the resonance frequencies when tuning bars are placed at origin should be higher than the transition frequencies. Therefore, by widen the diameter of the cavity, the resonance frequencies are close to the transition frequencies. However, there are gaps between in the simulation and the measurement (see Figure 4.29 and 4.31). To determine the length to be widen, more accurate estimation by simulation is needed.

Widen the diameter of the cavity is also able to contribute the uniformity of RF field. If the resonance frequencies are close to transition frequencies, smaller tuning bars or smaller displacement of the tuning bars are sufficient to reach the transition frequencies (Also the distance between the tuning bars and inner surface of the cavity at the origin point defined as 5 mm are able to be closer by changing the size of the tuning bar supports.) Since the tuning bars mainly cause the fluctuation of the RF field, this optimization acts as an improvement of uniformity of RF field.

4.3 RF cavity for zero field

The structure of the cavity for the zero field experiment is similar to the cavity for the high field experiment. It also has sets of three flanges to stretch foils of 25 μm

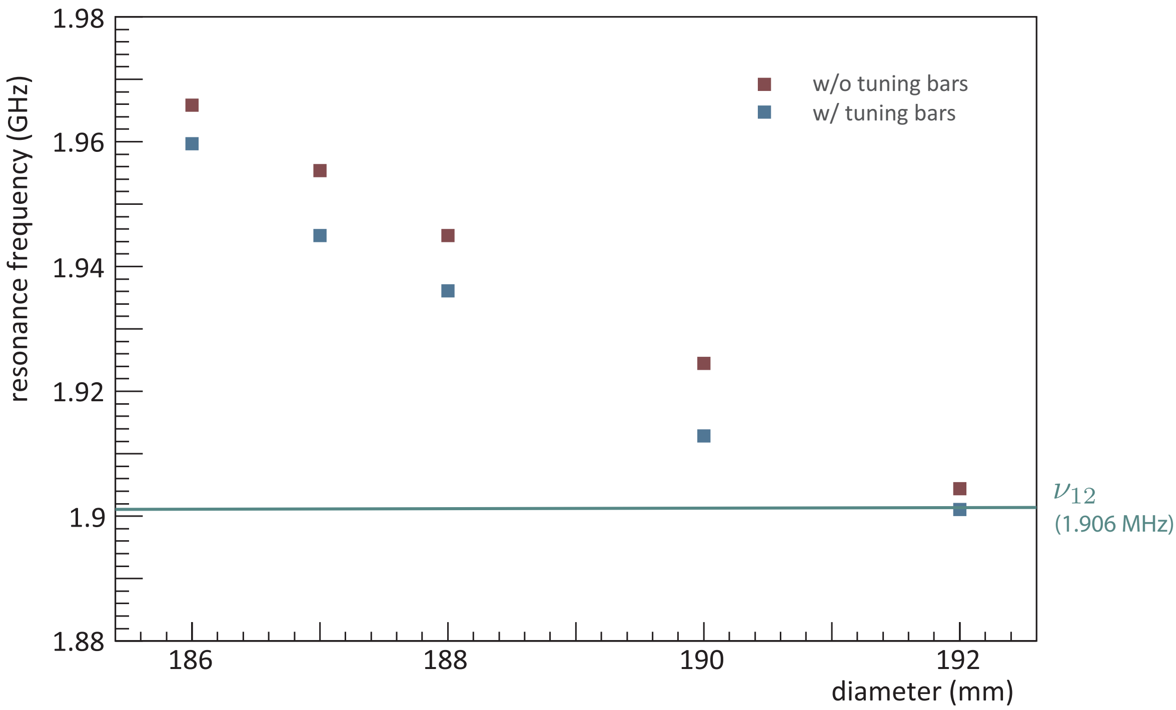

Figure 4.38: A relation between the diameter of the cavity and the resonance frequency of the TM110 mode by simulation. The red line shows a resonance frequency without tuning bars and the blue line shows with tuning bars put are placed at origin. The green line is the ν_{34} transition frequency.

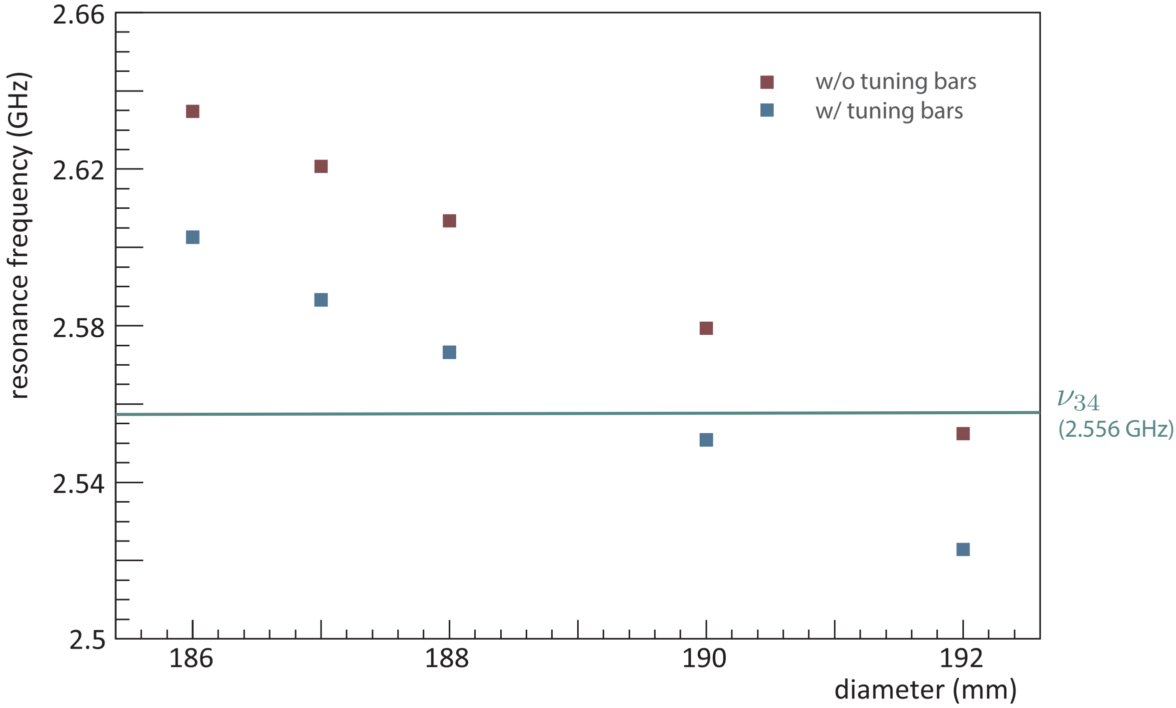

Figure 4.39: A relation between the diameter of the cavity and the resonance frequency of the TM210 mode by simulation. The red line shows a resonance frequency without tuning bars and the blue line shows with tuning bars are placed at origin. The green line is the ν_{34} transition frequency.

thickness (Figure 4.40).

Figure 4.41 shows resonance frequencies of TM110 and TM210 modes in the cylindrical cavity. Since the cavity for zero field experiment only need to resonant TM110 mode around 4.463 GHz, the radius of the cavity is around 40.9 mm.

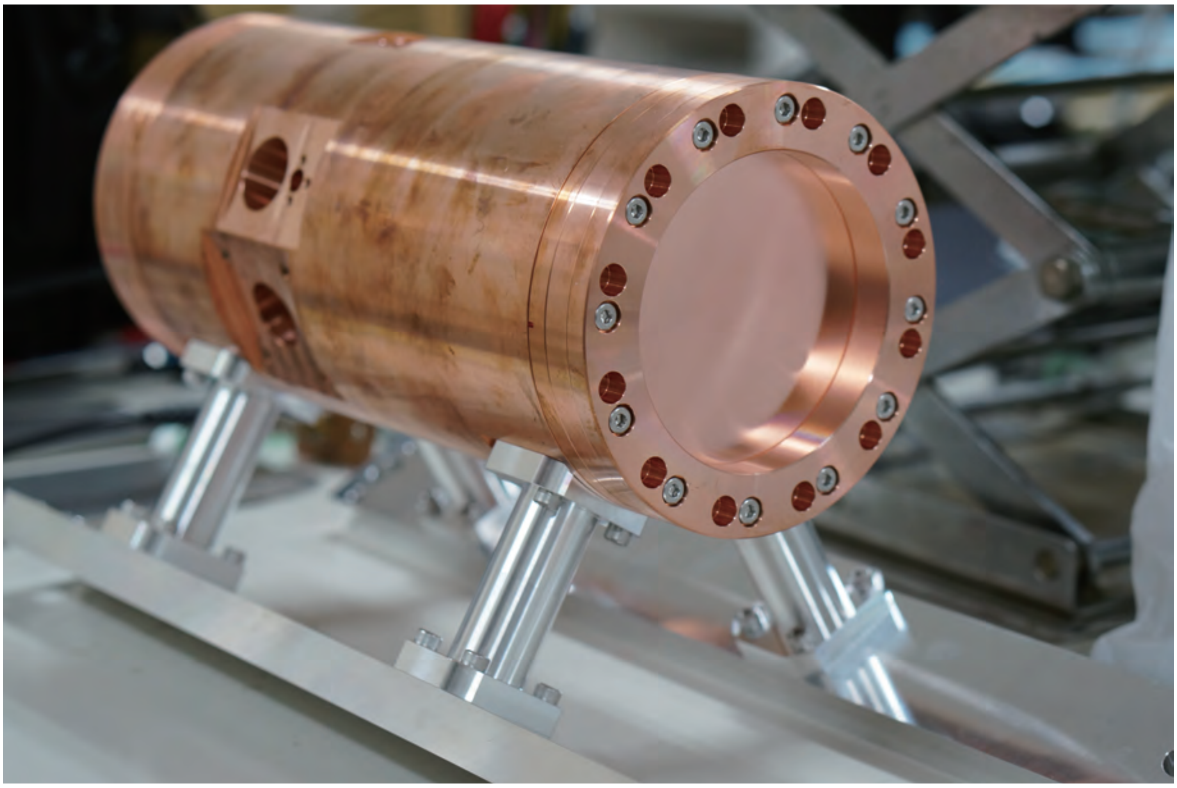

Figure 4.40: A photo of the cavity for zero field experiment. The cavity has support rail to insert into the chamber in common with the cavity for high field experiment.

4.3.1 Tuning bar

Compare to the cavity for high field experiment, the diameter of the cavity is so small that inner of the cavity can't be accessed (Figure 4.42). Thus the size of the tuning bar should be smaller than the diameter of the port (Figure 4.43).

Figure 4.44 shows a comparison of uniformity of RF field between by using a dielectric tuningbar and an electric tuning bar. Contrary to the cavity for high field,

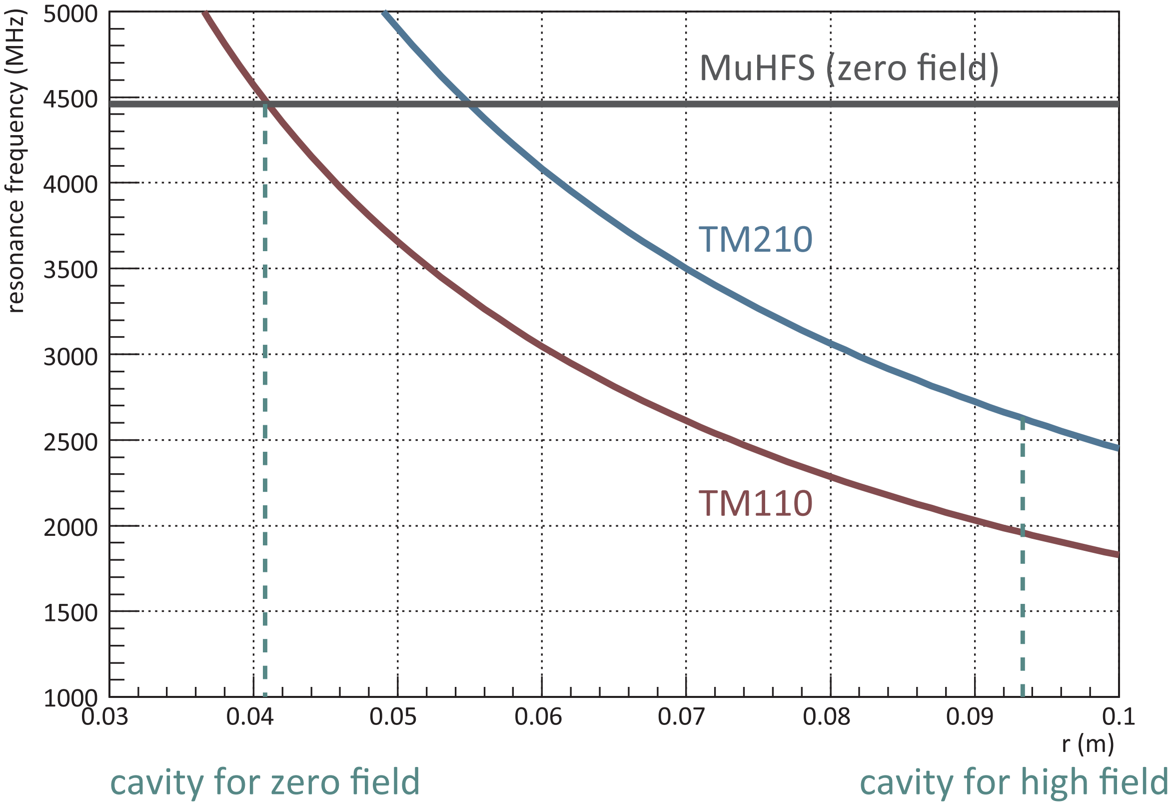

Figure 4.41: A relation between a radius of a cylindrical cavity and resonance frequencies of TM110 and TM210. The radius of the cavity for zero field should be 40.9 mm to adjust resonant frequency of the TM110 mode to the transition frequency of Mu HFS in zero field.

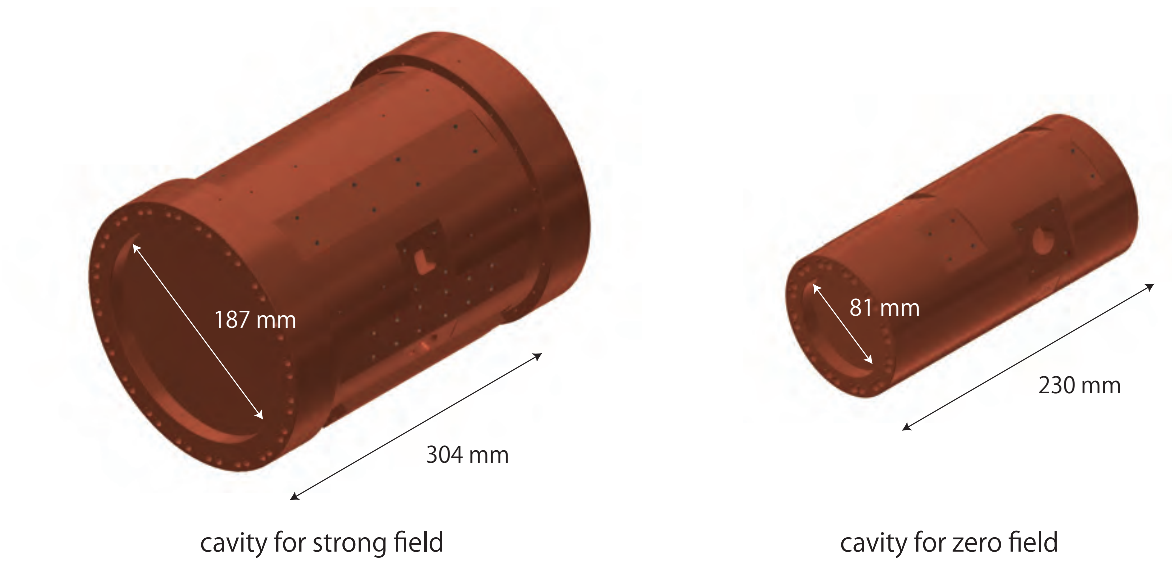

Figure 4.42: A comparison between the cavity for high field experiment and for zero field experiment. Inner diameter of the cavity for zero field experiment is shorter than for high field experiment because of resonance frequencies. The axial Length of the cavity for zero field experiment is optimized for the solid angle of decay positrons.

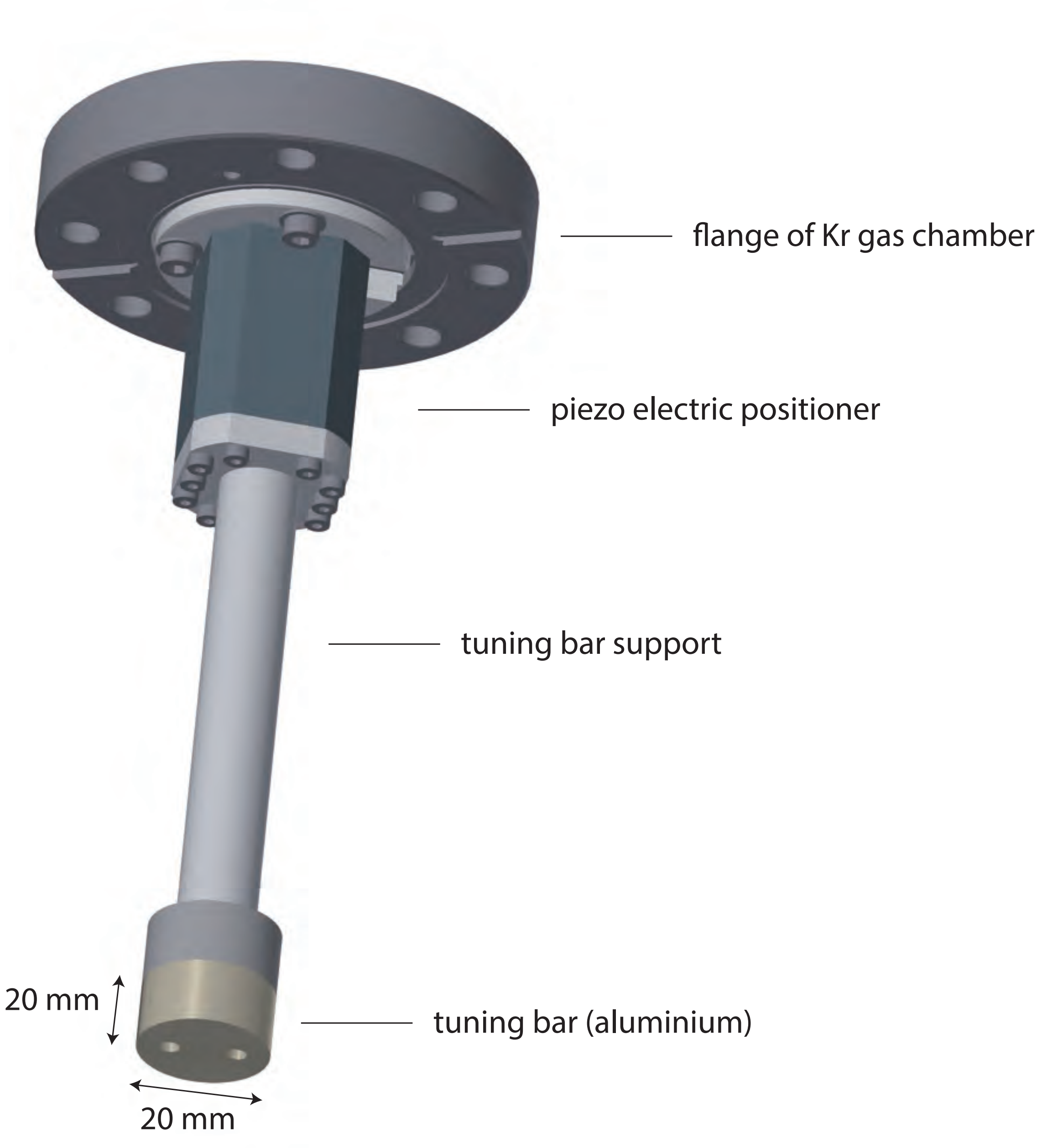

Figure 4.43: A schematic drawing of the tuning bar for zero field experiment.

An electric tuning bar is prefer for the uniformity on the axis in case of zero field experiment. Two different thicknesses (10 mm, 20 mm) of aluminum tuning bars are prepared for the measurement.

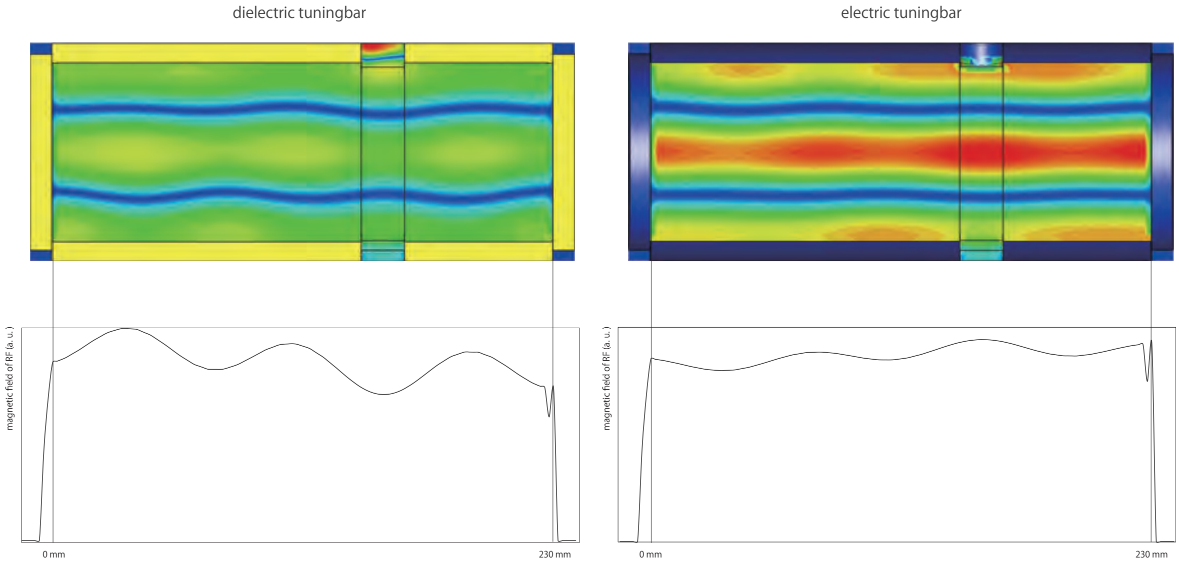

Figure 4.44: A comparison of uniformity of RF field between by using the dielectric tuningbar and the electric tuning bar. An electric tuning bar is prefer for the uniformity on the axis in case of zero field experiment as shown in below figures.

4.3.2 Cavity length

Although decay positrons move while rotating windingly around the magnetic field in the case of high field experiment, those go straight ahead from the position that muoniums decay in zero field experiment. Thus acceptable solid angle of positrons in zero field is depend on the axial length of the cavity. The cavity length is optimized by considering both generation efficiency of muonium in a low gas pressure and an acceptable solid angle of positrons (Figure 4.45). According to the simulation using GEANT4[7], the optimism length is 230 mm.

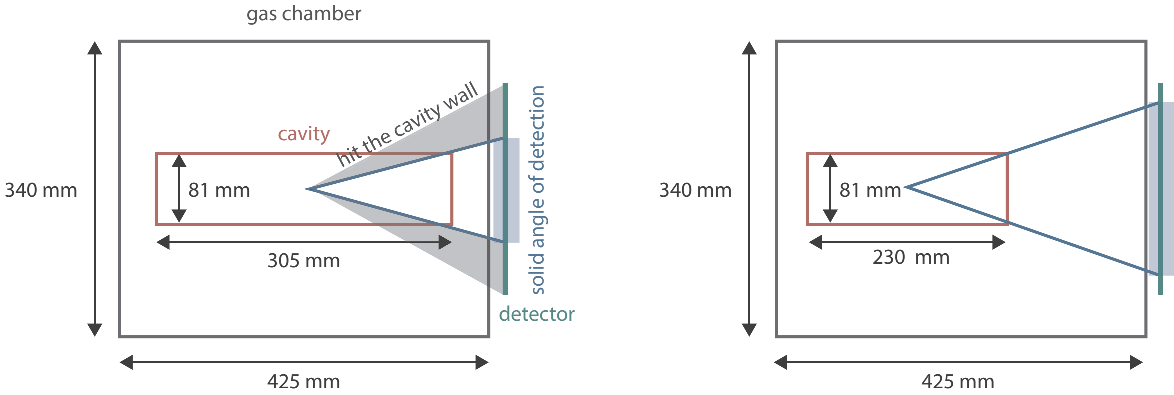

Figure 4.45: Decay positrons go straight ahead from the positions that muoniums decay. In case the axial length is 300 mm, Partly positrons hit the wall of the cavity before the detector (240 mm $\times$ 240 mm).

4.4 Performance test for the cavity for zero field

4.4.1 Test for the tunability of the cavity

Figure 4.47 shows a relation between a displacement of the tuning bar and a resonance frequency of the TM110 mode. As shown in this figure, the sweeping range of the system is from 4.458 GHz to 4.48 GHz and it includes the frequency value of Mu HFS.

4.4.2 Measurement of Q factor

Figure 4.48 shows a result of the measured Q factor of the TM110 mode. By fitting with a Lorentzian function, Q factor is calculated as 8.78×10^3.

4.5 RF system

4.5.1 RF system for zero field experiment

RF system for high field experiment is shown as Figure 4.49. The Microwave is generated from RF generator (HP Agilent 8671B), and amplified by the RF amplifier

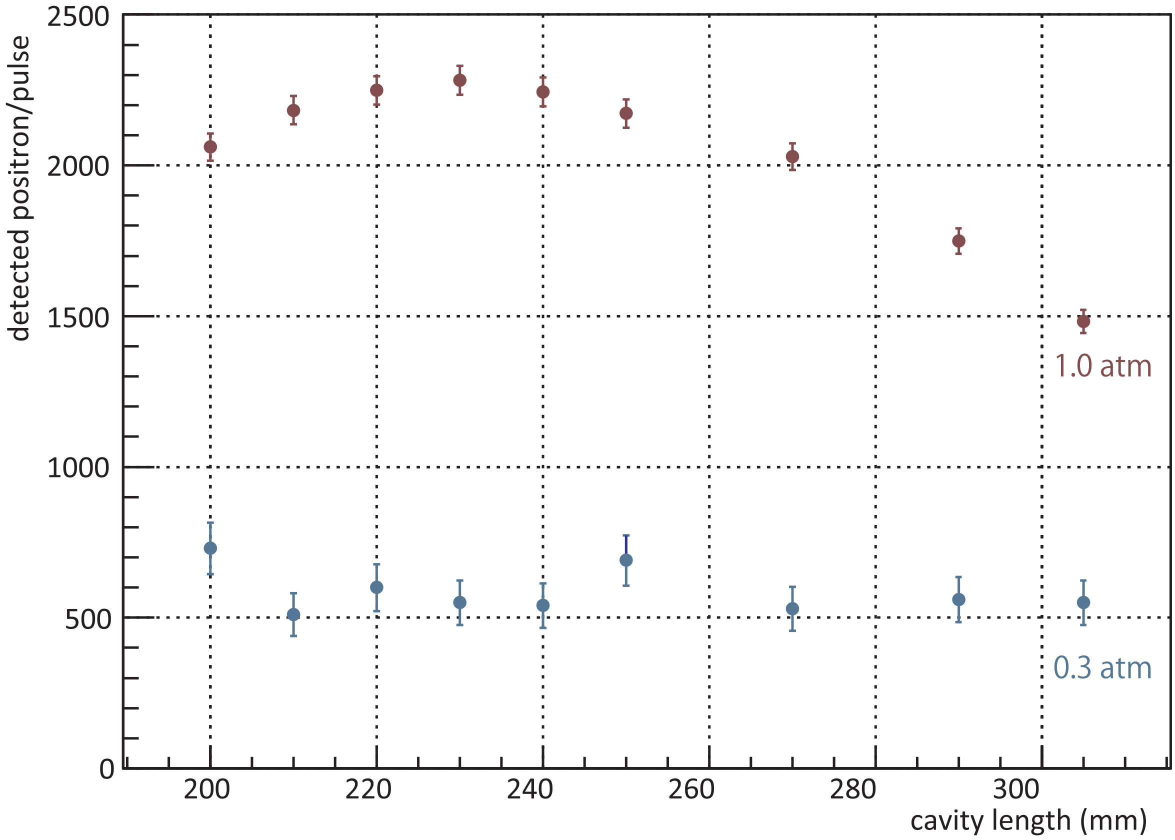

Figure 4.46: A relation between an axial cavity length and detected positon per beam pulse simulated by GEANT4[7]. 230 mm is an optimal length for the zero field experiment in 1.0 atm pressure.

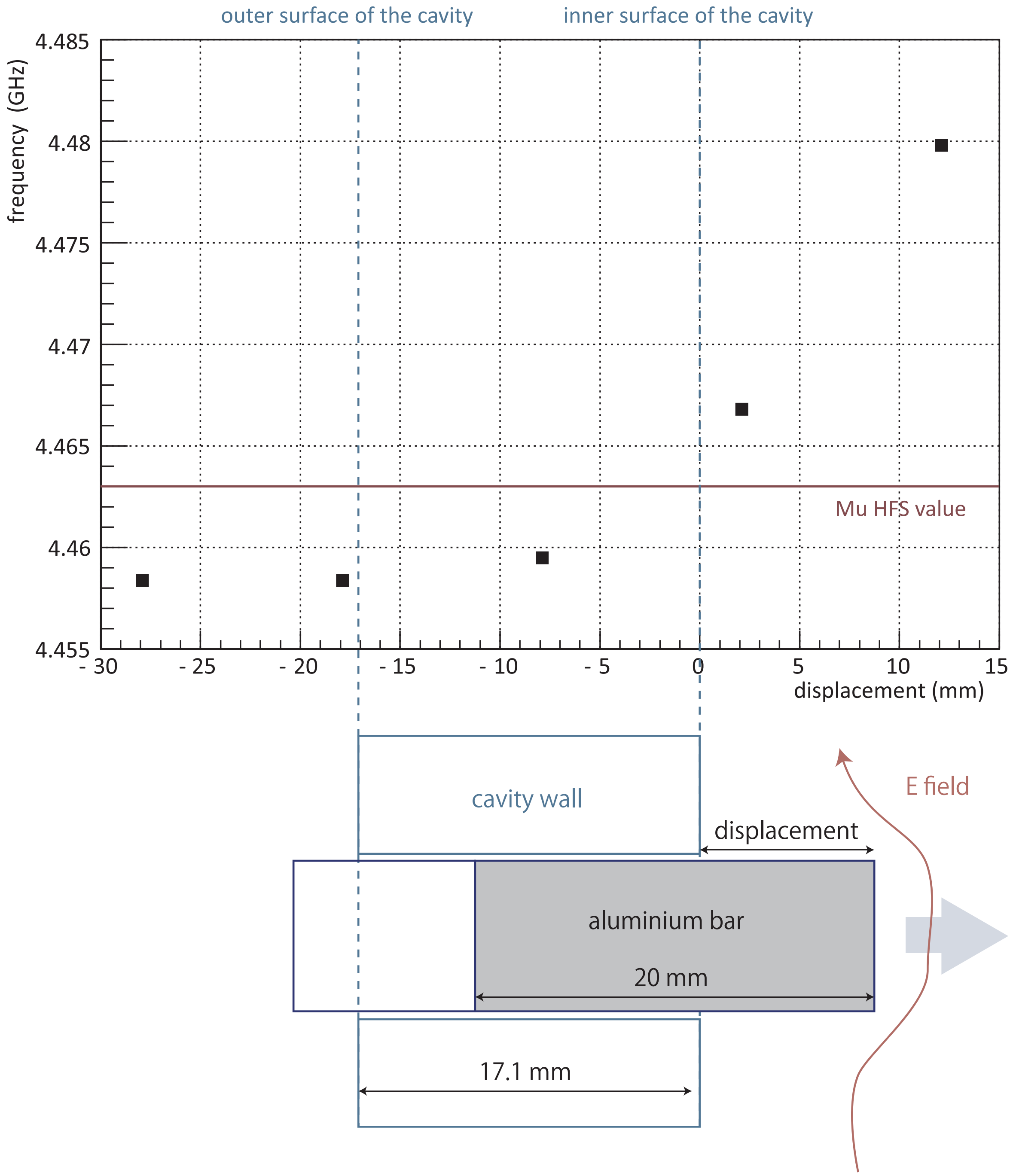

Figure 4.47: A relation between a displacement of the tuning bar and a resonance frequency of the TM110 mode. An origin of the displacement is defined that the front of the tuning bar is located on the inner surface of the cavity. The resonance frequency increases depend on the displacement at positive values. The sweeping range of the system is from 4.458 GHz to 4.48 GHz and it includes the frequency value of Mu HFS.

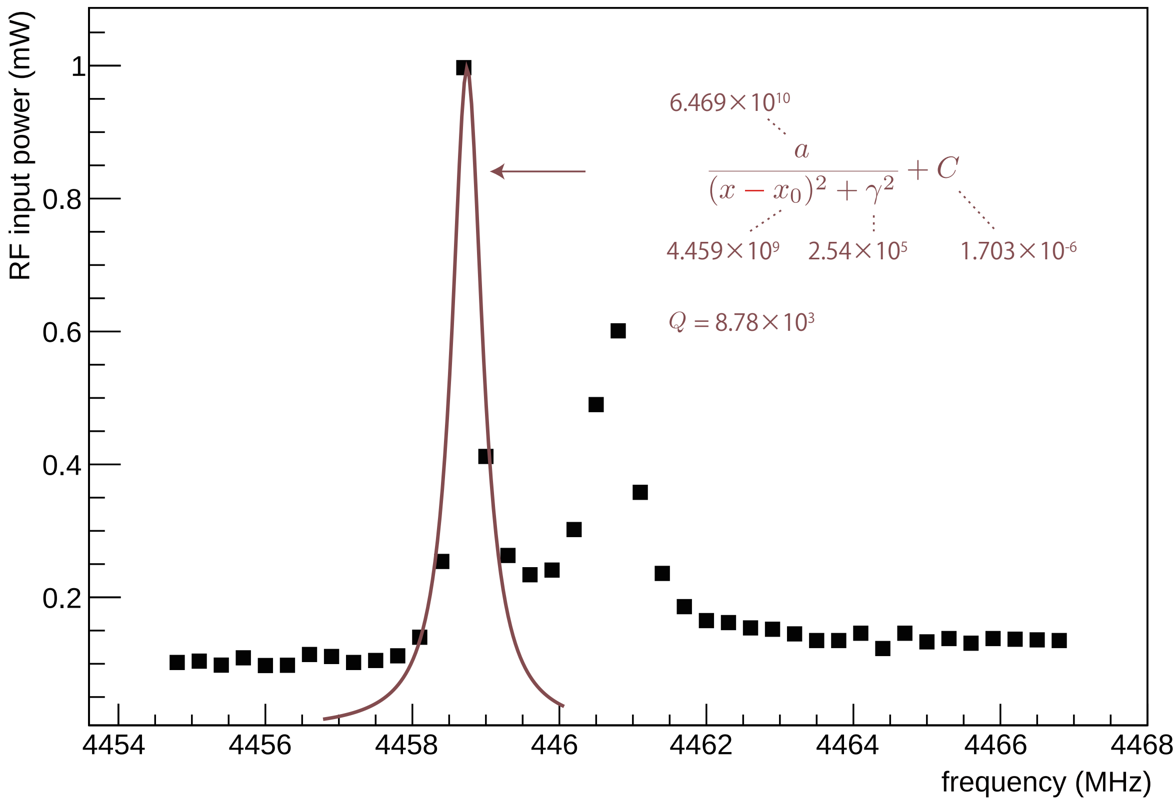

Figure 4.48: The measured Q factor of the TM110 mode. Q factor is calculated from FWHM of the resonance shape. FWHM is obtained from fitting with Lorentzian function.

(ZVE-8G). The maximum output power of the RF amplifier is 2.5 W. The microwave is delivered coaxial pipes and coupled into the cavity by the input loop. Coaxial pipes and couplers are under designing now to suppress a fluctuation of a RF power. The microwave power in the cavity is coupled into a pickup loop and measured by the thermal power sensor (R&S NRP-Z51). The measured power is feedback to the signal generator to stabilize the input microwave power.

4.5.2 RF system for high field experiment

RF system for high field experiment is shown as Figure 4.50. Microwaves for the TM110 mode and the TM210 mode are generated from RF generator (R&S SMBV100A). Even the aging of the reference frequency of the generator is 1×10^{-6} year, GPS frequency reference standard is prepared to stabilize the frequency. The maximum output power of the RF Amplifier is 15 W. Microwaves are amplified by RF amplifier (R&S BBA 150). Microwaves for both resonance modes are coupled into the cavity by two input loops. The system for RF power monitoring and feedback to RF generator is common with the system for zero field experiment.

4.5.3 RF ports

In performance tests of cavities, coaxial cables are used as substitute for coaxial pipes. Cables are connected to the network analyzer by N connectors and to the cavity by SMA connectors using converters. Antennas are used a 0.9mm ϕ enameled round copper wire jointed to the outer conductor by crimping terminal and solder-mounted to the inner conductor. Figure 4.51 are photographs of each RF antenna. Coupling of ports is determined by a planar dimension of loops. Area of input loops is tuned near the 7 cm^2 which is optimum value in simulation. On the other hand, output loop is made as small as possible not to couple strongly. Frequency characteristics depend on the shapes of antenna loops even areas of loops are same. Figure 4.52 shows a comparison of s_{11} of TM110 with two different shapes of antennas. Thus a Q value and a resonance frequency are varied with shapes of antennas which causes the difference

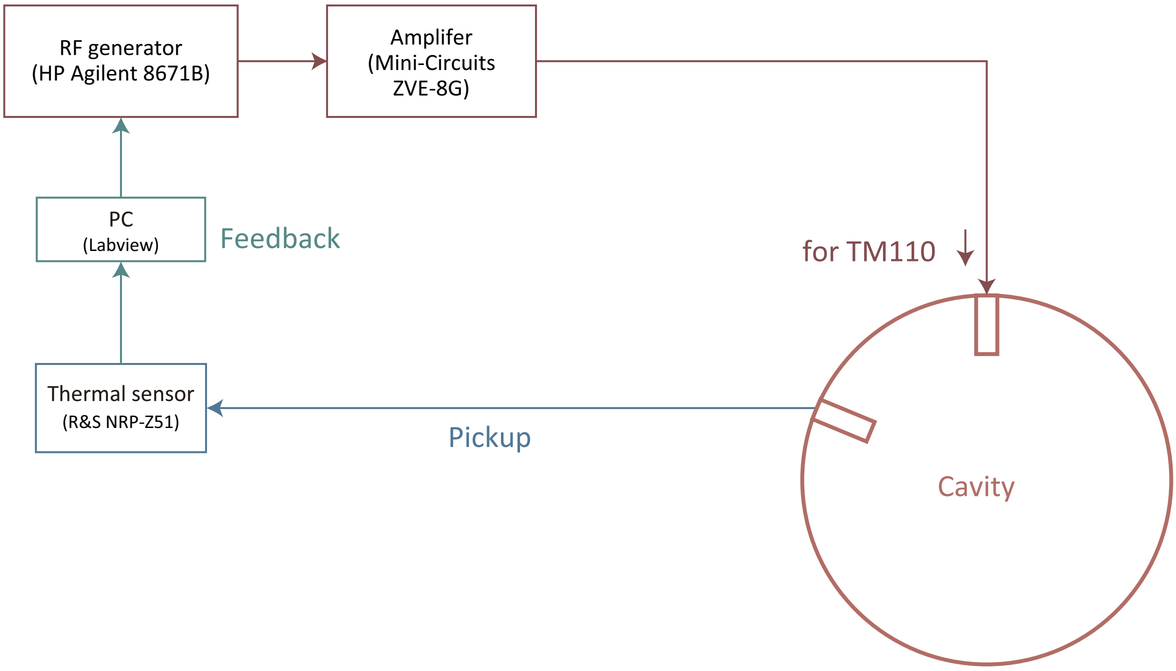

Figure 4.49: A diagram of RF system for zero field experiment.

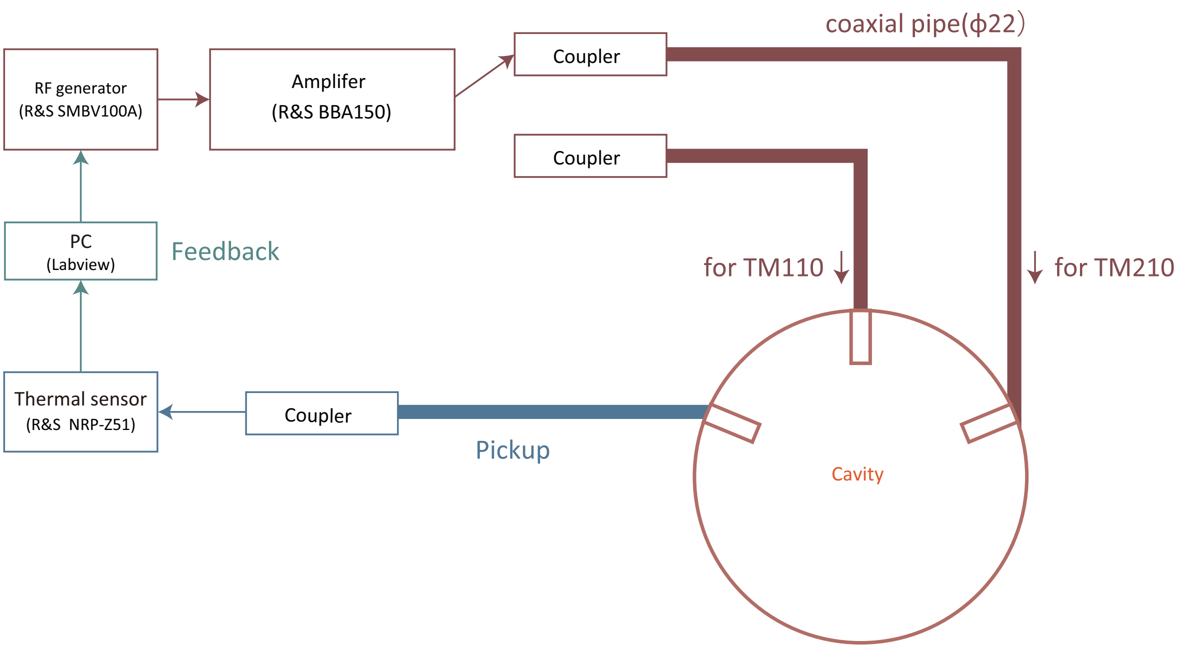

Figure 4.50: A diagram of RF system for high field experiment.

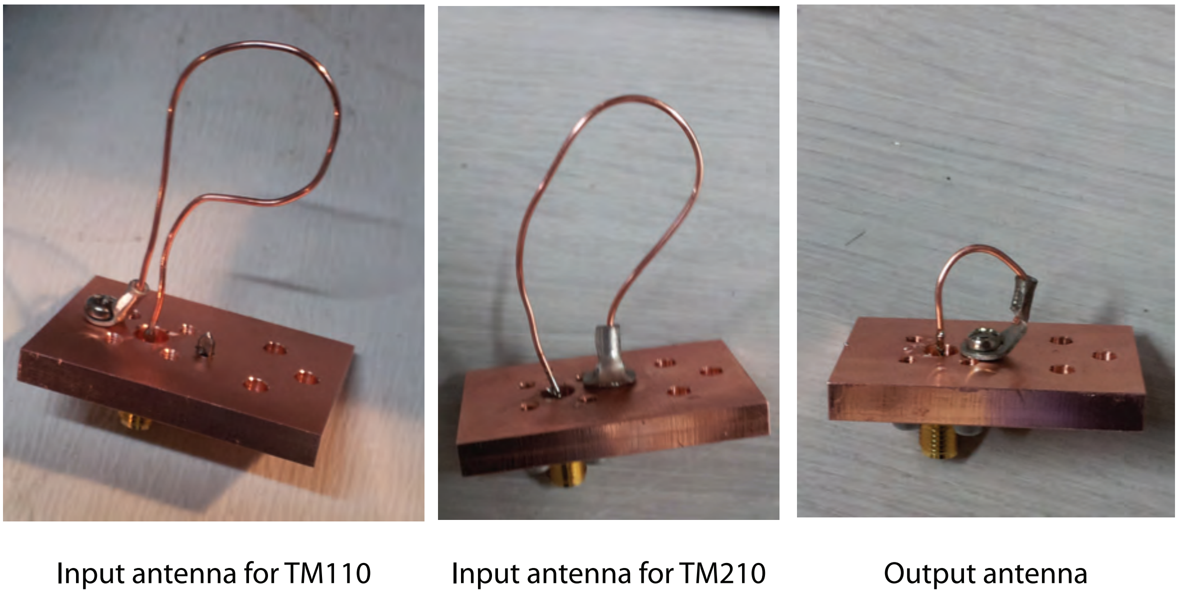

Figure 4.51: A photograph of RF antennas for the measurement.

between a measurement and a simulation.

4.5.4 Feedback test

RF power is stabilized by the feedback system. The RF power in the cavity is monitored by thermal sensor and the LabVIEW[59] program on a PC manipulates the RF generator from monitored values (Figure 4.50, 4.49). Figure 4.53 shows a result of RF power stability test for 4 hours. By using a RF feedback system, power drift is suppressed and the power is stabilized within 0.02 %.

4.6 Gas chamber

4.6.1 Overview of the gas chamber

A gas chamber is necessary for sealing the Krypton gas in the cavity. For high field experiment, the material of the chamber is only used aluminum (A2219) as a non-magnetism material. The chamber has the front window (diameter: 100 mm, thickness:

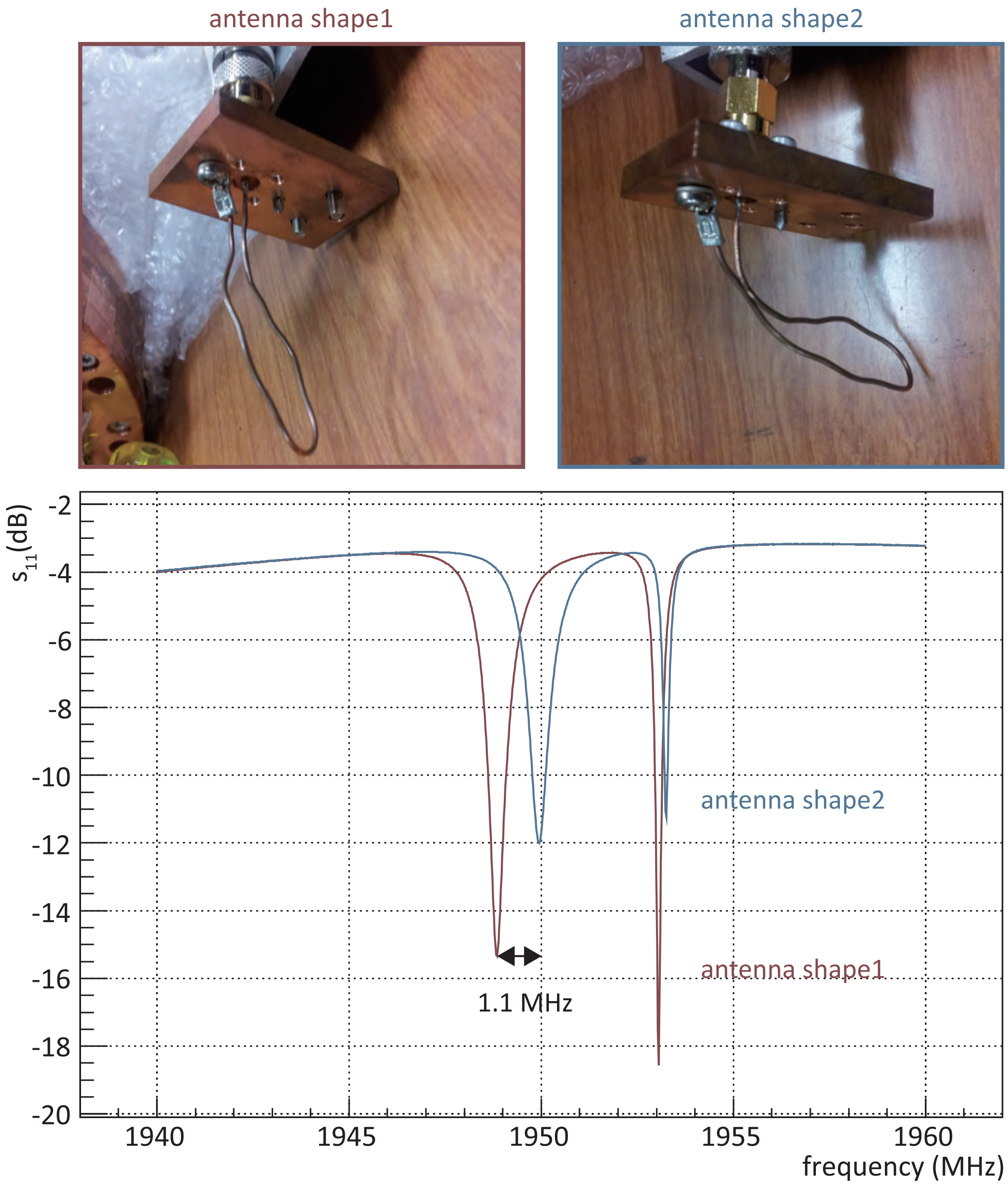

Figure 4.52: Comparison of s_{11} of TM110 with two different shapes of antennas. The resonance frequency of TM110-1 is varied about 1.1 MHz by the shape of the antenna loop.

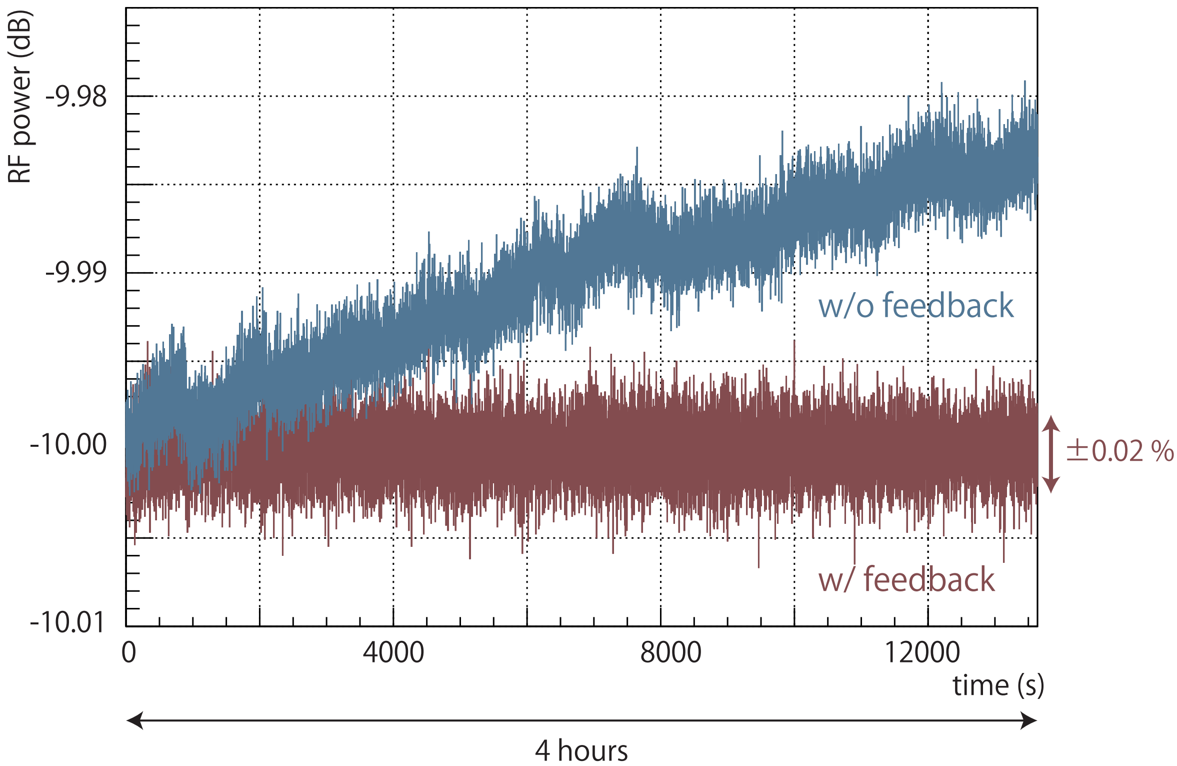

Figure 4.53: A result of RF power stability test for 4 hours. A blue line shows a RF power without a feedback system and a red line shows a RF power with a feedback system. By using a RF feedback system, power drift is suppressed and the power is stabilized within 0.02 %.

0.1 mm) on the front flange which allow the passage of muons. On the other hand, there is the back window (diameter: 180 mm, thickness: 10 mm) to pass decay positrons (Figure 4.54). The chamber has 13 ports for 3 RF ports, 2 ports for tuning bars, gas inlet and evacuation port, feedthrough ports for thermometers and NMR probes, feedthrough ports for cooling water inlet and outlet and 2 extra ports (Figure 4.55 and 4.56).

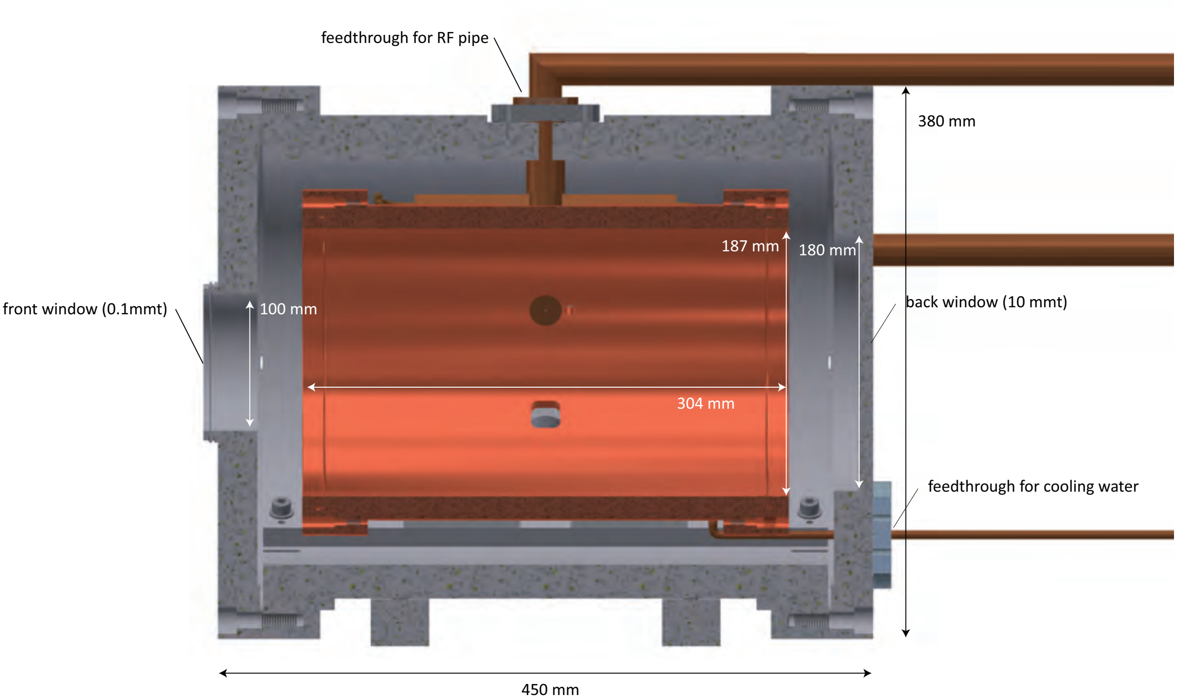

Figure 4.54: A schematic cross-sectional view of the gas chamber surrounding the cavity.

4.6.2 Pressure test for the foil

Two different test flanges are prepared for the pressure test (Figure 4.57) of the foil. When the pressure difference at the foil is 1 atm, the distortion at the center of the foil is negligible in case of test flange1, about several millimeters in case of test flange2. Thus the foil of that the thickness is 0.1 mm, diameter of 100mm satisfy to withstand pressure difference of 1 atm which is required for the Mu HFS measurement.

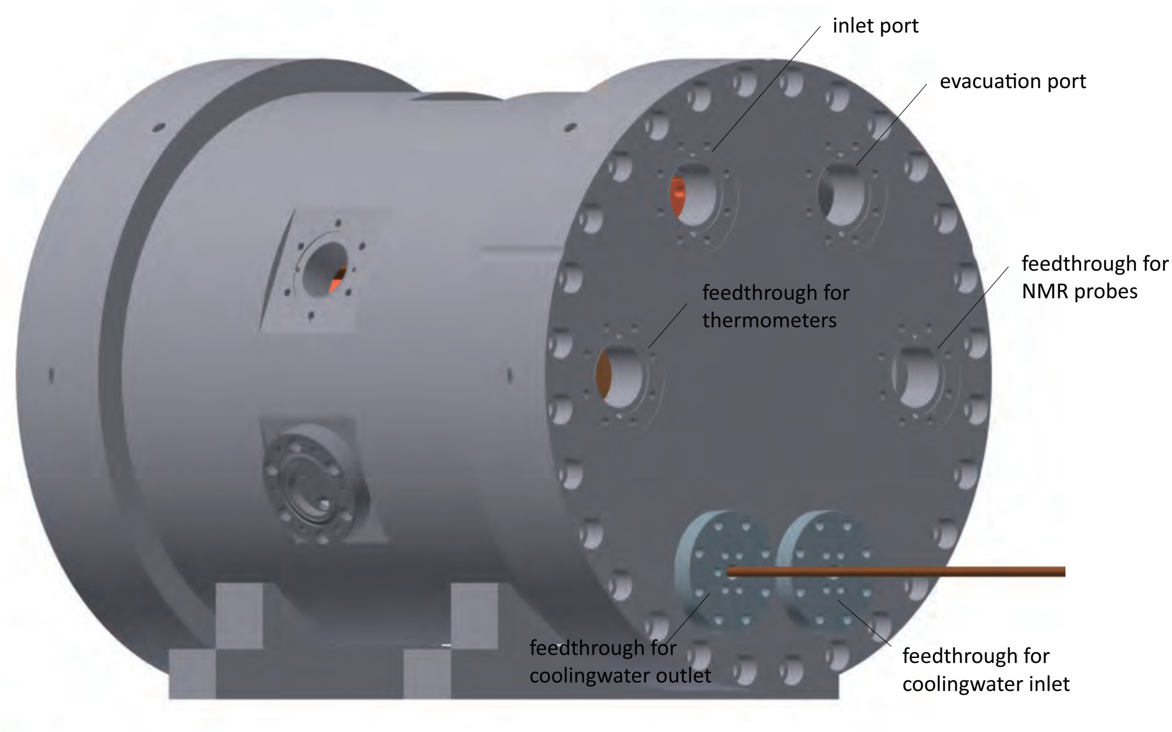

Figure 4.55: A schematic view of the back side of the gas chamber.

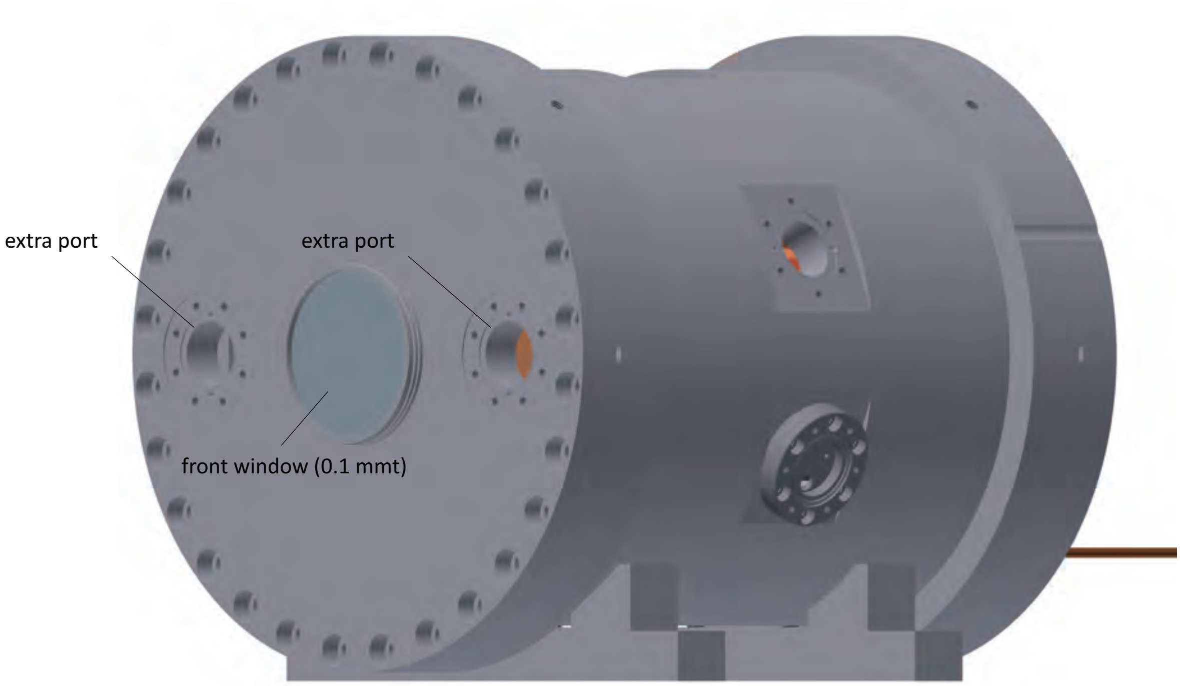

Figure 4.56: A schematic view of the front side of the gas chamber. The chamber has the front window (diameter: 100 mm, thickness: 0.1 mm) on the front flange which allow the passage of muons.

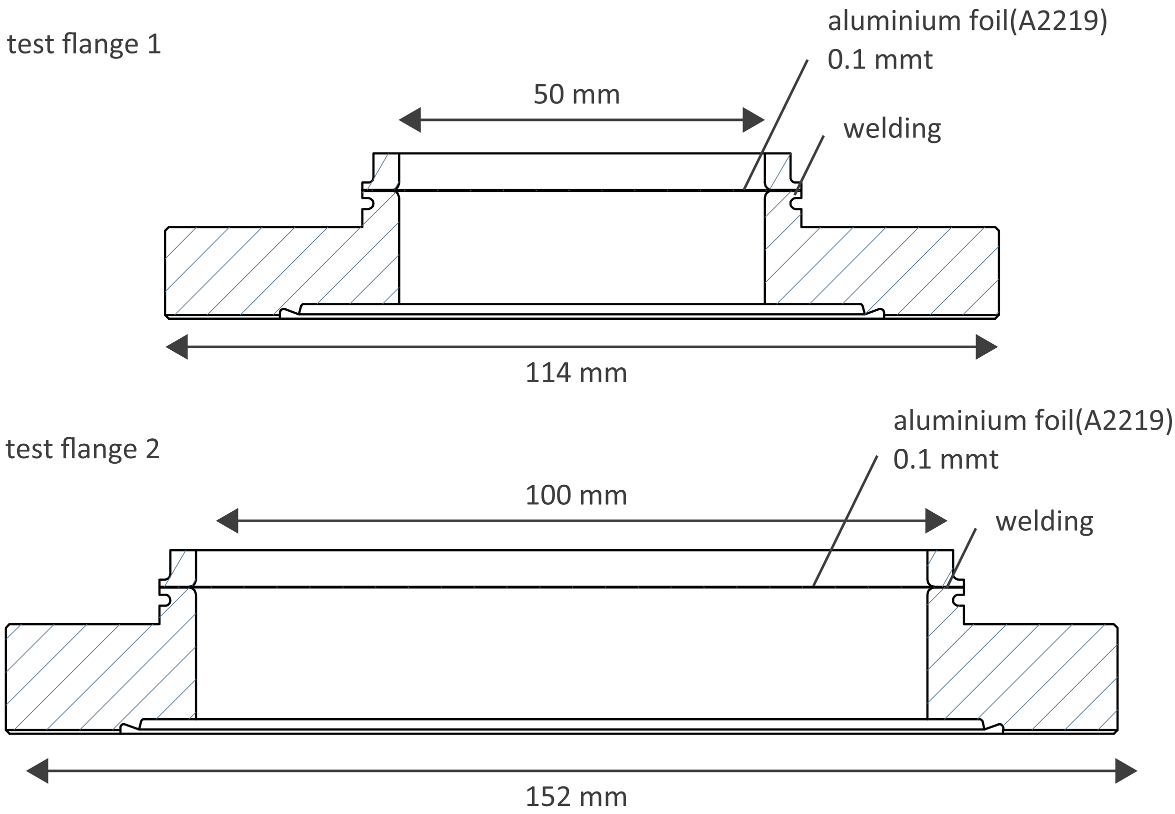

Figure 4.57: Drawings of test flanges. Test flange1 has the foil of that diameter is 50 mm, test flange2 has the foil of that diameter is 100 mm.

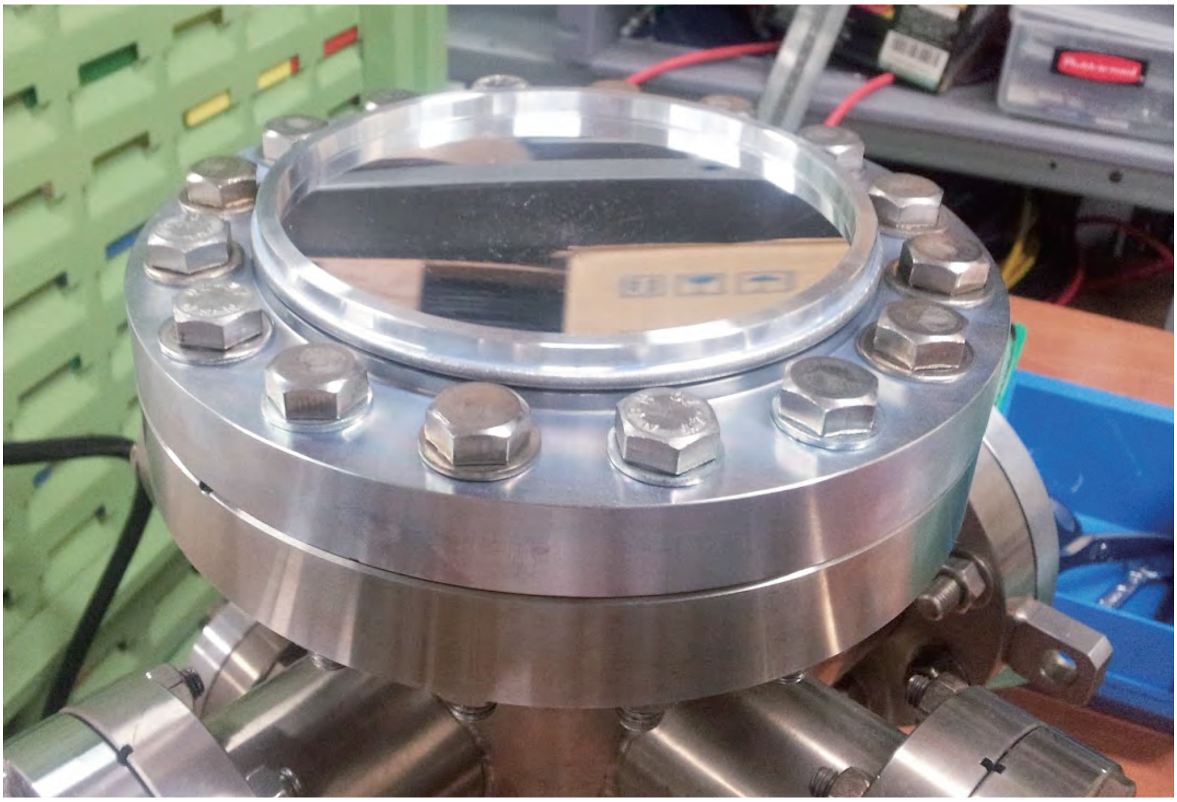

Figure 4.58: Photo of the pressure test for test flange2. The pressure difference at the foil is 1 atm since the chamber is evacuated by a rotary pump.

4.7 Gas system

The gas system is developed for stable controlling of a gas pressure and monitoring a gas pressure and a its purity in the chamber. As discussion in Subsection 4.7.1, gas purity is critical for the systematic uncertainties. Thus, all connections are using VCR and assembling of the system is done in CLASS 1000 clean room. The acceptable leak rate of welding points of the system is 4.0×10^{-10} Pa $\cdot$ m^3/s. Krypton gas is transferred from the system to the gas chamber by flexible metal tube of the length is 5 m and the thickness is 1/4 inch.

4.7.1 Gas sampling

In order to avoid chemical reactions and depolarizing collisions, we should carefully take care of the purity of Krypton gas. Especially, the cross section for a muonium – O^2 depolarizing electron spin exchange collision is very large ($\approx 5 \times 10^{-16}$ cm^{-2}) (see Table 4.7). The muon polarization P can be determined from the angular distribution

molecule	interaction	σ at 0.52 T (unit = 10^{-16} cm^2)	σ_{SE} (unit = 10^{-16} cm^2)
NO_2	$NO_2 + M \rightarrow NO + OM$	≤ 23	$\cdots$
O_2	Spin exchange	5.4(3)	5.9(6)
NO	Spin exchange	3.2(2)	7.1(1)
C_2H_4	$C_2H_4 + M \rightarrow C_2H_4M$	0.29(16)	$\cdots$
H_2, N_2, SF_6	$\cdots$	≥ 0.01	$\cdots$

Table 4.7: Muonium (M)-molecule cross sections [11, 12].

of the decay positrons and is assumed to vary with time t as

$$P(t) = P_0 \exp(-\lambda_2 t), \tag{4.7}$$

where P_0 is the initial polarization of the muons which form muonium. If the collision depolarization mechanism is an electron-spin exchange process, as is expected for a paramagnetic molecule, then the theory of the muon depolarization can be given in terms of a density matrix formulation of the equations for the populations of the four HFS levels. The dependence of λ_2 on H is found to be

$$\lambda_2 = \lambda_{20}/(1+x^2)^{\frac{1}{2}}, \tag{4.8}$$

in which λ_{20} is the depolarization rate for $H = 0$. λ_{20} of collision with oxygen is measured as [12]

$$\lambda_{20}/n \approx 3 \times 10^{-16}\mathrm{cm}^3/\mu\mathrm{s}, \tag{4.9}$$

where n is the number of interacting molecules per cm^3. This equation suggests that the effect of contamination is maximum in zero field experiment. Assuming a 1 ppm contamination of oxygen in 1 atm krypton gas, λ_2 at zero field is calculated as

$$\lambda_2 \approx 8.1 \times 10^3 \ /\mathrm{s} \tag{4.10}$$

A figure 4.59 shows a P_0 dependence on oxygen contamination. As shown in this figure, the contamination of oxygen should be less than a ppm.

The gas system has 6 sampling bottles which can be release independently from the system during a measurement. By measurement of sampling gas using a Q-mass (quadrupole mass spectroscopy), purity of the gas can be measured at the level of ppm. Requirement of a gas purity is discussed in Subsection 4.7.1.

4.7.2 Pressure guage

The transition frequencies of muonium measured in a gas vary with the gas density due to the distortion of the muonium wavefunction in collision. At a constant temperature, two-body collisions between a muonium atom and a krypton atom cause a shift which is proportional to the krypton pressure at fixed volume [60]. Also three-body interaction between muonium atom and two krypton atoms yield a shift proportional to the square to the krypton pressure at fixed volume [61]. The shift in the transition frequency is described as

$$\nu_{ij}(P) = \nu_{ij}(0)(1 + a_{ij}P + b_{ij}P^2). \tag{4.11}$$

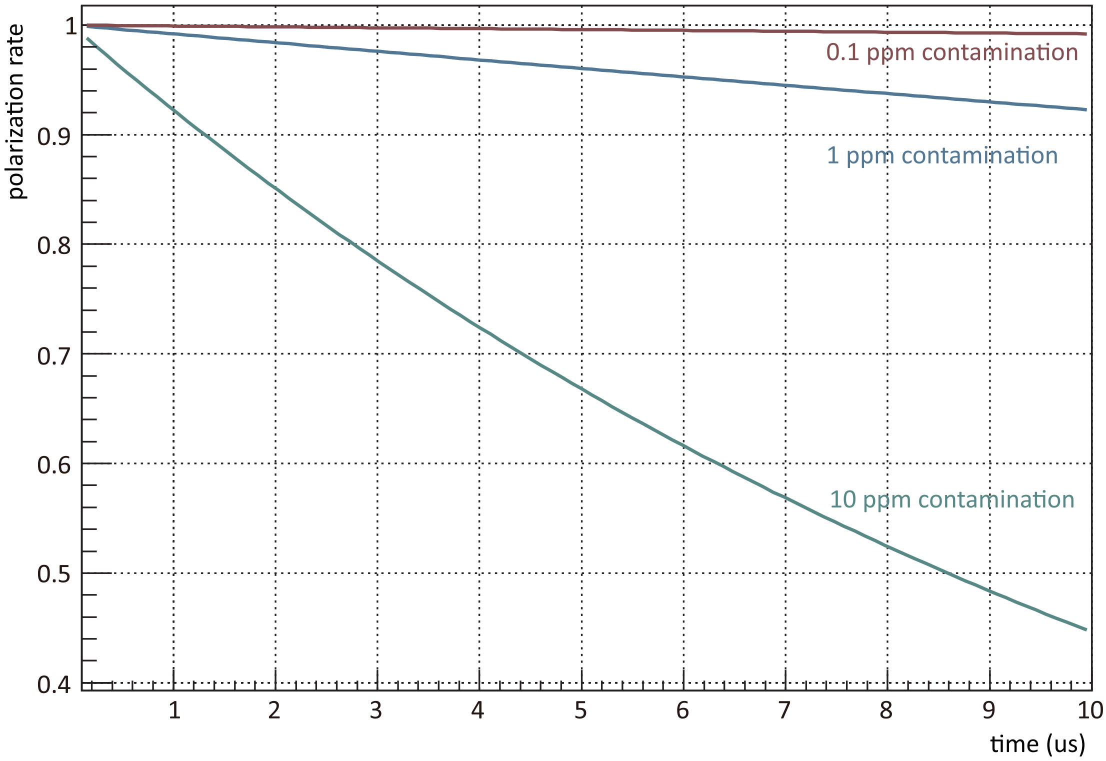

Figure 4.59: A P_0 dependence on oxygen contamination. The contamination of oxygen should be less than a ppm.

b is obtained by earlier experiment at LAMPF [62] as

$$b = (9.7 \pm 2.0) \times 10^{-14}\ \mathrm{Torr}^{-2}. \tag{4.12}$$

a is also obtained by latest experiment at LAMPF [4] as

$$a_{12} = -8.669(26) \times 10^{-6}\ \mathrm{atm}^{-1}, \tag{4.13}$$

$$a_{34} = -7.665(25) \times 10^{-6}\ \mathrm{atm}^{-1}. \tag{4.14}$$

Gas pressure is measured by the capacitance gauge (M-342DG-13). It has a measuring range of 1.33 kPa with an uncertainty of 0.20 % of reading. Moreover, the silicon gauge (RPM4-AD) is also plan to use. It has a measuring range of 1.6 kPa with an uncertainty of 0.020 % of reading.

The uncertainty from a gas pressure is described in Section 5.6.

4.7.3 Relief valve

Low-Pressure Proportional Relief Valve is prepared for safety. Maximum working pressure is 0.2 MPa.

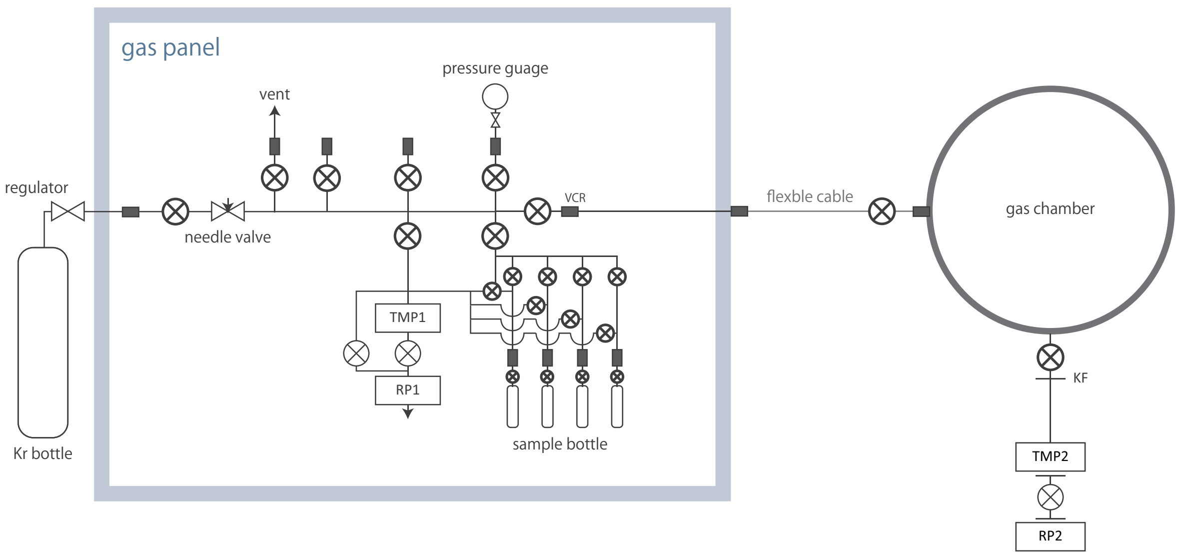

Figure 4.60: A diagram of the gas system.

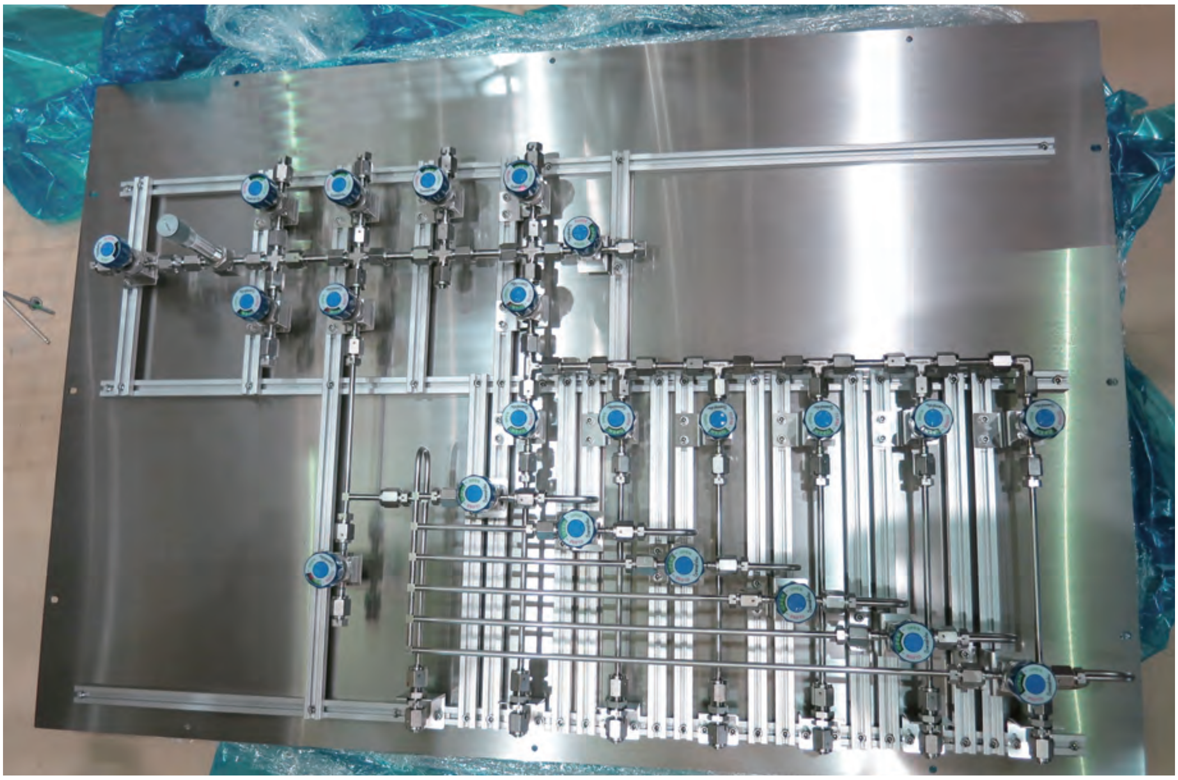

Figure 4.61: A photo of the gas system.

4.8 Magnetic shield for zero field

4.8.1 Measurement of the magnetic field in D2 area

For zero field experiment, a magnetic field in the cavity should be less than 100 nT. Figure 4.62 shows a measurement result of a magnetic field in case of magnet on and off in the experimental area of D Line (D2 area). Magnetic fields in the experimental area are coming from earth magnetism, magnetized poles under the base plate and quadrupole magnets to guide the muon beam. There is decay component of the magnetic field with a height from the base which is caused by the magnetized poles under the base plate as shown in Figure 4.63. From these measurement values, the magnetic field in the area is reproduced by simulations using TRICOMP (Figure 4.64, 4.65).1

4.8.2 structure of magnetic shield

Figure 4.66 shows a schematic view of the magnetic shield with other apparatus. The magnetic shield is composed of 3 layers of 1.5 mmt boxes made of permalloy. Figure 4.67 shows apertures of the shield. These apertures are located symmetrically to care about homogeneity of magnetic field in the shield.

4.8.3 simulation of magnetic shield

Simulation of the effect of apertures of magnetic shield

Figure 4.68 shows a comparison of magnetic fields in the shield between different diameters of the front window of the shield. Compared to the case of 20 cm, Leakage magnetic field from the front window in the case of the diameters are down to 14 cm are negligible compared with the exude magnetic field from plates of the shield.

Simulation of the effect of thickness of the plates

Figure 4.69 shows a comparison of magnetic fields in the shield between different thicknesses of plates of the shield. In this simulation, the relative permeability of the plates

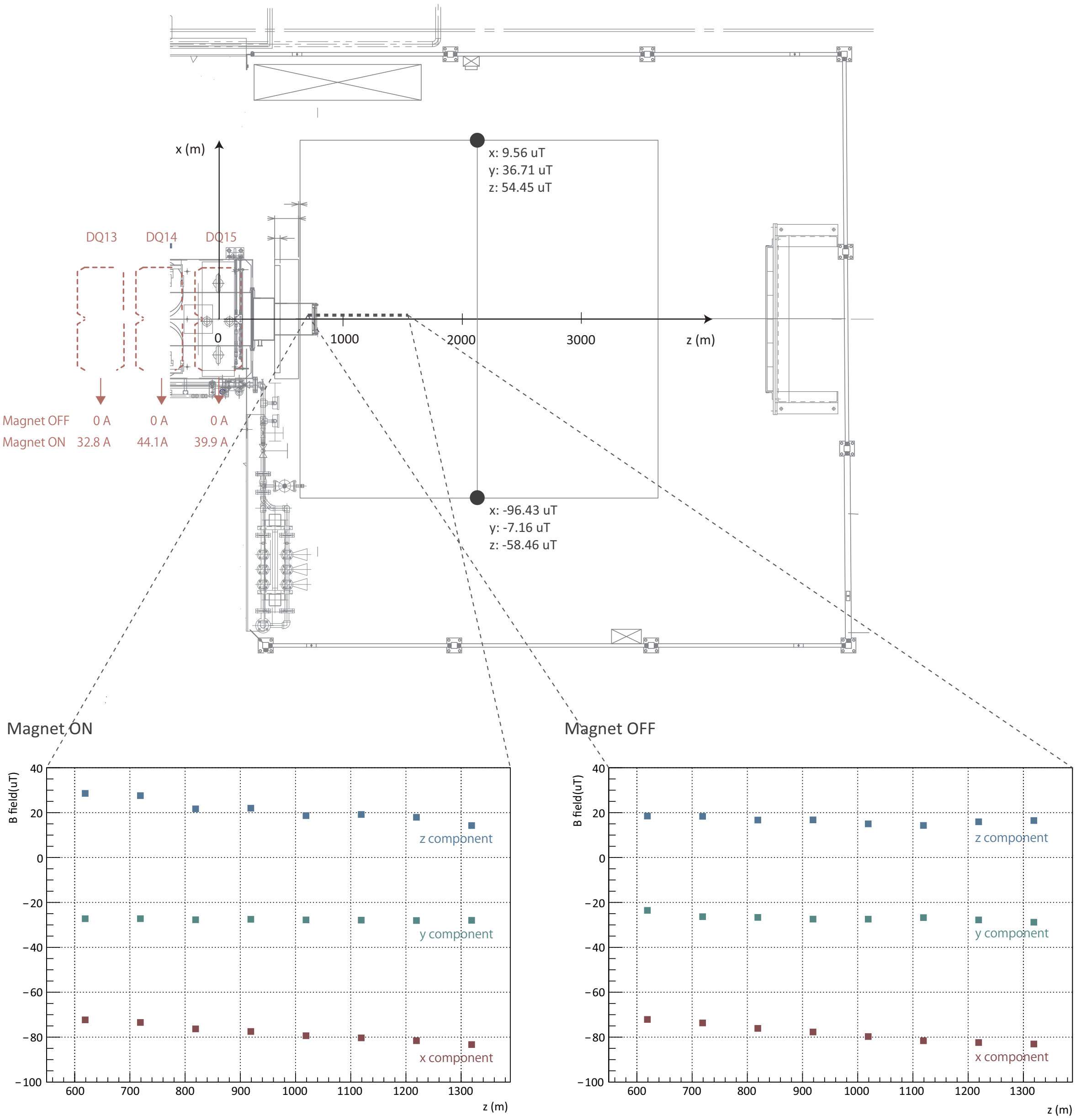

Figure 4.62: Measurement of the magnetic field at D2 area. A left figure shows the magnetic field on beam axis in case magnet on, a right figure shows the magnetic field in case magnet off.

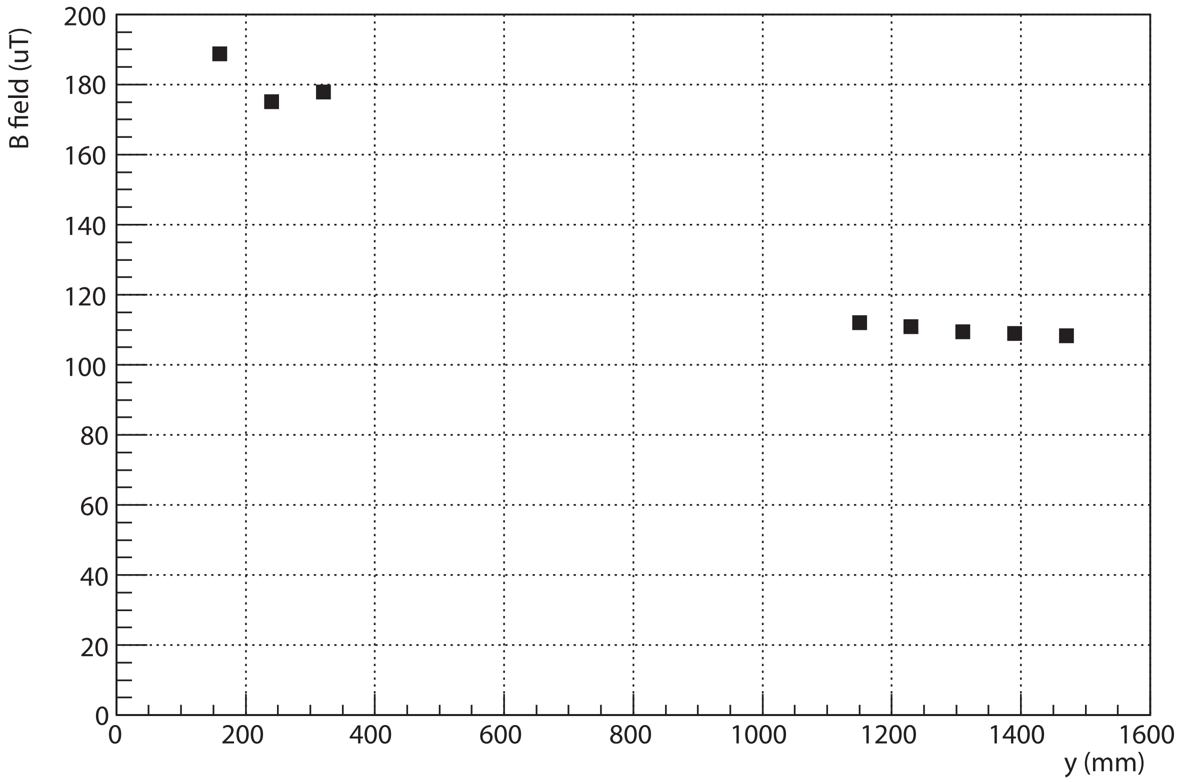

Figure 4.63: The magnetic field at D2 area in the direction of y axis. the origin of the y is defined as a position of the surface of the base plate.

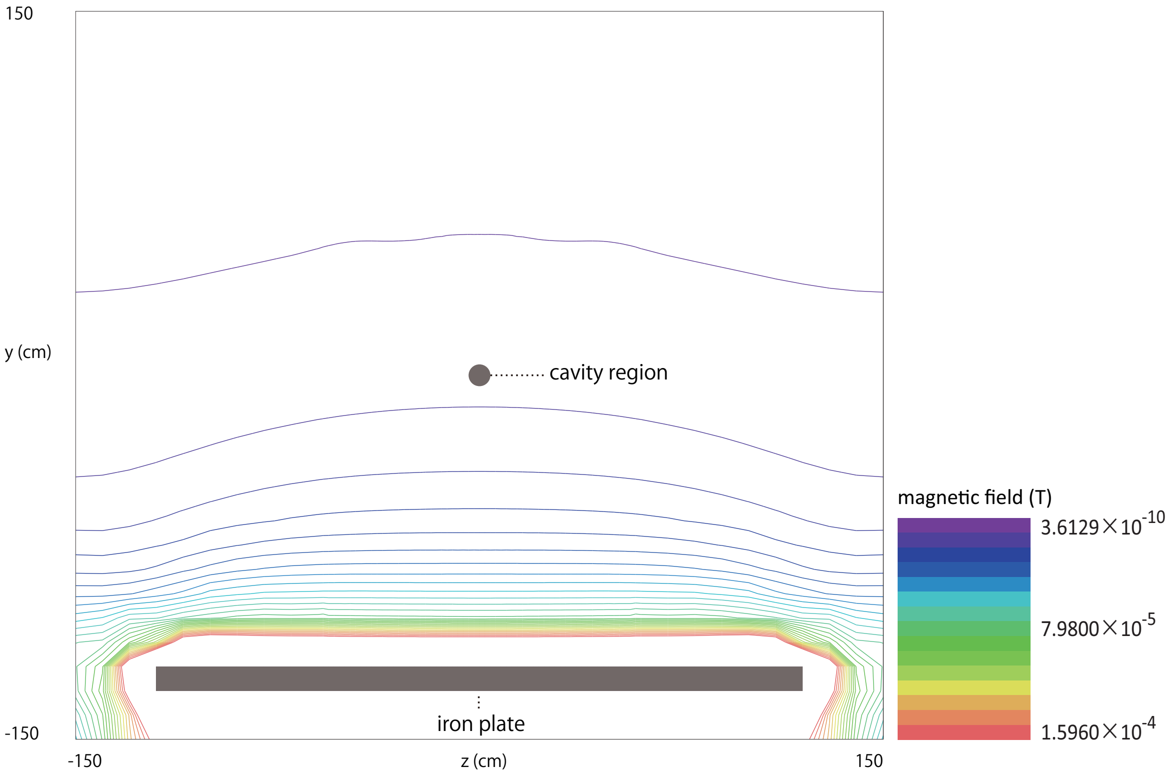

Figure 4.64: A xy cross sectional view of the magnetic field in D2 area generated by simulation. Magnetized poles generate the magnetic field depend on the height from the base plate.

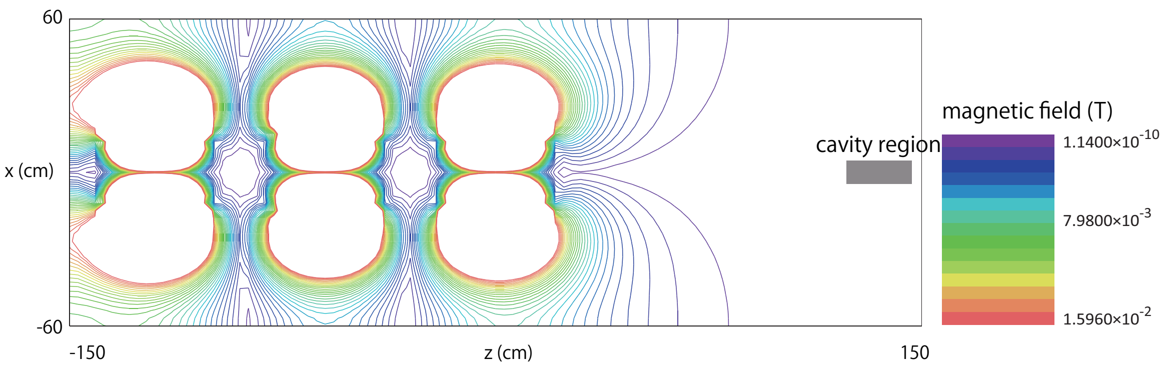

Figure 4.65: A xz cross sectional view of the magnetic field in D2 area generated by simulation. Quadratic magnets generate the magnetic field to guide the muon beam.

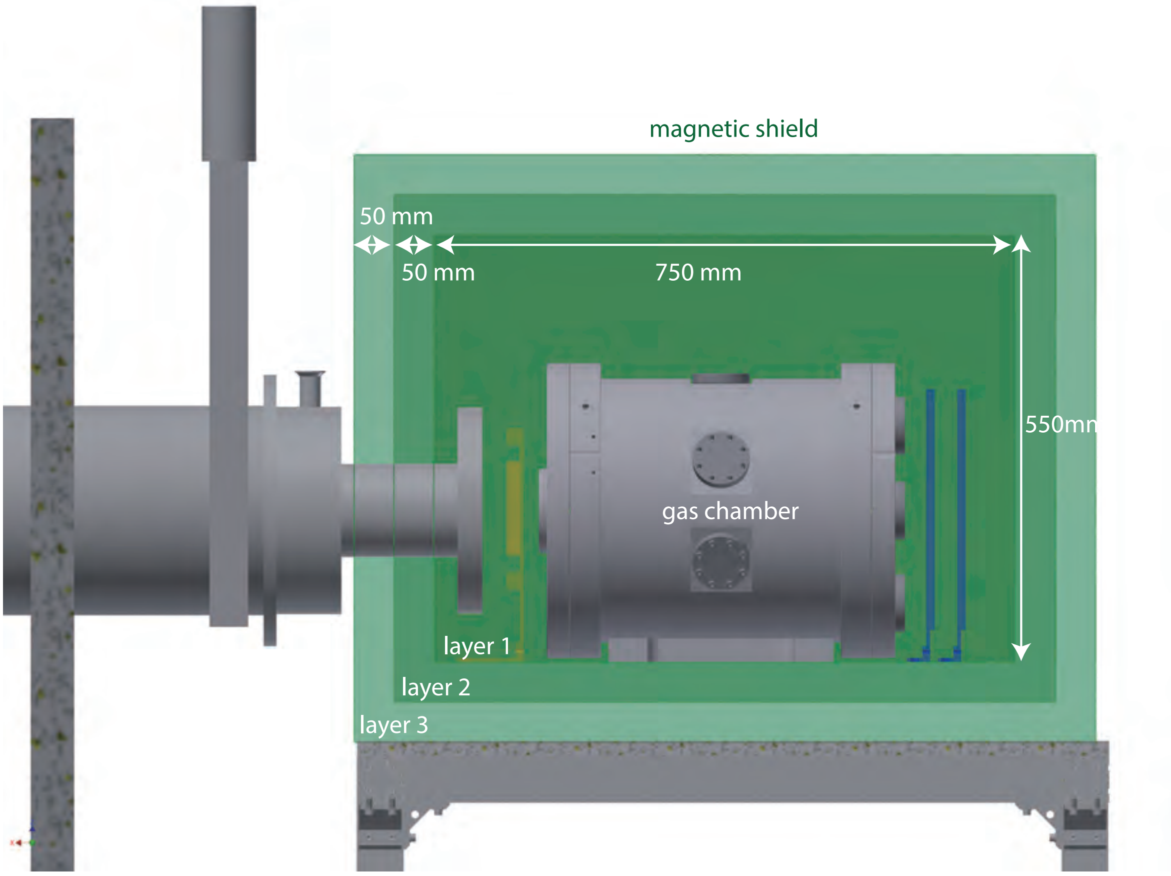

Figure 4.66: A schematic view of the magnetic shield surrounding the gas chamber. The magnetic shield is composed of 3 layers of 1.5 mmt boxes made of permalloy.

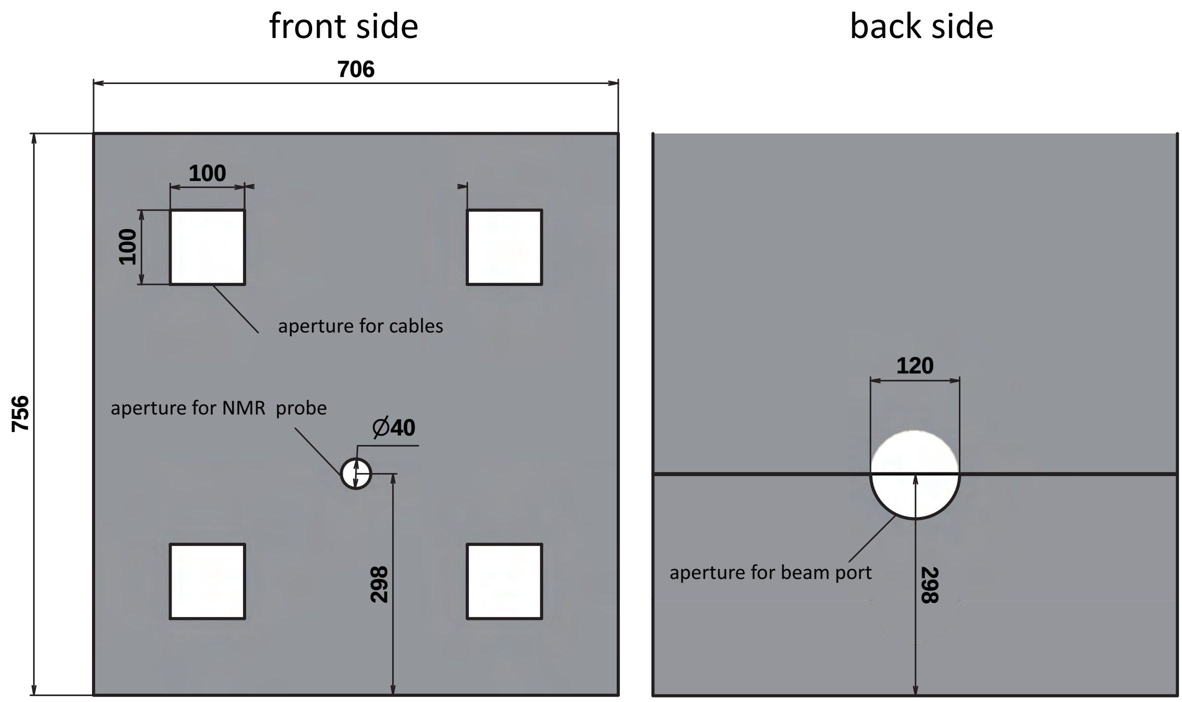

Figure 4.67: Drawings of front panels and a back panel of layer 3. Front panels are separated to upper part and lower part to install the beam duct extension after an installation of the magnetic shield.

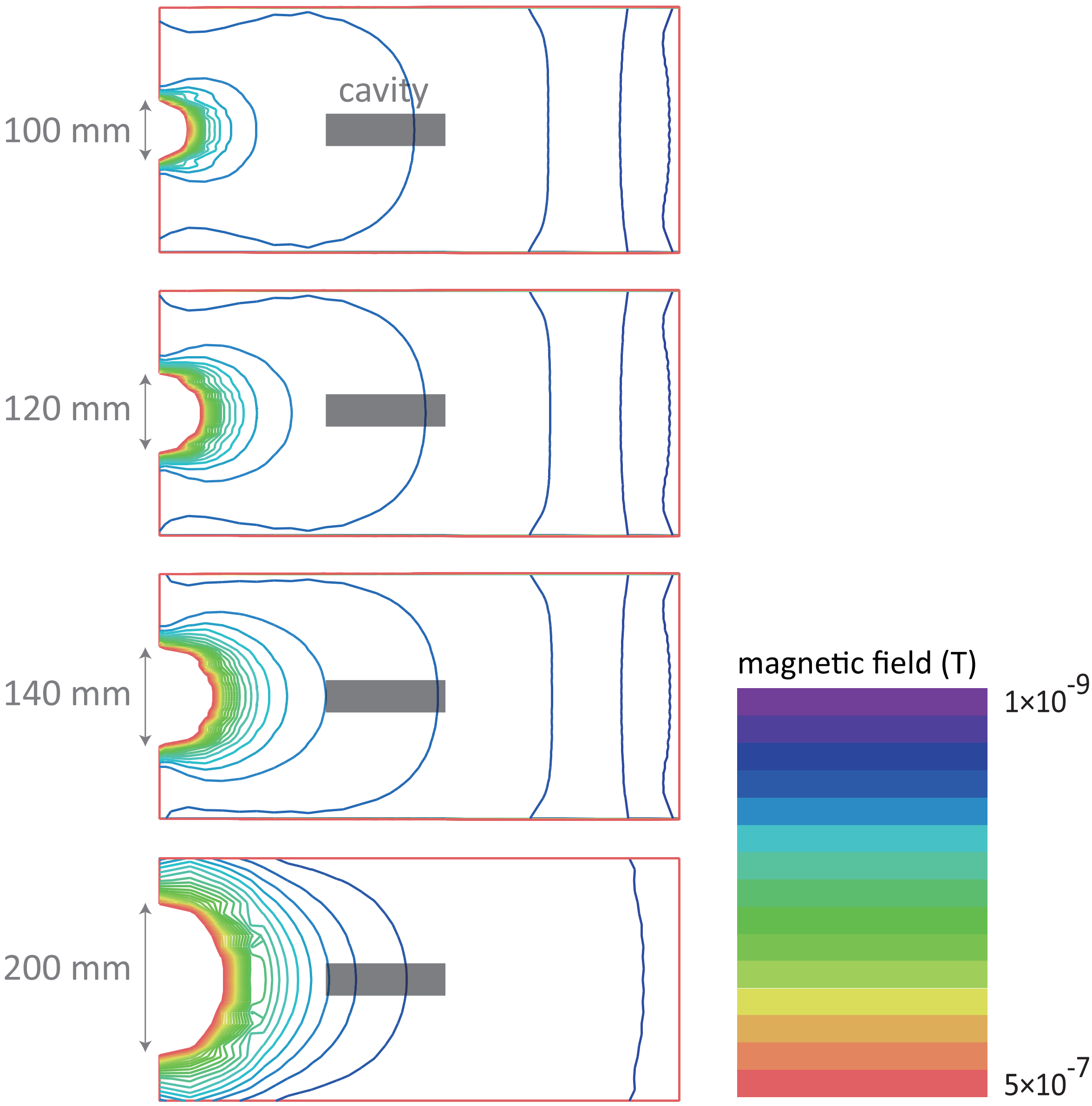

Figure 4.68: A comparison of different diameter of the front window of the magnetic shield. The magnetic shield is composed of 3 layers of 1.5 mmt boxes made of permalloy. In case that the diameter is from 100 mm to 140 mm, a leakage field in the cavity region from the front side is not dominant compared from other sides.

is set to 12000. From this simulation, 1.5 mmt is enough to achieve under 1 mG magnetic field in the shield.

4.8.4 Performance test for the magnetic shield

Performance test for the magnetic shield was held at S1 area. Figure 4.70 shows a setup of the test. Mounting bases for the magnetic shield and the magnetic probe system are installed at the S1 area. The magnetic probe can move independently from the magnetic shield in the range of the length of the shield (750 mm). First, Magnetic fields on the beam axis without the magnetic shield are measured (Figure 4.71). Then the magnetic shield is assembled on the mounting base, and magnetic field with the shield was measured. As shown in this figure, the magnetic field is suppressed at the level of mG in the magnetic shield.

System for a magnetic field scan

Figure 4.72 shows a schematic view of the system for magnetic field scan. The edge of the support rod can be attached and removed two different probe holders, for scan on axis and on cylinder surface.

Mechanism of a magnetic probe A magnetic probe for the measurement is used fluxgate magnetometer for 3 axis (MTI FM-3500). The linearity of the probe is 5 nT (0.5% of F.S.) and the precision is 0.5 nT for each axis. Fluxgate measures a magnetic field on a single axis by using a non-linear response of high-permeability material. Figure 4.73 shows a typical mechanism of a fluxgate. A relation between a magnetization ($M(H)$) and a magnetic field (H) can be expressed as

$$M(H) = \chi_1 H + \chi_2 H^2 + \chi_3 H^3. \tag{4.15}$$

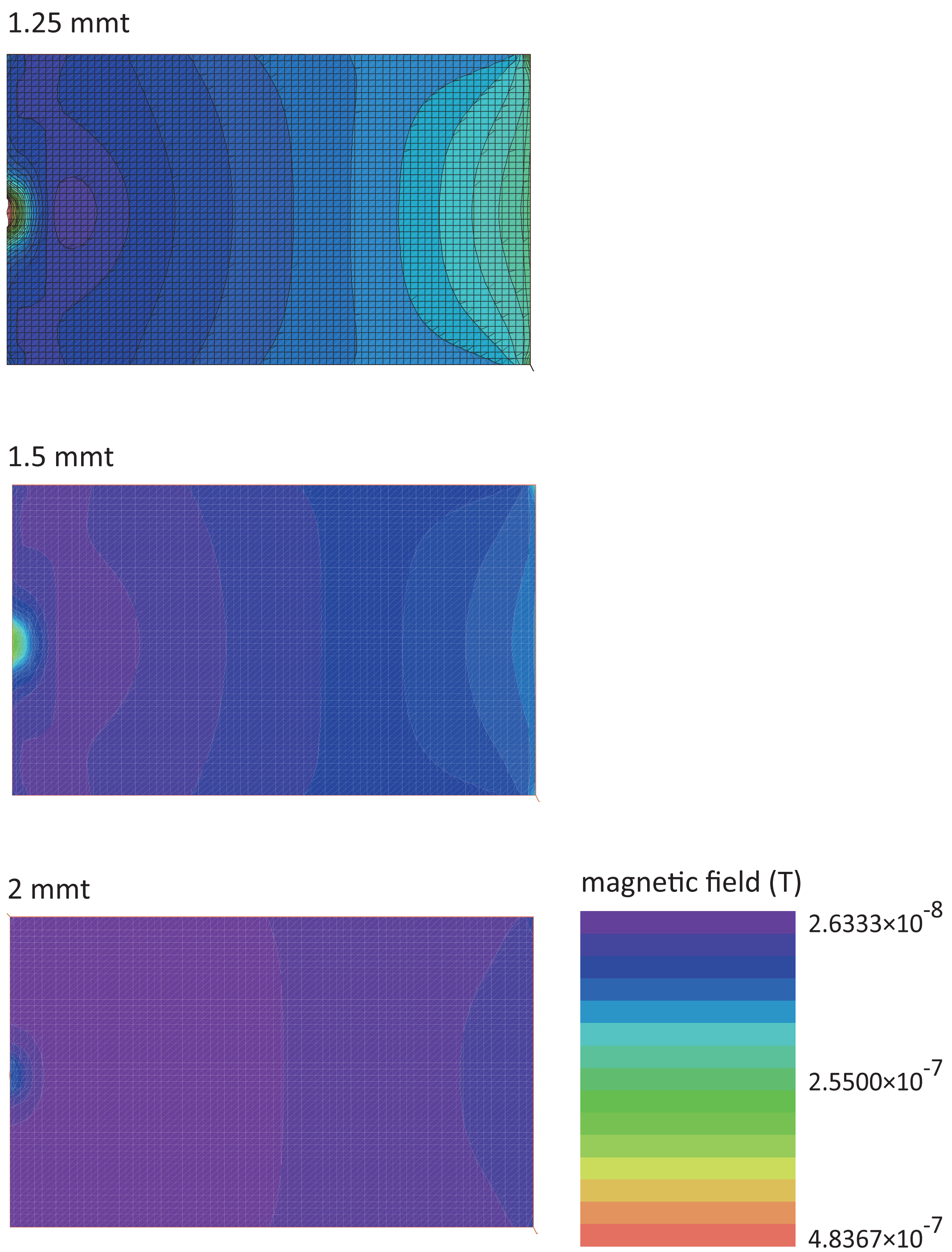

Figure 4.69: A comparison of magnetic fields in the shield between different thicknesses of plates of the shield. In this simulation, the relative permeability of the plates is set to 12000.

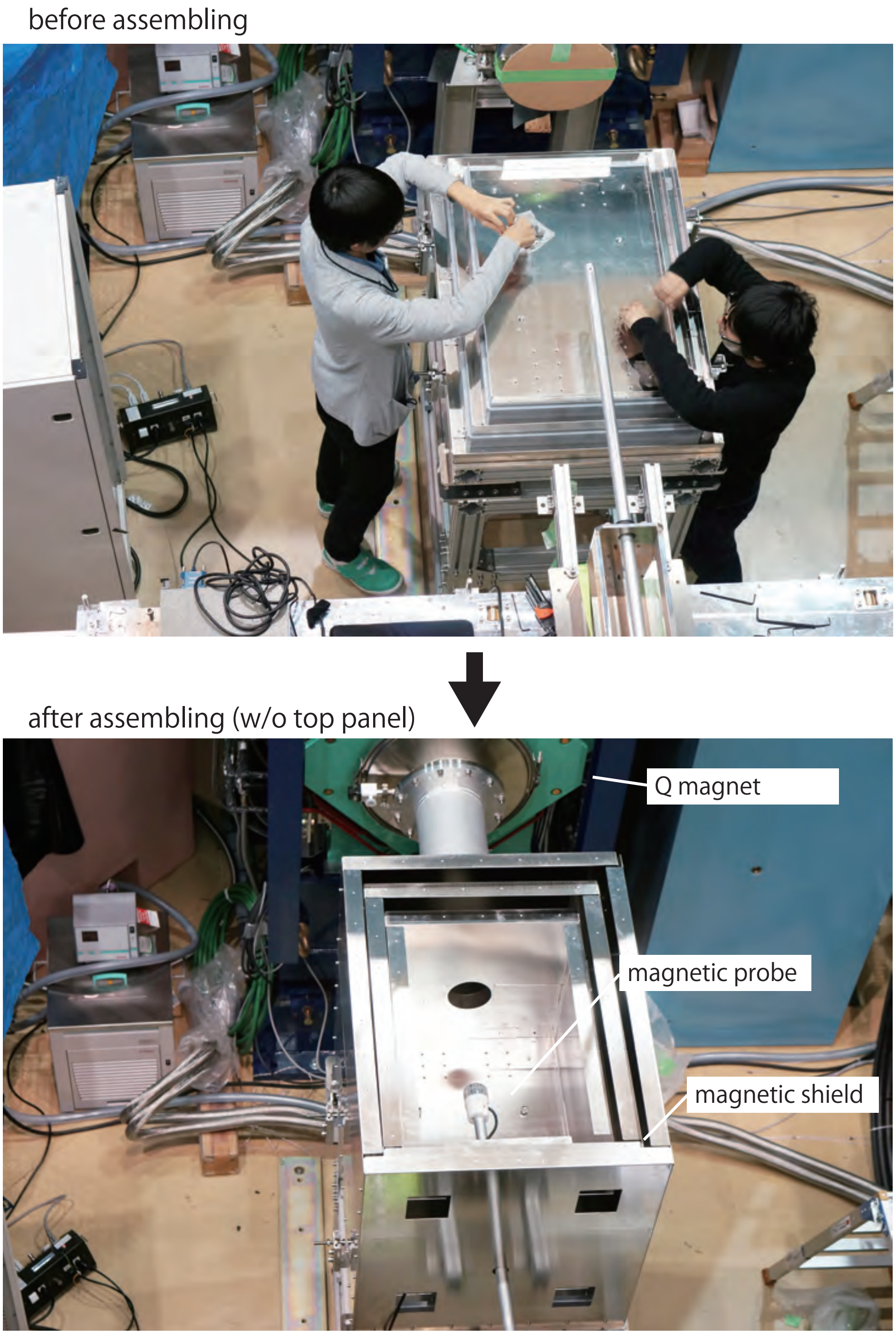

Figure 4.70: A photo of the installation of the magnetic shield and the system for magnetic field scan. Magnetic probes are inserted from the $\phi 40$ hole on back panels.

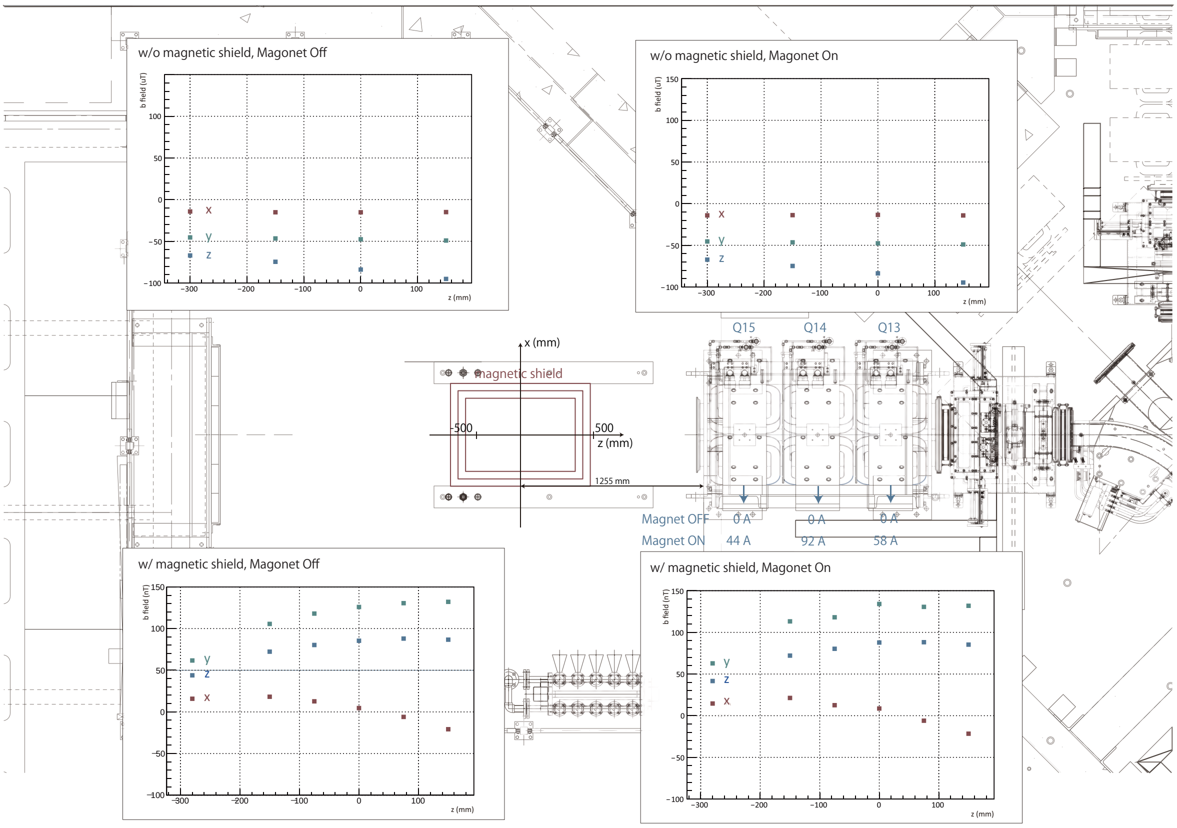

Figure 4.71: A result of the performance test of magnetic shield in S1 area. There is little variation of magnetic fields between magnet on and magnet off. The magnetic shield reduces the external field about one-thousandth.

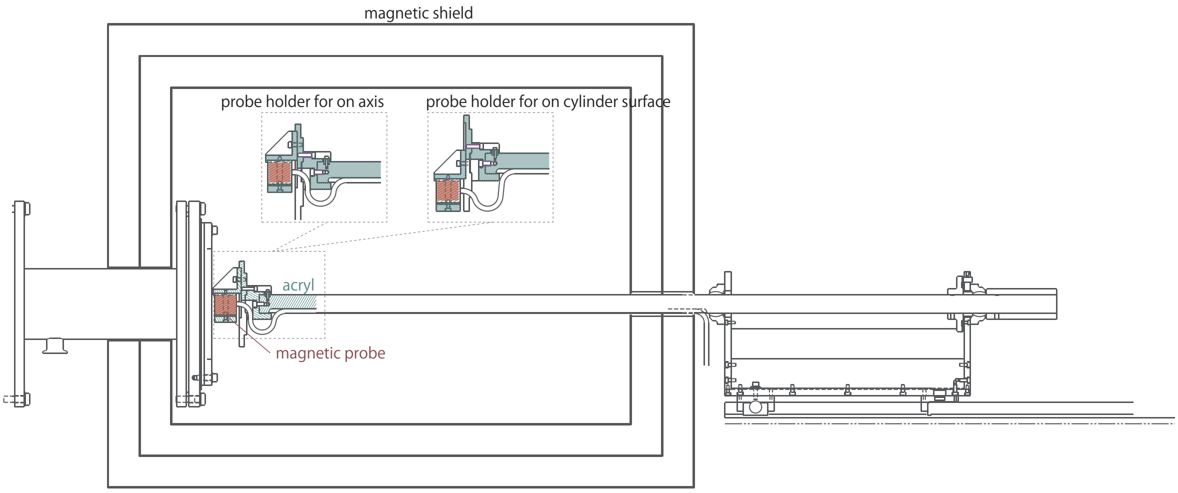

Figure 4.72: A schematic view of the system for magnetic field scan. The edge of the support rod can be attached and removed two different probe holders, for scan on axis and on cylinder surface.

Then the induced electromotive force (E) of 2nd coil from an external magnetic field (H_0) and a magnetic field of 1st coil (H_1) is

$$E = \frac{\mathrm{d}(M(H_0 + H_1) + M(H_0 - H_1))}{\mathrm{d}t} \tag{4.16}$$
$$= \frac{\mathrm{d}2(\chi_1 H_0 + \chi_2 H_0^2 + \chi_3 H_0^3 + (\chi_1 + 3\chi_3 H_0)H_1^2)}{\mathrm{d}t} \tag{4.17}$$
$$= 4A(\chi_1 + 3\chi_3 H_0)\sin(2\omega t). \tag{4.18}$$

If

$$H_1 = A\sin(\omega t), \tag{4.19}$$

then

$$E = C_0\cos(\omega t) + 3\chi_3 H_0 \sin(2\omega t) + 3\chi\sin(\omega t)^2\cos(\omega t). \tag{4.20}$$

By detecting a second order oscillation in 2nd term of the equation, the strength of the external magnetic field H_0 can be obtained.

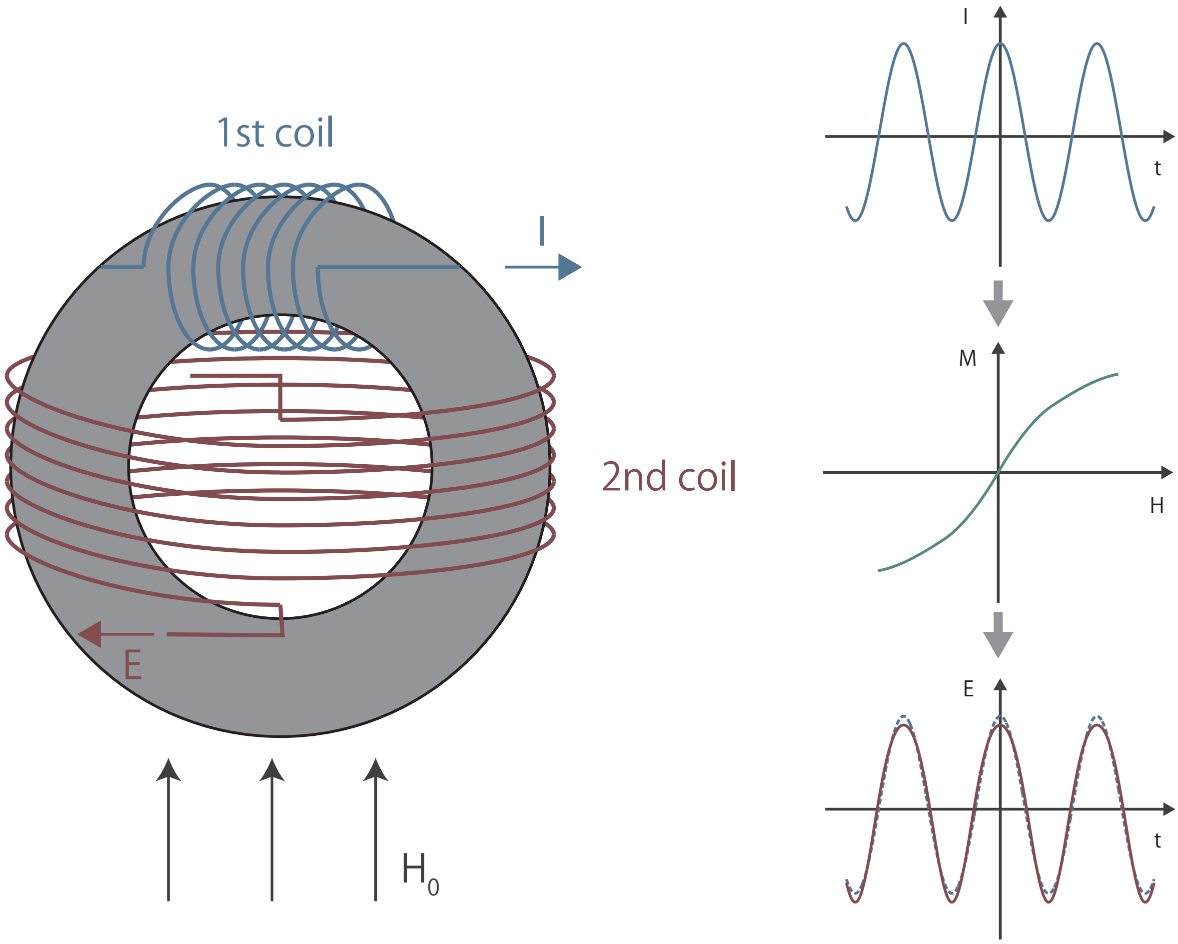

Figure 4.73: A typical mechanism of a fluxgate magnetometer. A fluxgate measures a magnetic field on a single axis by using a non-linear response of high-permeability material.

4.9 Data acquisition system

4.9.1 Data acquisition system for environmental monitoring

Figure 4.74 shows a schematic diagram of the monitoring system for RF system, gas system and magnetometers. These values are taken every minutes and recorded using a Labview software.

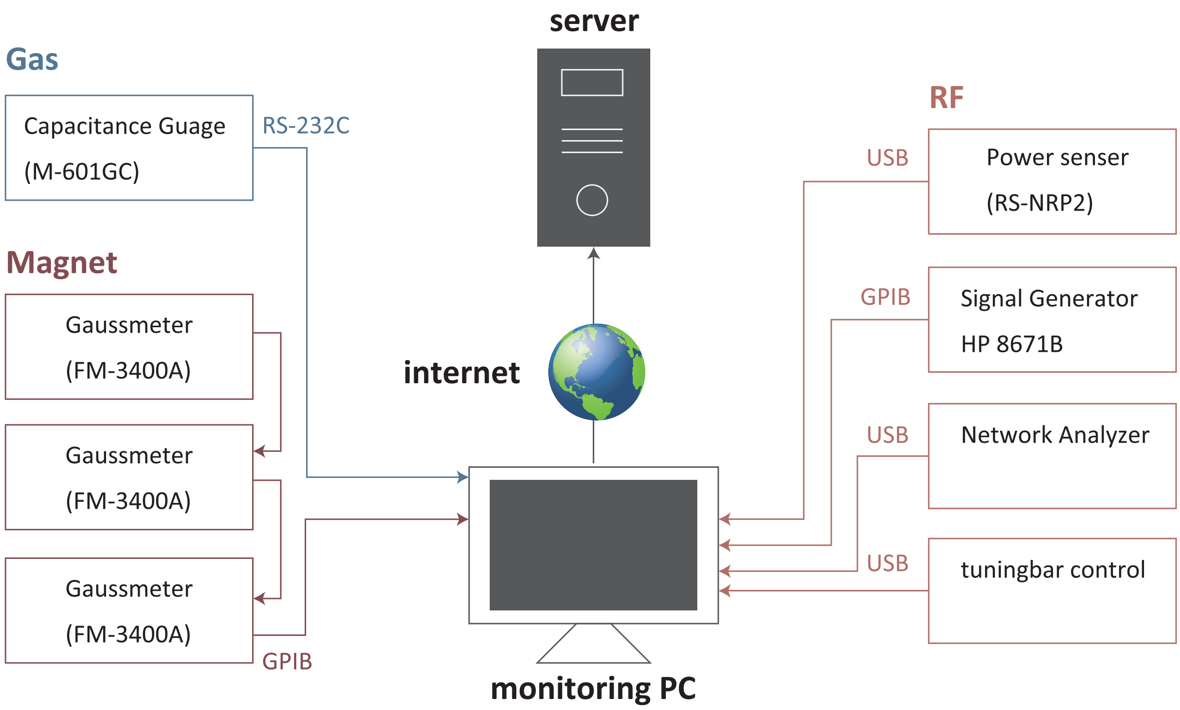

Figure 4.74: A schematic diagram of the monitoring system for RF system, gas system and magnetometers. These values are taken every minutes and recorded using a Labview software.

4.9.2 Data acquisition system for detectors

Data aquision system for detectors is developed by S. Kanda and others. Signals from positron detectors are read by Kalliope (KEK Advanced Liner and Logic board Integrated Optical detector for Positron and Electron) developed by the Electronics

Group and Institute of Material Structure Science (IMSS) of KEK[63]. Data of multi-hit TDC is transferred to the computer by Ethernet.

4.10 Beam monitoring system

Systematic uncertainties from a RF field and a magnetic field are able to be suppressed by analysis by using a field maps and muonium distributions from two different beam monitors.

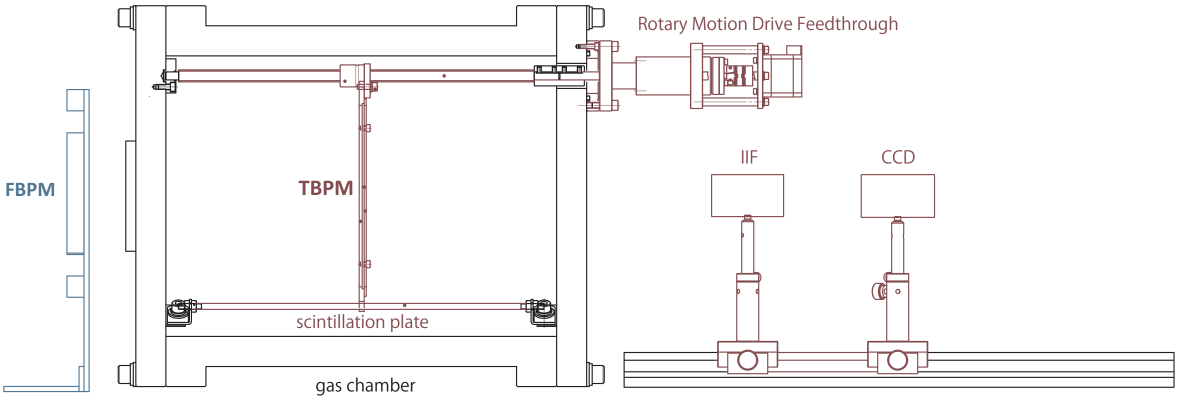

Figure 4.75: A schematic drawing of a beam monitoring system. Before a measurement, 3 dimensional muon stopping distributions in a certain gas pressure are taken by using a TBPM. Fluctuations of distributions are monitored by FBPM during a measurement.

FBPM

2–dimensional muon distribution is measured by a front beam profile monitor (FBPM) simultaneously for monitoring the stability of beam profile and relatively beam intensity during every data taking time developed by S. Kanda and others [91]. FBPM is composed of 2 layers of scintillation fiber arrays. The thickness of the fiber is 100 μm which allow the passage of muons. The detection area is 100 mm $\times$ 100 mm which cover the three standard deviation range of the muon beam.

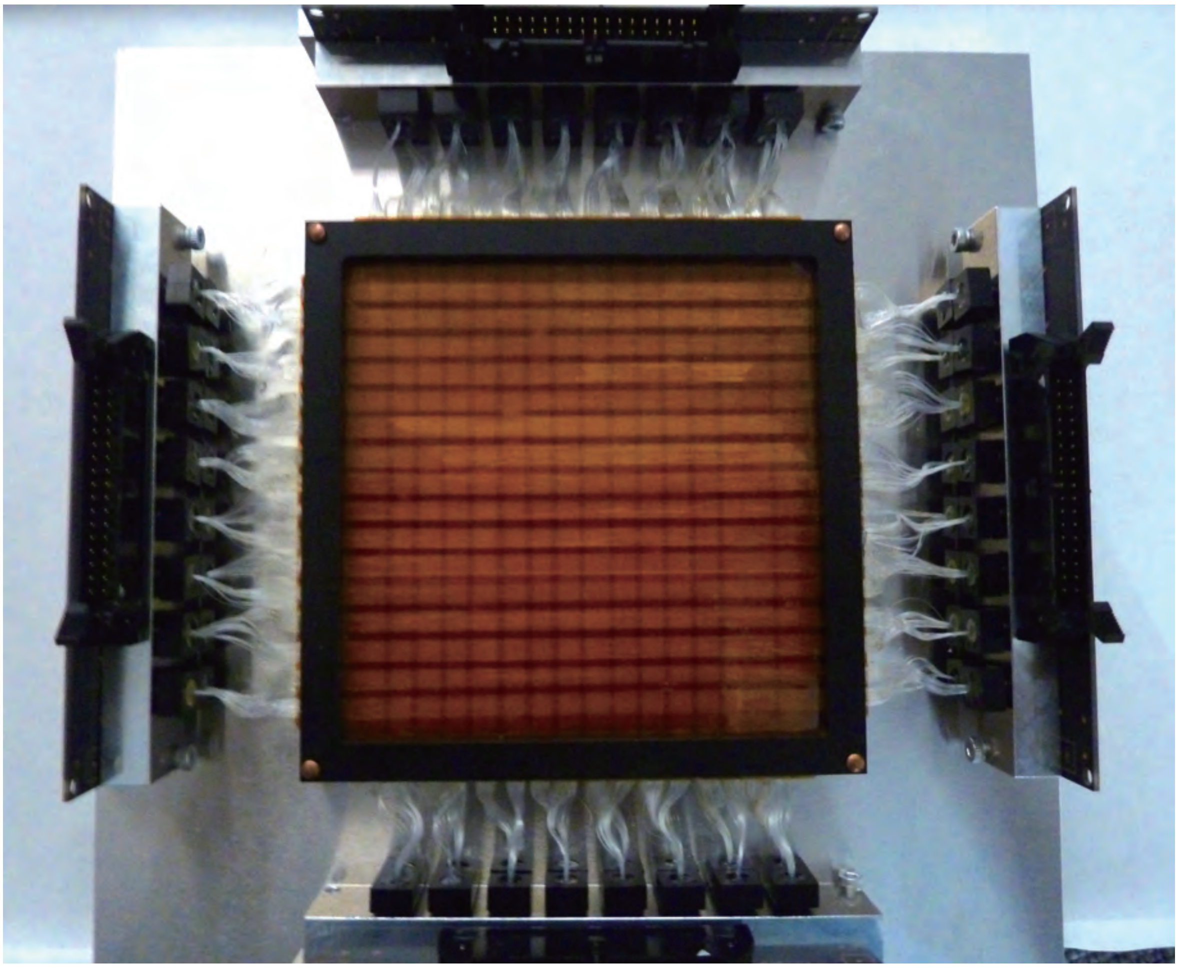

Figure 4.76: A photograph of FBPM.

TBPM

Before taking data, the 3-dimensional muon stopping distribution in the gas chamber is measured by a target beam profile monitor (TBPM) developed by S. Kanda, Y. Ueno and others[64]. Muons pass through in the chamber stop at the scintillation plate at the certain positon on the beam axis. Illuminations maps on the plate is taken by image intensifier (IIF) and CCD which are placed in the rear of the chamber.

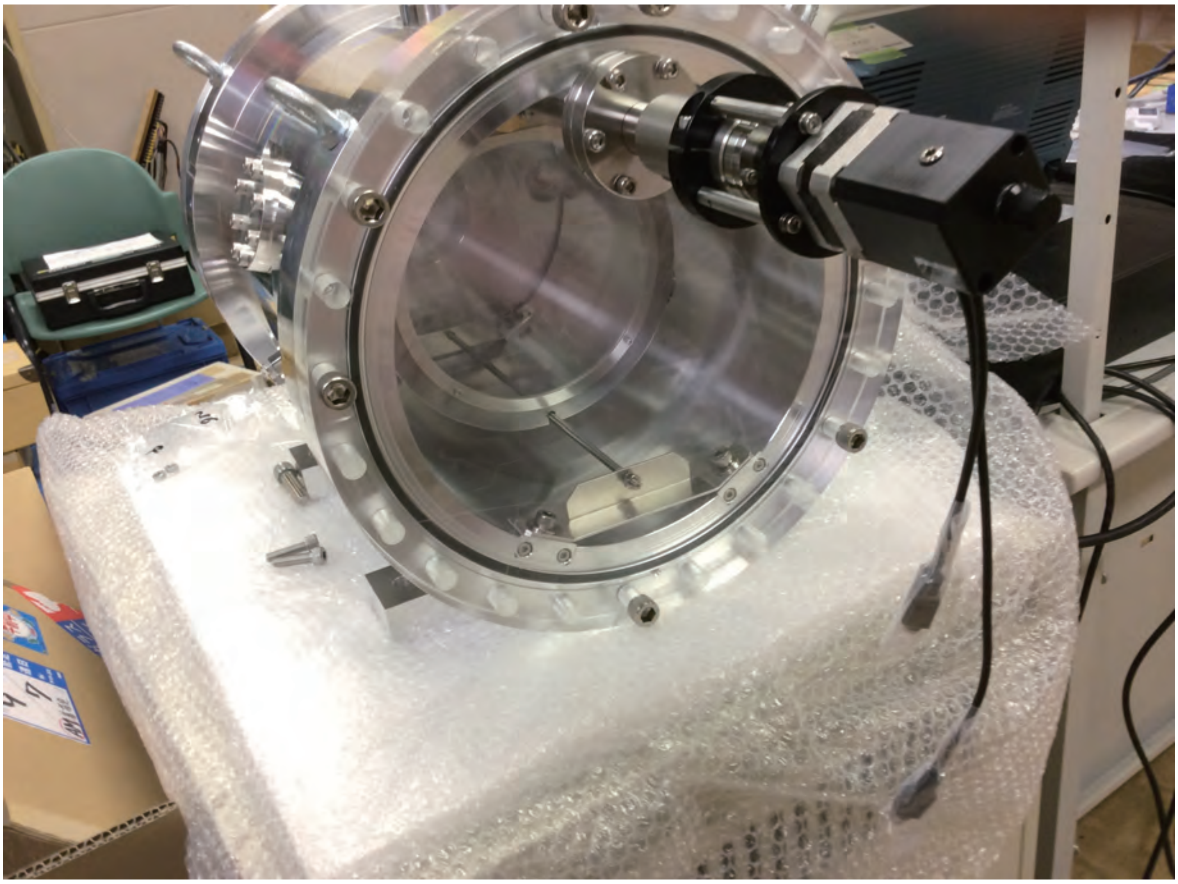

Figure 4.77: A photograph of TBPM.

4.11 Positron Detector

The detector for decay positrons is developed by S. Kanda and others[65]. The Positron detector is composed of 576 channels of segmented scintillators (10 mm $\times$ 10 mm $\times$

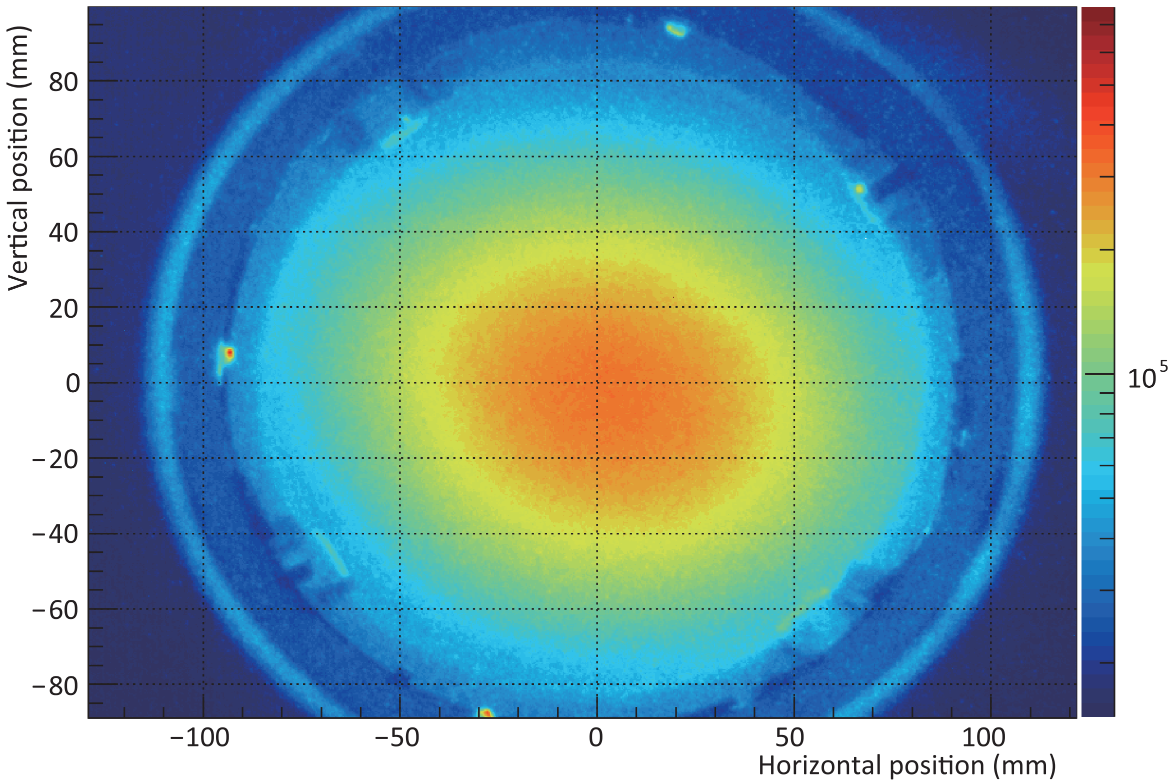

Figure 4.78: A typical measured muon beam profile. The scintillator plate is located on the center of the cavity and the gas pressure is 0.3 atm.

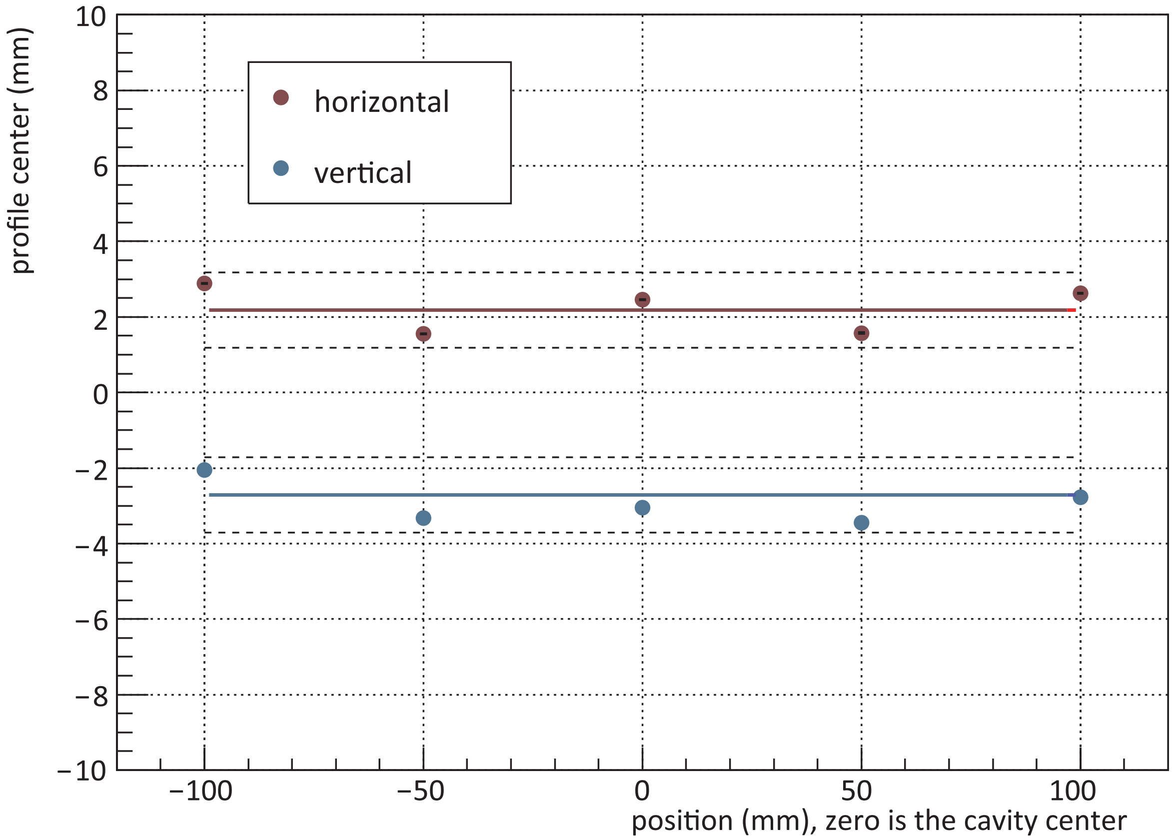

Figure 4.79: A relation between the profile position and the position of the scintillator. The origin point of the position is defined as the cavity center.

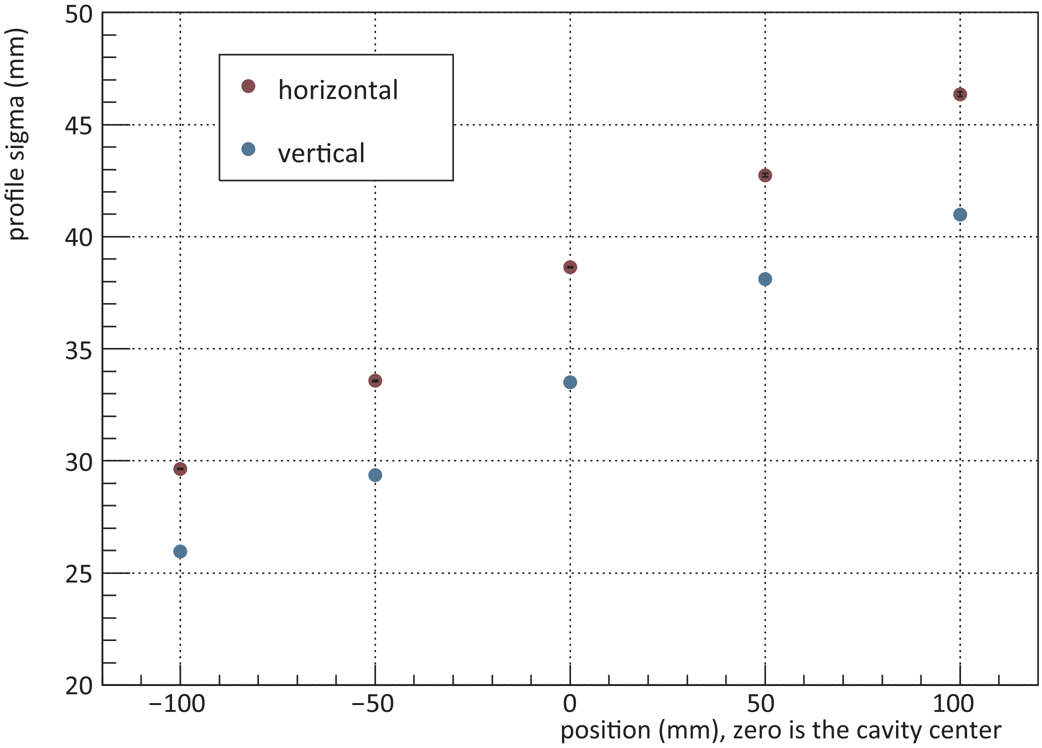

Figure 4.80: A relation between the profile width and the position of the scintillator. The origin point of the position is defined as the cavity center.

3 mmt) directly mounted on Multi-Pixel Photon Counter (MPPC). The detection area is 300 mm $\times$ 300 mm.

For measurement at high intensity pulsed muon beam line, it endures in use for high rate positrons such as 3400 e^+.

4.12 Superconducting magnet

The superconducting magnet developed by K. Sasaki and others is used for the high field experiment to apply 1.7 T magnetic field. The magnet provides a magnetic field with a stability of 0.003 ppm/hour. The field homogeneity reaches at the ppm level by using a shimming method. First, measure a magnetic field at 576 points on an ellipsoid surface. Then put iron pieces into pockets surrounding the inner surface of the magnet to correct a variation of a magnetic field.

The uncertainty from magnetic field is discussed in Subsection 5.9.

4.12.1 NMR probe

The magnetic field in the superconducting magnet is measured by the set of NMR (nuclear magnetic resonance) probes. The continuous-wave spectroscopy (CW spectroscopy) is used for this measurement. The NMR spectra is obtained as the RF absorption signal by applying the reference RF and the modulation magnetic field in a certain external magnetic field (Figure 4.82). The magnetic field map is obtained by the set of NMR probes driven by ultrasonic motor, and the fluctuation of the magnetic field during the measurement is monitored by several fixed NMR probes. The systematic uncertainties from NMR probes are discussed in Subsubsection 5.9.1. This system is developed by K. Sasaki, Y. Ueno and T. Mizutani and others.

4.12.2 Shimming

The inhomogeneity of the magnetic field in the superconducting magnet is reduced by mounting a shim plates made of iron on the inner coils. Figure 4.83 shows a positions

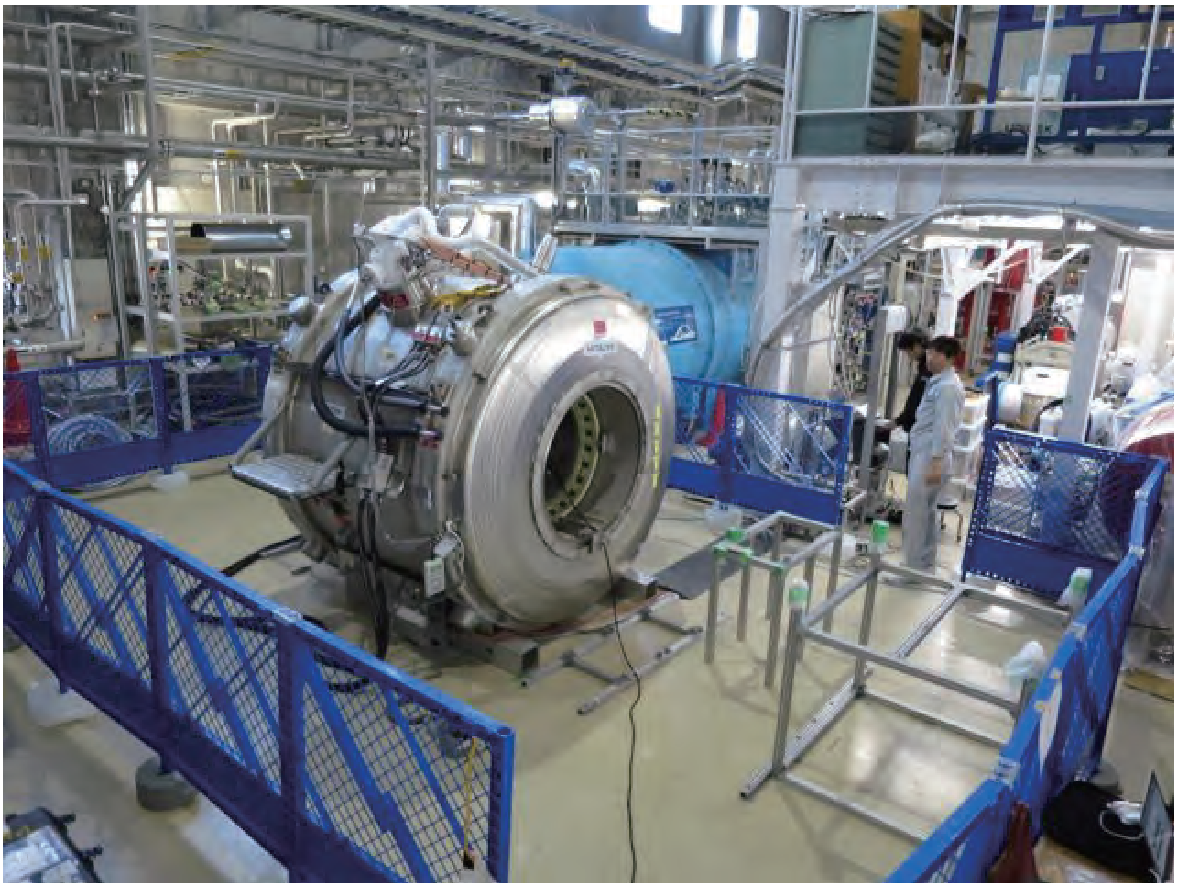

Figure 4.81: A photograph of superconducting magnet.

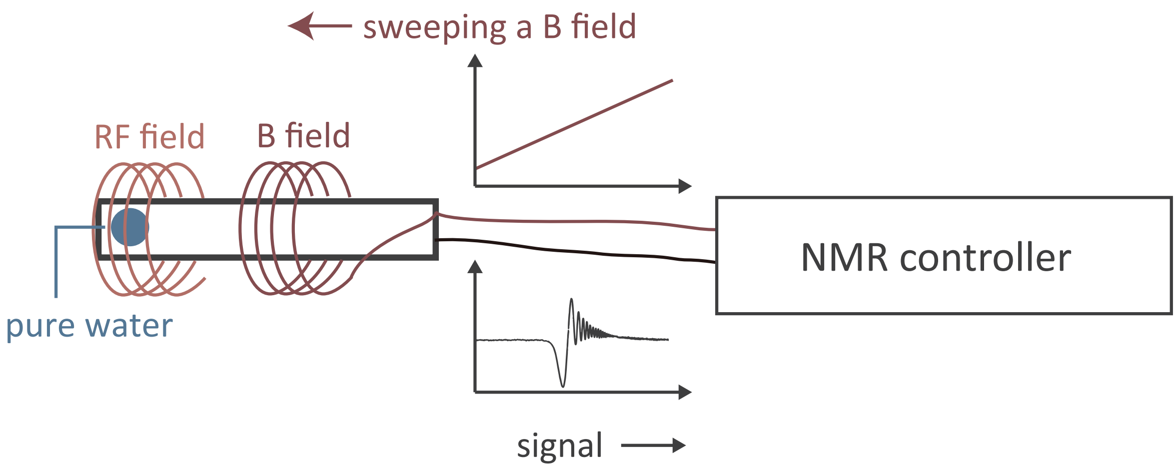

Figure 4.82: An overview of the CW spectroscopy of NMR. The NMR spectra is obtained as the RF absorption signal by applying the reference RF and the modulation magnetic field in a certain external magnetic field. External magnetic field is obtained by the reference magnetic field at the zero-crossing of modulation magnetic field.

to mount shim plates.

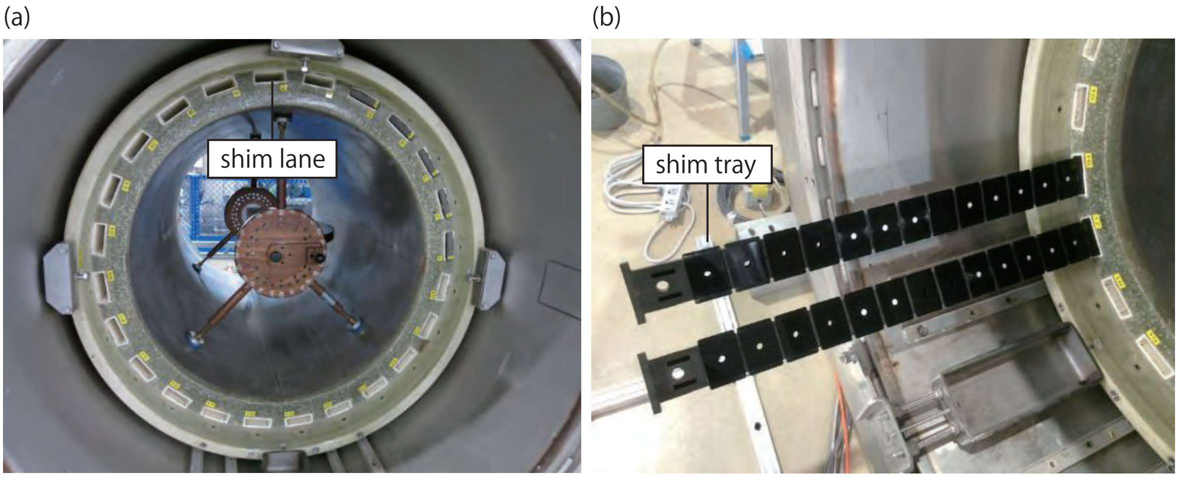

Figure 4.83: Photo of the superconducting magnet and shim trays on the inner surface of the magnet. (a) There are 24 shim lanes at regular intervals. (b) Each shim lanes have 24 shim trays which enable to load up to 13 cm^3.

Chapter 5

Analysis and evaluating uncertainties

The statistical uncertainty and systematic uncertainties are estimated in this chapter. For each kind of uncertainty, a summarized table is given for quantities we measure in the experiment (Table 5.1).

$\delta\nu_{12}$	an uncertainty of the ν_{12} transition in high field experiment
$\delta\nu_{34}$	an uncertainty of the ν_{34} transition in high field experiment Hz
$\Delta\nu_{\mathrm{HF}}$	an uncertainty of Mu HFS value in high field experiment
$\Delta\nu_{\mathrm{ZF}}$	an uncertainty of Mu HFS value in high field experiment
μ_μ/μ_p	an uncertainty of the muon-proton magnetic moment ratio in high field experiment

Table 5.1: A description of the summarized table of uncertainties.

5.1 General approach

We have developed a full Monte Carlo simulation package to reproduce the resonance line shape which will be observed in the experiment. The package tracks the whole process of the experiment which includes the muonium formation in krypton gas, transitions between atomic states via the interaction with a RF field under a magnetic field, the weak decay of muon which emits a positron, and positron detection by detectors. This package is used to evaluate systematic uncertainties of the experiment, and will be the base for the analysis code for the experimental data.

The simulation package consists of four parts (Figure 5.1). The first part generates the map of muon stopping distribution within experimental apparatus using GEANT4 Monte Carlo package. All apparatus such as beam line magnets and ducts, the front beam profile monitor, the gas chamber filled with krypton gas, the RF cavity within the chamber are all modeled in the code.

The second part generates the map of strength of RF field inside the cavity using CST STUDIO. The physical dimensions and properties of the RF cavity and tuning bars are taken into account in the calculation.

The third part calculates the detection efficiency of a positron emitted following the decay of muon as a function of the initial kinetic energy, direction and the positron muon decay using GEANT4 Monte Carlo package. The code follows the path of the positron from the positon where muon decays to where it stops in (or escapes from) our apparatus under the magnetic field.

The last part curries out a Monte Carlo simulation to determine the observed resonance line shape under as a function of RF frequency using the muon stopping distribution map(Equation 3.13), the RF field map, the positron detection efficiency map. Figure. 5.2 shows time evolutions of different resonance frequencies generated by the tool. Transition probabilities can be calculated by integrating time evolutions from t_1 to t_2. The code tracks the evolution of occupation probabilities of atomic states of a muonium with RF field.

5.2 Fitting method

Systematic uncertainties are estimated from the change of the simulated resonance line shape due to fluctuations of one of experimental conditions. If the variation results the shift of the estimated value, it is listed as the systematic uncertainty. If the variation results the widening of the confidence interval of the estimated value, the broadening

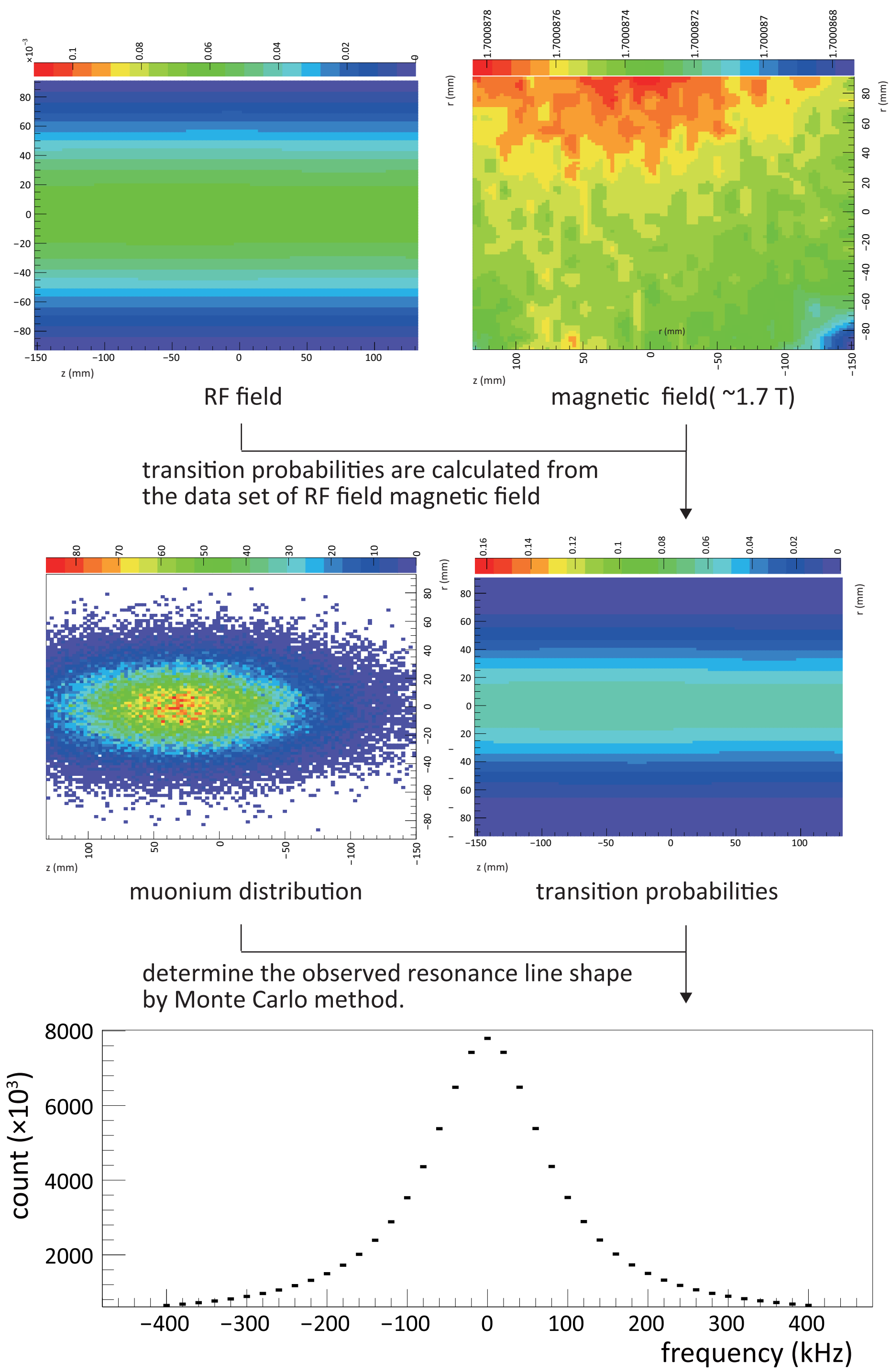

Figure 5.1: A diagram of the simulation package. Probabilities of transitions are calculated by using data sets of a magnetic field, a RF field. Then the observed resonance line shape is determined by the Monte Carlo method.

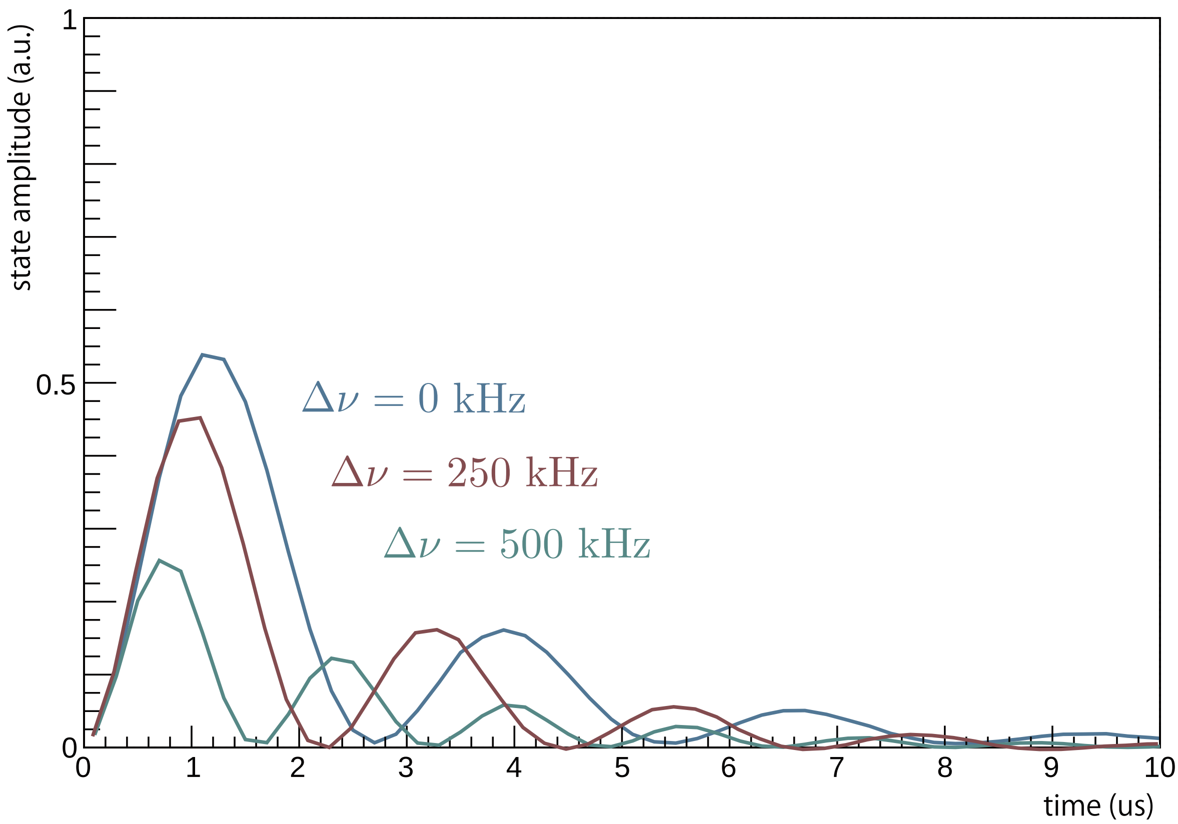

Figure 5.2: Typical time evolutions in case of the difference between the transition frequency and the resonance frequency (Δ_ν) is 0 kHz(blue line), 250 kHz(red line), 500 kHz(green line).

is listed as the systematic uncertainty. In following sections, we look at the functions to fit the simulated resonance line shape.

5.2.1 conventional resonance line

The simplest function to fit the resonance line shape would be a Lorentzian function as shown in Equation 3.15,

$$S(\omega) = N\frac{2|b|^2}{\omega'^2 + 4|b|^2 + \gamma^2}, \tag{5.1}$$

where $|b|^2$ is RF power. Though, this function gives poor fitting because the muonium atoms interact with RF field of different strength, depending on its position. Figure 5.3, shows a time evolution with constant strength of the RF and the magnetic field and distributed RF and magnetic field. According to this figure, the function to fit the resonance line shape is required to be taken into account the relaxation of the time evolution from the distributed RF field.

The fitting improves when the function is a convolution of the Lorentzian function and RF power distribution map over. Thus, more proper function for resonance line shapes by using a conventional method is

$$S(\omega) = \int_{b_{\min}}^{b_{\max}} N(b)\frac{2|b|^2}{\omega'^2 + 4|b|^2 + \gamma^2}\mathrm{d}b \tag{5.2}$$

Figure 5.4 shows a comparison of chi squares of Equation 5.1 and Equation 5.2. Thus Equation 5.2 enables proper fittings for resonance line shapes.

5.2.2 oldmuonium resonance line

In case of oldmuonium method, the fitting function is convolution of Equation 3.14 with the histogram of the RF power as

$$S(\omega) = \int N(b)\frac{2|b|^2}{\Gamma^2}(e^{-\gamma t_1}(1-(\cos\Gamma t_1 - \frac{\Gamma}{\gamma}\sin\Gamma t_1)\frac{\gamma^2}{\Gamma^2+\gamma^2}) \tag{5.3}$$

$$-\frac{2|b|^2}{\Gamma^2}(e^{-\gamma t_2}(1-(\cos\Gamma t_2 - \frac{\Gamma}{\gamma}\sin\Gamma t_1)\frac{\gamma^2}{\Gamma^2+\gamma^2})) \tag{5.4}$$

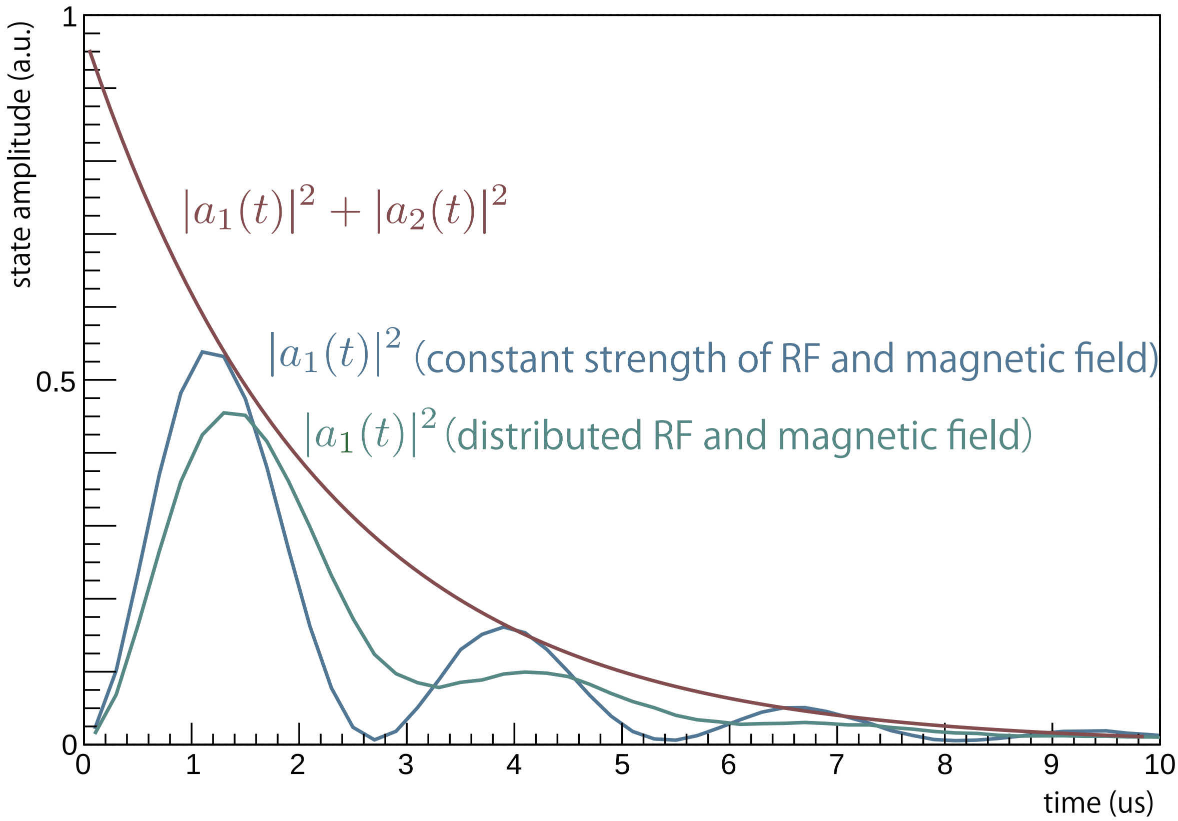

Figure 5.3: Typical time evolutions of a sum of state amplitudes $|a_1(t)|^2 + |a_2(t)|^2$ (red line), a state amplitude $|a_1(t)|^2$ with constant strength of the RF and the magnetic field(blue line), and an integrated state amplitude $|a_1(t)|^2$ with distributed RF and magnetic field (green line) obtained by the simulation package. There is a relaxation effect by distribution of a RF field and a magnetic field in case of distributed muoniums.

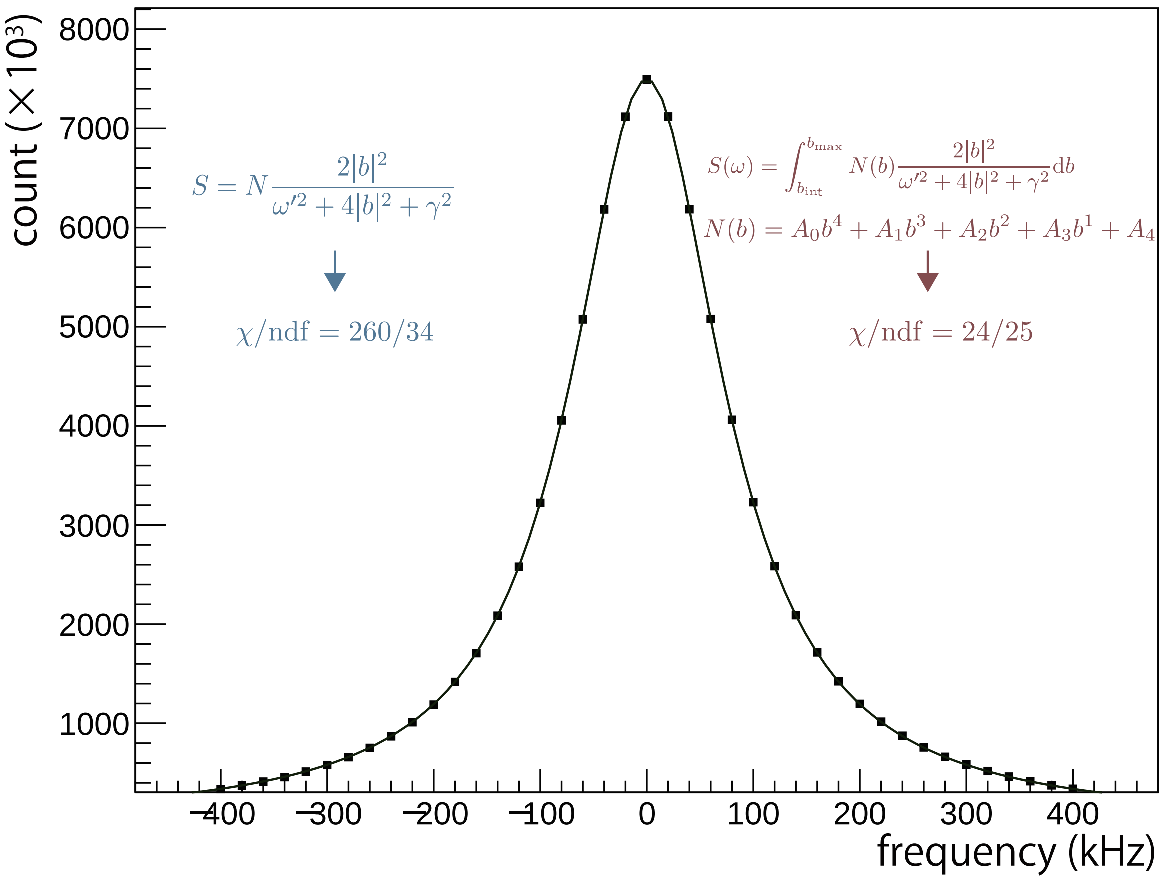

Figure 5.4: Comparison of chi squares of Equation 5.1 and Equation 5.2.

5.3 Statistical uncertainties

A statistical uncertainty can be improved by optimizing the t_1 and t_2 of Equation 3.14. Figure 5.5 shows a resonance line shape in case of $t_1 = 0$ and $t_2 = \infty$ which is called "conventional method" and upper of this figure show time evolutions of state amplitudes of each points.

Figure 5.6 shows a resonance line shape in case of $t_1 = 6$ μs and $t_2 = 7$ μs which is called "oldmuonium method". Signal ratios of each points are proportional to value of integral of time evolutions from t_1 to t_2. As Equation 3.13 shown, the time evolution is determined by the strength of microwave. Thus, a linewidths of a resonance line can be reduced by optimizing t_1 and t_2.

Figure 5.7 shows a relation between statistical uncertainties by using the oldmuonium method and t_1 in case of $t_2 - t_1 = 1$ μs. The horizontal line shows a statistical uncertainty using conventional method by using same number of muons. It assumes that scan range is 400 kHz and number of scan points is 21. The number of muonoiums to use of each points is 10^8. The line broadening from the microwave increase the statistical uncertainty in case of low t_1. On the other hand, since the number of observed muonium is decreased in case of high t_2, the statistical uncertainty is increased even the linewidth is narrow.

Figure 5.8 shows relation between t_1 and the center value of the resonance lines. It assumes the same scan range and the statistics as Figure 5.7. The red band shows the uncertainty bar of the average value of 6 results using the old muonium method from $t_1 = 0$ μs to $t_1 = 10$ μs. As a result, the uncertainty by using a conventional method is 18 Hz and by using an oldmuonium method is 9.4 Hz which is superior to a conventional one. Moreover, the average value of 6 results using the old muonium method which is so called time-slicing method enable to improve uncertainty such as 4.9 Hz.

The intensity of H Line is 1×10^8/s and D line is 1.5×10^7/s. The number of decay positrons per a muon is 0.7 % obtained by the result of GEANT4[7] simulation. Then the statistical uncertainty is under 5 Hz by measurement in high field for a week at

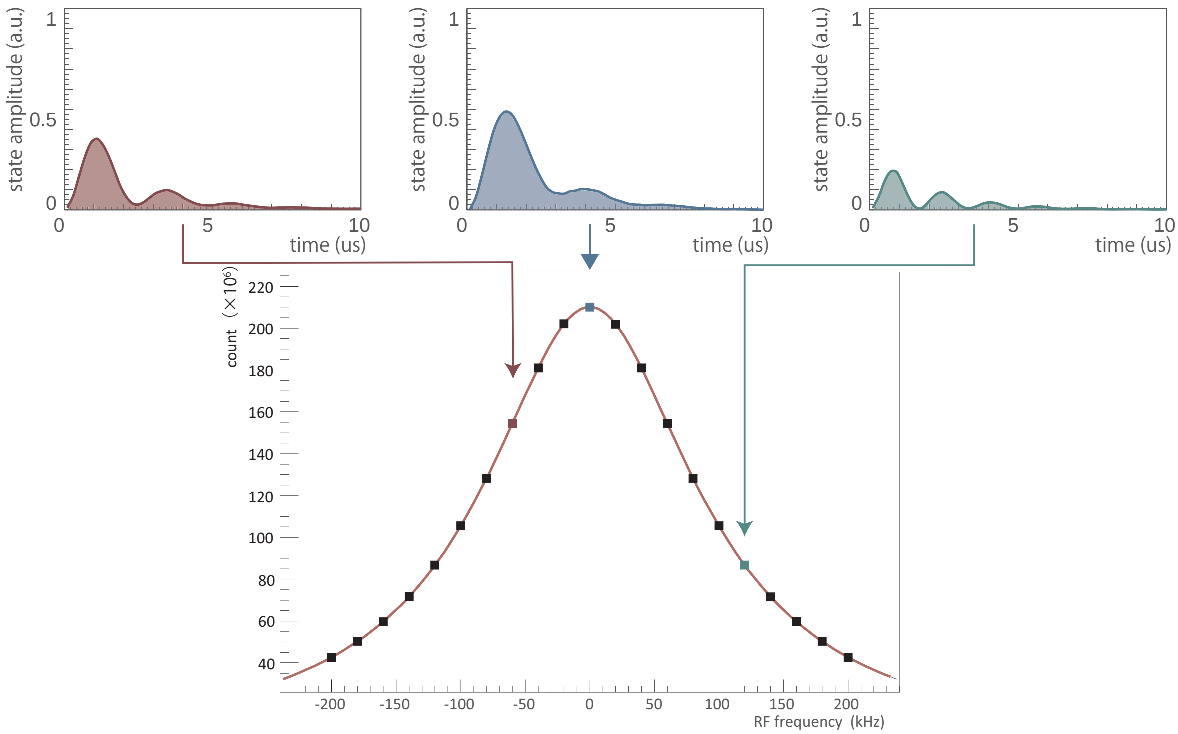

Figure 5.5: A typical resonance line shape using a conventional method obtained by the simulation package. The total number of muons are 10^8 at each frequency points. Total counts of decay positrons are proportional to the integrated values of state amplitude from $t = 0$ to $t = \infty$.

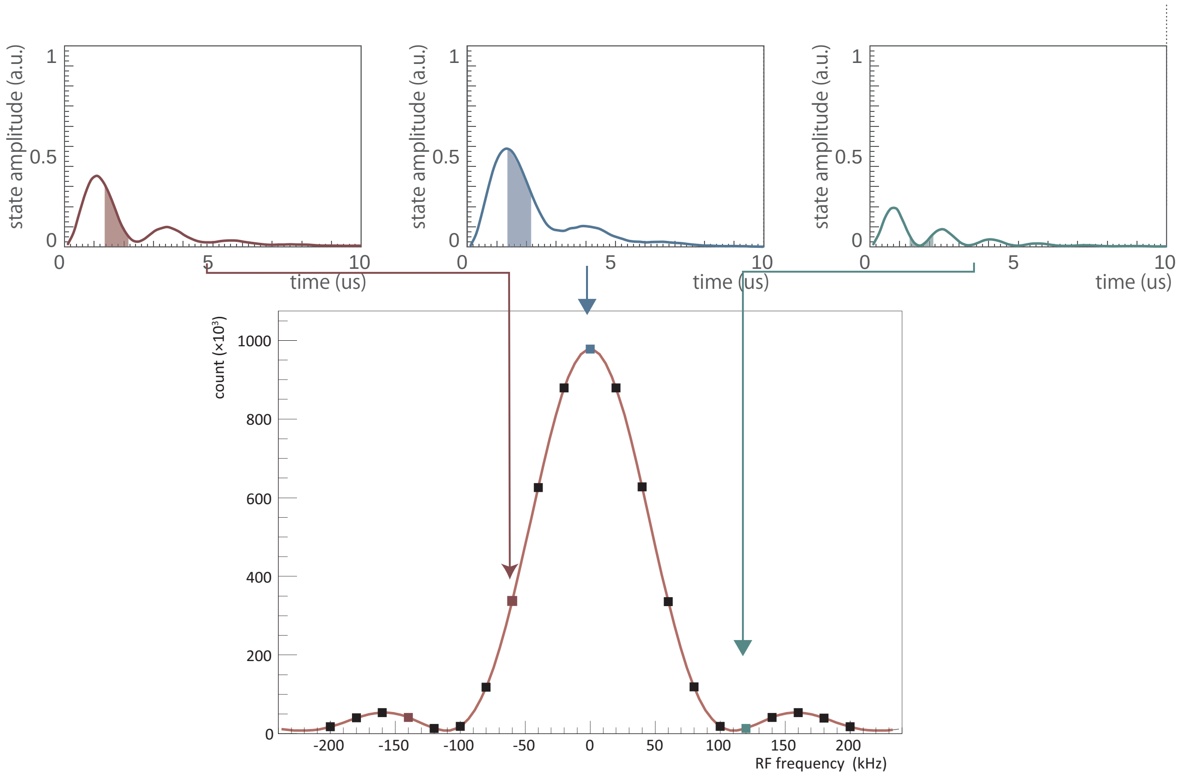

Figure 5.6: A typical resonance line shape using an oldmuonium method obtained by the simulation package. The total number of muons are 10^8 at each frequency points. Total counts of decay positrons are proportional to the integrated values of state amplitude from $t = t_1$ to $t = t_2$. Even the total counts are decreased, FWHM of the peak is narrower than the peak obtained by using a conventional method.

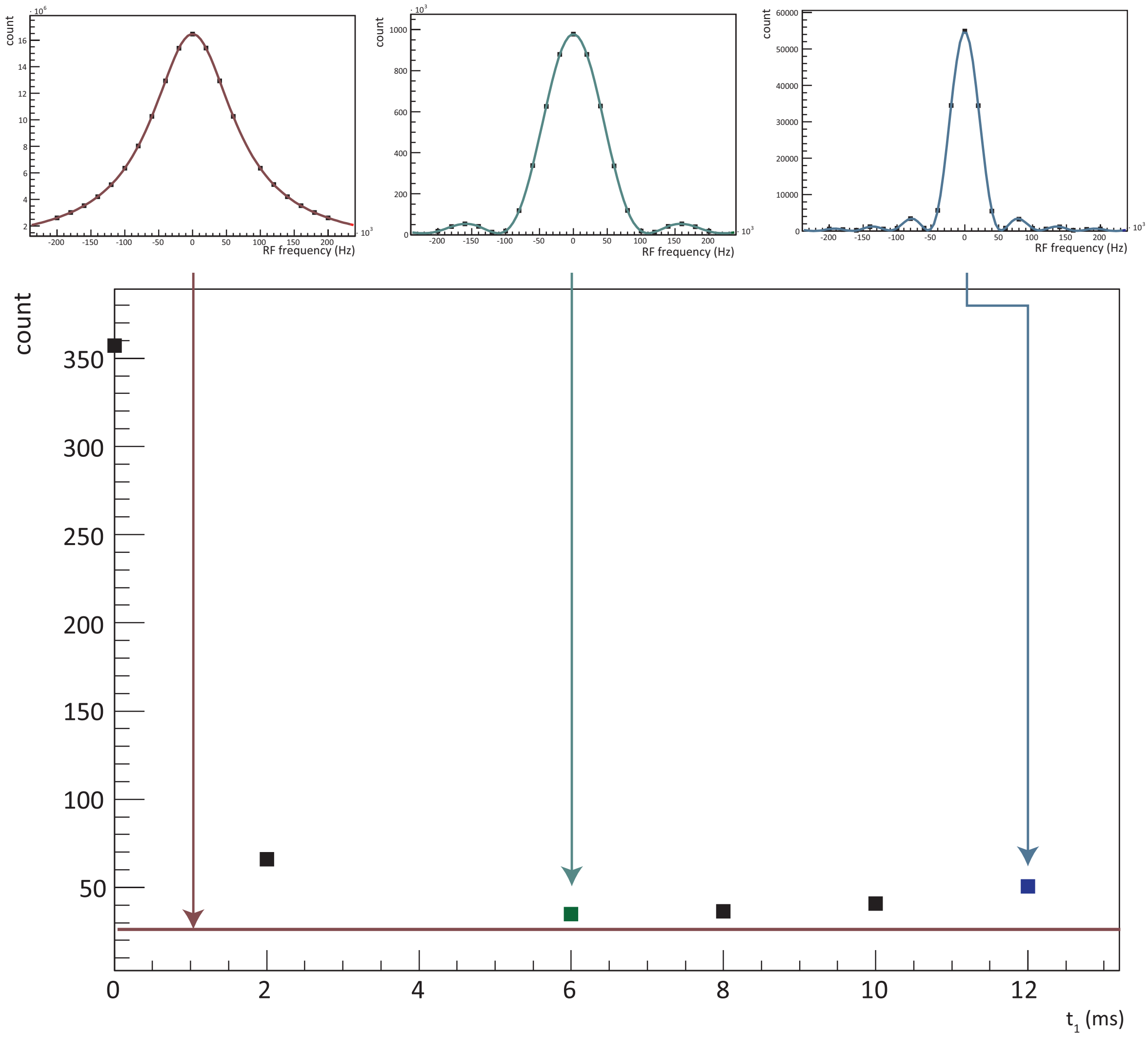

Figure 5.7: Relation between statistical uncertainties by using the oldmuonium method and t_1 in case of $t_2 - t_1 = 1$ μs. They assume that scan range is 400 kHz and number of scan points is 21. The number of muonoiums to use of each points is 10^8. The horizontal line shows a statistical uncertainty using conventional method by using same number of muons.

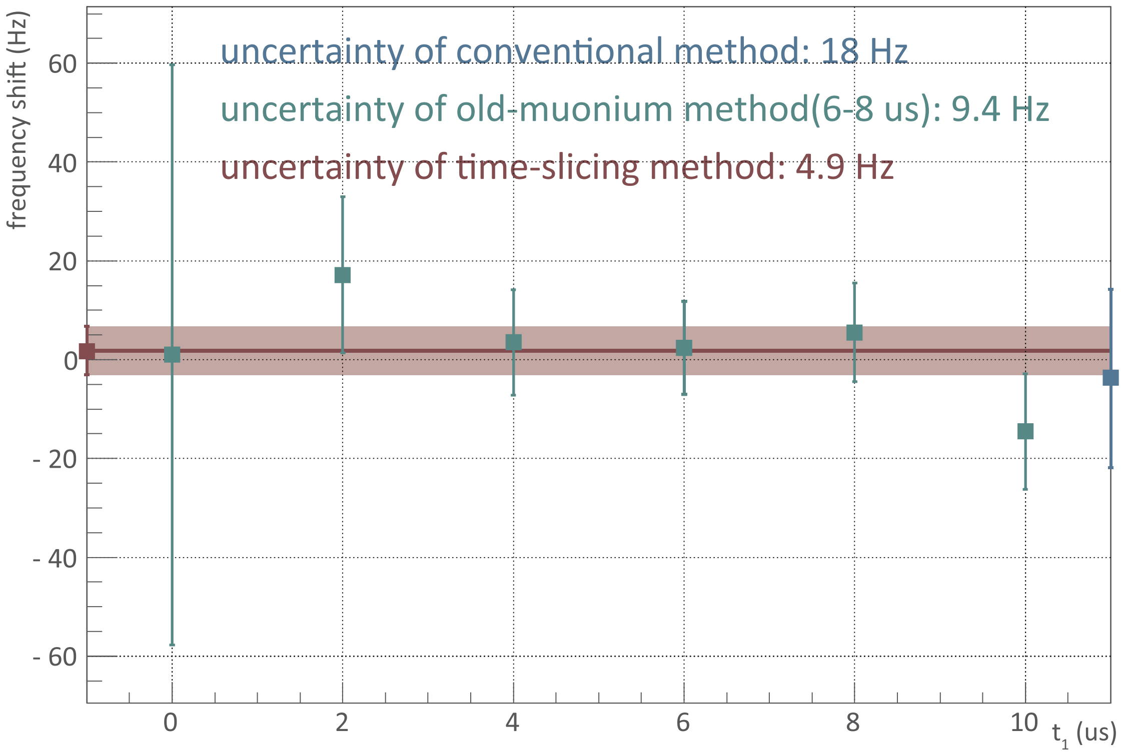

Figure 5.8: Comparison of statistical uncertainty between the conventional method and the oldmuonium method. A blue point show the resonance frequency obtained by the conventional method. Green points show the resonance frequencies obtained by the oldmuonium method with 2 μs time interval at each t_1 and the red band shows the uncertainty bar of the average value of 6 results using the old muonium method from $t_1 = 0$ μs to $t_1 = 10$ μs which is so called time-slicing method.

H Line including both ν_{12} and ν_{34}. Also, the statistical uncertainty is under 20 Hz by measurement in zero field for a day at D Line.

$\delta\nu_{12}$	3.5 Hz
$\delta\nu_{34}$	3.5 Hz
$\Delta\nu_{\mathrm{HF}}$	5 Hz
$\Delta\nu_{\mathrm{ZF}}$	20 Hz
μ_μ/μ_p	15 ppb

Table 5.2: Statistical uncertainty

5.4 Uncertainty from RF power

5.4.1 Evaluation at LAMPF experiment

As equation 3.15, the resonance line shape of conventional method ($t_1 = 0, t_2 = \infty$) can be expressed as

$$S = \frac{2|b_0^2|}{4\pi^2\alpha'^2x^2 + 4|b_0^2| + \gamma^2}, \tag{5.5}$$

where x is a difference between resonance frequencies and transition frequencies. The stability of the RF power in LAMPF experiment is 0.01% and they assumed that the fluctuation of RF power is proportional to the resonance frequencies such as

$$|b_0|^2 \rightarrow |b_0|^2(1 + kx). \tag{5.6}$$

Then Equation 5.5 is

$$S' = \frac{2|b_0|^2(1 + kx)}{4\pi^2\alpha'^2x^2 + 4|b_0|^2(1 + kx) + \gamma^2}. \tag{5.7}$$

By using approximation $|kx| << 1$,

$$S' \approx \frac{2|b_0^2|}{4\pi^2\alpha'^2(x + k'|b_0^2|)^2 + 4|b_0^2| + \gamma^2}. \tag{5.8}$$

By comparison between Equation 5.5 and Equation 5.8, $k'|b_0^2|$ expresses the frequency shift by fluctuation of the RF power and it is 2 Hz by substituting to 0.01 %. There are following two problems for this discussion.

1. Validity of approximation even they express the frequency shift by 1st order of k in Equation 5.8.
2. $k'|b_0^2|$ does not expresses the shift of the center value of the fitting function of the resonance line, but the peak of it.

To consider about first item, plotting Equation 5.5 and Equation 5.7. by using same parameters of LAMPF experiment (Figure 5.9). It shows that they underestimate the frequency shift from 8 Hz to 2 Hz.

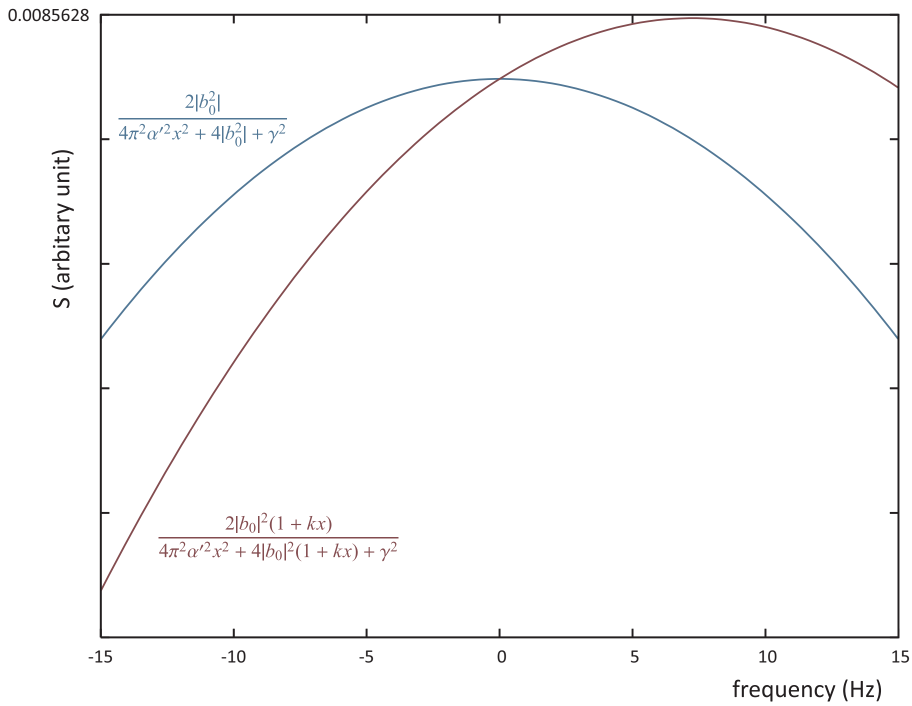

Figure 5.9: A comparison between Equation 5.5 and Equation 5.7. 8 Hz of shift is caused by 0.1 % fluctuation of the RF power.

5.4.2 Uncertainty from RF power

By using the simulation tool, uncertainty from RF power in this experiment is evaluated in this subsection. As described in 4.5.4, RF power is able to be stabilized within 0.02 %. Figure 5.10 shows systematic uncertainties from RF power depend on scanning frequencies. As shown in B, monotonically increasing of RF power within 1 % distort the resonance line shape. Due to this, the systematic uncertainty is 609 Hz. On the other hand, if the random sequence is used for the RF scanning as D, the systematic uncertainty is negligible.

$\delta\nu_{12}$	2 Hz
$\delta\nu_{34}$	2 Hz
$\Delta\nu_{\mathrm{HF}}$	3 Hz
$\Delta\nu_{\mathrm{ZF}}$	3 Hz
μ_μ/μ_p	9 ppb

Table 5.3: Systematic uncertainty from RF power

5.5 Fluctuation of RF field by tuning bars

The RF field in the cavity is fluctuated by the displacement of tuning bars. Fig 5.11 and Fig 5.12 shows a histogram of RF power $|b|^2$ affect to each muons in the cavity in case of displacements of tuning bar are 0 mm and 1 mm. The number of muons are 5.0×10^6 and RF fields are calculated by CST STUDIO[8]. Since peak position of both RF field and muonium distribution is located on the center axis of the cavity, this histogram is almost a monotonically increasing. However there is a small dip at $|b|^2 = 1.2 \times 10^{13}$.

Figure 5.11 shows color maps of each ranges of $|b|^2$. TM110 mode has one node along the radial direction, one node along the angular direction and no nodes along the axial direction. A weak RF field nearby nodes is shown in color map A and a strong

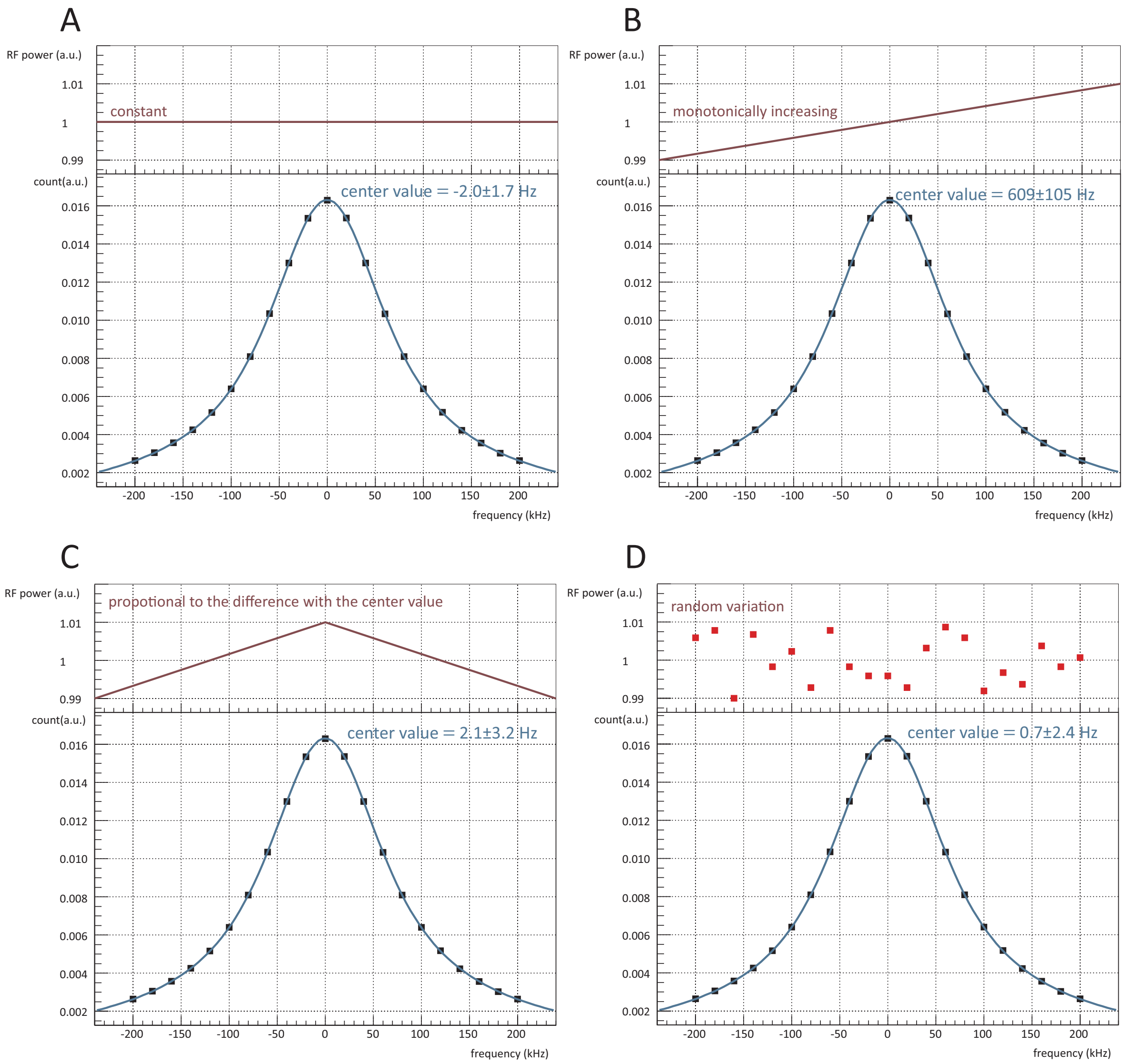

Figure 5.10: Relations between variations of RF power and systematic uncertainties. As shown in B, monotonically increasing of RF power within 1 % distort the resonance line shape. Due to this, the systematic uncertainty is 609 Hz. On the other hand, if the random sequence is used for the RF scanning as D, the systematic uncertainty is negligible.

RF field around the center of the axis is shown in color map C. In color map B, there is a dip caused by the widest area of a RF field of certain power.

Let‘s consider the case that tuning bar displace from 0 mm to 1 mm during a RF resonance scan. If the resonance lines are fitted by assuming a single RF field map, systematic uncertainty is 180 Hz. By assuming that the uncertainty from the fluctuation of RF field is proportional to the displacement of tuning bars, uncertainties are calculated as Table 5.4.

$\delta\nu_{12}$	4 Hz
$\delta\nu_{34}$	4 Hz
$\Delta\nu_{\mathrm{HF}}$	6 Hz
$\Delta\nu_{\mathrm{ZF}}$	4 Hz
μ_μ/μ_p	17 ppb

Table 5.4: Systematic uncertainty from RF field fluctuation

5.6 Gas pressure

Transition frequencies are changed by the variation of Hamiltonian through the collisions with Kr atoms. Since a collision rate is proportional to a density of the Kr gas, shifts of transition frequencies are expresses as

$$\nu_{ij}(P) = \nu_{ij}(0)(1 + a_{ij}P + b_{ij}P^2), \tag{5.9}$$

where $\nu_{ij}(0)$ is a transition frequencies in vacuum. Transition frequencies in vacuum can be extrapolated from values in certain gas pressures P_1 and P_2. Uncertainties from gas pressure is coming from both quadratic term ($b_{ij}P^2$) and a precision of a pressure gauge.

Quadratic coefficient b_{ij} is determined in a previous experiment as

$$b = (9.7 \pm 2.0)^{-15}\ \mathrm{Torr}^{-2}[62]. \tag{5.10}$$

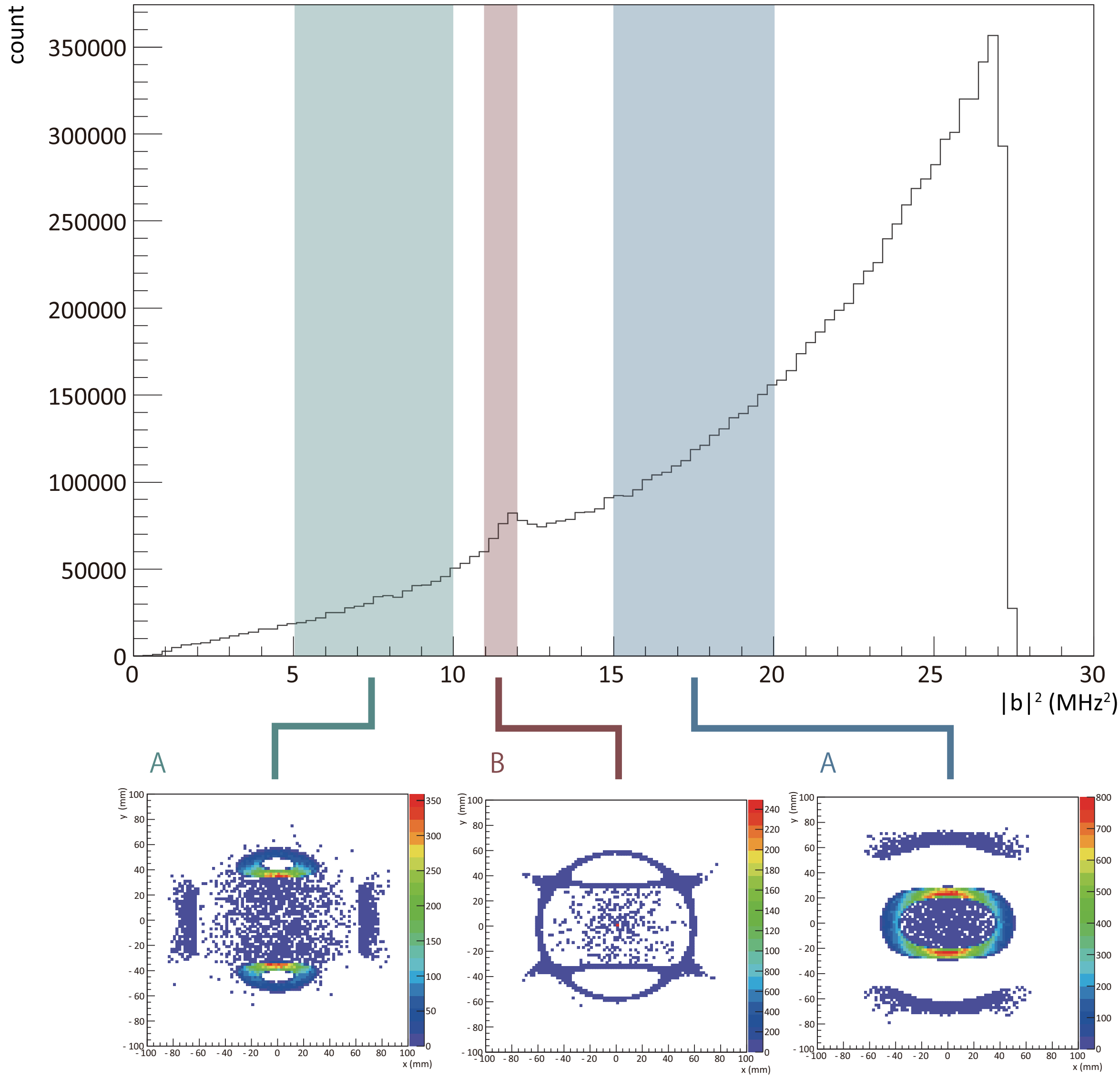

Figure 5.11: A histogram of RF power ($|b|^2$) in case the displacement of the tuning bar is 0 mm. The number of muons are 5.0×10^6 and RF fields are calculated by CST STUDIO[8]. Color maps shows a muonium distributions which feel certain range of the RF power.

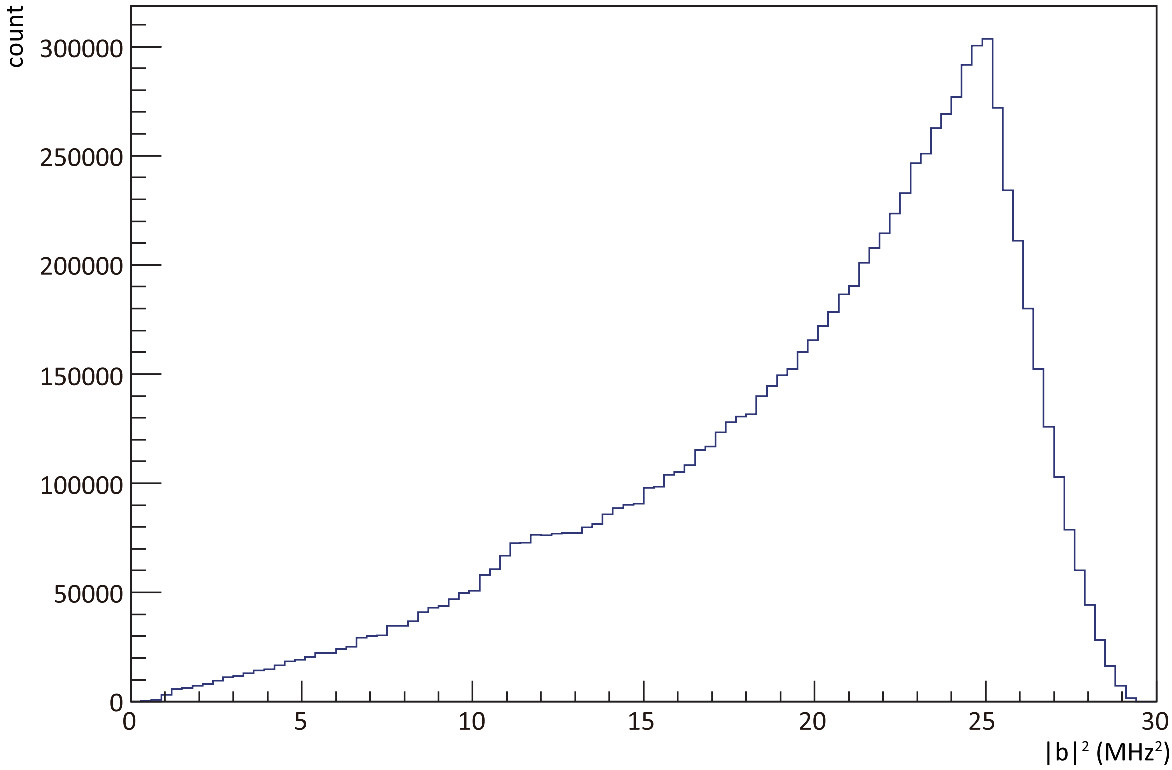

Figure 5.12: A histogram of RF power ($|b|^2$) in case the displacement of the tuning bar is 1 mm. The number of muons are 5.0×10^6 and RF fields are calculated by CST STUDIO[8].

The capacitance gauge (CANON ANELVA M-342DG-13) is prepared for the measurement. The precision of the gauge is 0.20 % of reading. Moreover, the silicon gauge (FLUKE RPM4-AD) is plan to prepare for the precise measurement. The precision of the gauge is 0.02 % of reading. Figure 5.13 shows a how the quadratic term and the precision of the gauge affect to an extrapolation. There are systematic uncertainties from a precision of pressure gauge and a quadratic shift.

Figure 5.14 shows a relation between P_2 and uncertainties. P_1 is fixed to 0.3 atm which is lower limit to stop muons in the cavity. It shows that the uncertainty from capacitance gauge is relatively large compared from the quadratic shift. Figure 5.15 is zoom up of Figure 5.14. It shows that the optimized P_2 value is about 0.9 atm in case of using a silicon pressure gauge.

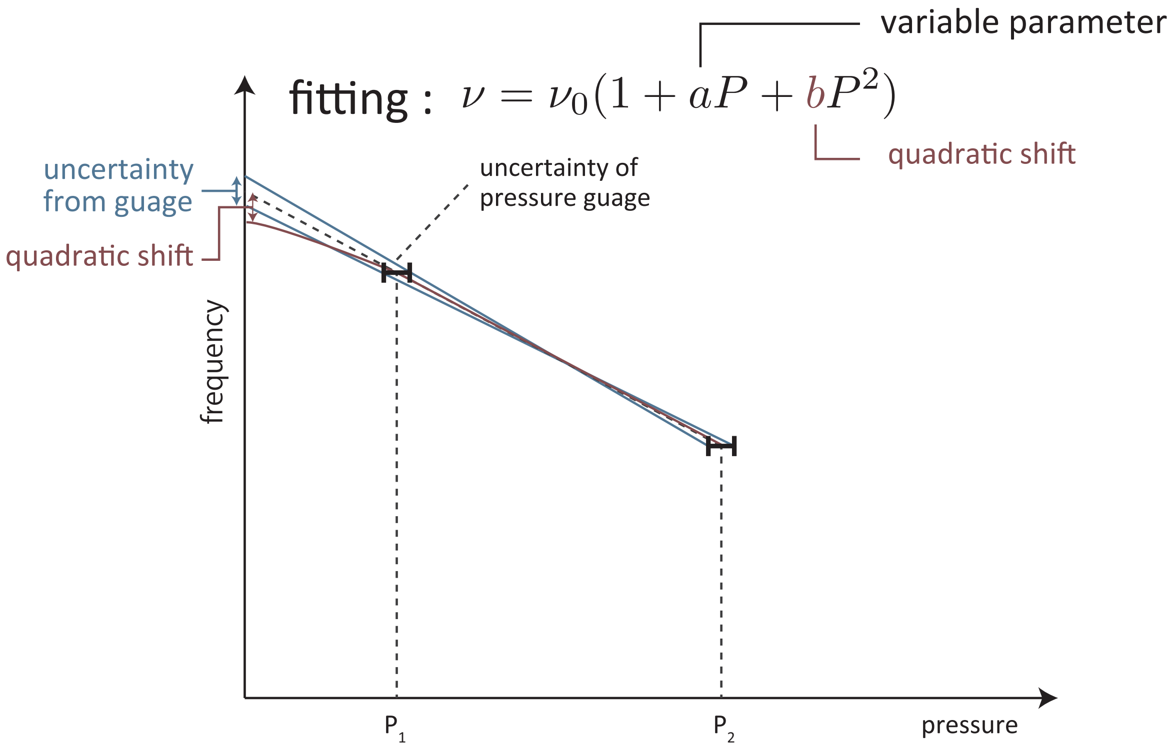

Figure 5.13: A relation between a gas pressures and transition frequencies. A transition frequency can be obtained by extrapolation using values in different gas pressures. There are systematic uncertainties from a precision of pressure gauge and a quadratic shift.

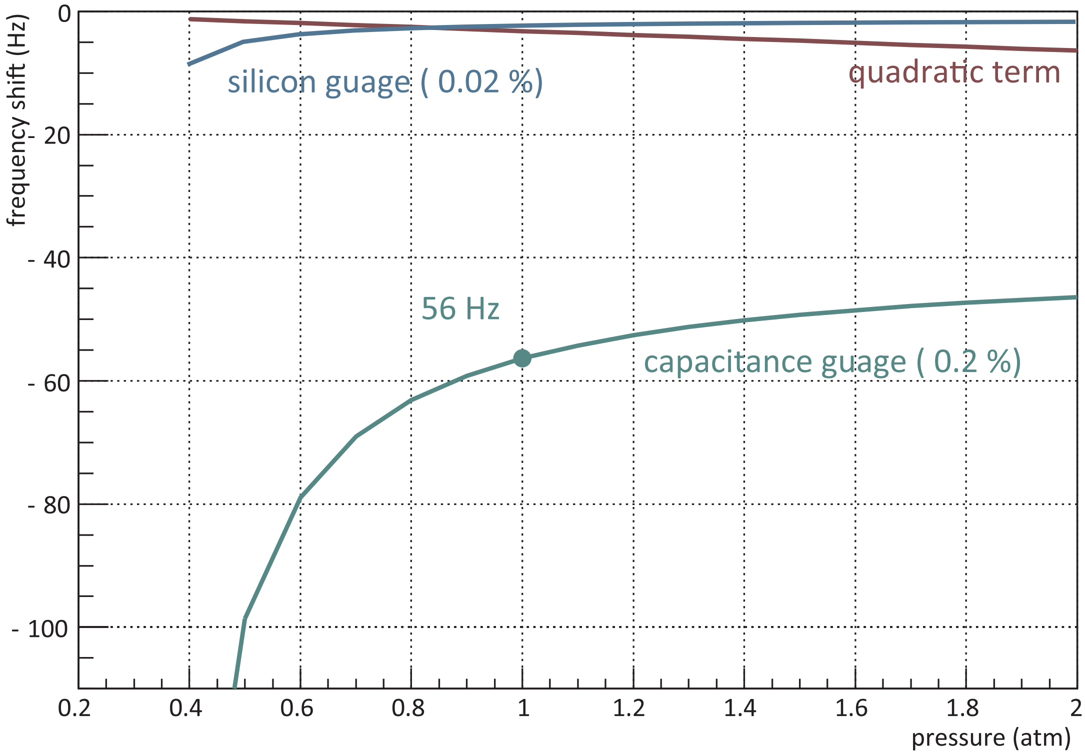

Figure 5.14: A relation between P_2 and uncertainties. P_1 is fixed to 0.3 atm which is lower limit to stop muons in the cavity with collision. The uncertainty from capacitance gauge is relatively large compared from the quadratic shift.

5.7 Temperature

Uncertainties from temperature results from two following parts (Figure 5.16). The first part is by atomic interaction with krypton gas. It was suggested that the shift results from a competition between the attractive-long-range (van der Waals) interaction decreases the electron density at the nucleus, and the repulsive-short-range (Pauli exclusion principle) part of the interatomic potential increases the electron density. This part gives vertical error bars to data points of Figure 5.16. In the case of collision between hydrogen and Argon gas, the shift is expressed as

$$(1/\nu_0)(\delta\nu/\rho) = A + B(T - T_0). \tag{5.11}$$

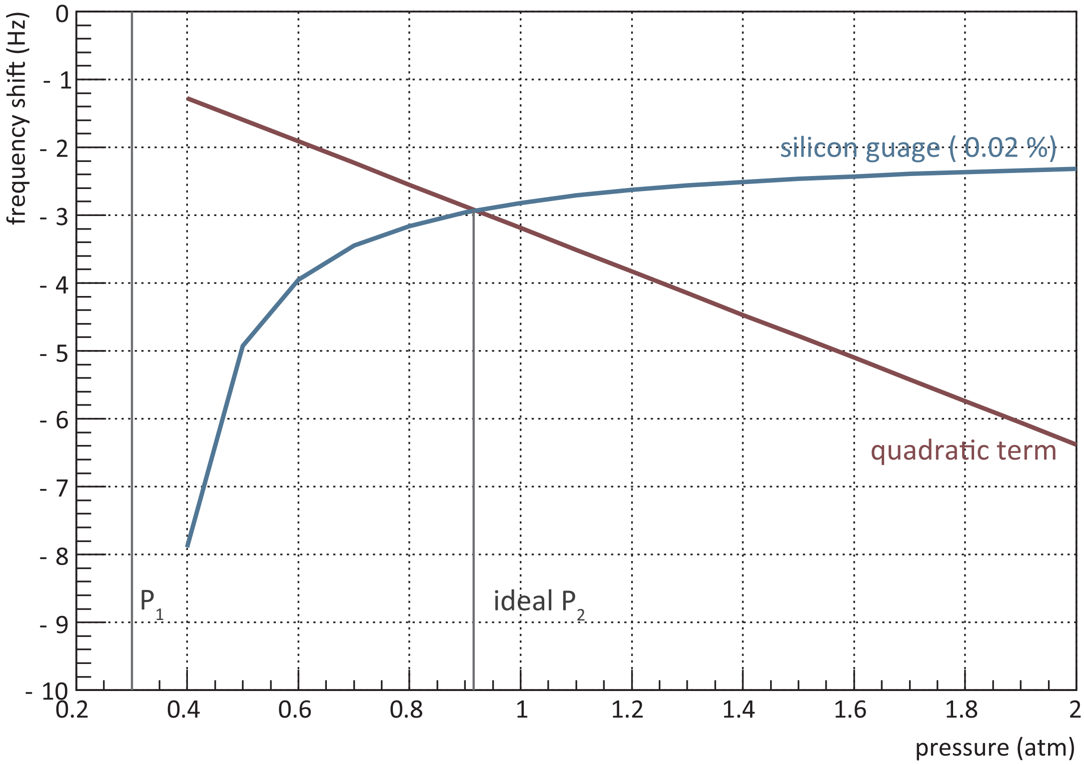

Figure 5.15: A zoom up of Figure 5.14. The optimized P_2 value is about 0.9 atm in case of using a silicon pressure gauge.

$\delta\nu_{12}$	4 Hz
$\delta\nu_{34}$	5 Hz
$\Delta\nu_{\mathrm{HF}}$	9 Hz
$\Delta\nu_{\mathrm{ZF}}$	9 Hz
μ_μ/μ_p	19 ppb

Table 5.5: Systematic uncertainty from gas pressure

A and B was obtained at Yale University [66] as

$$A = (-4.800 \pm 0.006) \times 10^{-9}\ \mathrm{Torr}^{-1}\ (0\ ^\circ\mathrm{C}), \tag{5.12}$$

$$B = (+0.956 \pm 0.011) \times 10^{-11}\ ^\circ\mathrm{C}^{-1}\mathrm{Torr}^{-1}\ (0\ ^\circ\mathrm{C}). \tag{5.13}$$

The secound part is from a variation of gas density by a temperature. We use pressures at 0 °C corresponded to gas densities calculated by monitored gas pressures and temperatrures. The pressure at 0 °C is calculated the real gas equation

$$(P + \frac{n^2 a_v}{V^2})(V - nb_v) = nRT. \tag{5.14}$$

The van der Waals constant are

$$a_v = 0.2325\ \mathrm{barL}^2/\mathrm{mol}, \tag{5.15}$$

$$b_v = 0.0396\ \mathrm{L/mol}[67]. \tag{5.16}$$

This part gives horizontal error bars to data points of Figure 5.16.

Figure 5.17 shows uncertainties of ν_{12} transition in high field experiment from density variation and atomic collision. Horizontal axis is the P_2 and P_1 is fixed to 0.3 atm. From this figure, the precision of the monitored temperature should be down to 0.01 K.

Stability of temperature in the chamber is achieved at the level of 0.1 K by both air circulation by air cooled chillers and water cooling surrounding the cavity. Both zero field and high field experiment, we plan to set 4 wires resistance temperature detectors and monitor at several points on the outer surface of the cavity. The precision of 0.01

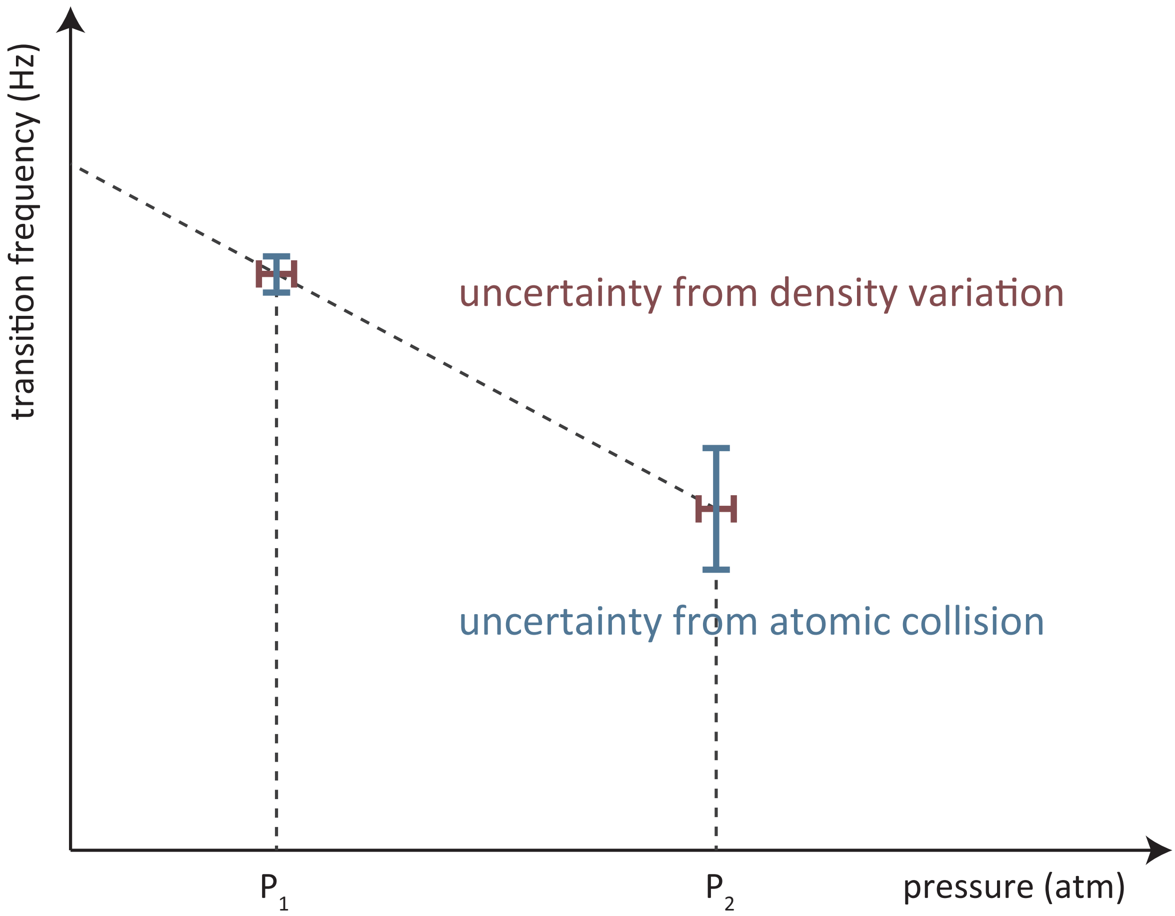

Figure 5.16: The uncertainty from temperature fluctuation has two sources, from density variation and from an atomic collision.

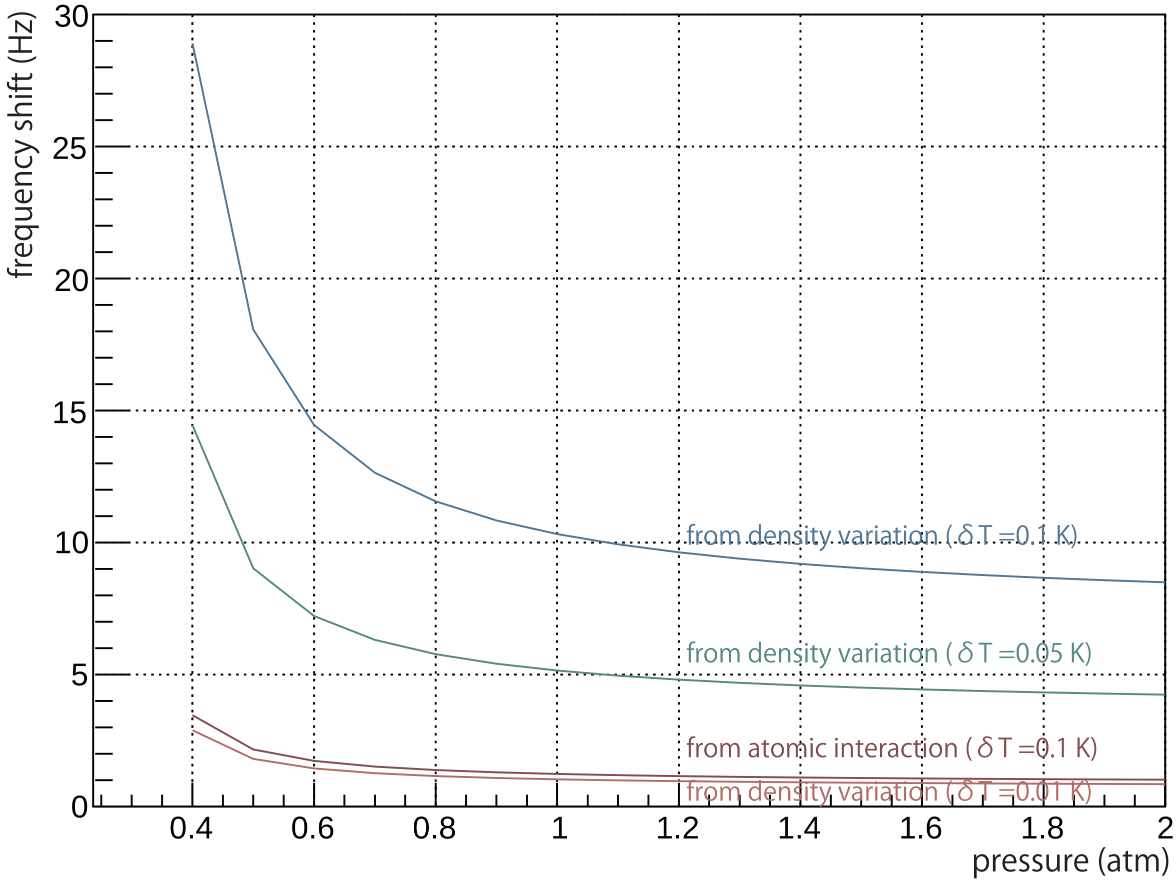

Figure 5.17: Frequency shifts from a density variation and an atomic interaction. Horizontal axis is the P_2 and P_1 is fixed to 0.3 atm.

K is enable by a commercial product such as CAB-F201, then the uncertainties from temperature can be summarized as Table 5.6.

$\delta\nu_{12}$	2 Hz
$\delta\nu_{34}$	3 Hz
$\Delta\nu_{\mathrm{HF}}$	4 Hz
$\Delta\nu_{\mathrm{ZF}}$	5 Hz
μ_μ/μ_p	11 ppb

Table 5.6: Systematic uncertainty from temperature

5.8 Muonium distribution

The muon stopping distribution is monitored by beam monitoring system. The 3-dimentional distribution can be obtained by TBPM at the precision of centimeter, the 2-dimentional projection is obtained by FBPM at the precision of millimeter (Subsection 4.10). The uncertainty from variation of muonium distribution during a RF frequency scan is estimated by using the simulation package. Figure 5.18 shows results of the estimation. In this estimation, the muonium distributions are assumed as gaussian of radial width is 3 cm and axial width is 6 cm from the result of the beam test (Subsection 4.10). According to this, the systematic uncertainty of a displacement of 1 mm in a radial direction is 4 Hz even in the worst case. Since RF field is uniform in an axial direction, the systematic uncertainty from displacement in an axial direction is negligible.

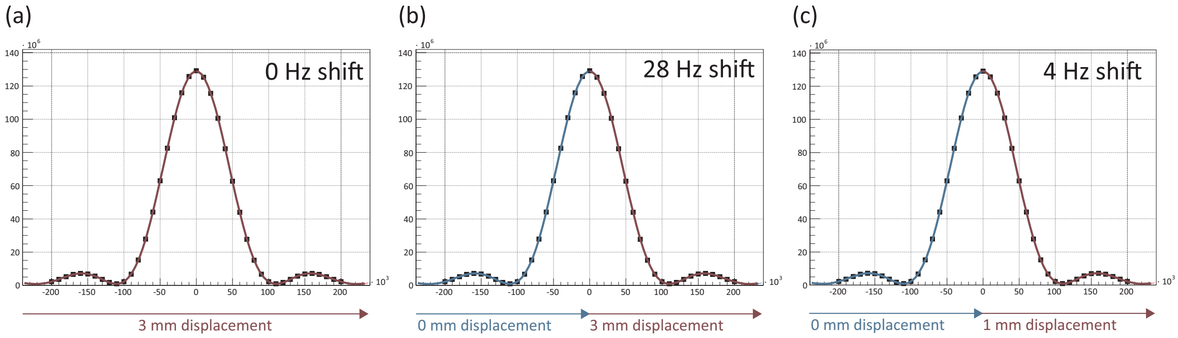

Figure 5.18: Results of the estimation in case of that (a) muonium distributions are constantly displaced of 3 mm in a radial direction, (b) muonium distributions are displaced of 3 mm in a radial direction at higher frequency than the center value, (c) muonium distributions are displaced of 1 mm in a radial direction at higher frequency than the center value.

$\delta\nu_{12}$	4 Hz
$\delta\nu_{34}$	5 Hz
$\Delta\nu_{\mathrm{HF}}$	9 Hz
$\Delta\nu_{\mathrm{ZF}}$	7 Hz
μ_μ/μ_p	127 ppb

Table 5.7: Systematic uncertainty from muonium distribution

5.9 Magnetic field

5.9.1 High field experiment

Dependence of a precision of magnetic probes

Magnetic field in the high field experiment is measured by NMR probe developed by K. Sasaki, Y. Ueno and T. Mizutani and others. (Subsection 4.12.1). We measure the NMR frequency not of free protons but of protons in a sample. The magnetic field at the location of the protons, H_p, deviates from the external field H_0,

$$H_p = (1 - \delta_t)H_0, \tag{5.17}$$

in which δ_t is the shielding constant expressed as

$$\delta_t = \sigma(H_2O) + \delta_b + \delta_p + \delta_s[68], \tag{5.18}$$

where $\sigma(H_2O)$ is from the internal diamagnetic shielding in the water molecule, δ_b is from bulk diamagnetism of the water sample which depends on the shape of the sample, δ_p is from paramagnetic impurities in the water sample, δ_s is from paramagnetic and diamagnetic materials nearby.

The value for $\sigma(H_2O)$ has been measured by comparing the NMR frequency of a spacial pure water sample with the frequency of a hydrogen maser in the same magnetic field as

$$\sigma(H_2O) = 25.680(25) \times 10^{-6}[69], \tag{5.19}$$

at a temperature $T = 25°\mathrm{C}$. The measured temperature dependence of σ is

$$\frac{\mathrm{d}\sigma(H_2O)}{\mathrm{d}t} = -10.36(30) \times 10^{-9}/°\mathrm{C}[70]. \tag{5.20}$$

Shape effect δ_b is improved from the previous experiment by using a cylindrical water container instead of spherical container. The value is estimated by OPERA[71] which is simulation software for magnetic field as -4.525 ppm.

Effect from paramagnetic impurities in the water sample δ_p can be neglected by using a ultra-pure water (Milli-Q by Merckmillipore).

Effects from paramagnetic and diamagnetic materials nearby are 0.08 ppb for Pyrex tube, 0.046 ppb cupper pipe, can be neglected for modulation coil.

On the other hand, the precision of the measured NMR frequency of 60 ppb is limited by the fitting to obtain the phase difference between the NMR signal and the signal of field modulation.

Dependence of a precision of field calculation

Magnetic field distributions after shimming are calculated by assuming certain number of magnetic moments surrounding the muonium distribution. The distribution is in good agreement with the result of magnetic field scan in a region of spheroid surface (z =380 mm, r= 140 mm) (Figure 5.19).

Dependence of a magnetic field distribution

As shown in Figure 5.19, the peak to peak fluctuation of the magnetic field is 1.3 μT of the region. The systematic uncertainty from the magnetic field distribution can be estimated from the histogram of magnetic field effect on muoniums (Figure 5.20). The result is

$$\Delta\nu_{12} = \pm 7 \text{ Hz}. \tag{5.21}$$

ν_{HF} is obtained by equation $\nu_{\text{HF}} = \nu_{12} + \nu_{34}$, thus the uncertainty of ν_{HF} is not depend on the absolute values of magnetic field in measurement of ν_{12} and ν_{34}.

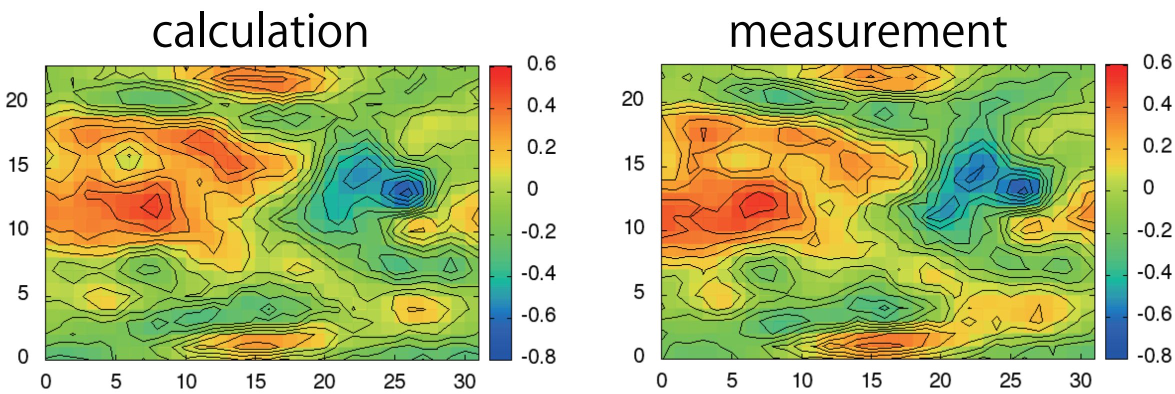

Figure 5.19: Comparison of magnetic field after shimming by calculation and measurement in a region of spheroid surface (z =380 mm, r= 140 mm).

5.9.2 Zero field experiment

Systematic uncertainty from a leakage magnetic field in a magnetic shield can estimate using a field maps by AMAZE simulation (Subsection 4.8.3) and muonium distribution. The systematic uncertainty from the analysis is

$$\Delta\nu = 9.7 \times 10^2 \pm 1.0 \times 10^2 \text{ Hz}. \tag{5.22}$$

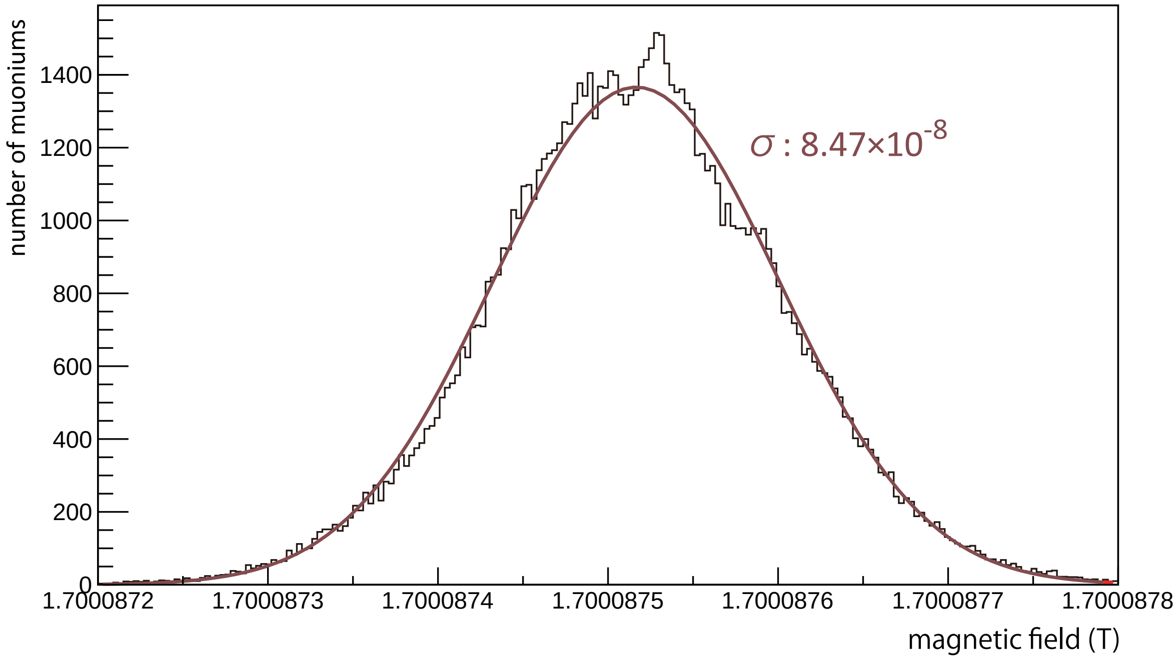

Figure 5.20: A histogram of magnetic field effect on muoniums. The number of the muons for each histograms is 10^9. The red line shows a result of Gaussian fitting and standard deviation is 8.47×10^{-8} T which correspond to 7 Hz frequency shift of ν_{12} transition.

To improve it, correction of using a scanning data of a magnetic field and Breit-Rabi formula (Equation 2.26, 2.27) is effective. Then, remained uncertainties from magnetic field is caused by dependence of a precision of fluxgate and a scan interval of magnetic fields (Figure 5.21).

Dependence of a scan interval of magnetic fields

If we adopt a nearest neighbor method to analyze a magnetic field from scanning result, there is a systematic uncertainty from a scan interval of magnetic fields. If both of scan interval of magnetic fields and muonium distributions are 30 mm, the uncertainty from the scan interval is

$$\Delta\nu = 19 \text{ Hz}. \tag{5.23}$$

Dependence of a precision of a fluxgate

Magnetic fields in the chamber are scanned by a fluxgate before measurements, and fixed monitored during measurements. The precision of fluxgate is 50 nT. The uncertainty from both the scan interval and the precision of a fluxgate is

$$\Delta\nu = 32 \text{ Hz}. \tag{5.24}$$

$\delta\nu_{12}$	11 Hz
$\delta\nu_{34}$	11 Hz
$\Delta\nu_{\mathrm{HF}}$	10 Hz
$\Delta\nu_{\mathrm{ZF}}$	32 Hz
μ_μ/μ_p	48 ppb

Table 5.8: Systematic uncertainty from magnetic field

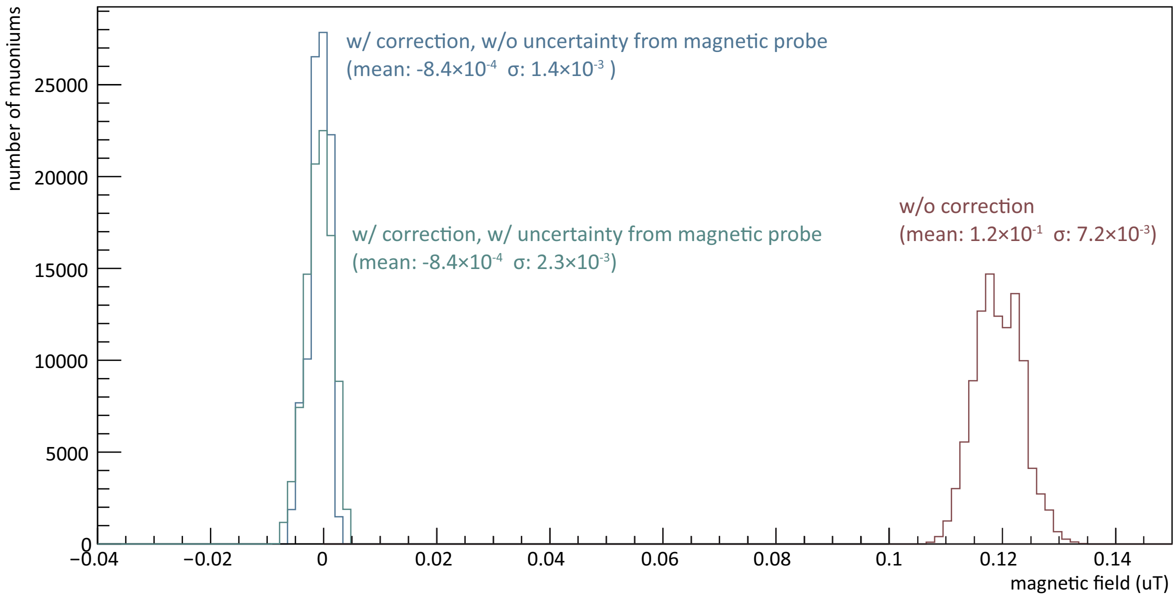

Figure 5.21: Histograms of magnetic field effect on muoniums. The number of the muons for each histograms is 10^9. The Red line shows a histogram without correction, the blue line shows a histogram with correction by the magnetic field scan data of 30 mm interval, but without 50 nT uncertainty from magnetic probe, the green line shows a histogram with correction and uncertainty from magnetic field. Without correction, The sub mG of magnetic field shift the transition frequencies of each muons. With correction by scanning results of the magnetic field improve the shift.

5.10 Summary of uncertainties

Figure 5.22 shows sources of uncertainty for the zero field experiment. Compared with the uncertainty of the latest experiment of 1400 Hz, this measurement can improve the experimental uncertainty by more than a factor of 10. On the other hand , Figure 5.23 shows sources of uncertainty for the high field experiment. it also improve the experimental uncertainty by a factor of 3 from the latest result at LAMPF.

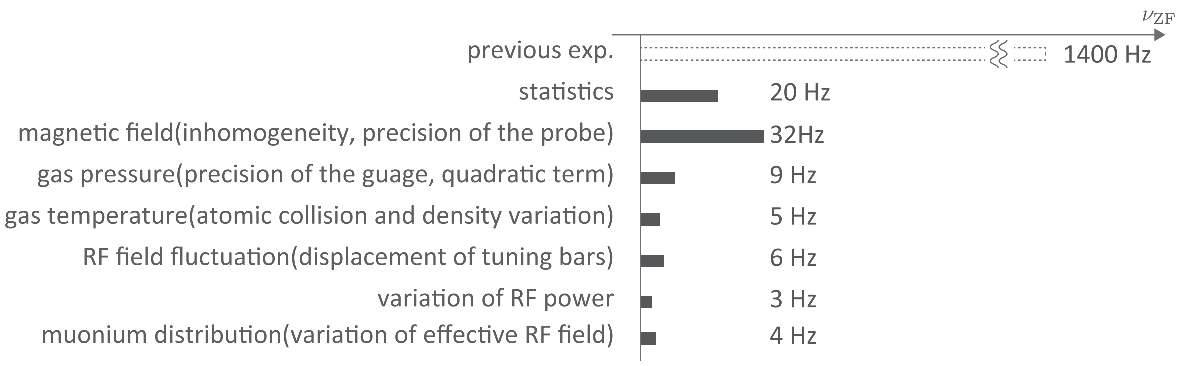

Figure 5.22: Sources of uncertainty for the zero field experiment(ν_{ZF}) are listed.

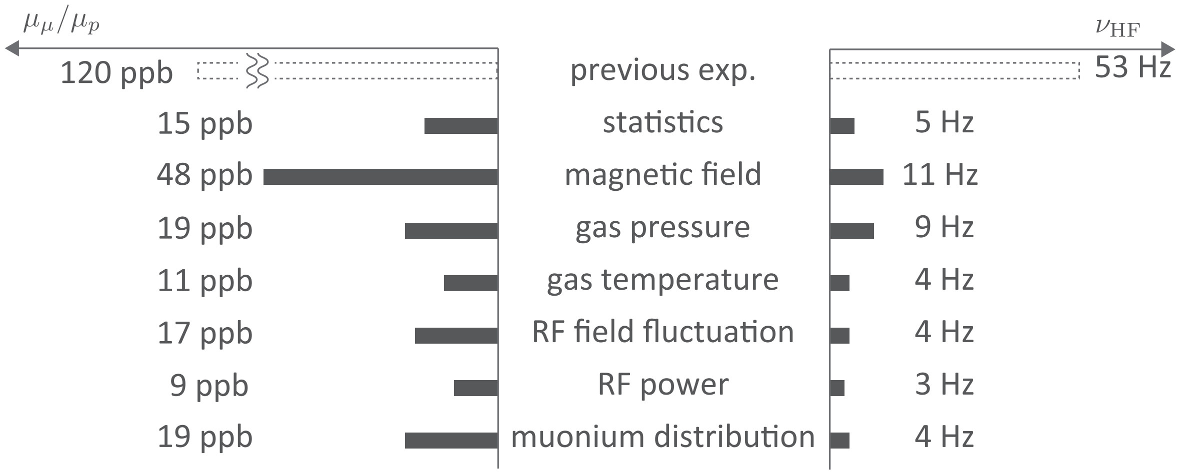

Figure 5.23: Sources of uncertainty for the high field experiment are listed. The left side of the figure shows a uncertainties of μ_μ/μ_p and right side shows a uncertainties of ν_{HF}.

Chapter 6

Discussion and conclusion

6.1 Current Status of the experiment

As described in Chapter 4, the apparatuses for experiments both in zero field and in high field have been constructed fully. As demonstrated in the discussion in Chapter 5, we are confident that all systematic uncertainties are well under control, and one day of beam time at J-PARC MUSE will supersede the precision of latest measurement of muonium HFS in a zero magnetic field. One week of beam time will supersede the precision in a high magnetic field. We had a plan to carry out the zero-field experiment at MUSE D Line in last November, but the beam time was aborted because of a trouble in J-PARC accelerator complex. We envisage the resumption of the experiment in early 2016 after restoration of the delivery of muon beams. The first beam at H Line is expected in late fiscal year 2016. The preparation of the high-field experiment is under way so that we can start the experiment right after the completion of the beam line.

6.2 Future prospects

Two possibilities are currently being considered to improve the systematic uncertainties of the experiment. One possibility is to measure both ν_{12} and ν_{34} transitions in a so-called “magic field”, which is about 1.137 T. Under this magnetic field, the magnetic

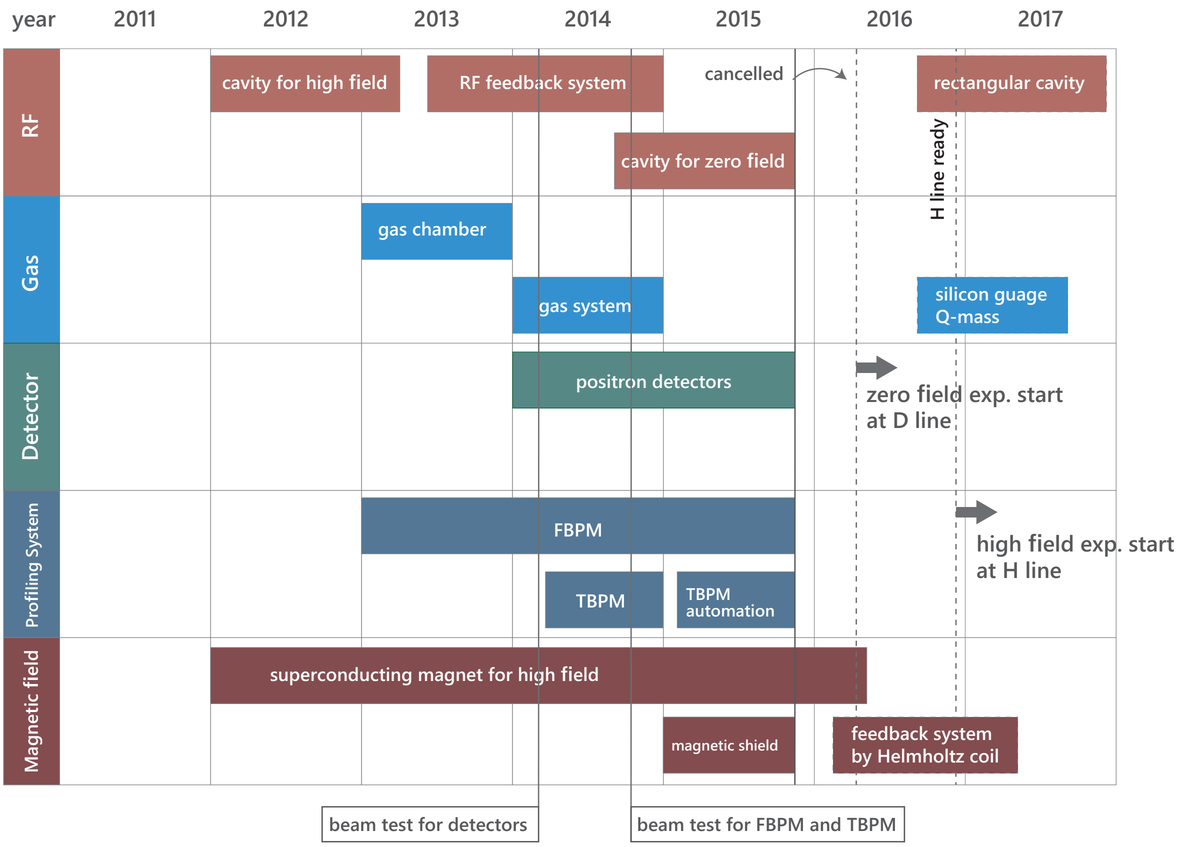

Figure 6.1: A road map of the experiment. Zero field experiment will be start in 2016 and high field experiment in 2017.

field dependences of both ν_{12} and ν_{34} becomes negligible (See Figure 6.2), thus the uncertainty on $\frac{\mu_\mu}{\mu_p}$ from the uncertainty of the field strength disappears as shown in Equation 2.26 and 2.27. We are currently designing a rectangular cavity which have two resonance frequencies which match ν_{12} and ν_{34}, because cylindrical cavities like the one described in Section 4.1 cannot have satisfying resonance modes. Figure 6.3 shows electric fields and magnetic fields of the TM120 and TM210 mode of the rectangular cavity(The TM mnp mode in a rectangular cavity is characterized by three subscripts m, n and p that corresponding to the number of half wave variations in x, y, z). Thus resonance frequencies of TM120 and TM210 can be tuned for both nu_{12} and ν_{34} transition frequencies by adjusting the length and width of the cavity.

If successful, we plan to measure the frequencies under the magic field after the high field experiment. Another possibility is use a mixture of krypton and helium gases as the target to reduce the uncertainty due to the pressure shift. According to a study, the pressure shift of hyperfine splitting of hydrogen atom in helium gas is

$$a_{He} = +3.7 \times 10^9 \text{ mmHg}^{-1}[72], \tag{6.1}$$

which is positive, while the frequency shift in krypton is negative. If the pressure shift for muonium atom is also positive in helium, there is a possibility that by mixing krypton and helium, we can eliminate the pressure shift. Helium is a rare gas, so that depolarization of muonium due to interaction with helium atom is negligible. There is no previous report of pressure shift for muonium atom in helium, so we are currently investigating theoretical models, and possibility to measure it by ourselves.

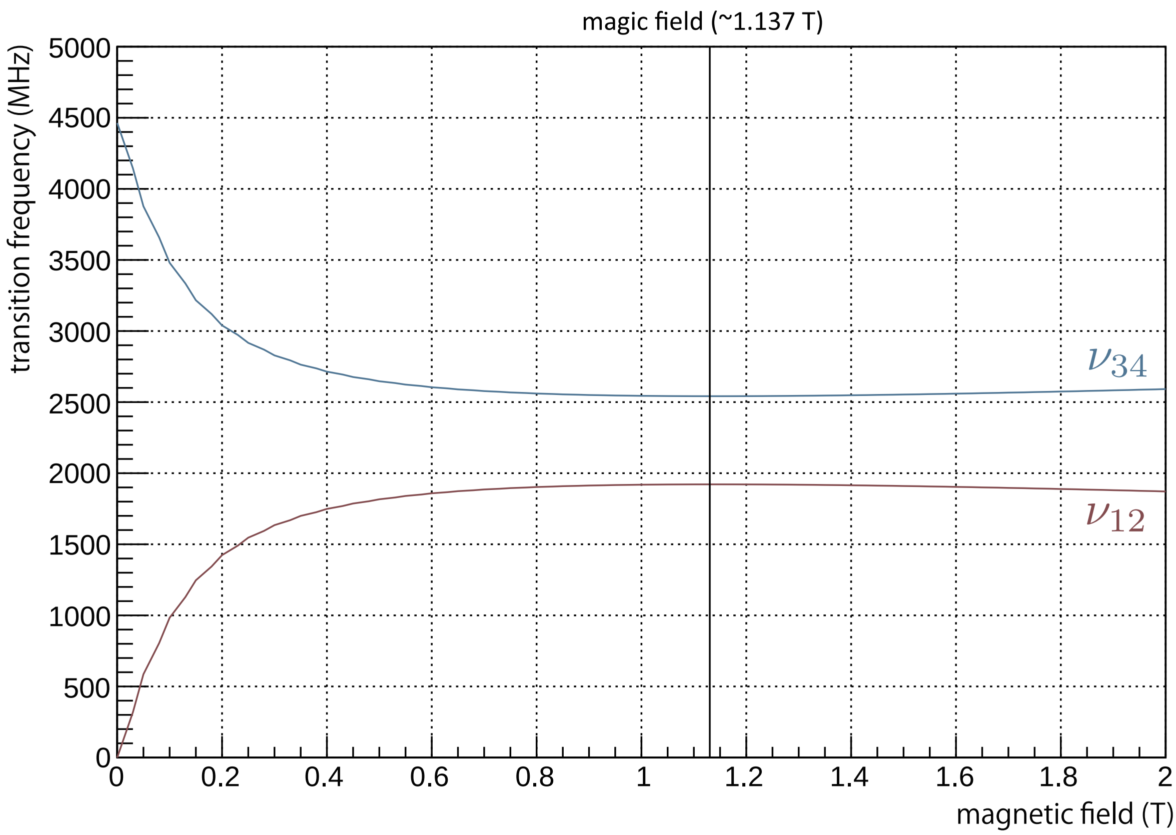

Figure 6.2: A relation between ν_{ij} and a magnetic field. In magic field, measured ν_{ij}(H) is independent to field changes δB.

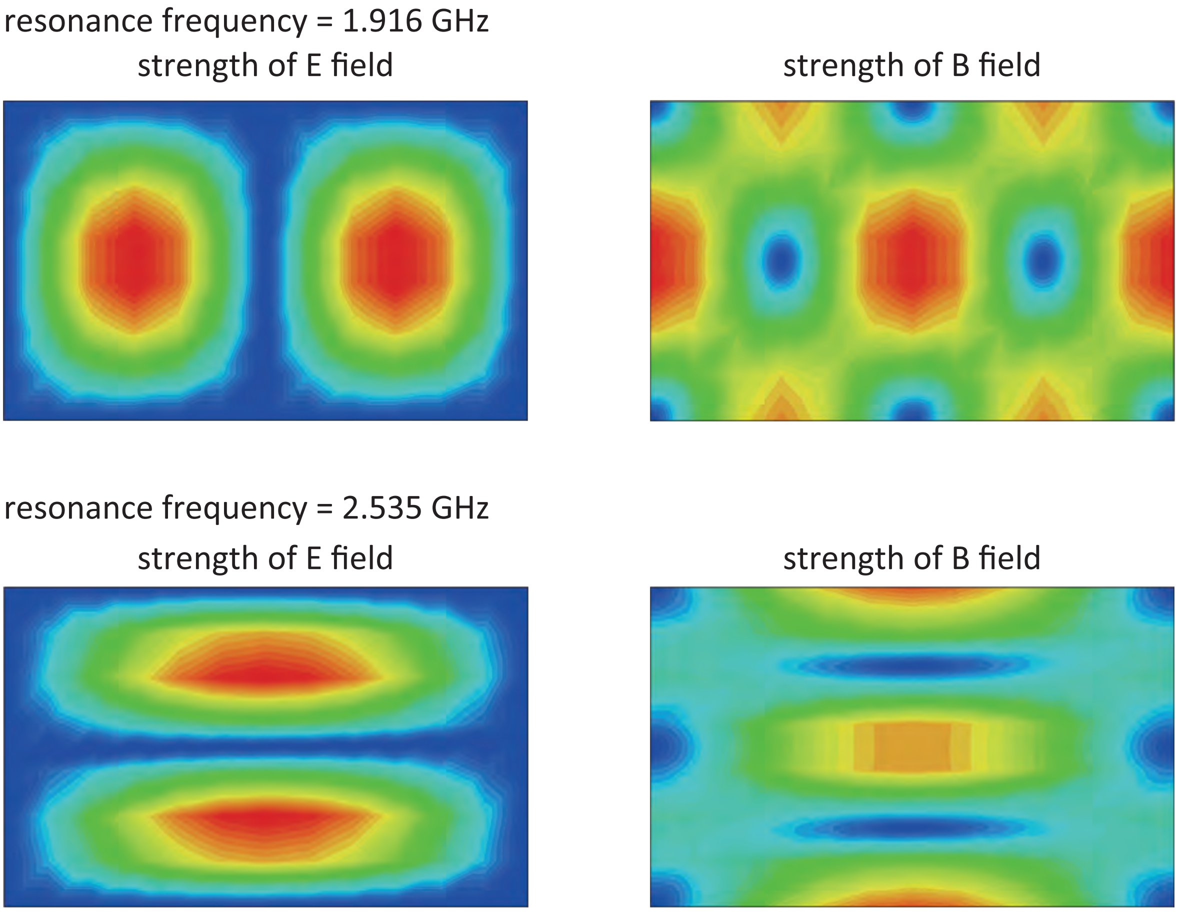

Figure 6.3: Electric fields and magnetic fields of the TM120 and TM210 mode of the rectangular cavity. the length of the cavity is 205 mm and the width is 123 mm to adjust both resonance frequencies of the TM120 and the TM210 to nu_{12} and ν_{34} transition frequencies at 1.137 T magnetic field.

Appendix A

RF fields of the TM110 mode and the TM210 mode

The amplitudes of the microwave electromagnetic field in the cavity are

$$H_r = -H_{110}\frac{J_1(x_{11}\frac{2r}{D})}{x_{11}\frac{2r}{D}}\sin\phi, \tag{A.1}$$

$$H_\phi = -H_{110}J_1'(x_{11}\frac{2r}{D})\cos\phi, \tag{A.2}$$

$$E_z = E_{110}J_1(x_{11}\frac{2r}{D})\cos\phi. \tag{A.3}$$

for the TM110 mode and

$$H_{1r} = -H_{210}\frac{2J_2(x_{21}\frac{2r}{D})}{x_{21}\frac{2r}{D}}\sin 2\phi, \tag{A.4}$$

$$H_{1\phi} = -H_{210}J_2'(x_{21}\frac{2r}{D})\cos 2\phi, \tag{A.5}$$

$$E_z = E_{210}J_2(x_{21}\frac{2r}{D})\cos 2\phi. \tag{A.6}$$

for the TM210 mode, in which H_{mnp} and E_{mnp} are amplitude, r is the radial coordinate and ϕ is the azimuthal angle measured with respect to the position of the input loop.

The microwave power spatial distribution is proportional to

$$H_1^2(r,\phi) = H_{1r}^2(r,\phi) + H_{1\phi}^2(r,\phi). \tag{A.7}$$

and Figure A.1 (A.2) and shows a radial cross sectional view of microwave power of the TM110 (TM210) mode.

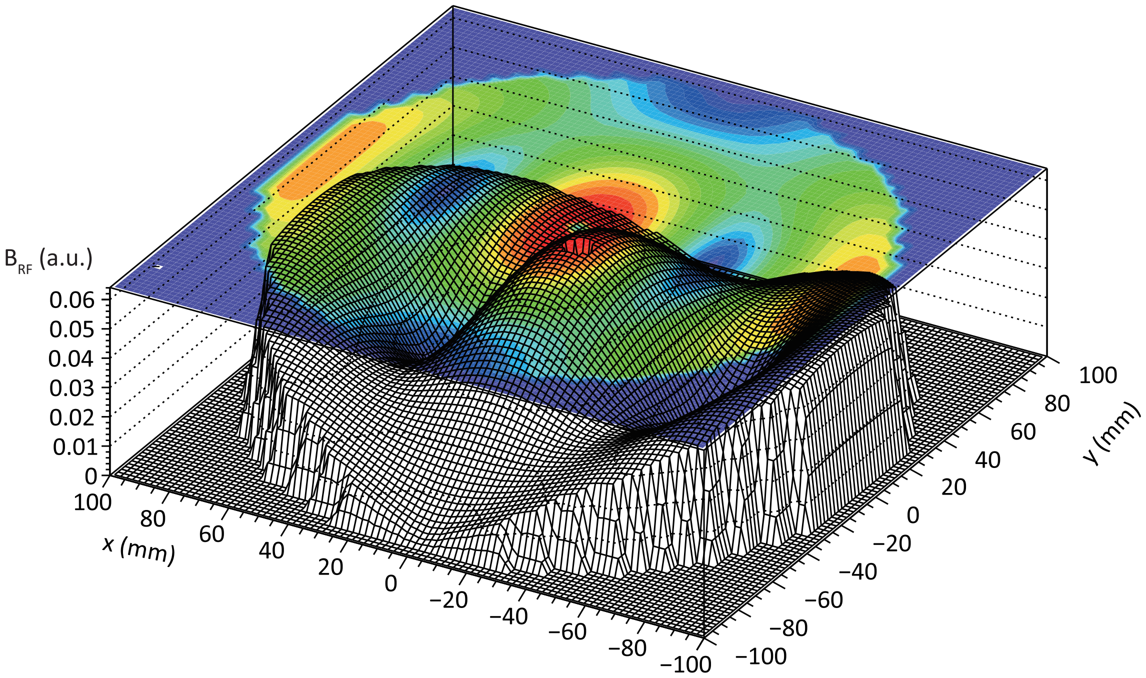

Figure A.1: Radial cross sectional view of microwave power of the TM110 mode.

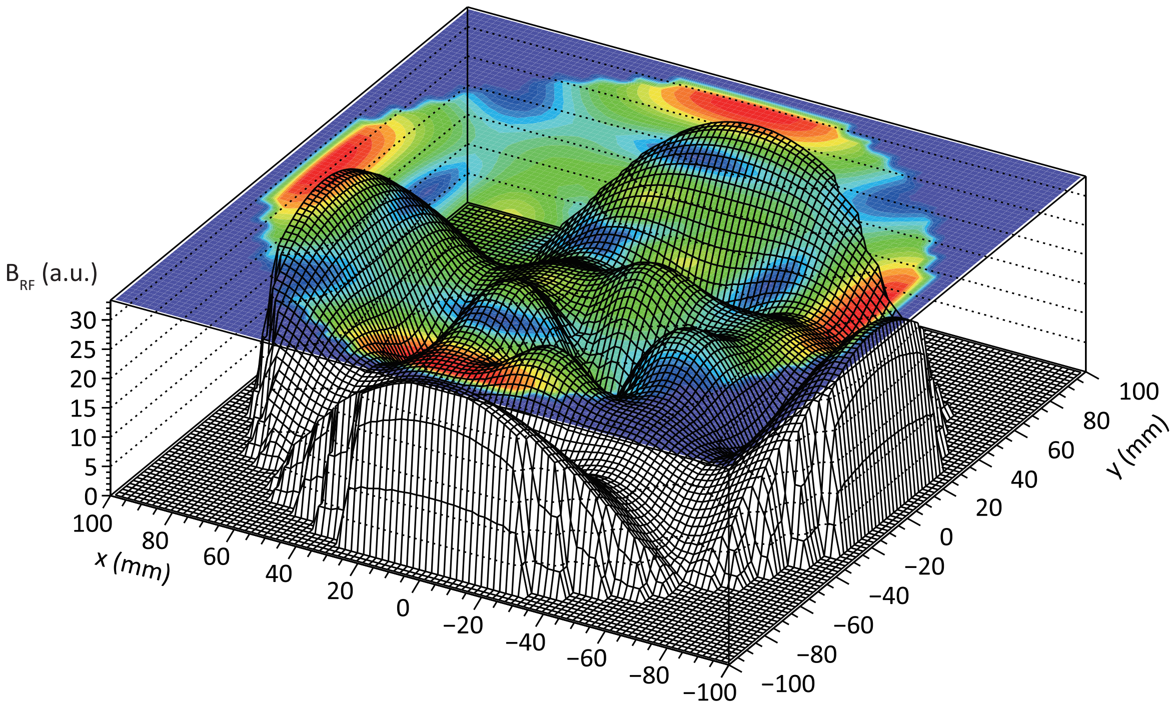

Figure A.2: Radial cross sectional view of microwave power of the TM210 mode.

Appendix B

Network Analyzer

A network analyzer is used for monitoring RF power in the cavity. It measures a reflecting and transmitting power as S-parameter. Frequency range of the network analyzer is 5 Hz to 3 GHz which is enough for this measurement. The input power is set to -10 dBm.

S-parameter

The S-parameter of 2-port network is expressed as

$$\begin{pmatrix} b_1 \\ b_2 \end{pmatrix} = \begin{pmatrix} S_{11} & S_{12} \\ S_{21} & S_{22} \end{pmatrix} \begin{pmatrix} a_1 \\ a_2 \end{pmatrix}, \tag{B.1}$$

where a_n is normalized amplitude of incident wave and b_n that of exiting wave defined as

$$a_i = \frac{V_{Ii}}{\sqrt{Z_R}}, \tag{B.2}$$

$$b_i = \frac{V_{Ri}}{\sqrt{Z_R}}. \tag{B.3}$$

where V_{Ii} is a voltage wave incident on each port, V_{Ri} is a voltage wave reflected from each port and Z_R is a reference impedance. In most cases including this network analyzer, the reference impedance is set to 50 Ω.

S_{mn} represent

- S_{11}: reflection coefficient of input port,
- S_{12}: reverse voltage gain,
- S_{21}: forward voltage gain,
- S_{22}: reflection coefficient of output port.

The measurement using network analyzer takes two steps. At first, input antennas should be tuned for resonance frequencies. It is taken as synonymous with that an input impedance is equivalent to reference impedance at resonance frequencies. Using Equation B.1, B.2 and B.3, the cavity impedance is described as

$$Z_I = Z_R \frac{1 + S_{11}}{(1 - S_1)}, \tag{B.4}$$

where Z_I is a input impedance and Z_R is a reference impedance. Thus coupling of input port is able to confirmed by S_{11}.

Secondly, RF power in the cavity is monitored S_{21} by RF input and output ports. RF power in the cavity is usually expressed as a Q factor which is described in Section B. When a input port couple to the cavity, the Q factor of the cavity is equivalent to Q_{ext} which is described in Section B [73]. Thus RF power in the cavity can be monitored by S_{21}.

Quality factor

Q factor is defined by two ways: in terms of the ratio of the energy and in terms of bandwidth.

Defined in terms of the ratio of the energy

RF energy stored in the cavity is expressed by a Quality factor (Q factor). It is defined as

$$Q = \frac{\omega_0 W}{P}, \tag{B.5}$$

where ω_0 is the resonance frequency, W is the energy stored in the cavity and P is the energy loss rate per unit time from the cavity. Designing the high Q cavity is same meaning as minimization of power losses in the cavity.

There are several types of Q factors:

- unloaded Q (Q_0),
- conductive Q (Q_c),
- external Q (Q_ext),
- dielectric Q(Q_d),
- loaded Q (Q_L).

where Q_c is result from the power loss in the walls which have finite conductivity. The absorbed power due to surface losses is calculated as

$$P_\mathrm{c} = \frac{1}{2}\sqrt{\frac{\pi\mu f}{\sigma}}\int |H|^2 \partial S, \tag{B.6}$$

where σ is the surface current density and f is the resonance frequency. Since the dominant part of the P_c is from the surface current flow between the components of the cavity, joint strength of them is important for high Q factor.

Q_ext is result from power loss through unclosed surfaces (holes) of the cavity. In case of our cavity, there are RF input and output ports and the ports for tuning bars as unclosed surfaces. To avoid the power loss, coupling of the input port which transports RF power should be strong, but the coupling of other RF ports should be weak and the size of the ports for tuning bars should be small as far as possible.

Q_d is result from the power loss in the lossy dielectric material which is described as

$$P_\mathrm{d} = \pi f \tan\delta \epsilon_0 \epsilon_r \int |E|^2 \partial V, \tag{B.7}$$

where ϵ_0 is the vacuum permittivity, ϵ_r is the electric permittivity and $\tan\delta$ is the dielectric tangent (see Section 4.1.5). This equation indicates that the power loss caused by the dielectric material depends on the dielectric tangent, the electric permittivity and the volume of the material. Since the sweep range of the tuning bar depends electric permittivity and the volume the material but not the dielectic tangent, a material which has low dielectirc tangent is good for Q factor.

Unloaded Q (Q_0) which is contained Q_{d} and Q_{c} but excluded Q_{ext} can be found as

$$\frac{1}{Q_0} = \frac{1}{Q_c} + \frac{1}{Q_d} \text{ [58]}. \tag{B.8}$$

Loaded Q (Q_{L}) contained all parts of Q factor can be found as

$$\frac{1}{Q_{\mathrm{L}}} = \frac{1}{Q_{\mathrm{c}}} + \frac{1}{Q_{\mathrm{ext}}} \text{ [58]}. \tag{B.9}$$

Thus the energy loss in the cavity is caused by the combination of the surface current on the cavity, microwave absorption by the dielectric material and the power loss through unclosed surfaces of the cavity.

Defined in terms of bandwidth

The other common definition of the Q factor is in terms of bandwidth. RF cavity can be regard as a parallel RLC circuit. A voltage of the parallel RLC circuit is expressed as

$$V(t) = \frac{1}{[R^{-2} + (\omega C - 1/(\omega L))^2]^{1/2}} \exp j(\omega t - \phi). \tag{B.10}$$

P is defined as

$$P = \frac{V^2}{R}. \tag{B.11}$$

According to B.10 and B.11,

$$P = \frac{1}{2}\frac{RV^2}{R^2 + (\omega L - 1/(\omega C))^2}. \tag{B.12}$$

When the consumption energy P is equivalent to half of consumption energy at the resonance point, the following equation holds;

$$\frac{RV^2}{2(R^2 + (\omega L - 1/(\omega C))^2} = \frac{V^2}{4R}. \tag{B.13}$$

FWHM (full width at half maximum) $\Delta\omega$ is calculated by ω_1 and ω_2 satisfy B.13,

$$\Delta\omega \quad = \omega_2 - \omega_1 \tag{B.14}$$

$$= \sqrt{C/L}R\omega_0 \quad = \frac{\omega_0}{Q}. \tag{B.15}$$

Thus Q factor also expresses a FWHM of a RF cavity. As mentioned Section B, Q_L of the cavity is equivalent to Q_{ext} when the cavity and a input port is coupled. The reason is that main part of Q_{ext} is result from the output port, Q_L is able to obtained by a FWHM of a S_{21}.

Calibration of Network Analyzer

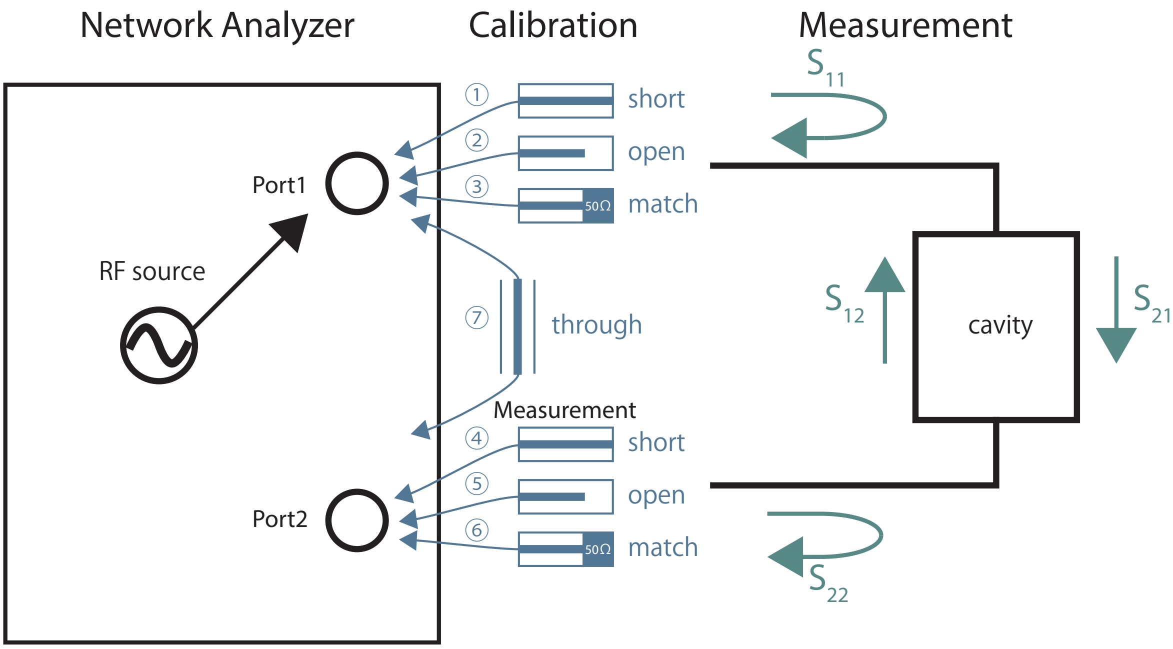

Figure B.1: A process of TOSM calibration and the measurement of S-parameter using the network analyzer.

Network analyzer can be plagued by three types of errors:

1. Systematic errors,
2. Random errors,
3. Drift errors.

And there are 6 types of systematic error:

1. Directivity and crosstalk errors relating to signal leakage,
2. Source and load impedance mismatches relating to reflections,
3. Frequency response errors caused by reflection and transmission tracking within the test receivers.

For preventing these errors, network analyzer should be calibrated each time measuring condition is changed. Random errors vary randomly as a function of time. Main contributor is noises of instruments. It is not solved by calibration. Drift errors occur mainly by variation of temperature and can be reduced by constant recalibration.

TOSM (Through-Open-Short-Match) calibration is a typical type of calibration to determine the 6 systematic error terms for each signal direction. It measures the open, short, and match one port standard on both ports and the through between them (see Figure B.1).

1. Open: Transmission line terminated with open. A reflected voltage keeps in phase with an incident voltage.

2. Short: Transmission line terminated with short. A reflected voltage is opposite phase with an incident voltage.

3. Match: Transmission line terminated with reference impedance. All the incident power is absorbed in the load.

4. Through: Transmission line connected port1 and port2 directly. Through is calibrate an amplitude and phase variation of transmission characteristic.

Appendix C

CST microwave studio

Unlike an ideal cylindrical cavity, simulation using finite element method is needed to evaluate the cavity considering a structure of RF ports and tuning bars. CST microwave studio [8] is a one of such software for the 3D EM simulation of high frequency components. There are several solvers are available. Among them, following two solvers are mainly used.

C.1 Overview of solvers

C.1.1 Eigenmode Solver

The Eigenmode Solver is dedicated to the simulation of closed resonant structures. It is for estimate the electromagnetic field of resonance modes and Q factor (see Chapter B).

C.1.2 Frequency Domain Solver

The general purpose Frequency Domain Solver solves the problem for a single frequency at a time, and for a number of adaptively chosen frequency samples in the course of a frequency sweep. The solution comprises the field distribution as well as the S-parameters (see Appendix B) at the given frequency so that it is appropriate solver for compared with the line shapes of S-parameter obtained from network analyzer (see Appendix B).

C.2 Dependence of number of mesh

Figure C.1 shows resonance frequencies in a simulation with a different numbers of mesh. Mesh views are shown in Figure C.2. According to both figrures, simulation results with less than about 10^5 meshes are not consistent with measurement, since small components such as RF antennas can not be considered.

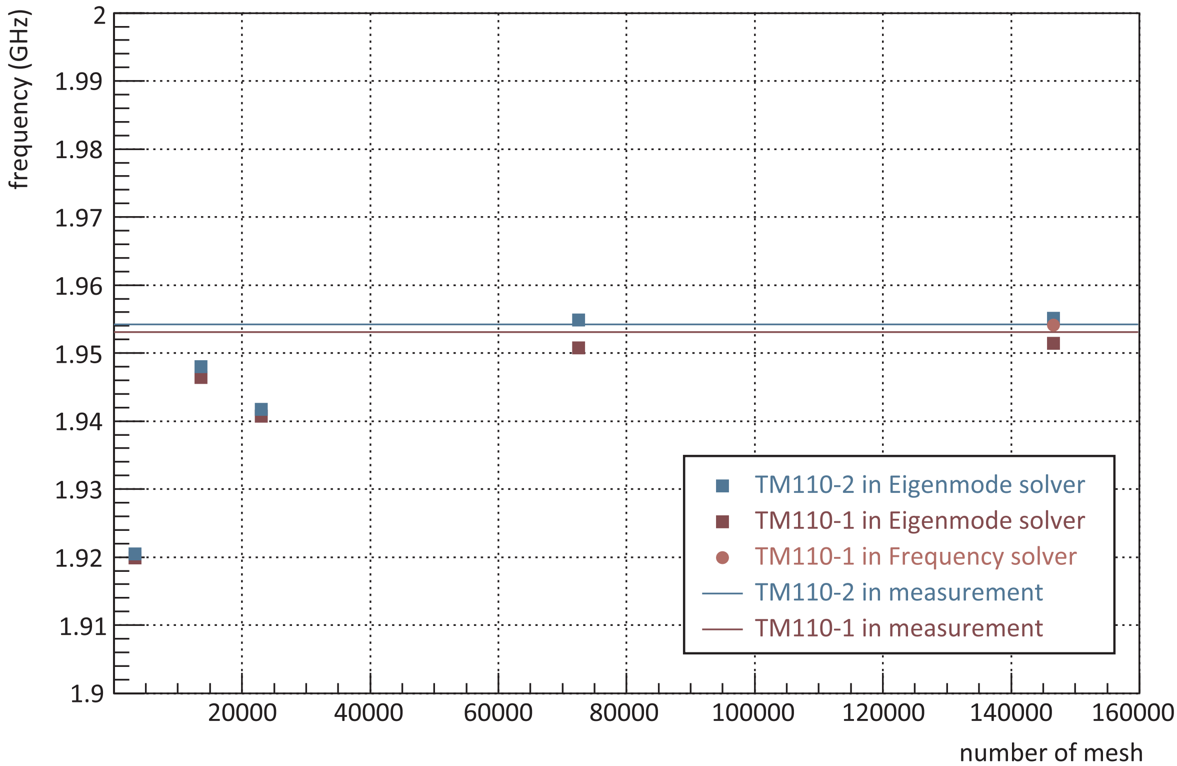

Figure C.1: Resonance frequencies in a simulation with a different numbers of mesh.

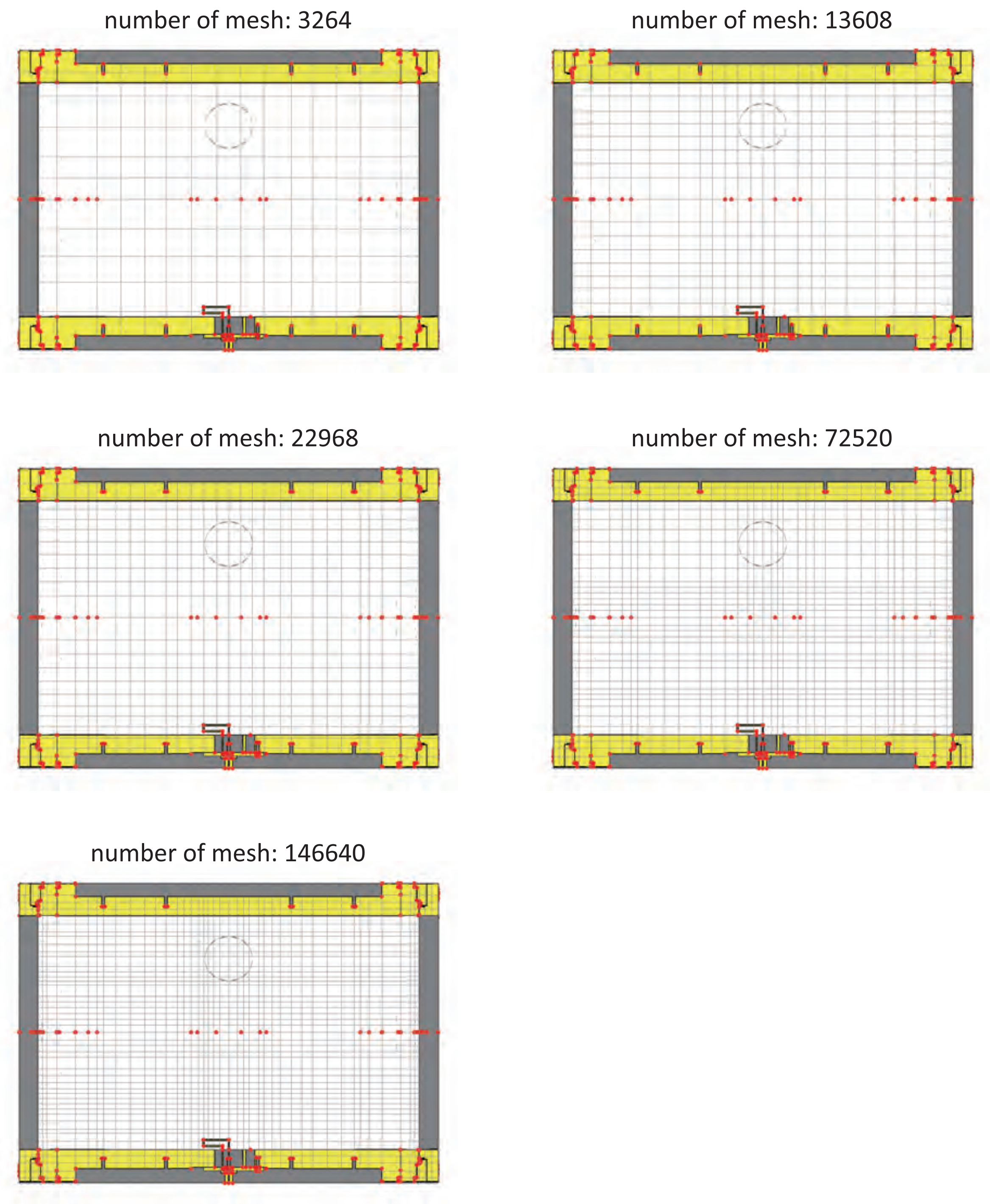

Figure C.2: Mesh views with different numbers of mesh. The geometry is imported from Autodesk Inventor Professional.

Bibliography

[1] P. J. Mohr, B. N. Taylor, and D. B. Newell. CODATA recommended values of the fundamental physical constants: 2010. *Reviews of Modern Physics*, 84:1527–1605, Nov 2012.

[2] K. Hagiwara, R. Liao, A. D. Martin, D. Nomura, and T. Teubner. $(g-2)_\mu$ and $\alpha(M_Z^2)$ re-evaluated using new precise data. *Journal of Physics G*, 38:085003, 2011.

[3] V. W. Hughes, M. G. Perdekamp, D. Kawall, W. Liu, K. Jungmann, and G. z. Putlitz. Test of CPT and Lorentz Invariance from Muonium Spectroscopy. *Physical Review Letters*, 87:111804, Aug 2001.

[4] W. Liu, M. G. Boshier, S. Dhawan, O. v. Dyck, P. Egan, X. Fei, M. Grosse Perdekamp, V. W. Hughes, M. Janousch, K. Jungmann, D. Kawall, F. G. Mariam, C. Pillai, R. Prigl, G. z. Putlitz, I. Reinhard, W. Schwarz, P. A. Thompson, and K. A. Woodle. High Precision Measurements of the Ground State Hyperfine Structure Interval of Muonium and of the Muon Magnetic Moment. *Physical Review Letters*, 82:711–714, Jan 1999.

[5] N. Kawamura, K. Ninomiya, H. Fujimori, Y. Kobayashi, K.Nishiyama, and Muon Sci. Sec. Improvement of Muon Beam Transport at D-line. *KEK-MSL Progress Report 2010*, 2011.

[6] N. Kawamura, MuHFS collab., DeeMe collab., and g-2/EDM collab. Present Status of the H-Line. *MLF ANNUAL REPORT 2013*, 2014.

[7] https://geant4.web.cern.ch/geant4/.

[8] http://www.cst.com/.

[9] V.W.Hughes and G. Putlitz. *Quantum electrodynamics*. Advanced series on directions in high energy physics. World Scientific, 1990.

[10] D. G. Fleming, R. J. Mikula, and D. M. Garner. μ^+ charge exchange and muonium formation in low-pressure gases. *Physical Review A*, 26:2527–2544, Nov 1982.

[11] R. M. Mobley, J. J. Amato, V. W. Hughes, J. E. Rothberg, and P. A. Thompson. Muonium Chemistry II. *The Journal of Chemical Physics*, 47(8):3074–3075, 1967.

[12] R. M. Mobley, J. M. Bailey, W. E. Cleland, V. W. Hughes, and J. E. Rothberg. Muonium Chemistry. *The Journal of Chemical Physics*, 44(11):4354–4355, 1966.

[13] C. G. Parthey, A. Matveev, J. Alnis, B. Bernhardt, A. Beyer, R. Holzwarth, A. Maistrou, R. Pohl, K. Predehl, T. Udem, T. Wilken, N. Kolachevsky, M. Abgrall, D. Rovera, C. Salomon, P. Laurent, and T. W. Hänsch. Improved Measurement of the Hydrogen $1S - 2S$ Transition Frequency. *Physical Review Letters*, 107:203001, Nov 2011.

[14] H. Hellwig, R. F. C. Vessot, M. W. Levine, P. W. Zitzewitz, D. W. Allan, and D. J. Glaze. Measurement of the Unperturbed Hydrogen Hyperfine Transition Frequency. *IEEE Transaction on Instrumentation and Measurement*, 19(4):200 –209, nov. 1970.

[15] N. F. Ramsey. Experiments with trapped hydrogen atoms and neutrons. *Hyperfine Interactions*, 81:97–103, 1993.

[16] M. Eides, H. Grotch, and V. Shelyuto. *Theory of light hydrogenic bound states*. Springer tracts in modern physics. Springer, 2007.

[17] M. W. Ritter, P. O. Egan, V. W. Hughes, and K. A. Woodle. Precision determination of the hyperfine-structure interval in the ground state of positronium. V. *Physical Review A*, 30(3):1331–1338, Sep 1984.

[18] B. A. Kniehl and A. A. Penin. Order $\alpha^7 \ln(1/\alpha)$ Contribution to Positronium Hyperfine Splitting. *Physical Review Letters*, 85(24):5094–5097, Dec 2000.

[19] A. Ishida, T. Namba, S. Asai, T. Kobayashi, H. Saito, M. Yoshida, K. Tanaka, and A. Yamamoto. New precision measurement of hyperfine splitting of positronium. *Physics Letters B*, 734:338 – 344, 2014.

[20] V. Hughes and C. Wu. *Muon physics*. Number v.2 in Muon Physics. Academic Press, 1977.

[21] R. Faustov. Magnetic moment of the hydrogen atom. *Physics Letters B*, 33(6):422 – 424, 1970.

[22] M. I. Eides. Weak-interaction contributions to hyperfine splitting and Lamb shift. *Physical Review A*, 53:2953–2957, May 1996.

[23] S. G. Karshenboim. Leading logarithmic corrections and uncertainty of Muonium hyperfine splitting calculations. *Zeitschrift fur Physik D Atoms, Molecules and Clusters*, 36:11–15, 1996.

[24] A. Czarnecki, S. I. Eidelman, and S. G. Karshenboim. Muonium hyperfine structure and hadronic effects. *Physical Review D*, 65:053004, Jan 2002.

[25] R. Bluhm, V. A. Kostelecký, and C. D. Lane. *CPT* and Lorentz Tests with Muons. *Phys. Rev. Lett.*, 84:1098–1101, Feb 2000.

[26] G. W. Bennett, B. Bousquet, H. N. Brown, G. Bunce, R. M. Carey, P. Cushman, G. T. Danby, P. T. Debevec, M. Deile, H. Deng, W. Deninger, S. K. Dhawan, V. P. Druzhinin, L. Duong, E. Efstathiadis, F. J. M. Farley, G. V. Fedotovich, S. Giron, F. E. Gray, D. Grigoriev, M. Grosse-Perdekamp, A. Grossmann, M. F. Hare, D. W. Hertzog, X. Huang, V. W. Hughes, M. Iwasaki, K. Jungmann, D. Kawall, M. Kawamura, B. I. Khazin, J. Kindem, F. Krienen, I. Kronkvist, A. Lam, R. Larsen, Y. Y. Lee, I. Logashenko, R. McNabb, W. Meng, J. Mi, J. P. Miller, Y. Mizumachi, W. M. Morse, D. Nikas, C. J. G. Onderwater, Y. Orlov,

C. S. Özben, J. M. Paley, Q. Peng, C. C. Polly, J. Pretz, R. Prigl, G. z. Putlitz, T. Qian, S. I. Redin, O. Rind, B. L. Roberts, N. Ryskulov, S. Sedykh, Y. K. Semertzidis, P. Shagin, Y. M. Shatunov, E. P. Sichtermann, E. Solodov, M. Sossong, A. Steinmetz, L. R. Sulak, C. Timmermans, A. Trofimov, D. Urner, P. v. Walter, D. Warburton, D. Winn, A. Yamamoto, and D. Zimmerman. Search for Lorentz and CPT Violation Effects in Muon Spin Precession. *Phys. Rev. Lett.*, 100:091602, Mar 2008.

[27] V. A. Kostelecký and N. Russell. Data tables for Lorentz and CPT violation. *Rev. Mod. Phys.*, 83:11–31, Mar 2011.

[28] R. Pohl, A. Antognini, F. Nez, F. D. Amaro, F. Biraben, J. M. R. Cardoso, D. S. Covita, A. Dax, S. Dhawan, L. M. P. Fernandes, A. Giesen, T. Graf, T. W. Hänsch, P. Indelicato, L. Julien, C.-Y. Kao, P. Knowles, E.-O. Le Bigot, Y.-W. Liu, J. A. M. Lopes, L. Ludhova, C. M. B. Monteiro, F. Mulhauser, T. Nebel, P. Rabinowitz, J. M. F. d. Santos, L. A. Schaller, K. Schuhmann, C. Schwob, D. Taqqu, J. F. C. A. Veloso, and F. Kottmann. The size of the proton. *Nature*, 466(7303):213–216, jul 2010.

[29] S. J. Brodsky, C. E. Carlson, J. R. Hiller, and D. S. Hwang. Erratum: Constraints on Proton Structure from Precision Atomic-Physics Measurements. *Physical Review Letters*, 94:169902, Apr 2005.

[30] S. G. Karshenboim. Constraints on a long-range spin-dependent interaction from precision atomic physics. *Physical Review D*, 82:113013, Dec 2010.

[31] S. G. Karshenboim and V. V. Flambaum. Constraint on axionlike particles from atomic physics. *Physical Review A*, 84:064502, Dec 2011.

[32] S. G. Karshenboim, D. McKeen, and M. Pospelov. Constraints on muon-specific dark forces. *Physical Review D*, 90:073004, Oct 2014.

[33] V. W. Hughes, D. W. McColm, K. Ziock, and R. Prepost. Formation of Muonium and Observation of its Larmor Precession. *Physical Review Letters*, 5(2):63–65, Jul 1960.

[34] R. Prepost, V. W. Hughes, and K. Ziock. Observation of the Hyperfine Structure Splitting of Muonium by Use of a Static Magnetic Field. *Physical Review Letters*, 6(1):19–21, Jan 1961.

[35] J. M. Bailey, W. E. Cleland, V. W. Hughes, R. Prepost, and K. Ziock. Muonium. II. Observation of the Muonium Hyperfine-Structure Interval. *Physical Review A*, 3(3):871–884, Mar 1971.

[36] R. D. Ehrlich, H. Hofer, A. Magnon, D. Stowell, R. A. Swanson, and V. L. Telegdi. Determination of the Muonium Hyperfine Splitting at Low Pressure from a Field-Independent Zeeman Transition. *Physical Review Letters*, 23(10):513–517, Sep 1969.

[37] W. E. Cleland, J. M. Bailey, M. Eckhause, V. W. Hughes, R. M. Mobley, R. Prepost, and J. E. Rothberg. New Value for the Fine-Structure Constant α from Muonium Hyperfine Structure Interval. *Physical Review Letters*, 13(6):202–205, Aug 1964.

[38] W. E. Cleland, J. M. Bailey, M. Eckhause, V. W. Hughes, R. Prepost, J. E. Rothberg, and R. M. Mobley. Muonium. III. Precision Measurement of the Muonium Hyperfine-Structure Interval at Strong Magnetic Field. *Physical Review A*, 5(6):2338–2356, Jun 1972.

[39] V. W. Hughes. Muonium. *Annual Review of Nuclear Science*, 16(1):445–470, 1966.

[40] P. A. Thompson, J. J. Amato, P. Crane, V. W. Hughes, R. M. Mobley, G. z. Putlitz, and J. E. Rothberg. Determination of Muonium Hyperfine Structure Interval Through Measurements at Low Magnetic Fields. *Physical Review Letters*, 22(5):163–167, Feb 1969.

[41] R. D. Ehrlich, H. Hofer, A. Magnon, D. Y. Stowell, R. A. Swanson, and V. L. Telegdi. Precision Experiments on Muonium. I. Determination of the Muonium Hyperfine Splitting in Low-Pressure Argon from a Field-Independent Zeeman Transition. *Physical Review A*, 5(6):2357–2375, Jun 1972.

[42] R. De Voe, P. M. McIntyre, A. Magnon, D. Y. Stowell, R. A. Swanson, and V. L. Telegdi. Measurement of the Muonium Hfs Splitting and of the Muon Moment by "Double Resonance," and a New Value of α. *Physical Review Letters*, 25(26):1779–1783, Dec 1970.

[43] P. A. Thompson, P. Crane, T. Crane, J. J. Amato, V. W. Hughes, G. z. Putlitz, and J. E. Rothberg. Muonium. IV. Precision Measurement of the Muonium Hyperfine-Structure Interval at Weak and Very Weak Magnetic Fields. *Physical Review A*, 8(1):86, Jul 1973.

[44] D. Favart, P. M. McIntyre, D. Y. Stowell, V. L. Telegdi, R. DeVoe, and R. A. Swanson. Precision Experiments on Muonium. III. Ramsey Resonance in Zero Field. *Phys. Rev. A*, 8:1195–1218, Sep 1973.

[45] D. E. Casperson, T. W. Crane, V. W. Hughes, P. A. Souder, R. D. Stambaugh, P. A. Thompson, H. Orth, G. Zu Putlitz, H. F. Kaspar, H. W. Reist, and A. B. Denison. A new high precision measurement of the muonium hyperfine structure interval . *Physics Letters B*, 59:397–400, November 1975.

[46] D. E. Casperson, T. W. Crane, A. B. Denison, P. O. Egan, V. W. Hughes, F. G. Mariam, H. Orth, H. W. Reist, P. A. Souder, R. D. Stambaugh, P. A. Thompson, and G. z. Putlitz. Erratum: New Precise Value for the Muon Magnetic Moment and Sensitive Test of the Theory of the hfs Interval in Muonium. *Physical Review Letters*, 38(17):956–959, Apr 1977.

[47] D. E. Casperson, T. W. Crane, A. B. Denison, P. O. Egan, V. W. Hughes, F. G. Mariam, H. Orth, H. W. Reist, P. A. Souder, R. D. Stambaugh, P. A. Thompson, and G. z. Putlitz. New Precise Value for the Muon Magnetic Moment and Sensitive

Test of the Theory of the hfs Interval in Muonium. *Physical Review Letters*, 38(25):1504, Jun 1977.

[48] F. G. Mariam, W. Beer, P. R. Bolton, P. O. Egan, C. J. Gardner, V. W. Hughes, D. C. Lu, P. A. Souder, H. Orth, J. Vetter, U. Moser, and G. z. Putlitz. Higher Precision Measurement of the hfs Interval of Muonium and of the Muon Magnetic Moment. *Physical Review Letters*, 49(14):993–996, Oct 1982.

[49] K. Olive et al. Review of particle physics. *Chin.Phys.*, C38:090001, 2014.

[50] N. Kawamura and A. Toyoda. H Line; A Beamline for Fundamental Physics in J-PARC. *JPS Conference Proceedings*, 2, 2014.

[51] K. P. Jungmann. Past, Present and Future of Muonium, 2004.

[52] S. Karshenboim. *The Hydrogen Atom: Precision Physics of Simple Atomic Systems (Lecture Notes in Physics)*. Springer, 2001.

[53] A. Badertscher, S. Dhawan, P. O. Egan, V. W. Hughes, D. C. Lu, M. W. Ritter, K. A. Woodle, M. Gladisch, H. Orth, G. z. Putlitz, M. Eckhause, J. Kane, F. G. Mariam, and J. Reidy. Formation of Muonium in the $2S$ State and Observation of the Lamb Shift Transition. *Physical Review Letters*, 52:914–917, Mar 1984.

[54] A. P. Mills, J. Imazato, S. Saitoh, A. Uedono, Y. Kawashima, and K. Nagamine. Generation of Thermal Muonium in Vacuum. *Physical Review Letters*, 56:1463–1466, Apr 1986.

[55] A. C. Janissen, G. A. Beer, G. R. Mason, A. Olin, T. M. Huber, A. R. Kunselman, T. Bowen, P. G. Halverson, C. A. Fry, K. R. Kendall, G. M. Marshall, and J. B. Warren. Muonium production from fine silica powder. *Physical Review A*, 42:161–169, Jul 1990.

[56] J. R. Musser, R. Bayes, Y. I. Davydov, P. Depommier, J. Doornbos, W. Faszer, C. A. Gagliardi, A. Gaponenko, D. R. Gill, P. Green, P. Gumplinger, M. D. Hasinoff, R. S. Henderson, J. Hu, B. Jamieson, P. Kitching, D. D. Koetke, A. A.

Krushinsky, Y. Y. Lachin, J. A. Macdonald, R. P. MacDonald, G. M. Marshall, E. L. Mathie, L. V. Miasoedov, R. E. Mischke, P. M. Nord, K. Olchanski, A. Olin, R. Openshaw, T. A. Porcelli, J.-M. Poutissou, R. Poutissou, M. A. Quraan, N. L. Rodning, V. Selivanov, G. Sheffer, B. Shin, F. Sobratee, T. D. S. Stanislaus, R. Tacik, V. D. Torokhov, R. E. Tribble, M. A. Vasiliev, and D. H. Wright. Measurement of the Michel Parameter ρ in Muon Decay. *Physical Review Letters*, 94:101805, Mar 2005.

[57] http://www.srim.org/.

[58] D. Pozar. *Microwave engineering*. J. Wiley, 2005.

[59] http://www.ni.com/.

[60] W. Happer. Optical Pumping. *Reviews of Modern Physics*, 44:169–249, Apr 1972.

[61] S. Ray and S. L. Kaufman. Theoretical Interpretation of the Quadratic Hyperfine Pressure Shift. *Physical Review Letters*, 29:895–898, Oct 1972.

[62] D. Casperson, T. Crane, V. Hughes, P. Souder, R. Stambaugh, P. Thompson, H. Orth, G. z. Putlitz, H. Kaspar, H. Reist, and A. Denison. A new high precision measurement of the muonium hyperfine structure interval. *Physics Letters B*, 59(4):397 – 400, 1975.

[63] K. M. Kojima, T. Murakami, Y. Takahashi, H. Lee, S. Y. Suzuki, A. Koda, I. Yamauchi, M. Miyazaki, M. Hiraishi, H. Okabe, S. Takeshita, R. Kadono, T. Ito, W. Higemoto, S. Kanda, Y. Fukao, N. Saito, M. Saito, M. Ikeno, T. Uchida, and M. M. Tanaka. New μSR spectrometer at J-PARC MUSE based on Kalliope detectors. *Journal of Physics: Conference Series*, 551(1):012063, 2014.

[64] S. Kanda and Y. Ueno and K. S. Tanaka for the MuSEUM collaboration. Development of 3D imaging of muon stopping distribution for Muonium HFS measurement. *KEK-MSL Progress Report 2014*, 2015. to be published.

[65] S. Kanda for the MuSEUM collaboration. Development of a new positron counting system with SiPM readout for muon spin spectrometers. *PoS*, PhotoDet2015, 2015. to be published.

[66] C. L. Morgan and E. S. Ensberg. Precise Hyperfine Pressure-Shift Measurements for Hydrogen Isotopes in Argon. *Physical Review A*, 7:1494–1502, May 1973.

[67] W. R. C. (Ed.). *Handbook of Chemistry and Physics (53rd Edn.)*. Springer tracts in modern physics. Chemical Rubber Company, 1972.

[68] W. Liu. *HIGH PRECISION MEASUREMENT OF MUONIUM GROUND STATE HYPERFINE INTERVAL AND MUON MAGNETIC MOMENT*. PhD thesis, Yale University, 1997.

[69] Y. I. Neronov and N. N. Seregin. Precision determination of the difference in shielding by protons in water and hydrogen and an estimate of the absolute shielding by protons in water. *Metrologia*, 51(1):54, 2014.

[70] B. W. Petley and R. W. Donaldson. The Temperature Dependence of the Diamagnetic Shielding Correction for Proton NMR in Water. *Metrologia*, 20(3):81, 1984.

[71] http://www.cobham.com/.

[72] G. A. Clarke. Effects of Helium Buffer Gas Atoms on the Atomic Hydrogen Hyperfine Frequency. *The Journal of Chemical Physics*, 36(8):2211–2216, 1962.

[73] O. Kamigaito. Circuit-model representation of external-Q calculation. *Physical Review ST Accelerators and Beams*, 9:062003, Jun 2006.

[74] D. Nomura and T. Teubner. Hadronic contributions to the anomalous magnetic moment of the electron and the hyperfine splitting of muonium. *Nuclear Physics B*, 867(2):236 – 243, 2013.

[75] M. Niering, R. Holzwarth, J. Reichert, P. Pokasov, T. Udem, M. Weitz, T. W. Hänsch, P. Lemonde, G. Santarelli, M. Abgrall, P. Laurent, C. Salomon, and A. Clairon. Measurement of the Hydrogen $1S$- $2S$ Transition Frequency by Phase Coherent Comparison with a Microwave Cesium Fountain Clock. *Physical Review Letters*, 84(24):5496–5499, Jun 2000.

[76] M. Fischer, N. Kolachevsky, M. Zimmermann, R. Holzwarth, T. Udem, T. W. Hänsch, M. Abgrall, J. Grünert, I. Maksimovic, S. Bize, H. Marion, F. P. D. Santos, P. Lemonde, G. Santarelli, P. Laurent, A. Clairon, C. Salomon, M. Haas, U. D. Jentschura, and C. H. Keitel. New Limits on the Drift of Fundamental Constants from Laboratory Measurements. *Physical Review Letters*, 92(23):230802, Jun 2004.

[77] S. G. Karshenboim. Nuclear structure-dependent radiative corrections to the hydrogen hyperfine splitting. *Physics Letters A*, 225(1-3):97 – 106, 1997.

[78] S. G. Karshenboim, S. I. Eidelman, P. Fendel, V. G. Ivanov, N. N. Kolachevsky, V. A. Shelyuto, and T. W. Hansch. Study of hyperfine structure in simple atoms and precision tests of the bound state QED. *Nucl. Phys. B, Proc. Suppl.*, 162(hep-ph/0608236):260–263, Aug 2006.

[79] D. Favart, P. M. McIntyre, D. Y. Stowell, V. L. Telegdi, R. DeVoe, and R. A. Swanson. Quadratic hfs Pressure Shifts of Muonium in Argon and Krypton. *Physical Review Letters*, 27(20):1340–1342, Nov 1971.

[80] H. G. E. Kobrak, R. A. Swanson, D. Favart, W. Kells, A. Magnon, P. M. McIntyre, J. Roehrig, D. Y. Stowell, V. L. Telegdi, and M. Eckhause. A new precision measurement of the muonium hyperfine interval in argon. *Physics Letters B*, 43(6):526 – 528, 1973.

[81] S. Karshenboim. Simple Atoms, Quantum Electrodynamics, and Fundamental Constants. In *Precision Physics of Simple Atomic Systems*, volume 627 of *Lecture*

Notes in Physics, pages 141–162. Springer Berlin / Heidelberg, 2003. 10.1007/978-3-540-45059-7-8.

[82] F. Jegerlehner and A. Nyffeler. The muon. *Physics Reports*, 477(1-3):1 – 110, 2009.

[83] S. G. and Karshenboim. Precision physics of simple atoms: QED tests, nuclear structure and fundamental constants. *Physics Reports*, 422(1-2):1 – 63, 2005.

[84] P. J. Mohr, B. N. Taylor, and D. B. Newell. CODATA recommended values of the fundamental physical constants: 2006. *Journal of Physical and Chemical Reference Data*, 37(3):1187–1284, 2008.

[85] http://www.fieldp.com/.

[86] http://www.autodesk.com/.

[87] Industrial platinum resistance thermometers and platinum temperature sensors, 2008.

[88] R. S. Van Dyck, P. B. Schwinberg, and H. G. Dehmelt. New high-precision comparison of electron and positron g factors. *Physical Review Letters*, 59:26–29, Jul 1987.

[89] P. J. Mohr, B. N. Taylor, and D. B. Newell. CODATA recommended values of the fundamental physical constants: 2006. *Reviews of Modern Physics*, 80:633–730, Jun 2008.

[90] S. G. Karshenboim. Precision Physics of Simple Atoms and Constraints on a Light Boson with Ultraweak Coupling. *Physical Review Letters*, 104:220406, Jun 2010.

[91] S. Kanda for the MuSEUM collaboration. Development of online muon beam profile monitor for the MuSEUM experiment. *RIKEN Accelerator Progress Report 2014*, 2015.

[92] D. Ciskowski, H. Ahn, R. Dixson, X. Fei, V. Hughes, B. Matthias, C. Pillai, and K. Woodle. A chopped high intensity muon beam at the Stopped Muon Channel at LAMPF. *Nuclear Instruments and Methods in Physics Research Section A: Accelerators, Spectrometers, Detectors and Associated Equipment*, 333(23):260 – 264, 1993.

Acknowledement

修士課程から博士課程に渡り、様々な機会でご指導くださった松田恭幸先生に感謝を致します。また、ミュオニウムの超微細構造という魅力的な研究の機会を与えてくださった高エネルギー加速器研究所の下村浩一郎先生に感謝致します。

山崎泰規先生には修士 1 年次の CERN における実験における研究の機会を与えてくださり、基礎物理に対して志すきっかけとなりました。研究室の鳥居寛之先生には、普段の研究生活を含めたあらゆる面においてご指導いただき、本論文執筆にあたっても貴重な助言を多くいただきました。黒田直史先生には修士 1 年次の CERN における実験において実験から生活面に関してご指導いただきました。理化学研究所岩崎先端中間子研究室の岩崎雅彦先生には博士課程 3 年次より理研の JRA として研究を行う機会を与えてくださり、本研究に打ち込むことができました。石田勝彦先生には本研究の計画段階からたくさんの助言をくださり、大いに励みになりました。

理化学研究所仁科センターの上垣外修一先生、坂本成彦先生、須田健嗣先生には CST microwave studio を使わせていただき、RF キャビティの性能評価のために修士２年次にネットワークアナライザ及び実験室をお貸ししていただきました。

本実験の共同研究者である齊藤直人博士、三部勉博士、佐々木憲一博士、豊田晃久博士、David Kawall 博士、Patrick Strasser 博士、深尾祥紀博士は装置開発から実験計画まで多岐にわたって様々な助言を下さりました。小嶋健児博士、幸田章宏博士、河村成肇博士、三宅康博博士にはビーム実験において多大なサポートをしてくださり MLF 施設における実験を円滑に進めることができました。神田聡太郎君、水谷丈洋君、上野恭裕君、東芳隆君は本実験において共同開発を行い多くの場面で助けてもらいました。

高エネルギー加速器研究機構加速器部門の吉田光宏博士、佐藤大輔氏にはゼロ磁場実験用の信号発生器やネットワークアナライザをお貸しいただき、強磁場実験と相補

的にゼロ磁場実験を行うというアイデアを進めることができました。

本テーマではありませんが、修士 1 年次の CERN においては、檜垣浩之先生、永田祐吾博士、榎本嘉範博士、満汐孝治博士には多くのことを教えていただき、本テーマをすすめる上で大きな基礎となりました。

私の研究室の同期にあたる大塚未来さん、藤居甲基君は研究室の様々な場面で支えあってきた仲間であり、大変感謝しています。

また、東京大学総合文化研究科山崎松田研究室の皆さま、高エネルギー加速器研究所の皆さま、理化学研究所の皆さまの他、多くの人々の助けによってこのように博士論文をまとめることができました。厚くお礼申しあげます。

最後に経済的にも精神的にも集中して研究する環境を支えてくれた家族に感謝します。